UNIVERSITY OF SOUTHAMPTON

FACULTY OF ENGINEERING & THE ENVIRONMENT

Energy Technology Research Group

Improvements to the Soluble Lead Redox Flow Battery

by

Muthukumaran Kandaswamy Krishna

Thesis for the degree of Doctor of Philosophy

June 2017

UNIVERSITY OF SOUTHAMPTON

ABSTRACT

FACULTY OF ENGINEERING & THE ENVIRONMENT
Energy Technology Research Group

Doctor of Philosophy

IMPROVEMENTS TO THE SOLUBLE LEAD REDOX FLOW BATTERY

by Muthukumaran Kandaswamy Krishna

Redox flow batteries are energy storage devices that have successfully been commercialised and demonstrated on the MW/MWh scale for various power applications, such as renewables capacity firming. The vanadium and zinc-bromine systems, having been developed over several decades, are currently the most advanced. However, their respective limitations have invited research into other chemistries. Soluble lead is one such alternative, in which both electrode reactions involve just one active species, Pb^{2+}. The electrolyte is inherently safer than many other systems, and proof-of-concept studies have highlighted its suitability for scale-up. In this thesis, the next stage of this process is reported. Fundamental gaps in electrolyte properties, such as conductivity and viscosity, are explored before extensive charge/discharge cycling experiments are carried out in order to optimise the electrolyte, which includes a novel combination of additives. Traditional soluble lead flow cells did not require a separator, which greatly reduced the cost and complexity of the system. However, by inserting a separator and exploring both a standard division and a novel semi-divided configuration, significant improvements to cell efficiency and lifetime are achieved compared to the literature. A flow cell with 100 cm^2 electrodes is used to investigate the cell power at different states of charge, peaking at 12.5 W. The results also infer that higher currents on discharge can be drawn than from other well-established chemistries. A method of regenerating a failed cell is also shown, where a series of maintenance cycles brings the system close to its initial conditions. The improvements in this project are used to model a flow battery stack, using another commercial device as a benchmark. Unaddressed gaps in the research for the next stage of scaling-up are also discussed.

Contents

List of Figures

List of Tables

Declaration of Authorship

I, Muthukumaran Kandaswamy Krishna, declare that the thesis entitled *Improvements to the Soluble Lead Redox Flow battery* and the work presented in the thesis are both my own, and have been generated by me as the result of my own original research. I confirm that:

- this work was done wholly or mainly while in candidature for a research degree at this University;
- where any part of this thesis has previously been submitted for a degree or any other qualification at this University or any other institution, this has been clearly stated;
- where I have consulted the published work of others, this is always clearly attributed;
- where I have quoted from the work of others, the source is always given. With the exception of such quotations, this thesis is entirely my own work;
- I have acknowledged all main sources of help;
- where the thesis is based on work done by myself jointly with others, I have made clear exactly what was done by others and what I have contributed myself;
- parts of this work have been published, and this is detailed in Chapter 1.9

Signed:.....

Date:.....

Acknowledgements

I would like to first convey my deepest gratitude to my PhD supervisor, Dr. Richard Wills. I cannot thank him enough for his kindness, teaching and patience throughout these past years, which instilled the importance of scientific methodology, electrochemical principles and laboratory safety into a young engineer. All the results in this thesis began by just "having a play" in the lab, as Richard often instructed. I would also like to extend these words of thanks to Dr. Carlos Ponce de León Albarrán, whose undergraduate module first sparked my interest in battery technology, and Professor Frank Walsh, who always had time to advise me on my work, or indeed, to discuss an episode from Star Trek. Both contributed greatly to my research and were always available whenever a problem arose. I must also thank Dr. Norberto Casillas Santana (Universidad de Guadalajara) for his excellent explanation of several electrochemical concepts, as well as other lessons. The passion these four scientists have for their work will always be an inspiration for me. Thank you to Dr. David Hall and Dr. John Collins (C-Tech Innovation Ltd.), who, along with supplying the 100 cm^2 flow cell and test rig, imparted their experience and knowledge to me during the early stages of my research. Thank you also to Dr. Pui-ki Leung, whose 9 cm^2 cell was used for several important experiments. I am also grateful to the Department of Energy & Climate Change for their financial support throughout my PhD.

My work in the Electrochemical Engineering Laboratory would not have been the same without the friends and colleagues who have moulded me into who I am today. Fernando Arenas in particular was always working beside me in the lab, sharing his ideas and enlightening me on several chemical techniques. In addition, I would like to mention Sarah Dreuilhe (for many things, including her help with MatLab), Arslan Ahmed, Rachel McKerracher, Derek Egan, Maria Kourasi, Badr Alshammary, Keletso Orapeleng, Lauren Wallis, Christian Harito, Horacio Figueredo, Alex Holland, Steven Broderick, Nicholas Hernandez & Alysson Martins for their friendship over the years. It has been a privilege working alongside you and I wish you all the best for the future. I would not have had the opportunity of a PhD if it had not been for all the excellent teachers throughout my life, from school to University. In particular, I would like to express my gratefulness to my maths teachers: Mrs. Bradley, Mr. Schuil and Mr. Homer; my chemistry teachers: Ms. Good, Mrs. Hopwood and Mr. Todd; and

my physics teachers: Mr. Ball, Mrs. Harris and Mr. Broomsgrove. Finally, words cannot express my gratitude to my oldest teachers, my parents. They provided me with everything and, along with my sister, always supported me.

Nomenclature & Symbols

Abbreviation	Description
AGM	absorptive glass mat
CV	cyclic voltammetry
EDTA	ethylenediaminetetraacetic acid
EDX	energy-dispersive X-ray spectroscopy
HDTMA	hexadecyltrimethylammonium
LAB	lead-acid battery
MSA	methanesulfonic acid
PVP	polyvinylpyrrolidone
RDE	rotating disc electrode
RVC	reticulated vitreous carbon
SCE	saturated calomel electrode
SEM	scanning electron microscope
SoC	state of charge
SHE	standard hydrogen electrode
SLFB	soluble lead redox flow battery
VRFB	all-vanadium redox flow battery
VRLAB	valve regulated lead-acid battery
ZBFB	zinc-bromine redox flow battery

Symbol	Description	Units
A	electrode active area	cm^2
B	Breadth of flow channel	cm
c	concentration of the active species	mol dm^{-3}
c_o	initial concentration of active species	mol dm^{-3}
d	characteristic dimension of a flow channel	cm
d_e	equivalent hydraulic diameter	cm
d_{ed}	thickness of electrodeposit	cm
D	diffusion coefficient	cm^2 s^{-1}
e	energy density of electrolyte	Wh kg^{-1}
E	electrode potential vs. reference electrode	V
E^e	electrode equilibrium potential vs. reference electrode	V
E^o	electrode standard potential vs. reference electrode	V
E_{cell}	cell potential	V
E^e_{cell}	cell equilibrium potential under non-standard conditions	V
E^o_{cell}	cell equilibrium potential under standard conditions	V
F	Faraday's constant	C $eq.^{-1}$
$\triangle G$	Gibbs free energy change for a certain reaction	J mol^{-1}
I	current	A
j	current density	mA cm^{-2}
k_m	mass transport (transfer) coefficient	cm s^{-1}
L	electrode length, parallel to flow direction	cm
L_p	length of pipe	cm
M_r	molecular mass	g mol^{-1}
n	moles converted at an electrode surface	-
$\triangle P$	pressure drop	Pa
Q	charge	C
Q_c	charge supplied to cell during charging	C
Q_{dc}	charge drawn from cell during discharge	C
r	radius of pipe	cm

R	universal gas constant (8.31)	J mol^{-1} K^{-1}
R_n	resistance of cell component n	Ω
S	inter-electrode / electrode-separator gap	cm
t_c	charging time	s
t_{dc}	discharge time	s
T	Temperature	K
v	linear flow velocity	cm s^{-1}
V	volumetric flow rate	cm^3 s^{-1}
W	pump power	W
z	electron equivalent (eq.) per mole reactant	eq. mol^{-1}
Re	Reynolds number	-
η	activation and/or concentration overpotential	V
μ	absolute (dynamic) viscosity	mPa·s
ρ	electrolyte or deposit density	g cm^{-3}
ν	kinematic viscosity	cm^2 s^{-1}
ϕ	Faradaic (current) efficiency	-
Ψ_{EN}	energy efficiency	%
Ψ_P	pump efficiency	%
Ψ_Q	charge efficiency	%
Ψ_V	voltage efficiency	%

To my Parents, Drs Usha and Kandaswamy Krishna,
and my sister Priya Krishna

"The probability, as a result of the specific series of natural events, and decisions made by each of my ancestors and those around them, that I should be here in Southampton at this time to conduct this research is incredibly infinitesimal."

"In short, this malleable and dense metal, once favoured for figurines, now powers and protects our modern world."
International Lead Association

Chapter 1

Introduction

1.1 Global Electricity Generation

According to the World Energy Council [1], the human population increased by 27% between 1993 and 2011 to 7 billion and is expected to surpass 8 billion by 2020. Due to the growth of technology and widespread economic development, 1993 - 2011 also saw a 78% increase in global electricity generation. Renewable energies, encompassing hydropower, solar, wind, biofuel, biomass, geothermal, tidal and wave energies, generated approximately 21% of the global electricity supply in 2011, and this share is expected to rise to 26% by 2020 [2]. This is summarised in Table 1.1.

	1993	**2011**	**2020**
Human Population / bn	5.5	7.0	8.1
Overall Annual Electricity Generation / PWh	11.9	21.2	23.0
of which generated by renewables / PWh	2.5	4.4	6.0
Overall Annual CO_2 Emissions[i] / Gt	21	30	42

Table 1.1: Summary of the changes in human population and global electricity generation over the period 1993 - 2011, and the forecast for 2020 [1,2]. [i]Overall emissions, from electricity generation, transport, industry etc., does not account for other greenhouse gas emissions.

Despite the growth in renewables, carbon dioxide emissions are expected to continue growing; emissions in 2020 will be twice that released in 1993 (not accounting for greenhouse gases

other than carbon dioxide). Research has made it evident that over the past 50 years, anthropogenic greenhouse gas emissions have led to a rise in the average global temperature. This has been linked with rising sea levels due to glacier melt and large variations in weather patterns across the world, such as extreme heat and intense rainfall [3]. Additionally, air pollution from greenhouse gas emissions has been linked with 5.5 million premature deaths in 2013, the majority in densely populated cities in China and India [4]. It is clear that such a heavy reliance on fossil fuels cannot be part of a sustainable future.

1.2 The Need for Energy Storage

A bold strategy is required to revolutionise the way electrical energy is generated in order to meet growing energy needs and to mitigate the effects of accelerated climate change. This would involve the vast deployment of renewable energies in addition to the modernisation of electrical grids worldwide. The majority of these grids are one way, i.e. from the generator to the consumer. It can be argued that this makes it difficult to respond quickly to the fluctuations of energy demand, leading to a system where power plants are constantly producing a greater amount than what is required, leading to much energy being wasted [5]. It is essential therefore to develop a system through the use of sensors across the grid where real time information is gathered on how energy is used by the consumer and generated by the supplier. This can be relayed to an automated centre, local or regional, which can optimise how to meet the energy demand in that area whilst minimising the energy wasted. This is known as a 'smart grid' [6]. Energy storage systems (ESS) would play a vital role in such networks, which would also benefit the integration of renewable energies. Presented below is a list of some of the most important applications of ESS, as defined by the US Department of Energy (DOE) [7]:

1. ***Renewables Capacity Firming***: The intermittent supply of power from renewable energy sources can place strain on the electrical network in terms of maintaining power and nominal frequency (i.e. ***Frequency Regulation***), for example sudden output dips due to cloud cover affecting solar farms and sudden output peaks due to high winds affecting wind farms. ESS can alleviate these fluctuations by storing and releasing

energy moment-by-moment accordingly in order to control these power swings, thereby smoothing the output into the grid.

2. ***Load Levelling and Peak Shaving***: This involves the storage of excess energy during longer periods (on the scale of hours) of low demand and supplying power during periods when the demand is high. This reduces the stress on power generation facilities and is particularly important for renewable energy, where the energy supply often does not match the energy demand. In 2014, wind farms in the UK were paid £53.1 mn to switch off during exceptionally windy weather in order to prevent overcharging the grid [8], wasting much energy. ESS could decouple energy demand and supply, minimising the energy wasted. Peak power generation is then reduced, leading to savings for consumers.

3. ***Energy Arbitrage***: Because the price of electricity varies during the day, energy can be stored during low price times and discharged when the price is high. This would increase the profit margin of the ESS owner and acts as a further incentive for renewable energy investment [9, 10].

4. ***Transmission and Distribution Congestion Relief***: 'Transmission' is the movement of electricity from power generation centres to electrical substations. 'Distribution' is the movement of electricity downstream, i.e. from substations to the customer. During periods of peak electricity demand, both electrical transmission and distribution (T & D) streams can become overburdened, requiring the constant upgrading of substations and other (T & D) systems, and leading to congestion charges for the downstream consumer. Energy storage can provide relief to these congested corridors and increase the interval between periods where the T & D systems need to be upgraded. This is also known as ***T & D Upgrade Deferral***.

5. ***Spinning Reserve***: ESS with fast response times can be used to provide power when there is a transmission outage in the grid. Here, the ESS is maintained at a specific charge state and comes online in emergencies to maintain the power supply until the main power or a backup generator comes online.

1.3 Types of Energy Storage

In 1929, the 29 MW Rocky river pumped hydroelectric plant in Connecticut, USA became the world's first ESS installation, and it is still operational today [11]. Pumped hydro is the most well-established storage system of modern time, accounting for 95% of the 188 GW of storage power in place around the world [12]. However, hydropower remains controversial: cement production and construction depends on energy from fossil fuels and once complete, methane and other greenhouse gases are released from flooded reservoirs from rotting organic matter [13]. Hydropower is also expensive to manage and sites are geographically limited. In addition, such structures have a significant impact on land use and natural ecosystems; work published by Agostinho et al. [14] in 2008 discusses the decline in fish diversity influenced by dams in the Paraná river basin in Brazil.

Since 1929, interest in alternative energy storage technologies has been growing alongside renewable energy capture. The battery market has grown and diversified with different chemistries emerging for applications as diverse as electronic equipment, electric vehicles and uninterruptible power supplies (UPS). There have been developments with supercapacitors, flywheels and superconducting magnetic energy storage (SMES), which offer rapid response times and high power for short durations, making them ideal for frequency regulation or as a spinning reserve. Each has its relative benefits and disadvantages, and has been critically reviewed [5, 15]. There is no one perfect ESS that would support all electrical applications. The choice is a compromise between power, energy and cost. Figure 1.1 places these numerous technologies in perspective, presenting the various power scales of each system. For example, pumped hydro is well suited for grid management, where long periods of high power is often required for load levelling and peak shaving. The figure is based on the graph published by Sandia National Laboratories [15] but modified with current information from the US DOE [12].

Most of the systems here are classed as 'electrochemical devices', i.e. supercapacitors and secondary batteries, the latter of which the lead-acid battery is the oldest and until recently the most popular in terms of global annual sales (45% of all sold batteries by revenue in 2002 [16]; this has now been overtaken by lithium-ion [17]). Flexibility in design makes this

battery popular for UPS services and grid support, as well as the automotive industry. At a rating of 50 MW/300 MWh, the largest battery installation in the world is the sodium-sulfur system at the Buzen substation in Fukuoka, Japan, constructed by Mitsubishi Electric Corp. for Kyushu Electric Power Co. [18]. Operational since March 2016, it is used for frequency regulation and renewables capacity firming. However, performance metrics are not yet available.

Thermal energy storage (TES), compressed air storage and pumped hydro, which all have geographical limitations [5], are capable of energy management on the scale of GWhs, particularly as spinning reserves, beyond the scope of modern electrochemical devices. In June 2016, there were 860 operational electrochemical storage installations connected to power grids worldwide, accounting for 2.2 GW of total installed storage power. Of this, 134 MW was contributed by 102 redox flow battery installations, of which 69 MW was the contribution from vanadium-based systems [12].

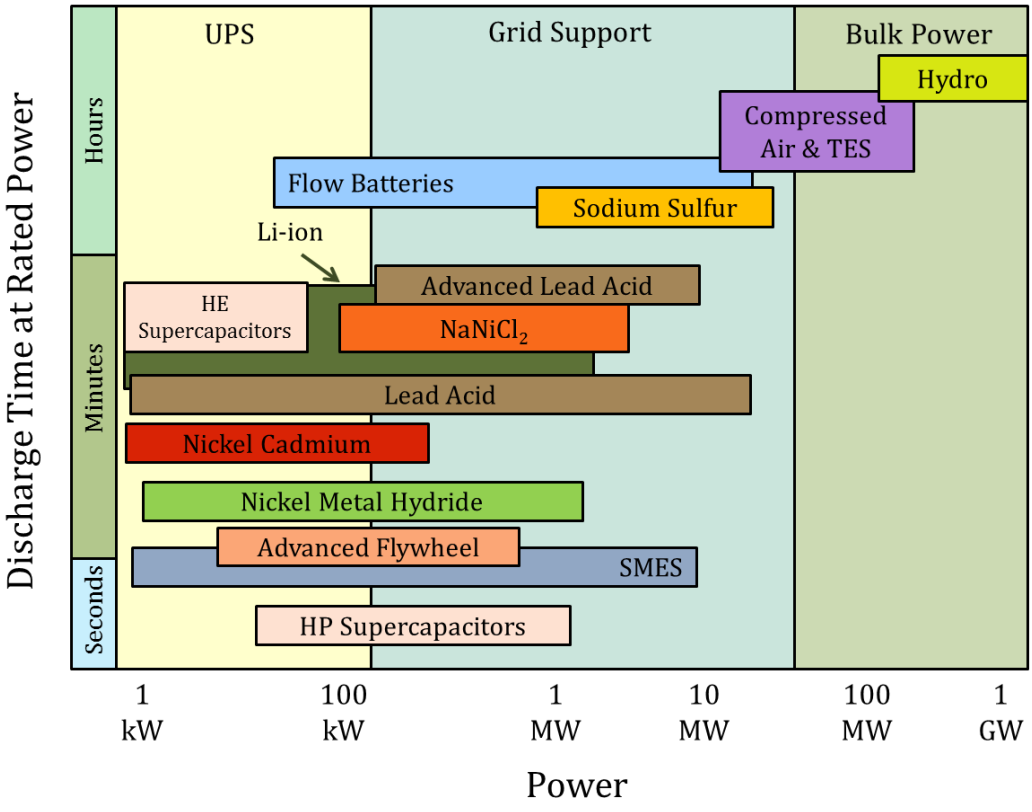

Figure 1.1: A variation of the Ragone chart comparing the main energy storage systems. *UPS* uninterruptible power supply, *SMES* superconducting magnetic energy storage, *TES* thermal energy storage, *HE* high energy, *HP* high power. This plot represents a broad picture of the operating ranges of the technologies presented. Data used from Sandia National Laboratories [15] and US DOE [12].

Redox flow batteries occupy a superior position in the Ragone chart to many other battery technologies and have attracted much attention. They are easily scalable, from kWs to MWs, and the vanadium flow battery has been shown to posses high efficiency (>90 % under certain conditions); lifetimes of 20 years; low initial costs (cost per kW decreases with greater storage capacity); low maintenance and flexible operation [19]. Safety is another key feature of flow batteries, which typically operate at ambient temperature. In contrast, sodium-sulfur batteries require temperatures around 300 - 350 C, which poses a significant engineering and safety challenge [15]. The number of flow battery installations around the world is second only to lithium-ion, summarised in Table 1.2.

Type	**No. of Projects**	**Total Power / MW**
Lithium-ion	578	1628
RFB	102	134
Lead-Acid	91	189
Sodium Based	76	222
Nickel Based	7	32
Metal Air	6	20
Total	860	2225

Table 1.2: An overview of the secondary battery installations around the world, recorded in June 2016 [12]. *RFB*: Redox flow battery.

1.4 Redox Flow Batteries

In the simplest form, a redox flow cell consists of an electrochemical cell akin to a chemical reactor divided into two half-cells via a separator. Two external tanks house the anolyte and catholyte separately, and pipes and pumps circulate the electrolytes through the respective half-cells. The electrodes are connected externally to a source/load. When power is supplied, the cell charges: electrochemical reactions occurring at the electrodes' surface result in a change in the oxidation states of the reactant species in the electrolyte, where one species will be oxidised at the positive electrode (anode on charge) and another reduced at the negative (cathode on charge). Energy is stored as these new, 'charged' species. The discharge reaction is thermodynamically spontaneous and when pumping the charged electrolytes through the

cell whilst attached to an electric load, the reactions are reversed and the cell discharges [19]. The most mature RFB technology utilises vanadium in aqueous sulfuric acid and is illustrated in Figure 1.2.

On charge, the V^{3+} species is reduced to V^{2+} at the negative electrode, whilst V^{4+} is oxidised to V^{5+} at the positive [20]. Gaskets are placed in between the cell components and end plates provide compression to prevent leakage. Several cells can be compressed together to form a stack, i.e. a flow battery. Typically, cells are connected in series electrically and in parallel hydraulically, meaning that electrolyte enters each cell simultaneously rather than one after the other [16]. Stacks can be connected electrically in parallel or series and this modular design makes the technology easy to scale up. The battery power is a function of the stack dimensions: the electrode size and number of cells in the stack. Energy storage capacity is a function of the concentration of the active species and the overall electrolyte volume [21].

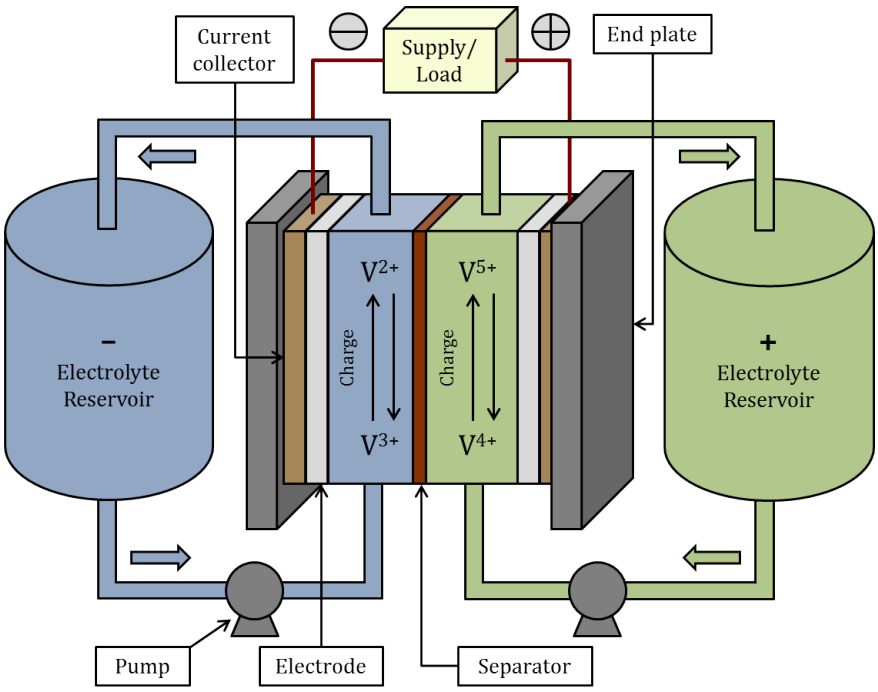

Figure 1.2: Schematic of the all-vanadium flow battery. The anolyte and catholyte are stored separately in external tanks and pumped through the cell using pumps. Energy is storage and released via redox reactions occurring at the electrode surface.

There are a multitude of different chemistries used in RFBs and these can be categorised into

four groups (where the forward reactions represent charge):

1. ***True RFB***: Electroactive species remain dissolved in the solution. Power and energy can be decoupled unlike other batteries as the electrodes are not directly involved with the reactions. There is also virtually no self-discharge as the charged species are kept externally to the electrochemical cell. The vanadium redox flow battery (VRFB) seen in Figure 1.2 is the most developed:

$$V^{3+} + VO^{2+} + H_2O \leftrightharpoons V^{2+} + VO_2^+ + 2H^+$$

2. ***Hybrid Type I***: One half-cell reaction experiences a phase change whilst the active species in the other remains in the aqueous state. In the zinc-bromine redox flow battery (ZBFB), bromine remains in solution as bromine or bromide whereas solvated zinc ions are deposited onto the negative electrode during charge and stripped on discharge:

$$Zn^{2+} + 2Br^- \leftrightharpoons Zn + Br_2$$

3. ***Hybrid Type II***: Both half-cells experience phase changes during operation. In the soluble-lead flow battery (SLFB), Pb^{2+} ions initially dissolved in an acidic electrolyte are deposited as solid lead and lead dioxide on the negative and positive electrodes respectively during charge. These deposits dissolve back into the electrolyte on discharge (Section 1.5).

4. ***Hybrid Type III***: This is a half-unitised regenerative fuel cell, where an air-breathing electrode is used in the positive half-cell. The zinc-air system falls into this category. Oxygen is evolved on charge and reduced on discharge, similar to a PEM fuel cell, whilst zinc is converted from an aqueous state to a solid state on charge and vice-versa on discharge:

$$Zn^{2+} + H_2O \leftrightharpoons Zn + \frac{1}{2}O_2 + 2H^+$$

The earliest flow battery research was conducted by NASA [22] and Mitsui [23] in the 1970s

and 80s, and the early research over these decades has been summarised by Bartolozzi [24]. Problems with ionic crossover through the separator, hydrogen evolution and slow kinetics hampered the iron-chromium project but research to address these issues continues today. NASA also pioneered the all-vanadium redox flow battery (VRFB). Because vanadium is the only electroactive species on both sides of the cell, ionic crossover between the positive and negative cell chambers is not a major issue. The reaction kinetics are fast and a catalyst is not required. The largest VRFB installation, at 15 MW/60 MWh, was constructed by Hokkaido Electric Power and Sumitomo Electric Industries in January 2016 at the Minami Hayakita substation in Hokkaido, Japan, for capacity firming of solar and wind power [25].

The specific energy of the VRFB is limited by the low solubility of the vanadium species, typically offering 25 - 30 Wh kg^{-1} (per kg electrolyte) [26] of storage energy. In comparison, lead-acid batteries and lithium-ion cells offer 30 - 40 Wh kg^{-1} and 80 - 200 Wh kg^{-1} (per kg overall, including electrodes and cell casing etc.) respectively [27]. However, for applications such as load-levelling, the cost, lifetime and flexibility of operation is preferred over battery energy density. RFBs therefore suit these applications very well; their capability for large-scale storage has been demonstrated on the MW scale.

The zinc-bromine flow battery (ZBFB), the only other commercially available flow battery, offers higher specific energies of around 65 - 75 Wh kg^{-1} (per kg electrolyte) and a higher unit cell potential (Table 2.1). However, ionic crossover (through the separator) is a problem, leading to self-discharge of the system and a drop in capacity and energy efficiency. Further information on all types of flow batteries and their remaining challenges have been reviewed [20, 26]. Engineering considerations, such as cell and stack design, have also been reviewed [28].

Fuel cells are not included in the ESS category as they do not store energy as such. They can be likened to a primary flow battery where reactants are constantly fed to the electrodes, generating electricity whilst the products are removed. The proton exchange membrane (PEM) fuel cell (or hydrogen fuel cell), which generates electricity through the formation of water from hydrogen and oxygen, is the earliest and most commonly available fuel cell. These devices come with their own technological problems, such as the poisoning of expensive catalysts, water and heat management issues and separator degradation. Their use is a

popular research topic for automobiles (the prototype Mercedes Benz A-class uses a 75 kW PEMFC) and combined heat and power (CHP) energy systems for stationary applications, at most a few hundreds of kWs [29]. However, even if technological issues are overlooked, the future of PEM fuel cells will rely on the development of a sustainable hydrogen economy that does not depend on the steam reformation process of natural gas.

ESS will be a key component of the smart grid of the future, and the flow battery has proven to be a reliable form of energy storage. Following the success of the all-vanadium and zinc-bromine technologies, systems that offer higher energy density, reliability and efficiency over a longer lifetime, whilst remaining cheap to manufacture, maintain and recycle are currently being researched, and one of these systems is the soluble lead flow battery, discussed in the next chapter. Chapter 1.6 discusses a future smart grid which incorporates a mix of ESS.

1.5 The Soluble Lead Redox Flow Battery

The SLFB is a Hybrid Type II flow battery that makes use of the variable oxidation states of lead: Pb, Pb^{2+} and Pb^{4+}. In its present configuration, Pb^{2+} ions are dissolved in aqueous methanesulfonic acid (MSA) and this solution is then circulated through an undivided electrochemical cell. During charge at the positive electrode, Pb^{2+} is oxidised to form a solid lead dioxide deposit on the electrode. Each ion is stripped of two electrons that flow through an external circuit to the negative electrode. Here, Pb^{2+} is reduced to form a solid lead deposit. The thickness of the deposits relate to the energy stored. During discharge, these deposits dissolve back into the solution, releasing the stored energy [30]. The electrochemical processes can be represented by the following equations, where the forward reactions represent charging of the cell:

$$\begin{aligned}
&Positive && Pb^{2+} + 2H_2O \leftrightharpoons PbO_2 + 4H^+ + 2e^- && E^o_{+ve} = +1.46\ V\ vs.\ SHE \\
&Negative && Pb^{2+} + 2e^- \leftrightharpoons Pb && E^o_{-ve} = -0.13\ V\ vs.\ SHE \\
&Overall && 2Pb^{2+} + 2H_2O \leftrightharpoons Pb + PbO_2 + 4H^+ && E^o_{cell} = +1.59\ V
\end{aligned}$$

The accompanying potentials are the reduction potentials under standard conditions. 'Standard' refers to conditions where the concentration of all dissolved species is 1 mol dm^{-3} (in this case, Pb^{2+}), the solution temperature is 25 C (298 K) and the solution is under a pressure of 101.325 kPa (1 atm). At 1.59 V, the standard equilibrium cell potential is higher than that of the VRFB at 1.26 V and comparable to that of the ZBFB at 1.85 V [21]. From these equations, it can be seen that the electrolyte composition is constantly changing during battery operation. Pb^{2+} concentration decreases during charge whilst the acidity increases, as two moles of H^+ are released per mole of Pb^{2+} deposited. This has important implications which will be discussed later. This mechanism is different to that of standard lead-acid batteries, in which lead and its compounds remain insoluble throughout. Sulfation limits the cycle life and depth of discharge of lead-acid batteries [27], and this is avoided in the SLFB. The SLFB reaches a 100 % state of charge (SoC) when all the lead in the solution has been converted to deposits on the electrodes. The operation is visualised in Figure 1.3.

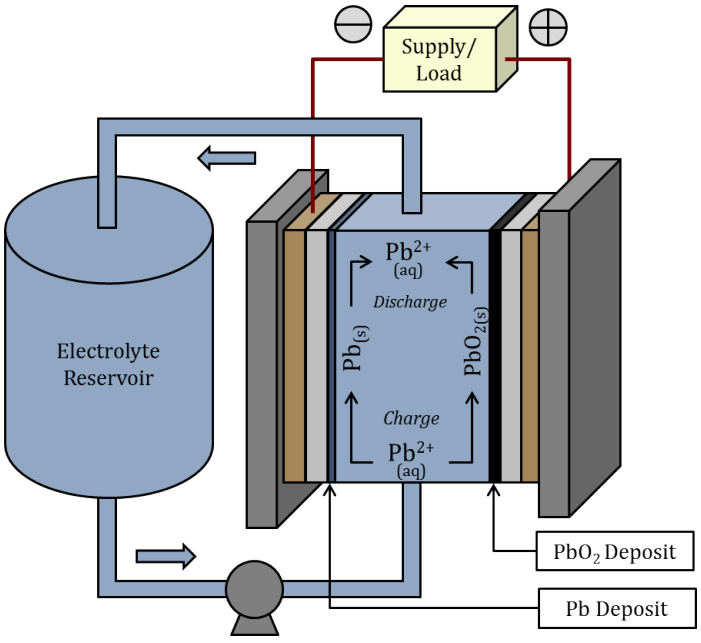

Figure 1.3: A simplified schematic of the undivided SLFB. A pump is used to circulate electrolyte around the system. During charge, Pb^{2+} ions are oxidised at the positive electrode to form solid PbO_2 and reduced at the negative electrode to form solid Pb. The process is reversed during discharge.

Unlike other RFB chemistries, the SLFB uses an electrolyte common to both electrode reactions and therefore a separator is not required. There is also only one electrolyte tank and one set of pipework, which greatly simplifies the design and cost of the system. There is

no issue of electrolyte crossover, and fewer cell components reduces the likelihood of leakage. Electrode degradation seen in the VRFB [19] could also be avoided, as electrodes in the SLFB soon become plated with passivating lead and lead dioxide deposits. Furthermore, lead is an abundant resource and can be sourced cheaply from recycled lead-acid batteries [30]. It is highly soluble in MSA, offering a higher specific energy than the VRFB (though lower than the ZBFB), at 41 Wh kg^{-1} (per kg electrolyte) in some experiments [31].

There are challenges at both the electrodes in the SLFB. Whilst lead deposition and stripping is highly efficient at the negative electrode [32], it does requires a surfactant; otherwise the deposit will tend towards rough, cauliflower-like crystals and the growth of dendrites. These are prone to being knocked off the electrode by the flowing electrolyte, leading to a loss in energy capacity, and can even grow across the internal cell walls towards the positive electrode, where electrical shorting can occur if contact is made. This too will lead to a loss in energy capacity [33]. At the positive electrode, the Pb^{2+}/PbO_2 redox couple is plagued by slower reaction kinetics and considerably higher overpotentials [32]. The poor reversibility of the Pb^{2+}/PbO_2 couple is the main limitation of the system and over prolonged battery cycling, leads to the build-up of deposits at both electrodes, depleting the solution of the active lead species, Pb^{2+}. These deposits cannot be dissolved via conventional cell discharge and will need to be forcibly removed by either applying power or dismantling the cell and manually removing the deposits. PbO_2 deposits can also creep across non-conducting surfaces, such as the internal cell walls and inlet/outlet flow distributor, causing shorting [31, 34]. In addition, cracks can form on the PbO_2 surface, causing flaking of the deposit. These insoluble, fallen deposits accumulate as a sludge at the bottom of the cell and can block the flow field [31]. It is important therefore to be able to deposit uniform, compact deposits at both electrodes.

SLFB research is relatively young, having begun just over 10 years ago. The literature therefore is limited. However, proof-of-concept studies [30, 31, 35, 36] have shown promising results despite this, indicating that the technology is suitable for scale-up whilst offering a wide scope for novelty. Similar problems to those hindering further SLFB development have been seen previously, such as dendritic growth in the ZBFB [20] and coatings industries [37]. This project will aim to identify and apply techniques used in these areas, in addition to lead-acid battery research, to bring the SLFB closer to commercial readiness.

1.6 An Illustrated Example of the Smart Grid Concept

According to the Rocky Mountain Institute (RMI) [38], there are three main stakeholders regarding the stream of electrical power: the utilities firms (generation and transmission - upstream and midstream), customers (downstream) and independent system operators and regional transmissions organisations (midstream). ESS can provide different benefits depending on where it is installed along this stream, and these are described in detail in RMI's report [38].

Figure 1.4 summarises the discussion on smart grids and types of energy storage, where *ES* represents an energy storage system, *T* represents substations and *V2G* represents the vehicle-to-grid strategy. Energy is generated upstream at the *Power station* and the *Large wind farm*, which is coupled to *ES1*. This could be a vanadium flow battery installation, used for renewables capacity firming, such as the 15 MW/60 MWh system used at the Minami Hayakita substation [25]. *ES2* would need to be on the scale of GWs, hence would need to be a system from the top-right of Figure 1.1, such as a pumped hydro installation.

The electrical energy then passes through *T1*, a step-up transformer, before being transmitted across the country. *T2* is a regional step-down transformer, and *T3* and *T4* are local step-down transformers. *ES3* could be used for energy storage arbitrage or for renewables capacity firming for a local microgrid. This could be accomplished with a zinc-bromine flow battery installation, such as the 250 kW/500 kWh system at the Fort Sill Microgrid in Oklahoma, USA [39]. Constructed by EnSync, this system is joined to a 2.5 kW wind turbine, 30 kW PV array and 400 kW natural gas generator.

Placed within or near substation *T2*, *ES4* would be used for frequency regulation and transmission and distribution congestion relief. This could be a lithium-ion installation, such as the 48 MW/12 MWh system at Gyeongsan substation in South Korea, constructed by Woojin industrial Systems/LG Chem and operated by Korea Electric Power Corporation [40].

Individual houses or apartment blocks could have installed PV panels coupled with batteries, *ES5*. For example, at the end of January 2016, Germany had 34,000 PV-battery systems in place, totalling 68 MW/204 MWh. In 2015, these systems stored 78.5 GWh of energy (instead of having fed this into the grid). 27% of the batteries installed were lead-acid

batteries, with the remainder composed of lithium-ion batteries [41]. Finally, for industrial applications where the smooth supply of power is vital, on-site gas or diesel generators could be replaced with a battery system, *ES6* (for frequency regulation, spinning reserve or black start applications) such as a flow battery, or litihum-ion or lead-acid system.

The vehicle-to-grid (V2G) strategy is a way of using the battery in electric vehicles to discharge energy into the grid during periods of low supply. For example, during night when the vehicle owner has plugged the vehicle into the grid at their home, the battery could be charged and discharged accordingly to offset disturbances in the grid. The growth of electric vehicles could result in a large storage capacity, therefore models have been published studying how such a system could be implemented and optimised [42].

The blue circles represent sensors at various points on the electrical stream. A data centre, the core of the smart grid, collects the data and decides how to optimise the power supply so as to best fit the needs of the demand, leading to a flexible electrical power distribution network.

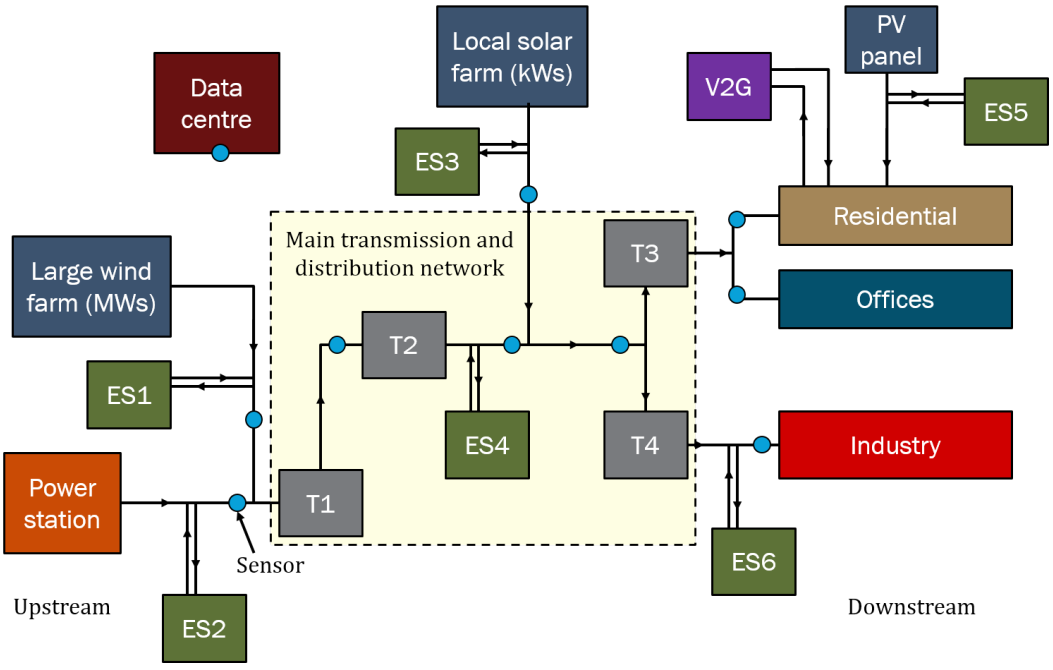

Figure 1.4: Basic example of how a 'smart grid' could work. A suite of energy storage systems, *ES*, comprising several installations at various points on the electrical power stream, is shown. *T* substations, where the voltage is stepped up or down: *T1* step-up transformer, *T2* regional step-down transformer, *T3* and *T4* local step-down transformers. *V2G* vehicle-to-grid. The blue dots represents sensors, where real-time data is relayed to a data centre. Image produced using data used from Sandia National Laboratories [15] and the US Department of Energy [6, 12].

1.7 Thesis Structure

This thesis reports on the development of a novel separator-divided soluble lead flow battery, introducing a novel electrolyte and cell configuration. The soluble lead system's current advantage is that it does not require a separator. The literature is filled with conceptual studies and lab-scale experiments, but in each case the difficulties highlighted earlier have prevented further scale-up of the system. It was therefore proposed to investigate the feasibility of a novel separator-divided soluble lead redox flow battery, aligning this technology with the standard flow battery design. This negated the simplicity and cost advantage that the SLFB previously offered but was found to bring a significant improvement to cell performance and operational life compared to the literature, which allowed further investigation of the system.

For example, this allowed the use of electrode-specific additives that otherwise interfered with the opposite electrode reaction. More importantly, the separator was found to act as a physical barrier to dendritic Pb growth and PbO_2 creep, preventing electrical shorting. Additionally, a novel 'semi-divided' separator configuration was explored. Two cells of differing size were used to test various combinations of electrolyte, separator and additives, and these stages are outlined below.

Chapter 2 presents a review of SLFB research literature, including discussions on the electrode kinetics and reaction mechanisms, and previous electrolyte compositions, electrodes and additives. The performance metrics of previous soluble lead flow cell cycling tests are also compared and discussed whilst highlighting important operating conditions. Finally, important benchmarks based on commercially available batteries are introduced before the gaps in the literature are summarised.

The novel work section of this thesis begins with a summary in Chapter 3 of the experimental apparatus used. Chapter 4 looks at the effect of varying lead and MSA concentrations on solution density, viscosity and conductivity. In Chapter 5, the potential drop across a variety of separators are measured; certain separators are then shortlisted to be used in cell cycling experiments. Chapter 6 looks at the cyclic voltammetry of solutions containing several reported and novel additives. Chapter 7 then combines the work from the previous

chapters, testing different combinations of electrolytes, separators and additives in galvanostatic charge/discharge cycling experiments using a 9 cm^2 static cell. The optimal initial concentration of Pb^{2+} and MSA in solution is also investigated.

The following chapters focus on flow cell cycling. The static cell is converted into a 9 cm^2 flow cell in Chapter 8, in which the best performing configurations from the previous chapter are compared using a different charge/discharge cycling regime. Chapter 9 scales the system further to a larger cell with 100 cm^2 electrodes. Here, the power characteristics at different states of charge are explored, along with cycling experiments to test the longevity of the system. Chapter 10 introduces a method of regenerating the system when it is near the end of its operational life. Finally, Chapter 11 discusses a theoretical model to scale the system into a stack, using the RedFlow ZBM 2 zinc-bromine flow battery as a benchmark. Chapter 12 summarises the novel work and highlights key areas for future research.

Note, in this report the terms 'electrolyte' and 'solution' are used interchangeably.

1.8 Key Novel Outcomes from this Project

Regarding the soluble lead electrolyte:

1. Chapter 4: the relationship between absolute viscosity and the concentration of lead methanesulfonate and methanesulfonic acid has been mapped. A surface plot has been devised to calculate (within ±1.1% on average) the viscosity of any combination of lead methanesulfonate and methanesulfonic acid up to 1.5 mol dm^{-3} concentration.
2. Chapter 4: The relationship between ionic conductivity and the concentration of lead methanesulfonate and methanesulfonic acid has been mapped. A surface plot has been devised to calculate (within ±2% on average on average) the viscosity of any combination of lead methanesulfonate and methanesulfonic acid up to 1.5 mol dm^{-3} concentration.
3. This has informed the selection of a novel combination of lead methanesulfonate and methanesulfonic acid to be used in the system.
4. Chapter 7: A combination of additives individually shown in the literature to have a

positive impact on the SLFB reaction mechanisms have been used in combination for the first time. These are lignosulfonate, bismuth(III) and fluoride.

Regarding the soluble lead flow cell design:

1. Chapter 8: the system was divided using a separator in a fully-divided format allowing the use of electrode-specific additives, and in a novel semi-divided format. In both cases, the separator was seen to act as a barrier to abnormal deposition of lead and lead dioxide.

2. Chapter 11: a theoretical 'bypass-flow' region has been added to a CAD model of the C-Tech-optimised soluble lead flow cell design with the intention of further hindering the growth of abnormal deposit growth.

Regarding soluble lead flow cell operation:

1. Chapter 9: The soluble lead flow battery described in this thesis, incorporating the above findings, was able to improve the lifetime of the system by almost four times from previously published work whilst increasing the energy efficiency to 73% from 65%.

2. Chapter 9: A peak discharge current density of 150 mA cm^{-2} and power of 12.5 W was achieved, the highest for a single soluble lead cell.

1.9 Publications Associated with This Project

1. M. Krishna, L. Wallis, R. Wills, D. Hall, and A. Shah, "Measurement of key electrolyte properties for improved performance of the soluble lead flow battery," International Journal of Hydrogen Energy, vol. 42, no. 29, pp. 18491 – 18498, 2017.

    - This paper incorporates data presented here in Chapters 4 and 7 regarding the electrolyte analysis and static cell cycling respectively.

2. M. Krishna, R. Wills, F.C. Walsh, D. Pletcher, J. Collins, D. Hall, D. Stratton-Campbell, "Improvements to the soluble lead acid flow battery", mini-paper published in the conference proceedings, International Flow Battery Forum, Jun 15, Glasgow.

- This paper incorporates data presented here in Chapter 9 regarding cycling of the 100 cm^2 flow cell, along with a general introduction to the soluble lead flow battery.

3. M. Krishna, E. Fraser, R. Wills, F.C. Walsh, "Developments in soluble lead flow batteries and remaining challenges: an illustrated review," submitted to the Journal of Energy Storage. Reference: EST_2017_325.

    - This review is largely composed of the discussion and analysis presented here in Chapter 2.

The author has also presented at the following external conferences:

1. The 67^{th} Annual Meeting of the International Society of Electrochemistry, The Hague, August 2016 (poster)
2. The International Flow Battery Forum, Glasgow, June 2015 (20 minutes oral presentation)
3. Electricity Storage Network: Open Symposium, London, January 2015 (poster)
4. UK Energy Storage, University of Warwick, November 2014 (poster)

Chapter 2

Literature Review of the Soluble Lead Flow Battery

2.1 Brief History of Lead-Based Batteries

The simplest form of the standard lead-acid battery (LAB) is known as a flooded cell, which consists of solid lead (negative) and lead dioxide (positive) electrodes immersed in a sulfuric acid solution. The electrodes are kept apart by the use of a separator (e.g. fibreglass [43], and lead and its compounds remain insoluble throughout operation; both electrodes are converted to lead sulfate on discharge and this is reversed on charge according to the following equations [27]:

$$Positive \qquad PbO_2 + SO_4^{2-} + 4H^+ + 2e^- \leftrightharpoons PbSO_4 + 2H_2O \quad E^o_{+ve} = +1.683V vs. SHE$$

$$Negative \qquad Pb + SO_4^{2-} \leftrightharpoons PbSO_4 + 2e^- \qquad E^o_{-ve} = -0.358V vs. SHE$$

$$Overall \qquad Pb + PbO_2 + 2H_2SO_4 \leftrightharpoons 2PbSO_4 + 2H_2O \qquad E^o_{cell} = +2.041V$$

The high reversibility of the forward reactions under different loads, the low cost of lead and sulfur (e.g compared to lithium-ion), the design simplicity and a high cycle life, amongst other

advantages, are behind the success of the LAB [44]. LABs are used for starting, lighting and ignition (SLI) applications, for example in automobiles where high surge currents are required for short durations, and can also be scaled up for UPS services as well as load levelling and renewables capacity firming. The largest LAB installation is the 36 MW/24 MWh array at the 153 MW Notrees wind power project in Texas, USA [12].

Since its inception in 1859 by Gaston Planté, the LAB has undergone over 150 years of development. The world's first fully electric car in 1881 and submarine in 1886 were powered by the LAB. In 1899, Jenatzy's LAB-powered automobile was able to surpass a speed of 100 km h^{-1} [27]. As the world's portable power demands grew, breakthroughs in manufacturing in 1898 by Barton and 1926 by Shimadzu paved the way for industrial scale production of LABs [27].

In the early second half of the 20^{th} century, the valve-regulated lead-acid battery (VRLAB) was invented. There are two forms of VRLAB: the absorbed glass mat (AGM), where the electrolyte is held within the pores of the glass mat separator, and the undivided gel battery, where silica is used to create a highly viscous gel-like electrolyte. These designs brought many improvements to the flooded system: the recharge time and self-discharge rate was decreased, and the cycle life and specific power was increased. Safety was also substantially improved: any evolution of hydrogen and oxygen was forced to recombine back into water, and in case this process did not occur rapidly enough, valves safely released any internal pressure build-up. Deeper cycles could also be achieved and maintenance became obsolete as the battery became self-regulating [45].

VRLABs offer a low specific energy and specific power, about 30-40 Wh kg^{-1} and 180 W kg^{-1} respectively, which does not compare favourably to the lithium-ion batteries currently used to power electric cars. These batteries can offer a specific energy of 160 Wh kg^{-1} and a specific power of 1800 W kg^{-1} [27]. However, lead batteries continue to be a popular area of research and advanced lead-acid batteries have shown significant improvements. Amongst these is the Ultrabattery, which was developed by CSIRO in 2006. Early studies showed that by combining a supercapacitor alongside the lead electrode in a single cell, the charge and discharge power can be improved by 50% and the cycle life tripled [46]. These promising results have invoked interest in using these batteries for hybrid-electric vehicles. Figure 2.1

summarises the key milestones in LAB development and the main stages of SLFB research. A detailed comparison between the LAB and SLFB can be found in the work by Zhang et al. [47].

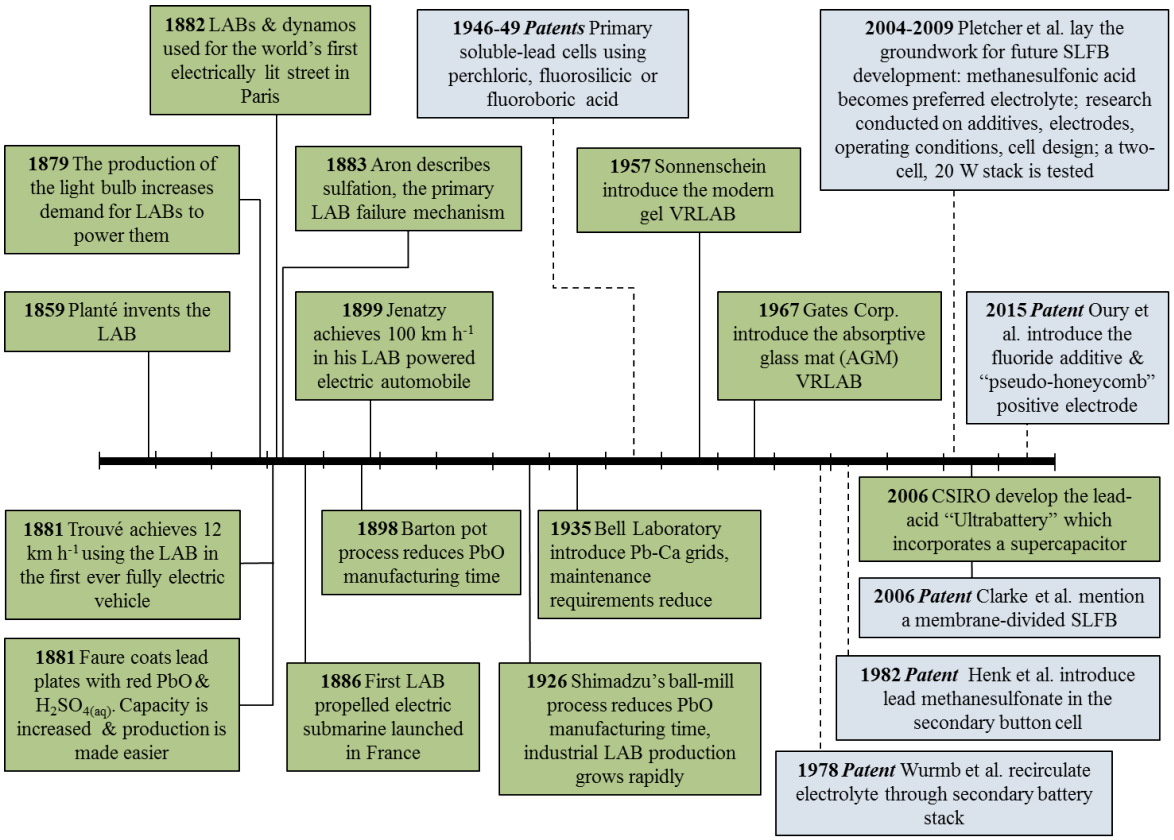

Figure 2.1: Timeline of important milestones in the development of the lead-acid battery and the soluble lead flow battery [27, 31]. Green squares represent LAB development and blue squares SLFB research.

The earliest record of battery research involving a soluble lead species dates back to the late 1940s [31]. These were primary batteries that used mostly solid lead negative electrodes and positive electrodes consisting of a lead dioxide coating [48, 49]. The supporting electrolyte used perchloric, fluoroboric or fluorosilicic acid, having taken inspiration from the lead plating industry at the time [37]. They were designed for small-scale, short term emergency applications, where the dry cell would be filled with acid just before operation. Of these early primary battery patents, the lead dioxide electrode was prepared by deposition onto a nickel substrate using a circulated lead nitrate solution [48].

Later in the 1970s and early 80s, several patents for secondary box, button and flow cells

were filed [50–52]. Hexafluorosilicic and amidosulfonic acids were introduced, again taken from the plating industry. A circulated electrolyte through a stack incorporating bipolar electrodes was used for the first time by Wurmb et al. [51] with the motivation of obtaining greater efficiency, higher current density and better performance than lead-acid batteries at the time. The SLFB's current problems regarding the reversibility of lead dioxide deposition were also first identified and various operating conditions, additives and electrode structures were recommended to minimise these issues. The phasing out of lead silicofluoride in favour of lead methanesulfonate (following the trend in the plating industry) began with Henk et al. [52], who also focused on producing bespoke graphite electrodes.

Further developments were later made during the 2000s by several groups. Wills et al. reported the use of a small flow cell with an active electrode area of 2 cm^2 [30, 33, 35, 36] and 8 cm^2 in studies supported by Regenesys Technologies Ltd [53, 54]. Larger cells with active electrode areas of 64 cm^2 and 100 cm^2 were introduced soon after and scaled up in collaboration with C-Tech Innovation Ltd [31, 34, 55, 56]. The initial papers carried out proof-of-concept studies regarding electrode kinetics [30], electrode materials and flowing electrolytes [35, 36], electrolyte composition and additives [33, 53–55], whilst the later papers focused on system scale up [31, 34]. There has also been work published on modelling of the system [57]. In 2006, a Nafion membrane was used to divide the positive and negative half-cells in the soluble lead flow cell (amongst other chemistries) and patented by Clarke et al. [58]. However, the reasons for this are unclear, the system design is vague, no electrode-specific additives are mentioned and zero performance metrics are given.

2000 cycles at 95% charge and 79% voltage efficiency were achieved by Verde et al. [59] in small-scale studies in 2013, indicating the potential of the soluble lead system. Velichenko et al. [60] have studied in depth the multi-stage process of lead dioxide deposition from MSA solutions (Chapter 2.4.2), whilst Pletcher et al. [55] have studied the effect of the electrolyte conditions on the morphology of lead dioxide (Chapter 2.5.3). The SLFB continues to be a promising area of flow battery research and efforts now are focused on the cyclability of the positive electrode reaction and the scaling up of the system.

2.2 Electrochemical Theory

2.2.1 Thermodynamics

The cell potential, E_{cell}, at any time whether on charge or discharge, can be calculated as the potential difference between the cathode (where reduction occurs) and anode (where oxidation occurs), so that

$$E_{cell} = E_{cathode} - E_{anode} \tag{2.1}$$

In secondary batteries, the positive and negative electrode is the cathode and anode respectively during discharge, and the anode and cathode respectively during charge.

For non-standard conditions, the Nernst equation can be used to calculate the equilibrium cell potential, E^e_{cell}, also known as the open-circuit or rest potential. There is zero net current flow at this potential, and it is equivalent to the minimum cell potential on charge and the maximum cell potential on discharge. The equilibrium potential for the positive electrode, E^e_{+ve}, is given by

$$E^e_{+ve} = E^o_{+ve} + \frac{RT}{zF} ln \frac{[H^+]^4}{[Pb^{2+}]} \tag{2.2}$$

where E^o_{+ve} is the standard electrode potential (Chapter 1.5); R is the universal gas constant (8.31 J mol^{-1} K^{-1}); T is the temperature in K; z is the electron equivalent per mole of reactant, i.e. the number of valent electrons in the stoichiometric equation, $z = 2$ in the SLFB reactions; and F is Faraday's constant, 96485 C electron equivalent^{-1}. The units of zF together are C mol^{-1}. $[H^+]$ and $[Pb^{2+}]$ are the concentrations of the enclosed species in mol dm^{-3}, often shortened to M. The exact equation uses the activities of the ionic species but this is difficult to measure, whereas the concentrations are easy to calculate and provide a good approximation. When $[\mathrm{H}^+]^4 = [\mathrm{Pb}^{2+}]$, $E^e_{+ve} = E^o_{+ve}$. The equation can be similarly written for the negative electrode reaction:

$$E^e_{-ve} = E^o_{-ve} + \frac{RT}{zF} ln[Pb^{2+}] \tag{2.3}$$

E^e_{cell} can then be calculated by subtracting Equation 2.3 from 2.2, as portrayed by Equation 2.1 (assuming discharge, where the positive and negative electrodes are the cathode and anode respectively):

$$E^e_{cell} = E^o_{cell} + \frac{RT}{zF} ln \frac{[H^+]^4}{[Pb^{2+}]^2} \tag{2.4}$$

It can be seen that at higher SoC, due to the higher $[H^+]$ and lower $[Pb^{2+}]$ in solution, E^e_{cell} will be higher than at lower SoC.

It was previously mentioned that in all batteries, the discharge current arises from a spontaneous chemical process that occurs when the charged electrodes are connected to a load via an external circuit. The driving force behind this is given by the Gibbs Free Energy, $\triangle G$. If $\triangle G < 0$, then the cell reaction is spontaneous, and the system is known as a galvanic cell. All primary batteries and fuel cells fall into this category. If $\triangle G > 0$, then the system is known as an electrolytic cell, and external energy will be required to force a chemical reaction. Secondary batteries are electrolytic cells on charge and galvanic cells on discharge. The equation is given by

$$\triangle G = -zFE \tag{2.5}$$

where E is the equilibrium potential. If E is substituted with E^o_{cell}, then $\triangle G^o_{cell}$ for the SLFB equals -307 kJ mol^{-1} (+307 kJ mol^{-1} on charge). This is the theoretical maximum amount of chemical energy under standard conditions that can be converted to electrical energy per mole of Pb^{2+}. However, much would be lost as heat due to losses in the cell (Chapter 2.2.2). Table 2.1 compares this value with those of other batteries. $\triangle G^o_{cell}$ in the SLFB is more than twice as high as in the VRFB and comparable with the ZBFB.

	VRLAB [47]	**VRFB [19]**	**ZBFB [19]**	**SLFB [61]**
E^o_{+ve} / V	1.69	1.00	1.09	1.46
E^o_{-ve} / V	-0.36	-0.26	-0.76	-0.13
E^o_{cell} / V	2.05	1.26	1.85	1.59
$\triangle G^o_{cell}$ / kJ mol^{-1}	-394	-121	-357	-307

Table 2.1: Comparison of thermodynamic properties of four different batteries: $VRLAB$ valve-regulated lead acid battery, $VRFB$ all-vanadium redox flow battery, $ZBFB$ zinc bromine flow battery, $SLFB$ soluble lead flow battery. All electrode potentials are vs. SHE.

2.2.2 Cell Polarisation

The principle of battery operation is the transfer of electrons between ionic species in the electrolyte and the surface of the electrode. This can be summarised in three stages:

1. Mass transport of reactants to electrode surface from bulk solution
2. Electron transfer at electrode surface, converting reactants to products
3. Mass transport of products away from electrode surface to bulk solution

In static-electrolyte cells, diffusion and migration are the primary forms of mass transport. The former describes the movement of species controlled by a concentration gradient, i.e. from high concentration to low, and the latter, the movement of species influenced by an electric field. In flow cells, the mass transport properties can be improved by increasing the flow velocity, known as forced convection. In the previous section only the equilibrium potential was discussed, where the net current flowing through the cell is zero. However, a flow of charge (the current) is required to draw or supply power. Therefore in order to drive this current, the cell potential must shift from the equilibrium; this 'overpotential' is dependent on the various resistances in the cell and is also referred to as the 'potential drop' or 'potential loss'. The resistive elements are summarised on charge as

$$E_{cell} = E^e_{cell} + \eta_a + \eta_c + \sum IR_n \tag{2.6}$$

and on discharge by

$$E_{cell} = E^e_{cell} - \eta_a - \eta_c - \sum IR_n \tag{2.7}$$

where η_a and η_c represent the activation and concentration overpotential respectively. The former is related to the energy barrier of the primary reaction at the electrode surface (charge transfer), defined by the Butler-Volmer and Tafel equations. The latter is related to the supply of active species to the electrode surfaces at high currents. $\sum IR_n$ represents the Ohmic losses through the various n cell components, such as the electrodes, current collectors, electrolyte and separator, where I is the current through the cell and R_n is each component's resistance. Note that E^e_{cell} at different states of charge will be different, as described by Equation 2.4. Furthermore, it can be seen that the charge potential is always greater than the discharge potential.

Flow cells often operate under galvanostatic control, where the current is controlled and the potential monitored. The cell potential will decrease as the current draw on discharge is increased. On charge, the cell potential will increase as the charging current is raised, as the resistive elements must be overcome in order to drive the reaction. The potential losses are visualised in polarisation plots, as seen in Figure 2.2. The figure is not to scale and the operating currents and potentials (and the size of each loss) will vary depending on the system. The activation overpotential is dominant at lower currents, and then at moderate currents a linear Ohmic loss is seen. Finally, at higher currents, depletion of the active species in the electrolyte leads to a sharp drop in cell potential. To minimise the activation overpotential, the cell should utilise reactions that have favourable kinetics and low energy barriers; a greater current can then be obtained from a lower overpotential. To minimise resistive losses, a highly conductive electrolyte should be used as well as low-resistance cell components and a small inter-electrode gap. In the flow cell, a fast flow rate and sufficient active species concentration at all times would reduce the concentration overpotential.

A similar shape is observed during charge, tending towards higher cell potential with increasing charge current; a sharp potential spike near the end of charge reflects a lack of active species in the electrolyte and the occurrence of a secondary reaction, such as oxygen evolution. This can be avoided by ensuring that a portion of the active species remains solvated

at 100% SoC. This portion will not contribute to energy storage but will reduce the concentration overpotential. In electrolytes such as the ZBFB therefore, [usable active species] < [overall active species].

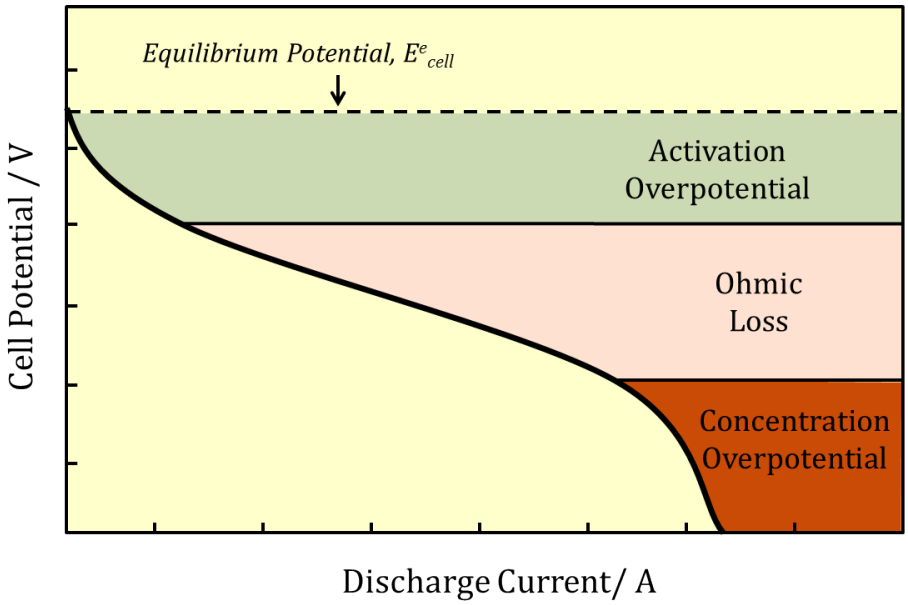

Figure 2.2: Polarisation curve showing loss in potential when discharge current is increased.

In the VRFB during discharge, the previously charged active species must be brought to the electrode surface, converted into the discharged species, and then removed from the surface. In the SLFB, the previously charged species is already available as solid deposits at the electrode surfaces, therefore only requiring conversion and transport away into the bulk electrolyte. Though as yet untested in flow cell cycling, this would suggest that the SLFB is capable of achieving higher discharge rates than the VRFB, which would result in a greater discharge power.

2.2.3 Fluid Dynamics

The region near the electrode surface can be split into three boundary layers: the electrical double-layer, the Nernst diffusion layer and the Prandl hydrodynamic layer. The former is on the scale of nm in width, and it is here that molecules are adsorbed or electrostatically attached to the electrode surface. The Nernst diffusion layer can be typically 1 mm in width,

and this region is modelled as a 'stagnant' zone, where diffusion is the dominant form of mass transport, i.e. bringing reactants from the bulk electrolyte to the electrode surface and removing products in the reverse direction. The Prandl layer is considered in classical fluid dynamics models and can be as wide as 10 mm from the electrode surface. In a flow cell, forced convection (i.e. the electrolyte flow velocity) is the dominant form of mass transport and is responsible for bringing reactants to, and removing products from, the edge of the Nernst diffusion layer. The motion of incompressible, Newtonian fluids can be described as the ratio of inertial to viscous forces, given by the dimensionless Reynold's number, Re:

$$Re = \frac{vd}{\nu} \tag{2.8}$$

where ν is the kinematic viscosity of the fluid in $cm^2\ s^{-1}$, v is a characteristic velocity and d a characteristic dimension. The kinematic viscosity is the ratio of the dynamic (absolute) viscosity, μ in mPa·s, to the fluid density ρ in g cm^{-3}. This relationship is given by

$$\nu = \frac{\mu}{\rho} \tag{2.9}$$

For flow through a pipe with a circular cross-sectional area, v is the linear flow velocity in cm s^{-1}, and d is the diameter of the pipe in cm. For a flow channel with a rectangular cross-section, i.e. a flow cell chamber, the characteristic length is given by the equivalent hydraulic diameter, d_e:

$$d_e = \frac{2BS}{B+S} \tag{2.10}$$

where B is the breadth of the flow channel and S is the inter-electrode or electrode-separator gap, both in cm. The volumetric flow velocity, Q_v, in $cm^3\ s^{-1}$, is related to linear velocity v (i.e. along the length of the electrode, from inlet to outlet), by the equation

$$v = \frac{Q_v}{BS} \tag{2.11}$$

Low Re values describe laminar flow, where the motion is smooth and the fluid layers slide easily over each other. Higher values describe turbulent flow, a chaotic motion composed of vortices which mixes the fluid layers. The Re number at which the flow transitions from laminar to turbulent can be decreased by any resistance to fluid motion in the flow circuit, such as roughness of the pipe walls.

The pressure of a fluid in motion inside a pipe will decrease with distance due to frictional losses at the pipe walls. For laminar flow of an incompressible, Newtonian fluid through a pipe with a constant circular cross-section, the pressure drop, $\triangle P$, across the length of the pipe, L_p, is given by the Hagen-Poiseuille equation:

$$\triangle P = \frac{8\mu L_p V}{\pi r^4} \tag{2.12}$$

where V is the volumetric flow rate in $cm^3\ s^{-1}$ and r is the pipe radius in cm. It can be seen that the pipe radius is the most influential factor: a pipe with a smaller radius will lead to a larger pressure loss than a pipe with a wide cross-section. Understanding the pressure drop in a flow circuit is important to minimising the energy requirement of the pump. Furthermore, turbulent flow will incur greater frictional losses, resulting in a pressure drop higher than that defined by the Hagen-Poiseuille law.

Despite having a rectangular cross-section, a similar principle can be applied to within the soluble lead flow cell. At higher states of charge, the inter-electrode gap is made narrower from deposition on both electrode surfaces; a greater pressure drop along the cell could therefore be expected. The pressure drop can be linked to the required pumping power [62], W, by

$$W = \frac{\triangle PV}{\Psi_p} \tag{2.13}$$

where Ψ_P is the efficiency of the pump.

Turbulent flow brings about a better mixing of the electrolyte, improving mass transport of species between the bulk electrolyte and the electrode surface. Turbulence can be promoted by using a rough electrode surface or by placing a plastic mesh in front of the electrode.

However, turbulent flow also results in a greater pressure drop, which would induce a greater pumping loss.

2.2.4 State of Charge and Energy Capacity

The state of charge of the soluble lead flow battery is given by

$$SoC = 1 - \frac{c}{c_o} \tag{2.14}$$

where c is the present $[Pb^{2+}]$ in solution and c_o the $[Pb^{2+}]$ at 0% SoC (e.g. at the start of the experiment).

Electrochemical conversion from a reactant to a product is proportional to the amount of charge passed through the system. This is defined by Faraday's law of electrolysis:

$$n = \frac{Q\phi}{zF} \tag{2.15}$$

where n is the number of moles converted at an electrode surface (e.g. Pb^{2+} to solid Pb), Q is the total charge passed through the system and ϕ is the current, or Faradaic, efficiency of the system, which is the proportion of current used for the main reaction to the overall current supplied. Some current is often 'lost' to secondary reactions competing at the electrode surface, such as oxygen evolution in aqueous solutions at the anode during charge, and other non-Faradaic processes, i.e. those that do not involve charge transfer, such as adsorption of species on the electrode surface (leading to double-layer charging).

In the SLFB, it would be useful to relate the thickness of the deposits to the charge passed through the system or the amount of molar conversion. Assuming perfectly uniform deposition onto 2D electrodes, the general formula for calculating the thickness of any electrodeposit, d_{ed} in cm, as a function of molar conversion is given by

$$d_{ed} = \frac{M_r n}{A\rho} \tag{2.16}$$

where M_r in g mol^{-1} is the molecular mass, ρ in g cm^{-3} is the deposit density and A in cm^2 the electrode area. The density of electrodeposited lead is known to be approximately equal to that of molten samples [63]. Assuming $\phi = 1$, the lead dioxide deposit will theoretically always be 1.4 times thicker than the lead deposit.

The specific energy of a soluble lead electrolyte, in Wh kg^{-1} (per kg electrolyte), can be calculated by

$$e = \frac{1}{2}.\frac{zFc_oE_{dc}}{3600\rho} \tag{2.17}$$

where ρ is the density of the electrolyte in g cm^{-3}, E_{dc} is the average E_{cell} on discharge and 3600 represents s hr^{-1}. The 1/2 is included here as one unit of charge deposits an equivalent amount of lead and lead dioxide. Multiplying e by ρ and dividing by E_{dc} leads to the charge density, in Ah dm^{-3}.

2.2.5 Cell Efficiency

Flow cells are generally operated by controlling the current and monitoring the potential response. A typical cycle consists of a charge phase and a discharge phase, for which a battery analyser is used to provide the supply and load power. The analyser then records the potential every second, or another pre-set time step, during the operation and plots a potential-time plot (Chapter 2.5.5). The charge efficiency, Ψ_Q, is a ratio of the charge stored on charge, Q_c, and the charge released on discharge, Q_{dc}, given by

$$\Psi_Q = \frac{Q_{dc}}{Q_c} = \frac{\int_0^{t_{dc}} I_{dc}dt}{\int_0^{t_c} I_c dt} \tag{2.18}$$

where I_c, t_c and I_{dc}, t_{dc} are the charge current, charging duration and discharge current, discharge duration respectively. If operating at constant current, where $I_c = I_{dc}$, the equation is simplified to:

$$\Psi_Q = \frac{t_{dc}}{t_c} \tag{2.19}$$

The energy efficiency, Ψ_{EN}, is the ratio of energy released on the discharge phase of the cycle to the energy stored initially on the charge phase of the cycle. It is the product of the voltage efficiency, Ψ_V, and the charge efficiency, and is given by

$$\Psi_{EN} = \frac{E_{dc}Q_{dc}}{E_cQ_c} \tag{2.20}$$

where E_c is the average cell potential during charge. This value is usually calculated at each time step by the battery analyser, offering a more accurate energy efficiency of the charge/discharge cycle than when using average cell potential values. Ψ_v is given by

$$\Psi_V = \frac{E_{dc}}{E_c} \tag{2.21}$$

This value is calculated manually, by dividing the energy efficiency with the charge efficiency.

The equations in this section will be used in the literature review discussion and/or used either empirically or qualitatively in the novel work section.

This section was written with consultation from books published by Pletcher [64], Walsh [65], Linden and Reddy [16], McCabe and Smith [66] and Menictas et al. [21].

2.3 Deposit and Electrolyte Properties

2.3.1 Lead

Lead is denoted by the symbol Pb, from the latin for lead, 'plumbum'. It has an atomic number of 82 and a molecular mass of 207.21 g mol^{-1}. It is a bluish-silver coloured heavy metal with a high density of 11.337 g cm^{-3} and a low melting point of 327.5 C [67]. Lead has a high hydrogen evolution overpotential, which is an important requirement for a battery material. This is due to the weakness of the Pb-H bond; placed at the lower left of the volcano plot for hydrogen evolution, this bond strength is 113 kJ mol^{-1} compared to 197 kJ mol^{-1} for Ni and 225 kJ mol^{-1} for Pt, which is at the peak of the volcano plot [68].

Lead is soft, malleable and has a high corrosion resistance. It is also extremely harmful to organic life, affecting most organs in the human body, particularly the brain [69]. Despite this, because of its mechanical versatility and the ease of extraction, lead has found numerous applications throughout history, such as for water pipes in ancient Rome where it is reported to have contributed to the demise of the Empire [70].

The full effect of lead on humans was not properly understood until the 20^{th} century, during which time lead was added to petrol as an anti-knock additive in the form of tetraethyl lead. The result of this added large amounts of lead to the atmosphere [71]. Following a public health campaign led by Clair Patterson in the USA, lead eventually started being phased out from petrol and other household items such as paint, plumbing and food tins in the 1970s. By the late 1990s, a study observed that the average blood lead level in American adults and infants had dropped by over 80% [71]. Today, the properties of lead are well understood and it continues to be used in the lead-acid battery inside which it is safely confined. Upon battery failure, the lead and other battery materials are completely recycled [44].

Figure 2.3 displays the potential-pH equilibrium diagram of the lead-water system, which shows the corrosion limits of lead and its thermodynamically stable forms under different pH and oxidising/reducing potentials (vs SHE) at 25 C, simplified from the original diagram by Pourbaix [72]. The dashed lines a and b contain the stability region of water, where oxygen is evolved above b and hydrogen is evolved below a.

A lead electrode will remain stable and not corrode in the region bounded by lines *16* and *24*. Passivation of the lead surface occurs in the region bounded by line *21*, where the stable Pb(IV) compound, PbO_2, is formed. Lead corrosion occurs in all other zones and should be avoided in battery operation.

Under acidic conditions (i.e. aqueous MSA), Pb would dissolve into Pb^{2+} as predicted by the region bounded by the lines *16* and *21*. If the cell is partially charged and not being used, this would suggest that the lead coating on a soluble lead cell's negative electrode would need to be cathodically protected by reducing its potential below -0.3 V in order to avoid self-discharge. Anodic protection for the PbO_2 coating at the positive electrode could similarly be required. This is also dependent on the reaction kinetics, which are not described by this diagram.

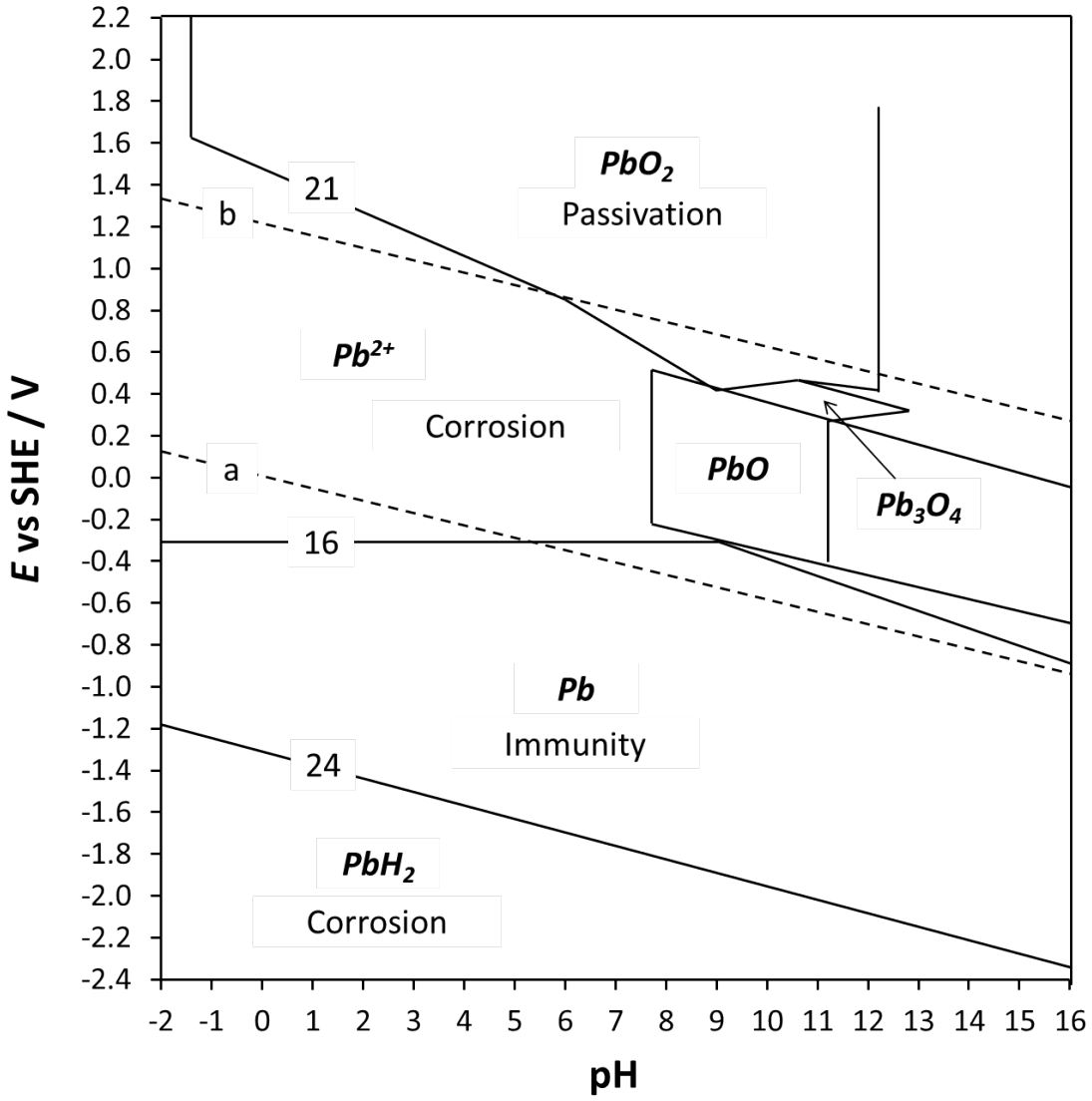

Figure 2.3: Recreated potential-pH diagram for the lead-water system at 25 C, based on the original diagram by Pourbaix [72].

PbO and other lead oxide compounds are formed in moderately alkaline conditions. This has been reported in practice, where deep within the lead dioxide deposit in the SLFB [36], and also the positive electrode in the LAB, proton starvation can lead to the formation of PbO [34] (Chapter 2.5.4). Lead hydride, which immediately breaks down into lead and hydrogen gas, occurs under very reducing conditions, i.e. below line *24*, which describes the high hydrogen evolution overpotential at a lead surface. The Pourbaix diagram of an aqueous Pb and H_2SO_4 system has previously been determined for the LAB [73]. A similar

study concerning an aqueous Pb and MSA system would provide much detailed insight for the SLFB.

2.3.2 Lead Dioxide

Also known as lead(IV) oxide, lead dioxide is denoted by the symbol PbO_2 and has a molecular mass of 239.21 g mol^{-1}. It is black in colour and possesses a crystalline structure, of which there are two allotropes, the α and β phase [27]. The density of plattnerite, the natural mineral form of β-PbO_2, is 9.375 g cm^{-3} [67]. The densities of α-PbO_2 and β-PbO_2 found in the electrode of the lead-acid battery is 9.72 g cm^{-3} and 9.57 g cm^{-3} respectively [27].

Even though the use of lead dioxide coatings has been studied for well over a century, the deposition mechanism is still debated; the most popular theory is presented in Chapter 2.4.2. Apart from the conversion to $PbSO_4$ in the LAB, there is little research concerning the reduction of lead dioxide to Pb^{2+}. Nevertheless, much experience gained from the coatings and LAB industries can be applied to SLFB research. Lead dioxide has been studied so extensively because of its many useful properties, which includes high electrical conductivity (the β phase is comparable to that of titanium), high oxygen evolution overpotential and good chemical stability in corrosive media, all important qualities for battery operation [74].

The wide region of stability of PbO_2 in the Pourbaix diagram describes its strong oxidising nature. The α phase has an orthorhombic shape with compact packing of the particles, whilst the β phase is tetragonal in nature, consisting of rough and larger, overlapping crystals [75].

The greater porosity of the β phase provides a higher surface area, making it well-suited for applications such as the oxidation of organic compounds in waste water treatment [76]. The effect of differing proportions of α and β in the LAB is also well understood, though the conditions affecting their respective formations from MSA media remains unclear (Chapter 2.5.3). It has been suggested that the superior surface morphology of the α phase makes it the preferred form in the SLFB [55], however recent experiments may have cast doubt on this theory (Chapters 2.5.4 and 2.5.6).

2.3.3 Methanesulfonic Acid

MSA is a strong acid with a pK_a value of -1.8 [77] (a measure of the acid's tendency to split into H^+ and its anion in water). It is completely ionised at 0.1 M in aqueous solution [78], dissociating into H^+ and the methanesulfonate anion $CH_3SO_3^-$. It has a molecular mass of 96.11 g mol^{-1} and a density of 1.481 g cm^{-3} [79]. Commercially available since 1964, it is the simplest, cheapest and most widely used of the alkylsulfonic acids [80].

MSA occurs naturally in the sulfur cycle, forming in the atmosphere from the photochemical oxidation of dimethyl sulfide. Following deposition by precipitation, microbial degradation breaks MSA into sulfate and carbon dioxide [81]. It is a less toxic and environmentally friendly alternative to fluorosilicic and fluoroboric acids, and has made these acids obsolete over the previous few decades in industrial applications such as the electroplating of lead alloys [78]. Furthermore, MSA is a non-oxidising acid that is less corrosive than sulfuric acid, which allows for easier and safer storage and transport, and circulation through a flow circuit [80].

A high electrolyte conductivity reduces energy loss in the cell by reducing $\sum IR$. The ionic conductivity of MSA compares well with hydrochloric acid, at 300 mS cm^{-1} compared to 346 mS cm^{-1} for HCl, which is suitable for battery operation. Another favourable battery requirement would be to hold a high level of lead in the electrolyte. The saturation solubility of the lead methanesulfonate salt, $Pb(CH_3SO_3)_2$, in water is 2.6 M, which provides a sufficiently high energy density for battery operation. In contrast, lead sulfate is insoluble in water and the solubility of lead chloride is also close to zero [78].

Lead and lead dioxide can also be deposited at high rates from aqueous MSA solutions, at 60 mA cm^{-2} [37] and 100 mA cm^{-2} [60] respectively. From Equation 2.16, this corresponds to a deposition rate of 3.4 μm min^{-1} for lead and 7.9 μm min^{-1} for lead dioxide. For lead dioxide, this is a higher rate than that possible from nitrate solutions. Additionally, the crystal structure of the deposits from MSA solutions are generally finer and well-oriented compared to those from nitrate solutions [60].

MSA is a well understood acid that has become very popular in electroplating applications. Because of this, its high conductivity, high metal salt solubility and overall safer nature, it is

clear that MSA is the acid of choice for the soluble lead flow battery.

2.3.4 Solubility of Lead Methanesulfonate

In solution, divalent pairing occurs between $CH_3SO_3^-$ and Pb^{2+}, forming a complex solvation shell involving molecules of H_2O and H^+. If water is removed from the solution or if the solubility limit of lead is surpassed, crystals of lead methanesulfonate will begin to precipitate.

There are three reported ways of producing electrolyte for soluble lead battery experiments. Electrolytes can be composed of MSA and lead methanesulfonate solution, which can both be bought directly from chemical manufacturers [31]. However, a more economical method of preparing electrolyte in the lab involves reacting lead oxide, PbO [82], or lead carbonate, $PbCO_3$ [30], directly with MSA. In each case, the formation of lead methanesulfonate proceeds as follows:

1. $PbO_{(s)} + 2CH_3SO_3H_{(aq)} \rightarrow Pb(CH_3SO_3)_{2(aq)} + H_2O_{(l)}$
2. $PbCO_{3(s)} + 2CH_3SO_3H_{(aq)} \rightarrow Pb(CH_3SO_3)_{2(aq)} + H_2O_{(l)} + CO_{2(g)}$

If the reactants are measured exactly, then it can be seen that the resulting solution will be neutral in pH. If excess MSA is then added, the solubility limit of the lead methanesulfonate will decrease. This relationship was studied by Wills [83] and is reproduced with permission as Figure 2.4.

The solubility of lead methanesulfonate falls with increasing MSA concentration, from approximately 2.2 M at 0.9 M MSA, to close to zero near 8 M MSA. Beyond 2 M MSA, the solubility limit drops below 1.3 M. When the temperature is increased from 298 K to 313 K, the solubility limit slightly increases. For example, at 2 M MSA, the solubility rises from 1.6 M to 1.8 M between 298 K and 313 K respectively [83]. The solubility limit offers a sufficiently high energy capacity for flow battery operation: a 1.5 M Pb^{2+} and <2.0 M excess MSA electrolyte would offer 40 Ah dm^{-3} of charge capacity (Equation 2.17).

Electrolyte compositions in the remainder of this chapter and in the novel work section are reported as x M Pb^{2+} and y M MSA, where the Pb^{2+} refers to the $Pb(CH_3SO_3)_{2(aq)}$

concentration and the MSA refers to the *excess* or *free* acid present in the solution.

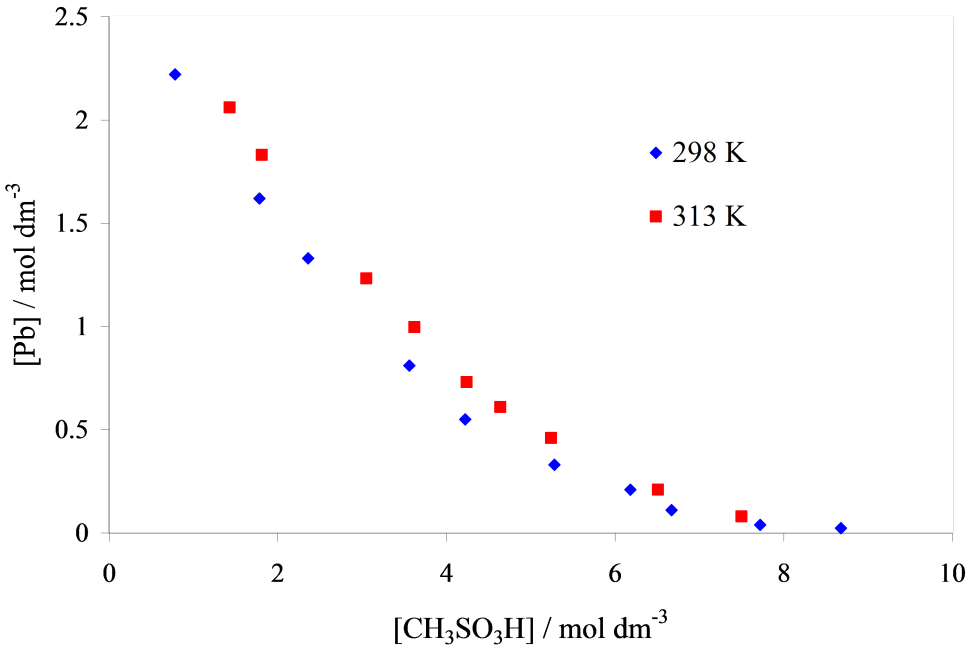

Figure 2.4: Solubility of lead methanesulfonate as a function of excess MSA concentration, reproduced with permission [83].

2.3.5 Electrolyte Conductivity

At present, the effect of lead(II) concentration, $[Pb^{2+}]$, and excess acid concentration, [MSA], on the overall solution conductivity is poorly understood. Figure 2.5 presents the only reported work concerning this relationship.

The conductivity is seen to decrease with increasing $[Pb^{2+}]$, from 0.004 M to 1.5 M. With 0.004 M Pb^{2+} in solution, the conductivity increases with increasing [MSA], peaking at 450 mS cm^{-1} at 3 M MSA. At higher $[Pb^{2+}]$, the conductivity initially increases proportionally with [MSA] until 2 M MSA. At higher [MSA], the conductivity sees a plateau, no longer increasing with extra MSA.

A high $[Pb^{2+}]$ would increase the electrolyte energy density but at the cost of a reduced solution conductivity, which would result in a greater Ohmic loss in the cell and therefore a lower cell potential. This trade-off requires further understanding in order to optimise an

electrolyte composition.

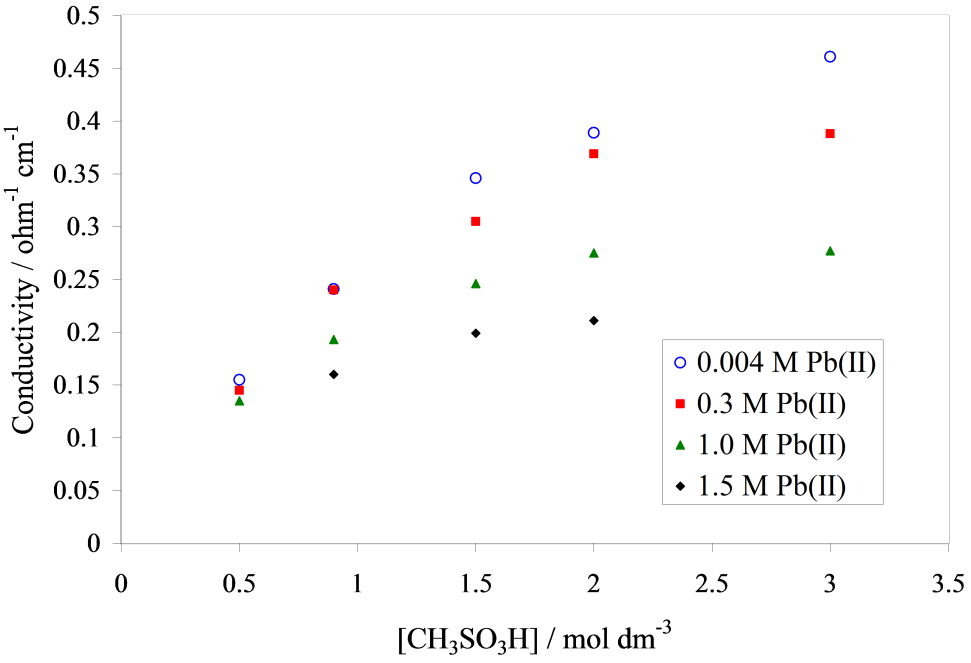

Figure 2.5: Conductivity as a function of [Pb^{2+}] and [MSA], reproduced with permission [83].

2.4 Electrode Kinetics

2.4.1 Negative Redox Couple

Cyclic voltammetry was carried out by Wallis and Wills [32] separately for each redox couple in order to understand the electron transfer kinetics and reversibility of both electrode reactions. The Pb^{2+}/Pb couple at the negative electrode was investigated using a three-electrode glass cell with 25 cm^3 of electrolyte. A glassy carbon rotating disc electrode (RDE) set at 900 rpm was placed in a solution of 10 mM Pb^{2+} and 1.5 M MSA. A platinum wire was used as the counter electrode and potentials were measured against a saturated calomel reference electrode (SCE). All potentials in the following section are stated versus SCE. The potential was cycled 200 times consecutively between -0.2 V and -0.7 V. The 1^{st} and 200^{th} cycle are superimposed together in Figure 2.6.

Sweeping negatively from -0.2 V, a cathodic reduction wave is seen at -0.55 V, reaching

a limiting current density of -5 mA cm^{-2}. This suggests the nucleation and growth of a solid metal species (deposition). On the reverse scan from -0.7 V, reduction continues until -0.48 V, at which point an anodic oxidation curve begins, later peaking at -0.39 V before sharply decreasing. This represents the dissolution of the deposit back into solution. Due to the low concentration of Pb^{2+} in solution, the reaction is mass-transport controlled on the forward scan (low flux of active species to electrode surface), hence the low current density on deposition. In contrast, a sharp stripping peak is seen on the reverse scan as the solid Pb is already present upon the electrode surface. Therefore, there is a sudden dissolution of Pb into Pb^{2+}, resulting in a brief, high generation of current.

The entire voltammogram is characteristic of the deposition and subsequent dissolution of a M^{2+}/M couple, where the kinetics are rapid and therefore the overpotentials are low. There is little change in the voltammogram shape after 200 cycles, suggesting that this is a highly efficient and repeatable process.

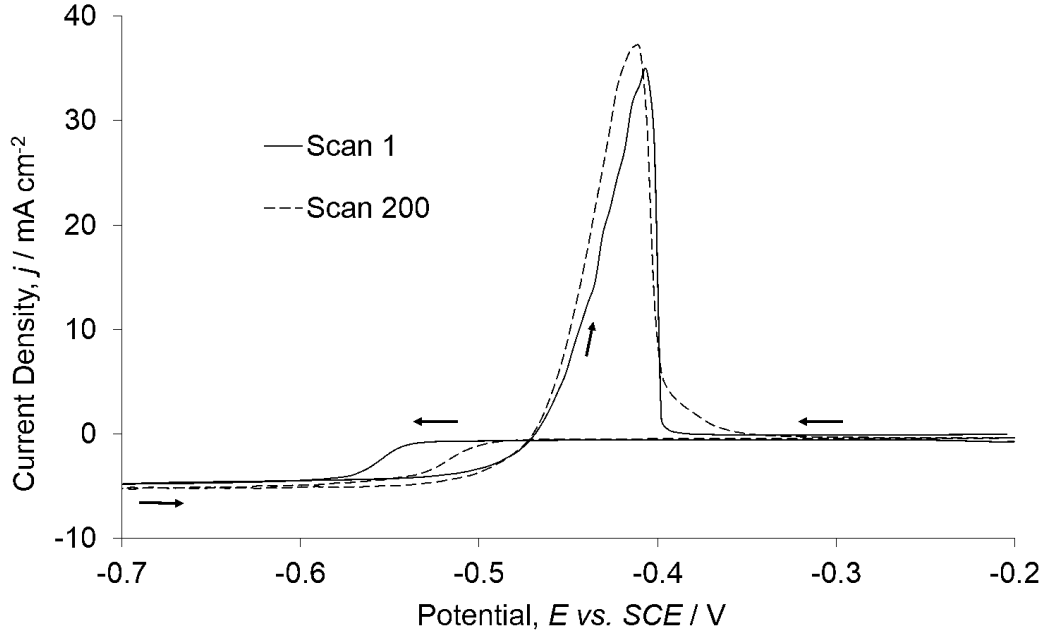

Figure 2.6: 1st and 200th cyclic voltammograms of the Pb^{2+}/Pb couple in 10 mM Pb^{2+} and 1.5 M MSA. RDE: glassy carbon. Rotation rate: 900 rpm. Temperature: 295 K. Reproduced with permission [32].

Furthermore, in a similar study yielding similar voltammogram profiles [30], the charge efficiency was calculated to be close to 100%. No substantial hydrogen evolution was observed, and this result held true under a variety of electrode materials (glassy carbon, gold, plat-

inum) and electrolyte concentrations (1 - 300 mM Pb^{2+} and 0.1 - 5 M MSA), with only minor differences in the peak potentials.

2.4.2 Positive Redox Couple

According to data from Fleischmann et al. [84], the oxidation of dissolved Pb^{2+} species in solution and the subsequent deposition of PbO_2 at an anode surface is a two-electron transfer process, which occurs over two stages. The mechanism is irrespective of the solution, which only affects the deposition rate. This was further explored by Velichenko et al. [60], who suggested the following mechanism:

1. $H_2O \rightarrow \cdot OH_{ads} + H^+ + e^-$
2. $Pb^{2+} + \cdot OH_{ads} \rightarrow Pb(OH)^{2+}$
3. $Pb(OH)^{2+} + H_2O \rightarrow Pb(OH)_2^{2+} + H^+ + e^-$
4. $Pb(OH)_2^{2+} \rightarrow PbO_2 + 2H^+$

H_2O is oxidised at the anode surface, splitting into H^+ and the ·OH radical, which adsorbs onto the electrode surface. This interacts with a Pb^{2+} ion, forming the soluble $Pb(OH)^{2+}$ compound. Following the second oxidation step, the soluble Pb^{4+} compound $Pb(OH)_2^{2+}$ accumulates near the electrode surface. This molecule then decomposes into PbO_2, which crystallises on the electrode surface.

Velichenko et al. investigated this mechanism in methanesulfonic and nitric acid media, and the process remained the same in both cases. However, the rate of deposition was found to be greater in the presence of methanesulfonate.

Cyclic voltammetry of the Pb^{2+}/PbO_2 couple at the positive electrode was also investigated by Wallis and Wills [32]. A solution of 0.5 M Pb^{2+} and 1.5 M MSA was used, and the set-up remained the same as that for the negative voltammetry test. The potential was swept between 0.2 V and 1.9 V for 100 consecutive cycles. The 1^{st} and 100^{th} cycles are presented together in Figure 2.7.

Sweeping positively, deposition of PbO_2 in the 1^{st} cycle is seen to commence at 1.85 V. This continues on the backward scan, from 1.9 V until 1.5 V, suggesting that the deposition of

PbO_2 onto layers of PbO_2 is kinetically more facile than onto a glassy carbon substrate. A similar deduction for Pb deposition can be made from the negative electrode voltammogram. Continuing the potential sweep negatively from 1.5 V leads to a well defined cathodic reduction peak between 1.2 V and 0.95 V, reaching a current density of -200 mA cm^{-2}. It is clear that PbO_2 is being deposited and later stripped back into solution. However, unlike the Pb^{2+}/Pb couple, the electron transfer kinetics are considerably slower, as seen by the large separation in potential between the oxidation and reduction peaks.

Whilst the deposition of PbO_2 takes place at high current densities at negatively shifted potentials in the cycles after the first, the stripping region is seen to broaden and the peak current density decrease. By the 100^{th} cycle, the stripping region ranges from 1.2 V to 0.2 V, peaking at just -75 mA cm^{-2}. This puts into perspective the difficulty of reducing layers of PbO_2, which leads to the gradual accumulation of the deposit with each cycle.

These results suggest that in a cell under operation, the accumulation of PbO_2 at the positive electrode would result in an accumulation of Pb at the negative. By improving the kinetics at the positive electrode, the negative electrode would therefore also benefit.

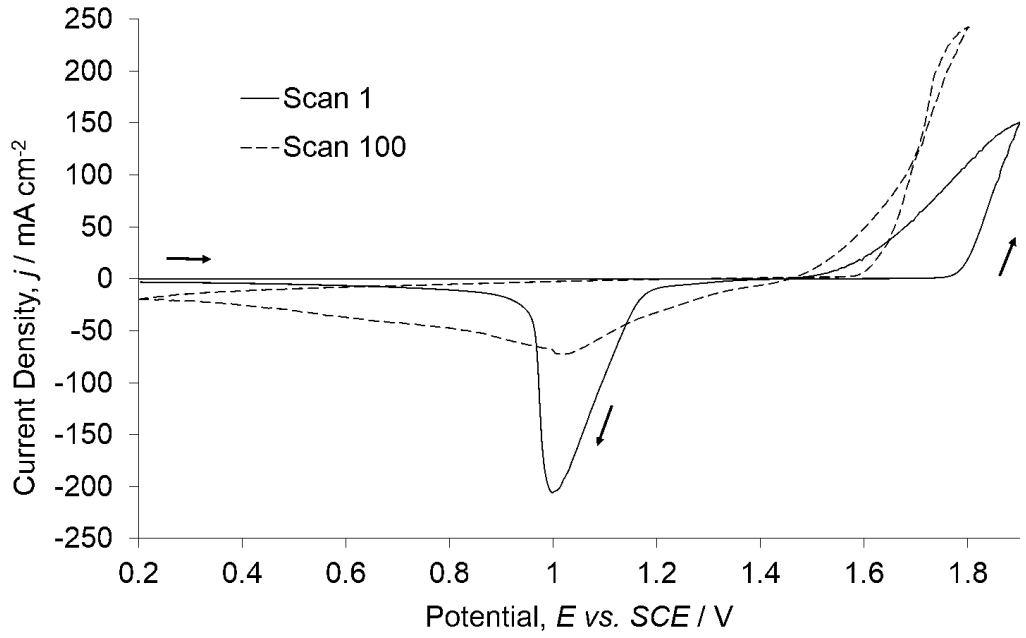

Figure 2.7: 1^{st} and 100^{th} cyclic voltammograms of the Pb^{2+}/PbO_2 couple in 0.5 M Pb^{2+} and 1.5 M MSA. RDE: glassy carbon. Rotation rate: 900 rpm. Temperature: 295 K. Reproduced with permission [32].

2.5 Operating Conditions

2.5.1 Introduction

To maximise the cell performance and lifetime, deposition on charge must be uniform across each electrode surface. The deposits should be smooth, compact and well-adhered whilst also remaining easy to dissolve on discharge. The morphology and other properties of the deposits will depend on the operating conditions, such as the electrolyte composition in terms of [Pb^{2+}] and [MSA], temperature, current density and flow rate.

In the following chapters, studies from the coatings field, lead-acid batteries, and studies specifically for the SLFB are combined, discussed and summarised for the negative and positive electrodes. The effect of the lead dioxide deposit morphology on the potential-time response of a cell cycling experiment is also discussed.

2.5.2 Negative Electrode

Lead coatings are used for corrosion resistance of the base metal, particularly if the material is to come into contact with sulfuric acid; the surface of the lead forms a passivating sulfate layer that protects the layers within. To ensure material integrity, the coating must be devoid of pits and cracks. Typically, coatings up to 0.2 mm are deposited [37], whereas the target for SLFB operation is often reported to be 1 mm [53].

In the absence of a suitable surfactant the formation of large crystals, referred to as dendrites, can be seen across the cathode surface. In particular, dendrites can grow rapidly along the internal cell walls at the edges of the electrodes, using the non-conducting surface as a scaffold (not to be mistaken with 'edge effects' that occur at non-parallel plate electrodes, such as the rotating disc electrode [65]). This type of growth is also seen with lead dioxide at the positive electrode.

Dendrites, and other rocky forms of growth, can short the cell and are more susceptible to being dislodged by the electrolyte flow. The current density is highest where the distance between the negative and positive electrodes is lowest [65]. Hence, any slight growth of lead towards the positive electrode will result in an increase in the current density in that area,

resulting in a greater deposition rate [65]; the further the tip of the growth is from the cathode surface, the faster it grows in size. This positive feedback loop allows Pb dendrites to form rapidly, stressing the importance of uniform, smooth deposition at all times. In addition, high temperatures lead to coarser grain sizes, which would exacerbate this mechanism. In industry, the lead plating bath temperature is controlled between 293 K and 313 K [37]. PbO_2 is far less conductive as Pb, which is why it is not possible to produce PbO_2 dendrites as the rate of electron transfer is slow.

Figure 2.8: Image of a rough, dendritic lead deposition onto a carbon/polyvinyl ester electrode from a flowing MSA solution in the absence of additives (further details in Chapter 8). Flow direction is into page. The large dendrite at the bottom was supported by the non-conducting internal cell wall.

Additives must be used in order to produce compact, smooth deposits and many organic surfactants are used routinely in industry. They work by inhibiting the deposition process; the rate of deposition can therefore be controlled by selecting the concentration of the additive. Work carried out by Pletcher et al. [53] trialled over 30 additives in lead deposition experiments focusing on stirred MSA baths. Two additives stood out for their ability to produce good quality lead deposits: lignosulfonate (as the sodium salt, or lignosulfonic acid) [33] and hexadecyltrimethylammonium hydroxide (HDTMA) [53].

Their experiments also investigated other conditions affecting deposition quality. In Figure 2.9, four SEM images display the effect of increasing $[Pb^{2+}]$ and current density at ambient

temperature on the deposit morphology. Deposition time was 2 hrs, and the substrate material was carbon/high density polyethylene (C-HDPE), with a scraped nickel surface (Chapter 2.7). An unstirred Hull cell was used for each test [53].

Images (a) and (b) show samples deposited from a solution composed of 0.5 M Pb^{2+} and 1.0 M MSA, with 5 mM HDTMA. Images (c) and (d) used the same MSA and HDTMA concentration, but [Pb^{2+}] was increased to 1.5 M. Furthermore, images (a) and (c) were deposited using a current density of 25 mA cm^{-2}, whilst images (b) and (d) used 50 mA cm^{-2}.

Image (a) shows the smoothest produced deposit. Compact, circular grains of equal size with few voids in between can be seen, and there are no protrusions from the surface. When the current density is increased to 50 mA cm^{-2} in image (b), larger grains up to 200 μm in width are formed and several protrusions can be seen. The grains now vary in size and the surface appears rougher. However, the grain orientation is relatively ordered.

At higher [Pb^{2+}], the deposit is markedly different: image (c) consists of a variety of grain sizes with numerous pores across the surface. There are many protrusions and the grains are more randomly orientated. When the current density is increased to 50 mA cm^{-2} in image (d), there is little to zero order in grain orientation. Grain size varies from as small as those seen in image (a) to extremely large, dendritic structures that rise high above the deposit surface.

Several tests were also conducted varying the HDTMA concentration. There was little difference to image (a) when zero additive was used. However, the grains in image (b) were less refined and more varied in shape in the absence of HDTMA, creating a rougher surface. When test (c) was repeated with 20 mM HDMTA, the deposit was improved, appearing more uniform and compact than image (b) but not as fine as image (a). Test (d) was also repeated with the higher HDTMA level, and the improvement was even greater than that seen for test (c). Though the grain orientation appeared unaffected, the larger crystals were subdued and there was greater uniformity across the surface. Furthermore, the deposits were also visibly more reflective. If the SLFB is to contain a high Pb^{2+} concentration and is charged at high current densities, then a high concentration of HDTMA becomes necessary to ensure reliable deposition.

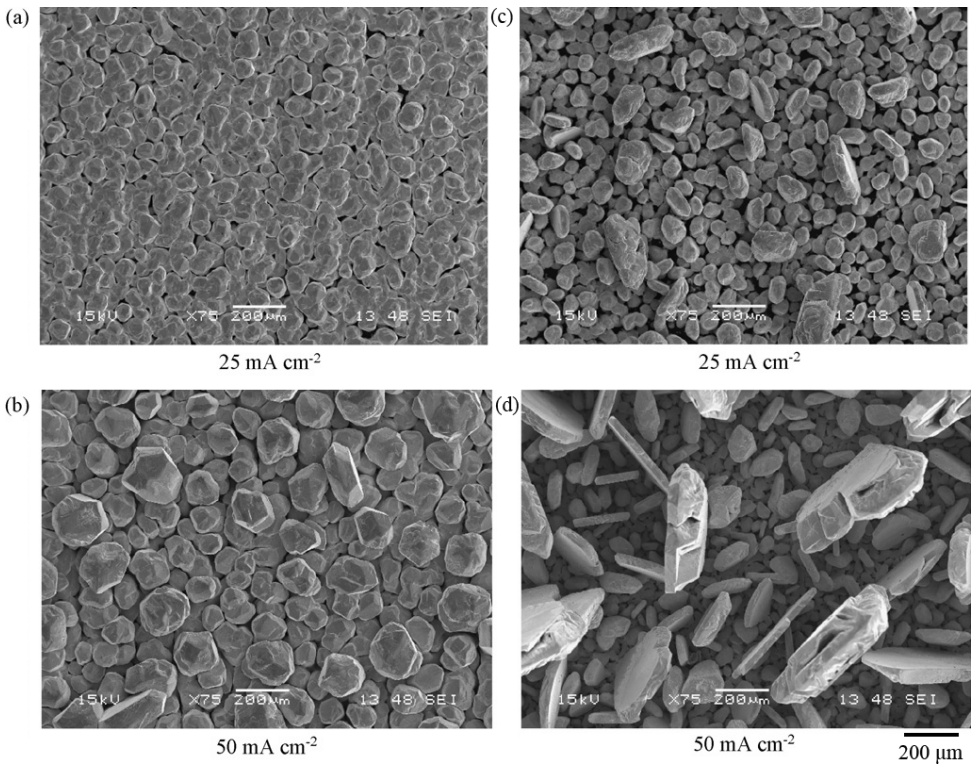

Figure 2.9: The effect of increasing [Pb^{2+}] on the deposit morphology of lead at the negative electrode. Unstirred Hull cell. Electrolyte: (a) and (b) 0.5 M Pb^{2+} and 1.0 M MSA, with 5 mM HDTMA; (c) and (d) 1.5 M Pb^{2+} and 1.0 M MSA, with 5 mM HDTMA. Deposition time: 2 hrs. Electrode: scraped Ni C-HDPE. Ambient Temperature. SEM image reproduced with permission [53].

The effect of increasing [MSA] was also studied, and the results can be seen in Figure 2.10. Images (a) and (b) show SEM images of samples deposited from a solution containing 0.3 M Pb^{2+} and 1.0 M MSA, with 5 mM HDTMA. Images (c) and (d) use the same Pb^{2+} and HDTMA concentration, but [MSA] is increased to 2.4 M. In addition, images (a) and (c) were deposited under a current density of 25 mA cm^{-2}, whilst images (b) and (d) used 50 mA cm^{-2}.

There are not significantly more void areas in image (c) compared to (a). Whilst (a) appears to be very smooth with tightly packed grains, (c) appears to have elevated regions, each consisting of a cluster of grains. This differs from the images in Figure 2.9, where any protrusion was seen to be of a single grain.

As seen in image (d), the greater level of MSA and the high current density results in rocky, dendritic clusters scattered randomly across the deposit surface, with randomly oriented, moderately sized grains forming the base layer. The authors therefore suggest that [MSA] in

SLFB electrolytes not exceed a limit of 2 M MSA [53].

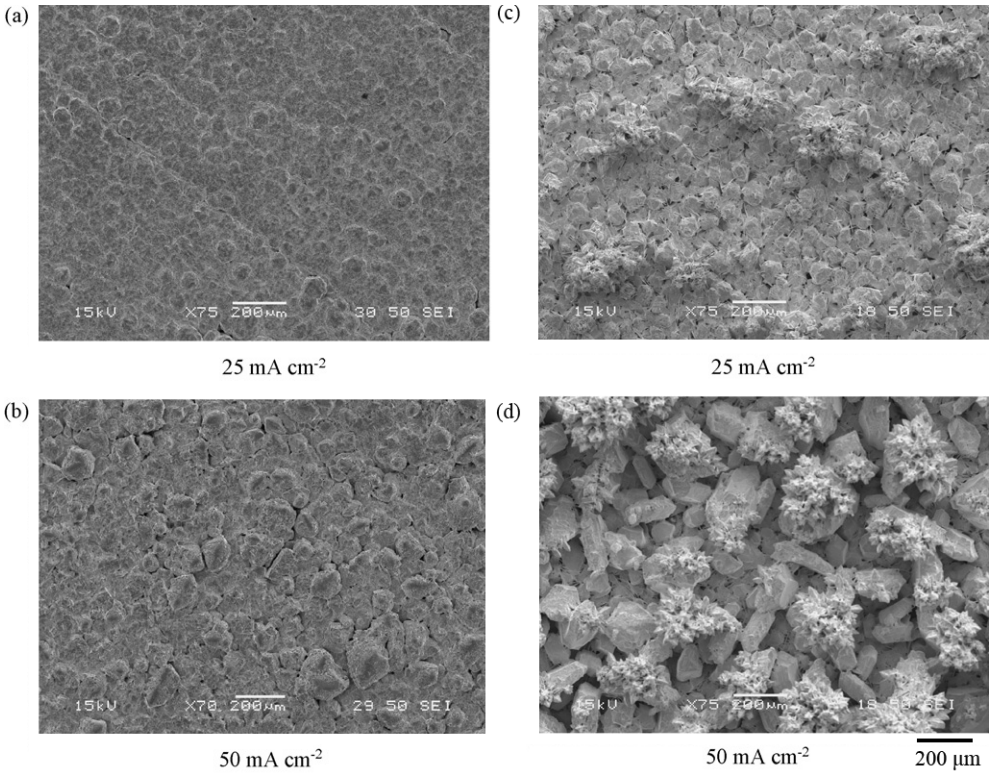

Figure 2.10: The effect of increasing [MSA] on the deposit morphology of lead at the negative electrode. Unstirred Hull cell. Electrolyte: (a) and (b) 0.3 M Pb^{2+} and 1.0 M MSA, with 5 mM HDTMA; (c) and (d) 0.3 M Pb^{2+} and 2.4 M MSA, with 5 mM HDTMA. Deposition time: 2 hrs. Electrode: scraped Ni C-HDPE. Ambient Temperature. SEM image reproduced with permission [53].

Finally, it was found that time is also an important factor in determining the quality of the deposit. As deposition time wore on, the deposit quality from all electrolyte compositions was seen to tend towards Figure 2.9d or 2.10d, depending on [Pb^{2+}] and [MSA].

2.5.3 Positive Electrode

It is possible to deposit pure α or pure β-PbO_2, as well as a mixture of both phases. However, the deposition conditions from aqueous solutions required to accurately achieve a certain purity of either phase is still inconclusive. It was believed that the α phase is deposited from high pH solutions, whereas β is preferred under acidic conditions [74]; studies regarding MSA based solutions by Pletcher et al. [54], Li. et al. [55], Sirés et al. [85] and Velichenko et al. [60] showed that this is not always the case. The phase and morphology depends on

the electrolyte composition and temperature, the substrate material, the rate of deposition and the deposit thickness, in addition to repeated deposition and stripping during battery operation.

Pletcher et al. [54] studied the deposition of PbO_2 onto C-HDPE electrodes from stirred MSA solutions. It was found that compact, well-adhering layers up to 1 mm could be deposited under a variety of electrolytes, with [Pb^{2+}] and [MSA] ranging from 0.1 - 1.5 M and 0 - 2.4 M respectively, and with 5 mM HDTMA in solution. Higher current density was seen to create more compact deposits. Figure 2.11 presents a selection of SEM images where certain deposit defects can be seen.

Images (a) and (c) present SEM images of a PbO_2 surface deposited from a solution containing 0.5 M Pb^{2+} and 0.3 M MSA, with 5 mM HDTMA (stirred solution 500 rpm, parallel-plate beaker cell). Images (b) and (d) use the same HDTMA concentration, but [Pb^{2+}] and [MSA] are both increased to 1.5 M (unstirred Hull cell). Regarding the deposition rate, images (a) and (d) were deposited at 50 mA cm^{-2}, whilst images (b) and (c) used 20 mA cm^{-2} and 150 mA cm^{-2} respectively.

In general, the deposits appear smooth at all three scales of magnification, from 1000 μm in image (c), to 500 μm in image (a), to 100μ in images (b) and (d), with round grains of uniform size and no voids in between. There is little difference between the deposits, despite the wide range of current density, concentration of [Pb^{2+}] and [MSA], and the fact that (a) and (c) were deposited under stirred conditions whilst (b) and (d) from static conditions. There are, however, two other notable observations.

In the 150 mA cm^{-2} deposition seen in image (c), the black spots indicate damage caused by oxygen evolution. The current density at which gassing occurred was seen to decrease with decreasing [Pb^{2+}] and increasing [MSA]. For example, in another study that used a solution of 0.3 M Pb^{2+} and 2.4 M MSA, oxygen evolution was observed at 50 mA cm^{-2}. This was also confirmed by Velichenko et al. [60], where it is suggested that high [MSA] inhibits PbO_2 deposition due to excessive complexation.

In image (d), a large fissure is seen running across the centre of the image. This is not seen in image (b), which used the same electrolyte but was deposited at 20 mA cm^{-2}. It

is suggested that at a high MSA concentration of 1.5 M and a high current density of 50 mA cm^{-2}, the compact deposit becomes stressed, leading to cracks at the deposit surface. In a flow battery, this would likely result in the breaking away of layers into the electrolyte. The conditions during operation therefore must be carefully controlled to avoid such losses in energy capacity [54].

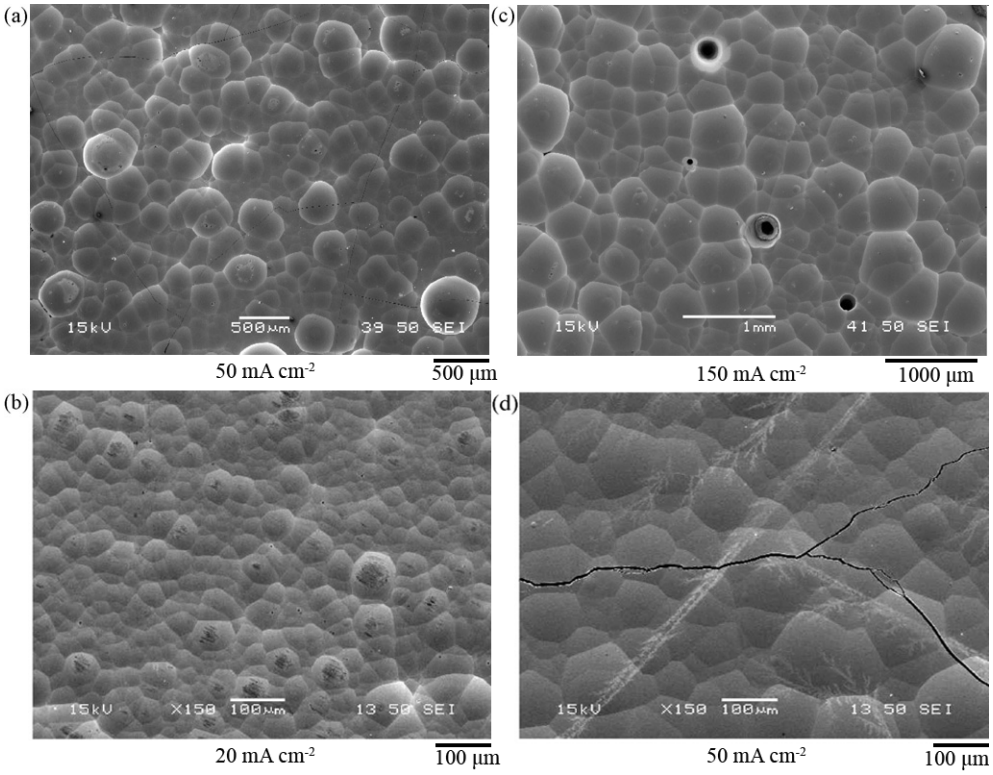

Figure 2.11: The effect of $[Pb^{2+}]$ and [MSA] on the deposit morphology of lead dioxide at the positive electrode. (a) and (c) 500 rpm stirred parallel-plate beaker cell, (b) and (d) unstirred Hull cell. Electrolyte: (a) and (c) 0.5 M Pb^{2+} and 0.3 M MSA, with 5 mM HDTMA; (b) and (d) 1.5 M Pb^{2+} and 1.5 M MSA, with 5 mM HDTMA. Deposition time: 2 hrs. Electrode: C-HDPE. Ambient Temperature. SEM image reproduced with permission [54].

Voltammograms conducted by Li et al. [55] studied further the consequences of thick PbO_2 deposits. On reduction, thicker deposits were seen to increase the overpotential, shifting the reduction potential to more negative values whilst broadening the reduction peak. The difficulty of this mechanism appears to be the main impediment to further SLFB development, and it is attributed to the slow reaction kinetics and an insufficient supply of protons to the inner layers of the PbO_2 deposit (Chapter 2.5.6).

In further morphology studies, Li et al. saw a correlation between α-PbO_2 and smooth

deposits. In addition, whilst both phases were seen to form compact deposits, it was suggested that the presence of β layers amongst the α layers could be a precondition leading to powdery deposits. Temperature was discovered to be the most influential parameter on determining the phase: α deposits were favoured at lower temperatures, producing pure α-PbO_2 at 298K. Pure β-PbO_2 was deposited between 333 K and 348 K, and a mixture of both phases occurred between 298 K and 333 K. The mean grain size was also seen to grow, from 18 nm at 298 K to 57 nm at 348 K.

Deposition under mass transport control also resulted in the deposition of the β phase. The deposit is also powdery and poorly-adhering. Higher [Pb^{2+}], at least above 0.3 M, was seen to deposit α as the dominant phase. In a charge/discharge study using a stirred beaker cell filled with 0.5 M Pb^{2+} and 0.5 M MSA, at 298 K, the PbO_2 deposit was seen to accumulate and become rougher with each cycle; the early cycles deposited a majority α-PbO_2 deposit, with the proportion of β structures growing with each following cycle.

The proportion of α-PbO_2 in the LAB is also seen to decrease with cycling. The positive active mass is prepared by mixing leady oxide (PbO) with other components. After curing, the electrode is oxidised in a cell to form PbO_2 (known as the Planté formation process). In experiments reported by Yeh et al. [86], one of these electrodes contained 13.9% and 82.0% of the α and β phase respectively. Following 100 charge/discharge cycles, the proportions were seen to reduce to 8.8% and 81.7% respectively (with the proportion of $PbSO_4$ increasing).

Sirés et al. [85] are largely in agreement with Pletcher et al. and Li et al. Whilst temperature shows the greatest influence on phase, low [MSA] and high [Pb^{2+}] are required to avoid extremely porous deposits riddled with many cracks and voids. Defects such as these result in a poorly-adhering, powdery deposit.

2.5.4 Further Discussion on the Structure of Lead Dioxide

The discussion so far has assumed a stoichiometric PbO_2 deposit. However, it is known that both α and β structures instead exist as PbO_x, where $1.85 < x < 2.05$ in the LAB [16]. H_2O is also widespread inside the pores. The theory proposed by Rüetschi [87], and backed up by

experimental data, suggests that there are cation vacancies separating ordered, crystal zones within the lattice. Pb^{2+} ions could occupy these vacancies, leading to a structure proposed as $(Pb^{4+})_{1-x-y}(Pb^{2+})_y(O^{2-})_{2-4x-2y}(OH^-)_{4x+2y}$, where x and y are the number of vacant cation sites and incorporated Pb^{2+} ions respectively, as a fraction of the overall number of cation sites (i.e. involving those occupied by Pb^{4+} as well).

Dopant cations can also occupy these vacant positions, affecting the properties and the ratio of α and β structures [88]. For example, large cations such as bismuth are reported to promote α growth [89] (Chapter 2.6.2).

Such lattice defects lead to conductive properties. PbO_2 therefore is regarded as a n-type semiconductor [27], but β-PbO_2 has also been considered as a semi-metal [90]. Despite α-PbO_2 having a more compact structure, there is greater ionic mobility in β-PbO_2. The conductivity of the latter is therefore higher, at the 10^4 S cm^{-1} scale compared to the 10^3 S cm^{-1} scale of the former [75].

In the LAB, the compactness of α structures provides mechanical stability with the current collector grid, but this also makes it more difficult to discharge (i.e. reduce to $PbSO_4$) [91]. In contrast, the β structures offer a greater energy storage capacity and can be discharged at higher current densities, but the susceptibility for active mass shedding is greater [92]. Therefore, the balance between LAB performance, capacity and lifetime depends on the ratio of α and β-PbO_2 within the positive active mass, amongst other factors [16]. The former provides integrity by acting as a binding agent, whilst the latter provides the electrochemical performance. It is claimed by Kiessling [92] that during cycling, the proportion of α-PbO_2 and β-PbO_2 decreases and increases respectively, until an equilibrium is reached at 20% and 80% respectively.

2.5.5 Potential-Time Plots

In order to continue the discussion on lead dioxide, it is useful to first understand the shape of a potential-time response during a galvanostatic charge/discharge cycling experiment of a soluble lead flow cell. Figure 2.12 presents a typical result. The 100 cm^2 sized positive and negative electrodes were composed of a 2D carbon polymer surface, with impregnated

reticulated vitreous carbon (RVC) fragments (Chapter 2.7). The electrolyte consisted of 1 dm^3 of 1.5 M Pb^{2+} and 1.0 M MSA, with 1 g dm^{-3} lignosulfonic acid, and this was circulated through the undivided cell at 2.5 cm s^{-1}. The cell was operated throughout at 20 mA cm^{-2} [31].

Nine cycles are presented overall. The first 6 cycles each consist of a 15 mins charge followed by a discharge to 1.2 V (or for a maximum of 15 mins). In the subsequent 3 cycles, the charge/max discharge time is increased to 60 mins. The potentials of the individual electrodes vs. SCE, E_+ and E_-, are presented alongside the overall cell potential, U_{cell}, providing insight as to which electrode limits the overall cell potential during operation.

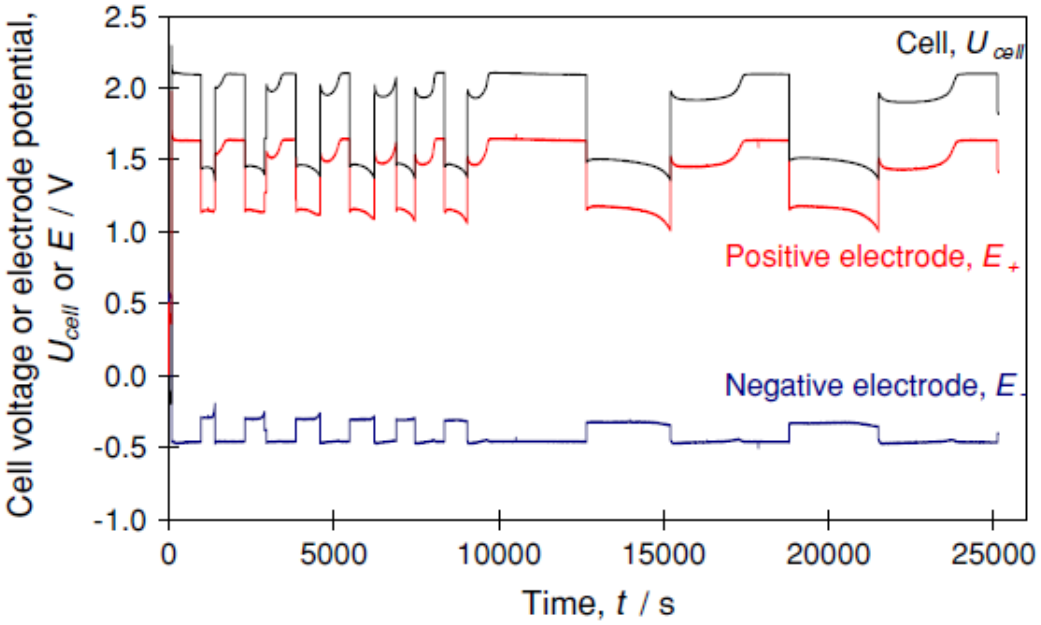

Figure 2.12: Potential-time response of a soluble lead flow cell galvanostatic charge/discharge experiment. Electrolyte: 1 dm^3 of 1.5 M Pb^{2+} and 1.0 M MSA, with 1 g dm^{-3} lignosulfonic acid. Electrode: 100 cm^2 C-HDPE, with impregnated RVC. Charge density: 20 mA cm^{-2} throughout. Flow rate: 2.5 cm s^{-1}. Reproduced with permission [31].

The charge and discharge potentials of the negative electrode are close to -0.5 V and -0.3 V respectively, approximately corresponding to the deposition and stripping potentials seen in the cyclic voltammetry of the Pb^{2+}/Pb couple (Chapter 2.4.1). The potentials are generally flat and stable throughout the experiment, particularly in the latter cycles.

In contrast, the positive potentials are more complicated. The discharge potential is flat in

the 1st cycle, at 1.25 V, before starting to decrease from 1.25 V in each consecutive discharge phase. The charge potential is stable only for the 1st cycle, at 1.6 V. In all other cycles, the charge potential starts at lower potentials (1.5< E_+ <1.6 V) after an initial spike, before instantly dropping to ≤1.5 V, and finally rising again to 1.6 V later on. The gap between the upper and lower potential is clearer in the latter cycles, where over half the charge phase takes place at the lower potential.

In the 1st cycle, the negative potential rises sharply towards the end of discharge, which causes the cell potential to drop to 1.2 V. This voltage spike decreases in size with each following cycle, finally becoming flat in the 5th cycle. During this time, the limiting electrode on discharge transitions from the negative to the positive. The shape of the positive electrode's potential-time response is discussed further in the following section.

2.5.6 Discharge at the Positive Electrode

Chapter 2.5.5 introduced a potential-time response of a cycling experiment involving a soluble lead flow cell, where the positive electrode potential on charge is seen to follow a complex pattern. There is an initial potential spike at the start of charge that is likely due to a high nucleation overpotential (part of activation overpotential, Chapter 2.2.2), followed by a dip in potential that subsequently increases later on during the charge phase.

The voltage dip on charge could be explained by the properties of PbO_x, where x could have a low value, possibly as low as 1. PbO could be formed during the discharge phase of the previous cycle. EDAX analysis conducted by Pletcher and Wills [36] did indeed identify the presence of PbO after several charge/discharge cycles in a separate cycling experiment.

In the charge phase of the first cycle in Figure 2.12, only Pb^{2+} is oxidised to a near stoichiometric PbO_2, resulting in a constant charge potential. It was seen in Chapter 2.4.2 that the deposition/dissolution mechanism of PbO_2 is a complex, multi-stage procedure. During discharge, high [Pb^{2+}] exceeding the solubility limit near the deposit surface, in addition to low [H^+] near the surface or within the pores, could lead to the formation of PbO [36], or perhaps a low x-value PbO_x. Proton starvation would result in a relatively high local pH. This condition could be created if the PbO_2 deposit becomes very compact, i.e. a large α-

PbO_2 presence. The formation of PbO could then be facilitated as predicted by the Pourbaix diagram for lead, seen in Figure 2.3.

In the following cycle's charge phase, PbO/PbO_x would be preferentially oxidised to PbO_2, resulting in the lower potential. Once all the conductive PbO_x has been oxidised, normal oxidation of Pb^{2+} into PbO_2 is resumed and the potential returns to its higher level. Because this charge profile is seen in every cycle but the first, it can be assumed that the rate of PbO/PbO_x formation during the discharge phase is equal to or greater than the rate of oxidation of PbO/PbO_x into PbO_2 on charge, or that there is a proportion of PbO/PbO_x that remains insoluble.

As x reduces from 2 to 1, its conductivity also drops. Certain PbO_x compounds therefore could remain insoluble. Described by Oury et al. [93] as a 'passivating' layer within the deposit, this could cause the accumulation of the PbO_2 deposit with each cycle by preventing the thorough dissolution of the overall deposit. H^+ is required to instigate the dissolution mechanism. With a high MSA bulk electrolyte concentration, Oury et al. suggest that H^+ can penetrate deep into the deposit and reduce the inner layers to passivating PbO_x compounds, creating an insulating layer between the electrode and the outer PbO_2 layers, preventing the dissolution of these outer layers. With a low MSA bulk electrolyte concentration, PbO_x formation is restricted to isolated clusters on the deposit surface, which can then be further reduced during discharge, or oxidised to near stoichiometric PbO_2 during charge.

This theory appears to disagree with that of Pletcher and Wills, who suggested that low $[H^+]$ near the electrode surface instead of high $[H^+]$ leads to PbO formation [36]. Regardless, previous claims that α-PbO_2 is better suited to the SLFB [55] are premature. Whilst forming a compact deposit is favourable for energy capacity and cell design in the SLFB, this same property makes α-PbO_2 more likely to suffer from surface cracks (Chapter 2.5.3). Furthermore, the compactness could also lead to a lack of protons inside the pores making it difficult to reduce on discharge. This difficulty is also seen in the LAB; β-PbO_2 is more conductive but tends to powdery deposits prone to flaking from the electrode surface (Chapter 2.5.4). A better understanding of the PbO_2 deposit formed in the SLFB during cycling is needed along with further comparisons to the LAB, as it is likely that a certain ratio of α to β-PbO_2 is required to improve the performance and cycle life of the SLFB.

2.5.7 Further Observations at the Positive Electrode

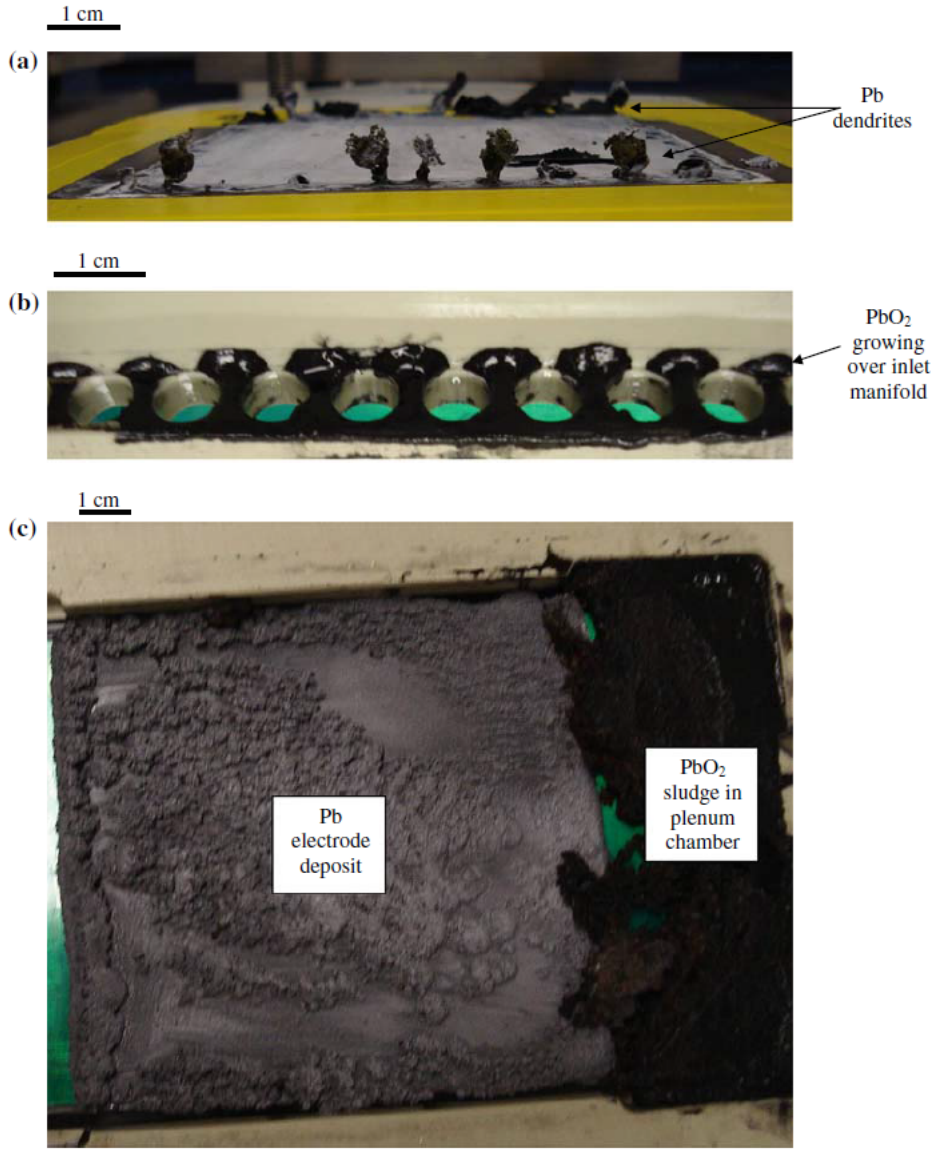

Figure 2.13: Common SLFB failure mechanisms. (a) lead dendrites protruding from surface of negative electrode; (b) creep of PbO_2 over inlet distributor; (c) rocky Pb deposits and PbO_2 sludge. Reproduced with permission [31].

A powdery deposit, or one that is cracked at the surface, is poorly-adhering and is more prone to breaking away from the electrode. Insoluble particles of PbO_2 stuck in the flow circuit or in the electrolyte reservoir have been seen in several SLFB studies [31,34,56]. This poses two problems: firstly, energy capacity is lost as these particles cannot be dissolved electrochemically. $[Pb^{2+}]$ in solution is therefore decreased, which affects the deposition

quality during subsequent charging. Secondly, if not filtered out, PbO_2 particles can restrict or block the electrolyte flow and damage the pump. Additionally, the amalgamation of these particles can lead to a gel-like, black, insoluble PbO_2 sludge [31]. The sludge is soft and can collect in areas which are stagnant or which see low flow velocity, as well as damaging the positive electrode by forming a thin film over it.

Additionally, Wills et al. [31] reported the 'creep' of PbO_2 deposits along the cell wall and inlet/outlet flow distributor, adhering strongly to the non-conductive polymer surfaces which were seen to act as a scaffold (similar to the Pb dendritic growths). These were difficult to dissolve on discharge and contributed to cell shorting. These various failure methods are illustrated in Figure 2.13.

A strategy for redissolving Pb and PbO_2 deposits remaining on the electrode and cell wall, and solid particles in solution has been proposed by Collins et al. [56], and this is discussed in Chapter 2.10.2.

2.5.8 Flow Rate

A high flow rate providing uniform mass transport of active species to the entire electrode surface, and removal of products including gas bubbles from the electrode surface (especially at high current densities), will ensure a uniform current distribution across the electrode. Secondary reactions will be minimised and the uniform flux of Pb^{2+} to the electrode surfaces will ensure well-adhered, uniform deposits [65]. This is continued in relation to 3D RVC electrodes in Chapter 2.7.

There is little work regarding the flow rate in the soluble lead flow battery. Understanding the relationship between flow rate and cell performance is important, as this can minimise the pumping power whilst maintaining good electrochemical performance (Chapter 2.2.3). The flow rate was briefly explored by Pletcher and Wills [36], where little difference in performance of a small flow cell with 2 cm^2 electrodes was seen between 2 and 10 cm s^{-1}. However, a low current density (20 mA cm^{-2}) and a high [Pb^{2+}] (1.5 M) were used. Control of the flow rate becomes more important at higher current densities and at higher states of charge, where there is lower [Pb^{2+}] in solution.

2.5.9 Summary of Conditions

The conditions required to produce smooth and uniform lead and lead dioxide deposits have been discussed in relation to battery performance and is summarised in Table 2.2. As the parameter in the vertical column is increased from its lowest value, ↑ represents that this has an effect of increasing or improving the corresponding horizontal property. ↓ shows a negative effect. *Pb Deposit Quality* refers to a uniform, smooth deposit without the presence of dendritic growth or rocky clusters. *PbO_2 Deposit Quality* refers to a smooth surface without the presence of oxygen evolution damage, surface cracking or powdery deposits.

	Pb^{2+} Solubility	**Electrolyte Conductivity***	**Pb Deposit Quality**	**PbO_2 Deposit Quality**
Ref.	[30, 83]	[83]	[37, 53]	[55, 85]
Section	2.3.4	2.3.5	2.5.2	2.5.3
[Pb^{2+}] ↑ 0.3 - 1.5 M	-	↓	↓	↑
[MSA] ↑ 0 - 2.4 M	↓	↑↑	↓	↓
Current Density ↑ 10 - 100 mA cm^{-2}	-	-	↓	↓
Temperature ↑ 298 - 348 K	↑	↑	↓	↓

Table 2.2: A table summarising the effects of various conditions on the properties and performance of the SLFB. As the conditions in the vertical column are increased from their lowest values, the arrows in the grid represent the effect on the corresponding horizontal property. ↑ represents an increase or an improvement, and ↓ represents a decrease or a deterioration. *Electrolyte ionic conductivity is studied in more detail in Chapter 4.

It is clear that several trade-offs are needed. Increasing [Pb^{2+}] reduces ionic conductivity and worsens the quality of the lead deposit. However, high [Pb^{2+}] is required for an increased energy density, to minimise the competing oxygen evolution reaction at the positive electrode and to prevent a powdery PbO_2 deposit. Increasing [MSA] reduces the quality of both deposits and decreases the electrolyte energy density by reducing the solubility limit of lead

methanesulfonate. However, a high [MSA] is needed for a good conductivity which would reduce energy loss in the cell.

A high current density promotes dendritic Pb formation and leads to a poor PbO_2 quality, increasing the chances of surface cracking in highly acidic electrolytes. Whilst the temperature is seen to slightly increase the solubility limit and improve conductivity, the quality of the lead deposit falls. At the positive electrode, a high temperature saw the formation of β-PbO_2 dominant deposits, which were often powdery and weakly-adhering. It is also unclear whether there is an optimal α-β ratio for improving the cell efficiency and lifetime.

2.6 Additives

2.6.1 Negative Electrode

The need for additives to inhibit the rate of lead deposition and produce non-dendritic, uniform, smooth deposits was introduced in Chapter 2.5.2. Pletcher et al. [53] studied a comprehensive set of additives for the negative electrode, and two additives were selected and subsequently used in flow cell experiments. These were sodium lignosulfonate or lignosulfonic acid, at a preferred concentration of 1 g dm^{-3}, and hexadecytrimethylammonium hydroxide (HDTMA), $CH_3(CH_2)_{15}N(OH)(CH_3)_3$, preferred at 5 mM. The preferred average M_W value of the lignosulfonate is not reported.

Lignin, a naturally occurring polymer found in wood, can be sulfonated to form lignosulfonate. It is a macromolecule with a complex structure based around the bonds between phenylpropane groups, with micropores in between. When adsorbed onto an electrode, these micropores allow the movement of ions through the structure. It is used as part of an 'expander' in the LAB, creating a porous $PbSO_4$ layer and preventing the formation of an insulating sulfate layer on discharge [27].

Whilst dendrite-free, compact deposits were produced, electrochemical studies showed that lignosulfonate adversely affects the overpotentials and charge efficiency at both electrodes, leading to a lower overall energy efficiency in flow cell cycling [33]. In addition, the amber colour of the electrolyte, due to the lignosulfonate, was seen to fade during these tests.

It is likely that these molecules are oxidised at the positive electrode, potentially affecting the additive's ability to control the quality of the lead deposit. However, the relation between discolouration and cell performance is not clearly seen in the results. Furthermore, a separator-divided soluble lead flow cell could confine the additive to just the negative electrode as a comparison in stability (Chapter 8).

Pletcher et al. place HDTMA in the same high 'lead deposit quality' category as lignosulfonate but a direct comparison as to which additive produces better deposits is not discussed. However unlike the latter, HDTMA was not seen to adversely affect the positive electrode reaction or affect the overpotential at either electrode. Additionally, it is considerably more expensive than lignosulfonate [79]. Both additives have been tested in short term flow cell studies, but the long term stability at elevated temperatures has not yet been investigated.

2.6.2 Positive Electrode

Lead dioxide coatings can be doped with both metallic and non-metallic ions in order to enhance a certain property of the coating. This has been reviewed by Li et al. [74], where lead dioxide composites, i.e. those containing solid particles such as other metal oxides, are also discussed. Bismuth, Bi^{3+}, is known to improve the coating's ability to oxidise inorganic ions [94] whereas fluoride, F^{-}, is known to improve the adhesion of the coating to the substrate [95] whilst inhibiting oxygen evolution [96].

Wallis and Wills [32] investigated the use of bismuth in the soluble lead system. Through cyclic voltammetry, Bi^{3+} (at a preferred concentration of 10 mM) was seen to improve the kinetics of the Pb^{2+}/PbO_2 couple, shifting the stripping peak in later cycles to more positive potentials whilst preventing the broadening of the stripping region. However, similar experiments showed the Bi^{3+}/Bi deposition potential from MSA solution to be more positive than that of Pb^{2+}/Pb, suggesting that in a flow cell, bismuth would be preferentially deposited at the negative electrode before the lead, or forming an alloy. Wallis and Wills also report a series of charge/discharge experiments using a soluble lead cell with static electrolytes. In order to avoid depletion of Bi^{3+} from the electrolyte through deposition at the negative electrode, a separator is introduced to confine Bi^{3+} to the positive half-cell. The cell lifetime

was seen to increase in this configuration, and this remains to be tested in larger cells using flowing electrolytes.

Chen et al. [89] have studied the use of bismuth in the LAB. Doping leady oxide with Bi^{3+} promotes the growth of the more-compact α-PbO_2 phase during formation, yet also making the PbO_2 active material more porous. Together, this has the effect of improving battery capacity and lifetime. The pore-creating ability of bismuth therefore could be useful in the soluble lead system, where a compact PbO_2 deposit was attributed to the difficulty in reducing the deposit (Chapter 2.5.6).

Oury et al. [82] have trialled fluoride-containing electrolytes in flow cell cycling tests. In the presence of the preferred concentration of 60 mM, the amount of powdery lead dioxide particles in the electrolyte reservoir (dislodged from the positive electrode) was substantially reduced. The lead dioxide adhesion to the electrode had improved without any detrimental impact on the reaction kinetics at either electrode.

Whilst other additives such as Fe^{3+} and Ni^{2+} have been tested for use in the SLFB [33], only Bi^{3+} and F^- are reported in the literature for successfully improving the positive electrode reactions during cell cycling. A more comprehensive investigation is needed to identify further additives, and combinations of additives, that could enhance the reversibility of the Pb^{2+}/PbO_2 reaction, either by creating a deposit with a good compromise between compactness and porosity and/or improving the reaction kinetics.

2.7 Electrode Materials

Lead coatings are deposited onto metals such as steel for protection from corrosive, mainly sulfuric acid-containing media [37], whereas lead dioxide coatings are commonly deposited onto a lead/lead alloy, carbon, or titanium substrate depending on the application [74]. Since the 1970s, flow battery researchers and manufacturers have sought to employ low cost electrodes with a good electrical conductivity and chemical stability. Carbon based materials satisfy these requirements and have been widely used in a number of flow battery systems, including all-vanadium, zinc-bromine and soluble lead [97].

2D electrodes refer to an electrode with a flat surface, such as a carbon polymer electrode. 3D electrodes, such as reticulated vitreous (glassy) carbon, meshes and felts, exist as a matrix through which the electrolyte can flow past or through. These can be attached through heat bonding, conductive adhesives or compression to a 2D electrode, or directly to the current collector [97].

Pletcher and Wills [35] initially experimented with carbon/high density polyethylene composites (C-HDPE) onto which nickel foam and reticulated vitreous carbon (RVC) were heat bonded. These could be modified by scraping away the attached layer after bonding, leaving behind a rough surface with Ni or RVC protrusions. The scraped RVC electrode was preferred as the positive electrode in early flow cell tests whilst the non-scraped Ni and RVC C-HDPE electrodes were preferred as the negative.

Various porosity grades and thicknesses of RVC positive electrodes, and both non-scraped 1 mm Ni and scraped Ni negative electrodes were reported by Wills et al. [31] in a flow cell employing 10 cm $\times$ 10 cm electrodes in a flow-by configuration (Chapter 2.10.1), with copper plates as current collectors. However, the experiments focus on other operating conditions and there is little discussion on the optimal electrode material, thickness and pore size. The authors here also report the use of another carbon polymer, and others have been reported elsewhere alongside a solid nickel plate as the negative electrode [34, 56]. Again however, the discussion in these publications does not focus on the properties, merits and shortfalls of the electrodes. There is also no detail on the nature of these carbon polymers, but they are thought to be carbon/polyvinyl ester, purchased from Entegris GmBH.

Scraped Ni C-HDPE was used for the lead deposition studies discussed in Chapter 2.5.2. Plain C-HDPE was used for lead dioxide deposition discussed in Chapter 2.5.3. Scraped Ni C-HDPE was trialled as the positive electrode and it was found to be stable despite the highly oxidising potentials there. However, the adhesion of PbO_2 was found to be poor, resulting in layers being dislodged from the electrode during flow cell cycling [54].

RVC is a form of carbon foam, consisting of open pores arranged (reticulated) within a rigid network of vitrous carbon [98]. It is a versatile, three-dimensional material available in various sizes and porosities. It has a low relative density (typically 3% - meaning that 97% is empty space) and a honeycomb structure that offers a high surface area. It is structurally rigid in the

presence of fluid flow, though its fragility can make it difficult to handle. It also possesses low thermal expansion and good electrical conductivity. The corrosion resistance of RVC is good, but it is susceptible to degradation at high temperatures in oxidising environments [99].

Because of these qualities, RVC is a popular electrode material. In flow reactors, it can be an effective and economic alternative for the removal of metal ions from wastewater through electrodeposition, including Pb^{2+} [100]. It has also found use in fuel cells and batteries. Iacovangelo and Will [101] studied different grades of RVC in flowing zinc electrolytes. Using a flow-by configuration, deposition mainly occurred at the RVC surface and the interface between the RVC and graphite plate underneath. However, a high flow rate was found to improve the amount of zinc deposition throughout the RVC. By using a 2 mm thick RVC electrode, organic additives and a high flow rate (Re 500), dendrite-free zinc deposits were achieved deep into the pores, even at a high current density of 100 mA cm^{-2}.

Czerwiński and Żelazowska have studied the deposition of lead and lead dioxide onto RVC, concluding that each deposit was almost identical in terms of electrochemical behaviour to lead [102] and lead dioxide [103] respectively deposited onto a lead substrate, which was seen to be kinetically more favourable than onto a 2D glassy carbon rotating disc electrode (Chapter 2.4).

Recently, Oury et al. [82, 104] have reported the use of a novel 'pseudo-honeycomb' graphite positive electrode placed between two copper-plate negative electrodes. The electrolyte flows in through one of the negative electrodes, continuing through the holes in the positive electrode before finally exiting via the opposite negative electrode. The active surface area of the negative and positive electrodes is 29 cm^2 and 171 cm^2 respectively. Performance in general was good, achieving 95% and 75% charge and energy efficiencies respectively over 100 cycles, and the formation of passivating PbO_x layers (Chapter 2.5.6) was not detected. Despite the presence of 5 mM HDTMA in the electrolyte and a low operating current density, the negative copper electrodes were covered in a rough lead deposit composed of large, rocky boulder-like nodules. Lead dendrites were also the primary cause of failure during cycling tests [82]. This electrolyte composition is discussed further in Chapters 2.8 and 2.9 and other SLFB cell designs are discussed in Chapter 2.10.1.

RVC, carbon polymer and nickel electrodes are the most widely reported in the SLFB lit-

erature. However, the effect of RVC on the phase composition of lead dioxide from MSA solutions remains to be explored. Cycling tests have so far been brief, limited by failure from shorting. Longer term studies are required to test the suitability of these electrodes, but at present it is clear that 3D over 2D electrodes are favoured at both ends of the cell.

2.8 Electrolyte Composition

Typically, a MSA-based lead plating bath contains 200 g dm^{-3} of lead (0.97 M Pb^{2+}) and 100 g dm^{-3} (1.0 M) of MSA. Deposition occurs at 30 - 60 mA cm^{-2} between 293 - 303 K with the use of organic additives [37].

It has been suggested by Oury et al. [82] that the H^+ concentration never exceed 1 M during cell operation due to the formation of insoluble, non-stoichiometric lead oxides which passivate the positive electrode surface, affecting cell longevity (Chapter 2.5.6). Using the novel pseudo-honeycomb cell design (Chapter 2.7), Oury et al. preferred an electrolyte consisting of 1.0 M Pb^{2+} and 0.25 M MSA, with 5 mM HDTMA *p*-toluene sulfonate and 60 mM NaF.

The most successful proof-of-concept study was conducted by Verde et al [59]. The authors achieved 2000 cycles at 95% charge and 79% voltage efficiency using a 0.7 M Pb^{2+} and 1.0 M MSA electrolyte, albeit on a small scale that is unrepresentative of flow battery conditions.

The largest electrodes tested in a soluble lead flow cell is 100 cm^2. One of these experiments was conducted by Wills et al. [31], where 100+ cycles at $\backsim$90% charge and $\backsim$80% voltage efficiency were achieved. The preferred electrolyte was 1.5 M Pb^{2+} and 1.0 M MSA electrolyte, with 1 g dm^{-3} of lignosulfonic acid.

2.9 Performance

2.9.1 Flow Cells

Table 2.3 summarises the results of the most developed soluble lead flow cells reported in the literature.

	Collins et al.	**Wills et al.**	**Oury et al.**
Reference	[34]	[31]	[82, 104]
Active Electrode area / cm^2	100	100	29 (-ve) and 171 (+ve)
Dimensions / cm	10 (B) × 10	10 (B) × 10	6.5 (B) × 4.5 (S)
Cells	1	1	2[i]
Positive Electrode	Entegris	C-HDPE	3D Graphite[i]
Negative Electrode	Nickel	C-HDPE	Copper
Current Collector	Copper	Copper	*n/a*
Inter-Electrode Gap / cm	1.2 (S)	1.0 (S)	0.5[i]
Electrolyte	0.5 Pb^{2+}	1.5 Pb^{2+}	1.0 Pb^{2+}
/ M	0.5 MSA	1.0 MSA	0.25 MSA
Additive	HDTMA[ii]	None	HDTMA[iii] and NaF
/ mM	5		5 and 60
Electrolyte Volume / cm^3	1500	500	500
Volumetric Flow Rate / $cm^3\ s^{-1}$	27.6[iv]	14	5
Linear Flow Rate / $cm\ s^{-1}$	2.30	1.40[iv]	0.18[iv]
Reynolds Number	448	144	55
Temperature / K	*n/a*	298	*n/a*
Current Density / $mA\ cm^{-2}$	20	10	20 (-ve) and 7 (+ve)
Charge Length / mins	60	15	60
Discharge Cut-Off / V	1.1	1.2	*n/a*
Cycles Achieved	40	100	100[v]
Av. % Charge Efficiency	88	90	95
Av. % Voltage Efficiency	74	80	79[iv]
Av. % Energy Efficiency	65[iv]	70	75
Failure Mode	Shorting	*Stopped*	Shorting[v]

Table 2.3: A summary of results from charge/discharge cycling using the most advanced soluble lead flow cells to date. *Entegris* refers to carbon/polyvinyl ester. Reynolds number, calculated using Equations 2.8 and 2.10; B and S are reported in the table. [i]There are no bipolar electrodes, but the electrolyte flows through one negative electrode, then through holes drilled into the graphite positive electrode (which has a 'pseudo-honeycomb' shape and is placed 0.5 cm away from each negative electrode), before exiting through another negative electrode (Chapter 2.7); [ii]hexadecyltrimethylammonium hydroxide; [iii]hexadecyltrimethylammonium p-toluene sulfonate; [iv]calculated values from reported information, using Equation 2.20; [v]100 cycles, though shorting is seen in the potential-time response as early as cycle 30; n/a data not available.

Collins et al. [34] used a low Pb^{2+} concentration of 0.5 M to simulate mass transport problems that could occur during cycling at higher states of charge. Aside from the study reported in Table 2.3, Wills et al. [31] conducted several other charge/discharge cycling tests with their 100 cm^2 cell, varying the current density between 10 and 100 mA cm^{-2}, and involving electrodes of RVC, nickel foam (only at the -ve electrode) and carbon felt. Leit-C conductive carbon cement was used to glue the electrodes to the current collectors. Following charge, deposition is mentioned to be evenly distributed over and throughout the RVC electrodes, and in most cases there were no substantial growths along the internal cells walls at the edges of the electrodes (there is no discussion on whether the nickel foam was also coated evenly within). Different flow dispersion manifolds and turbulence promoters were also investigated to prevent the creep of PbO_2 and dendritic Pb growth (Chapter 2.10.1).

Efficiency is good in general, averaging $\geq$65% energy efficiency, but cycle life is limited by shorting caused by the contact between deposits. Collins et al. were able to achieve only 40 cycles at 20 mA cm^{-2}. They also achieved 19 cycles at 30 mA cm^{-2} and 164 cycles at 10 mA cm^{-2} in separate tests. The low current density and charge time used by Wills et al. ensured that Pb dendritic growth and PbO_2 creep was kept under control. Oury et al. recorded a 75% average energy efficiency across 100 cycles, despite the fact that shorting noise is reported as early as cycle 30. This shows that contact between deposits does not necessarily mean complete failure of the cell. At 448, the Reynolds number in the experiment by Collins et al. was over 8 times larger than in the experiment by Oury et al. and just over 3 times as much as that used by Wills et al. At present, the effect of the flow properties on electrochemical efficiency is unclear. The results presented here represent the latest stage of SLFB development, and future work must aim to increase lifetime, efficiency, operating current density and charge/discharge duration.

2.9.2 Flow Battery

The ICI FM01-LC is an electrochemical filter-press cell with an active electrode area of 64 cm^2 (16 cm $\times$ 4 cm). It is designed for laboratory-scale experiments and the design is based on the industrial FM21-SP electrolyser used in the chlor-alkali industry [105]. It was adapted by Wills et al. [31] into a 2-cell bipolar SLFB stack and used for charge/discharge experiments.

RVC and Ni foam was used for the positive and negative electrodes respectively and the electrolyte consisted of 1.5 M Pb^{2+} and 1.0 M MSA, with 1 g dm^{-3} lignosulfonic acid. After a series of conditioning cycles at 20 mA cm^{-2}, the stack was subjected to a series of 1 min charge/discharge cycles, where the current density was incremented by 20 mA cm^{-2} between 20 and 160 mA cm^{-2}. The stack potential at the end of each 1 min phase was recorded and plotted in potential vs. current density plots. This data was used to create power density vs. current density and stack potential plots on discharge, and this is presented in Figure 2.14.

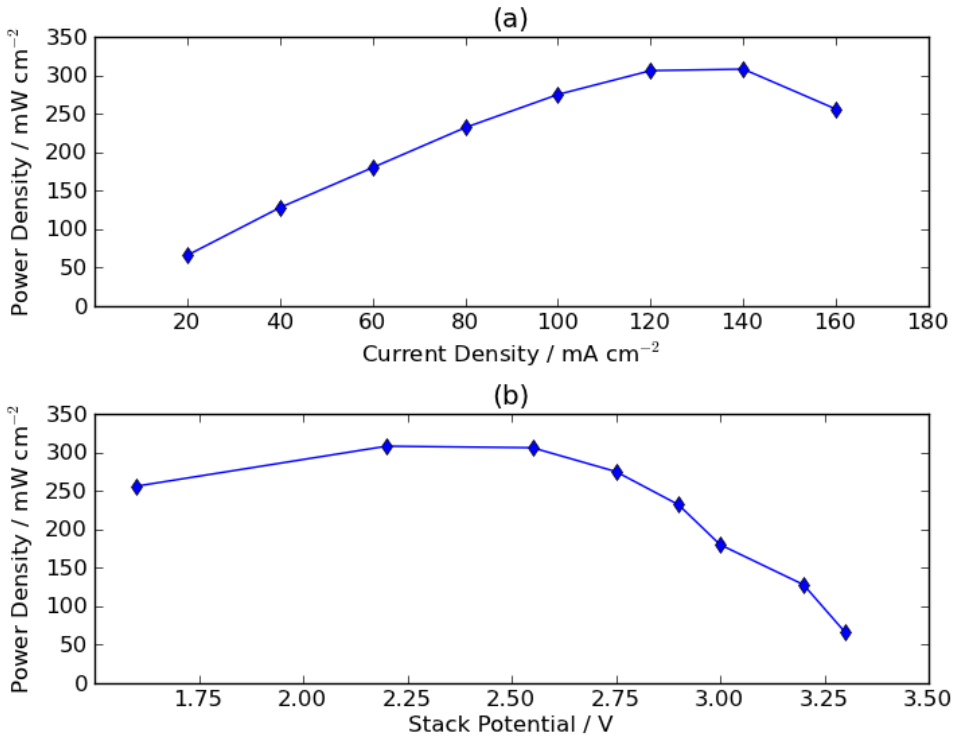

Figure 2.14: Power density of the 64 cm^2 FM01-LC 2-cell bipolar stack as a function of (a) current density and (b) cell potential based on the published work of Wills et al. [31]. Electrolyte: 0.5 dm^3 of 1.5 M Pb^{2+} and 1.0 M MSA, with 1 g dm^{-3} lignosulfonic acid. Electrode: undivided configuration with 1.3 cm thick, 90 ppi RVC (+ve) and 1 mm thick, 90 ppi Ni foam (-ve), with 5 mm inter-electrode gap. Flow rate: 3 cm s^{-1} (15 cm^3 s^{-1}). Temperature: 298 ± 2 K with no active control.

The power density is seen to rise with current density, from 50 mW cm^{-2} at 20 mA cm^{-2} to a peak of 308 mW cm^{-2} at 140 mA cm^{-2}. In regards to the stack potential, the power density is relatively stable between 1.6 V and 2.55 V and the potential was seen to be equally split between the two cells, before decreasing at higher potentials beyond 2.55 V [31]. The

system is able to charge and discharge at high current densities over short durations. It is best to avoid long charges at high current densities to avoid poor deposit formation (Chapter 2.5.9). The soluble lead system could be discharged at higher rates over longer periods, but the effect of this on the deposit quality has not been explored.

2.10 Flow Cell Engineering

2.10.1 Cell Design

Reviews on the engineering of flow cells have previously been published [28, 106], and a book published by Walsh is dedicated to electrochemical reactor engineering [65]. This section introduces several important concepts. The design of the flow cell must consider the following: a uniform current density and potential distribution across the electrode surface, sufficiently high and uniform mass transport rates, simplicity of design and ease of maintenance in relation to manufacturing and operating costs [107].

Electrodes should be held parallel to each other within the cell in order to establish a uniform electric field between them (in order to avoid edge effects) [65]. In the SLFB particularly, the inter-electrode gap is an important trade-off; the space needs to be wide enough for deposits to form without electrically shorting the cell and to minimise the pressure loss, whilst also being small enough to minimise the potential drop across the electrolyte. The favoured width in the soluble lead flow cell is 1.0 - 1.2 cm; Collins et al. [34] were able to extend cell lifetime by increasing the width to 2.4 cm, as shorting was delayed, but at a cost of an increased IR drop (Equation 2.7) and thus lower voltage efficiency. The rise in pressure drop with SoC due to deposition narrowing the inter-electrode gap was introduced in 2.2.3, but there are no publications discussing this in further detail. Pressure drop is also greater when using highly viscous electrolytes (Equation 2.12), but the change in viscosity with SoC in the soluble lead system also remains to be investigated (Chapter 4).

In a flow battery, a part of the overall power will be used for ancillary systems, such as thermal management and pumping, and energy will be lost through heat or shunt currents (when current flows through the electrolyte flow path instead of through the cells in a bipolar stack).

When modelling the cost and performance of an all-vanadium flow battery, Viswanathan et al. [108] calculated the pumping losses as a percentage of battery power to be $\leq$1.6%. In large zinc-bromine systems, energy lost through pumping and shunt currents can be as low as 2% of the overall input energy [16].

Cells can employ a 'flow-by' and 'flow-through' electrode configuration. In a flow-by system, the electrolyte flows past the surface of an electrode (either 2D or 3D), through the inter-electrode or separator-electrode gap. In a 'flow-through' system, a 3D porous electrode is compressed between the separator and electrode, causing the electrolyte to flow through the porous electrode. The direction of the fluid motion can be parallel or perpendicular to the flow of current [65]. The latter is more commonly used in industrial reactors (and also the VRFB [109]). So far, SLFB research has preferred a flow-by configuration, but the cell design of Oury et al. [82] can be classed as a flow-through, parallel to current direction, flow reactor (Chapter 2.7).

Cells can be connected in series with bipolar electrodes to produce a stack. Stacks can then be connected electrically in parallel or series depending on the voltage and current requirements. Cells can also be connected in series or in parallel hydraulically. In series, the electrolyte flows successively from one cell into the other, so that each subsequent cell sees a slightly decreased active species concentration due to reactions in the previous cell. In parallel, the same electrolyte flows simultaneously through each cell, but this is a more complex design requiring a more sophisticated flow circuit. In both, there is the possibility of shunt currents, which occur when the charge flows through the flow channels from cell to cell rather than through the bipolar electrodes. This leads to a non-uniform potential distribution amongst the stacks in the cells, and in hybrid flow batteries there would be a varying amount of deposition between inner and outer cells. Shunt currents can be minimised by increasing the resistivity of the flow path: by using a less conductive electrolyte or a narrower, longer flow path. However, the former would also reduce the voltage efficiency whilst the latter would increase the pressure drop [16].

The role of Figure 2.15 presents three manifold designs developed by Wills et al. and C-Tech Innovation Ltd [31]. The 10 cm $\times$ 10 cm electrodes would be attached in the centre of the frames, denoted by the labels (A), (B) and (C).

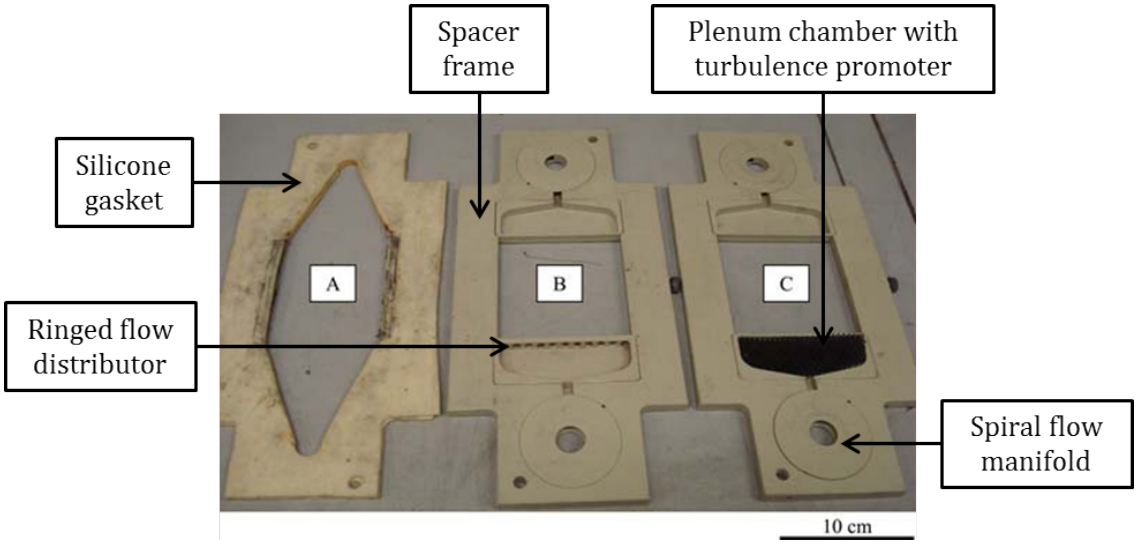

Figure 2.15: Various components of the 100 cm^2 cell used by Wills et al [31]. (A) silicone gasket; (B) cell frame with spiral inlet and outlet manifold, plenum chamber and ringed flow distributor; (C) as (B), but with a plastic mesh in the plenum chamber to induce turbulent flow. Reproduced with permission.

The authors describe three cell configurations: (A) a silicone gasket providing a 'V'-shaped inlet and outlet path (used without the spiral inlets/outlets); (B) cell spacer frames incorporating a spiral inlet/outlet manifold, plenum chamber and ringed distributor; (C) plastic mesh in the plenum chamber to promote flow turbulence (though the flow will still be laminar overall). The addition of these features is a compromise between pressure drop (as they act as obstacles to the flow) and ensuring a well-mixed flow. The plenum chamber is designed to mix the electrolyte, equalise the pressure and to provide a uniform linear velocity across the electrode surface. The flow would otherwise be faster nearer the inlet ports. The spiral manifolds extend the flow path between cells in the stack, increasing pressure drop whilst reducing the shunt loss [65].

However, the authors do not report studies on this and the cell was not tested in a multi-cell configuration. The non-conductive ringed distributor was seen to act as a scaffold for well-adhered PbO_2 growth, leading to shorting. The authors avoided its use in later experiments and describe attaching an insulating polyester tape around the perimeter of both electrodes in order to prevent the growth and creep of deposits along the edges, but there is no more discussion regarding this. Particles of PbO_2 dislodged from the electrode surface were also seen to accumulate at the bottom of the plenum chamber and over time were seen to form a gel-like sludge (Chapter 2.5.7). Apart from these observations, there is no other discussion

on the preferred cell design.

2.10.2 Maintenance

Most types of flow battery use different active species in the positive and negative half-cells, which are kept apart by a separator. However, crossover of ions and water molecules through the separator is inevitable, irrespective of the selectivity quality of the separator. This causes a loss in energy capacity and also affects the battery efficiency. Rebalancing is therefore required to reverse these effects, and the difficulty of doing so depends on the active species [28].

This is not a problem in the SLFB, but a different type of maintenance is necessary. Selecting a suitable electrode material and optimising the cell design, operating conditions and electrolyte may minimise dendritic Pb growth or PbO_2 creep, but it is likely that the accumulation of deposits at the electrodes as well as particles dislodging and falling into the electrolyte cannot be completely prevented. A strategy therefore is required to dissolve these dislodged particles and completely strip the electrodes of deposits, returning the electrode and the electrolyte to the initial conditions.

The battery could be discharged at low current densities until the potential drops to 0 V, which would signify that the electrodes are completely free of deposits. Alternatively, the polarities could be switched and a low *charging* current applied, with the potential maintained below 0 V. This would preferentially oxidise Pb into Pb^{2+} at the new positive electrode rather than oxidising Pb^{2+} into PbO_2 (and similarly for the new negative electrode) [51]. Alternatively, a faster method would be to short the electrodes across a low impedance shunt whilst circulating the electrolyte. Such strategies are employed in the zinc-bromine flow battery [110], where stripping cycles are employed to fully remove the zinc deposits from the negative electrode.

However, these techniques would not dissolve any dislodged particles suspended in the flow network. Hydrogen peroxide, H_2O_2, is known for its oxidative and reductive properties. Aliquots of 0.86 M H_2O_2 were periodically added during a cycling test conducted by Collins et al. [56] following a discharge phase, with the cell on open-circuit. The lead dioxide in

the electrolyte and on the electrode reacted instantly and soon dissolved completely. Lead deposits at the negative electrode were also seen to react but at a much slower rate. Nevertheless, the procedure successfully extended the cell lifetime and was capable of returning the system close to its initial condition. However, the average charge efficiency was seen to decrease over the cycles following the additions and was attributed to an excess amount of H_2O_2 remaining in the electrolyte. Furthermore, though satisfied with the results, when considering the cost of H_2O_2, the authors did not find this to be an economical strategy.

2.11 Commercial Benchmarks

Table 2.4 compares four different batteries for energy storage applications. They are all commercially available products and have been chosen to provide an overview of the small-scale energy storage battery market: two are static batteries and two are redox flow batteries. They are approximately comparable in terms of warranty and power, and otherwise vary in energy capacity, size, mass and chemistry.

Exide Absolyte GP

The Exide Absolyte is an AGM valve-regulated lead-acid battery, which is the most similar to the SLFB in terms of chemistry. It can provide 'flash' currents up to 1866 A for short durations and operate over the widest temperature range for a battery. However performance, capacity and lifetime depend on the charge/discharge conditions and suffer if the temperature is not maintained at 25 C. Its uses include off-grid telecommunications, UPS, railroad signalling, photovoltaic systems and marine applications. Furthermore, there is zero maintenance and the system is completely recyclable upon failure [111].

Tesla Powerwall

The Tesla Powerwall is a lithium-ion battery advertised as a way of maximising the potential of solar power for domestic or business use. It requires no maintenance and is completely automated, charging when the electricity utility rate is low. At 66 Wh kg^{-1}, it offers the highest specific energy of the four selected devices, but falls behind the Absolyte GP and ZBM 2 in terms of energy density, at 31 Wh dm^{-3} compared to 53 and 36 Wh dm^{-3} (total

	Absolyte GP VRLAB	**Powerwall Li-ion**	**5-20 VRFB**	**ZBM 2 ZBFB**
Manufacturer	Exide	Tesla	RedT	Redflow
Reference	[111]	[112]	[113]	[110, 114]
Maximum Capacity / kWh	8.4[i]	6.4	20	10
Discharge				
Nominal Power / kW	0.4-4.4	3.3	5	3
Peak Power / kW	9.8[ii]	3.3	10	5
Peak Power Duration / mins	1	∽120	5	120
Peak Current / A	1866	9.5	125	125
Peak Voltage / V	6	350-450	40-60	40
Charge				
Peak Power / kW	*n/a*	3.3	5	4
Peak Current / A	*n/a*	*n/a*	95	60
Peak Voltage / V	*n/a*	*n/a*	53-62	66
Stacks × Cells	1 × 3	*n/a*	*n/a*	3 × 33
Battery Dimensions L × W × H / mm	1082 × 218 × 671	1302 × 862 × 183	2000 × 1800 × 2100	845 × 400 × 823
Total Volume / dm^3	158	205	7560	278
Electrolyte Volume / dm^3	-	-	*n/a*	100
Electrolyte Mass / kg	-	-	1400	146
Total Battery Mass / kg	361	97	2900[iii]	240[iii]
Energy Density[iv] / Wh dm^{-3}	53	31	3	36
Specific Energy[iv] / Wh kg^{-1}	23	66	7	42
Min/Max Temp. / C	-40/+50	-20/+50	-25/+30	+10/+50
% DC-DC Efficiency	*n/a*	92.5	70-80	80
Warranty	1200 cycles, 25^{o}C, to 80 % DoD	10 yrs	10 yrs	10 yrs or 36.5 MWh

Table 2.4: Comparison of four different commercially available batteries. *VRLAB* valve-regulated lead acid battery; *VRFB* vanadium redox flow battery; *ZBFB* zinc-bromine redox flow battery; *DoD* depth of discharge. [i]based on 1600 Ah capacity and 1.75 volts per cell (VPC); [ii]based on 1866 A and 1.75 VPC; [iii]including electrolyte; [iv]based on total battery mass/volume. *n/a* indicates unavailable data and - indicates not applicable.

battery volume) respectively. A single unit can be conveniently placed on a wall inside or outside and is sufficient for most houses; however its modular design allows several to be incorporated together for higher energy needs. It is also the most efficient system with a DC-DC efficiency of 92.5% [112].

RedT 5-20 VRFB

Flow batteries operate at higher currents and lower voltages to static batteries. RedT's vanadium flow battery system is also modular in design, consisting of several stacks of cells connected electrically in series and parallel. Hydraulically, each stack is connected in series. It has a very low energy density and specific energy, at just 3 Wh kg^{-1} and 7 Wh dm^{-3} (total battery mass and volume) respectively. Because of this, the system is large and heavy, but space restrictions are not important for its range of applications, which are primarily renewables capacity firming and isolated off-grid telecommunication installations.

The system comes housed in a container that resembles a freighter crate. The manufacturer mentions low maintenance and an expected lifetime of 20 years, at which point the electrolyte can be transferred to another VRFB. A 'climate control' is also built in to prevent overheating of the electrical components inside. Furthermore, the ease of scalability of this technology is demonstrated by the fact that 14 different models are available, from 5 kW/20 kWh to 60 kW/300 kWh [113]. This is an important advantage of flow batteries over lithium-ion or other static-electrolyte batteries.

Redflow ZBM 2

From an operational perspective, the ZBFB is the most similar to the SLFB. It relies upon the deposition of zinc during charge whilst bromide ions are oxidised to elemental bromine at the positive [21]. Redflow's ZBM 2 consists of 3 stacks (each containing 33 cells) placed above the electrolyte tanks [110]. Its total internal volume is comparable to the Powerwall but it is designed to be placed on the ground, as it is more suited to off-grid applications such as telecommunications (though a different version, known as the 'ZCell' is available for home use). It boasts a range of superior features, primarily safety, 100% full daily discharge, an unlimited shelf life and no maintenance (only if the battery is frequently fully discharged). There is no battery degradation when left completely discharged [114]. In contrast, lithium-

ion batteries lose the ability to retain charge if left at zero SoC; instead, it is recommended to leave them at 50% SoC if they are to be stored for long periods [115].

The battery is built from recyclable polyethylene and aluminium. Regarding safety, the zinc-bromide electrolyte, like its vanadium counterpart, is non-flammable and there is no thermal runaway, a phenomena that plagues lithium-ion technology [116]. The manufacturer specifies that the system is well-suited to 'tough' conditions, and that the system can tolerate temperatures up to 50 C without any climate control.

2.12 Summary

The development of the SLFB has been summarised and its present state of development compared to the lead-acid battery, and the all-vanadium and zinc-bromine flow batteries. The electrode kinetics were discussed, as well as the operating conditions necessary to produce the right quality of deposits to ensure efficient cell performance over extended periods. Electrode materials, cell design, electrolyte compositions and additives were also reviewed. The main failure mechanisms, dendritic/rocky Pb deposition and PbO_2 'creep', were discussed. The literature is still young and much work is needed to scale the system further. Several gaps required for further development were highlighted, and the most important are listed here:

1. Pourbaix diagram of Pb-MSA system, perhaps including additives
2. Understanding pressure drop through the cell with SoC
3. Better understanding of the optimal α and β-PbO_2 ratio for the SLFB
4. An improved electrode material for the positive electrode
5. Better understanding of electrolyte conductivity with $[Pb^{2+}]$, [MSA] and SoC
6. Better understanding of electrolyte viscosity with $[Pb^{2+}]$, [MSA] and SoC
7. F^-, HDTMA and lignosulfonate have been trialled in flow cell tests, and similar studies are required for Bi^{3+}

8. The effect of discolouration in lignosulfonate-containing electrolytes on the ability of the additive to control the lead deposit
9. Investigating combinations of additives
10. Improved cell designs to prevent shorting
11. Further regeneration strategies to return a failed cell (e.g. electrolyte depleted of Pb^{2+}, or shorted cell) to starting conditions

Wallis et al. [32] introduced a separator-divided soluble lead static cell, and the work presented in the following chapters will aim to build on this work whilst investigating the gaps in the literature. A novel separator-divide soluble lead flow cell is introduced, featuring a novel electrolyte with a new combination of additives that seeks to balance energy density and performance with good deposit morphology and cell longevity. A thorough understanding of how electrolyte conductivity and viscosity is affected by $[Pb^{2+}]$ and $[H^{+}]$ is also established. Finally a theoretical discussion on the cell design is proposed for a future SLFB stack.

Chapter 3

Experimental Apparatus

3.1 Chemicals and Electrodes

All solutions were prepared using lead(II) methanesulfonate solution, $Pb(CH_3SO_3)_2$, 50% wt. in water; methanesulfonic acid (MSA), CH_3SO_3H, >99.5% wt. in water; and deionised water from a Purite Ondeo 15 purifier. As in Chapter 2, electrolyte compositions in the following chapters are reported as x M lead(II) methanesulfonate and y M MSA, with z additives. For example: 1.5 M Pb^{2+} and 1.0 M MSA, where Pb^{2+} refers to the $Pb(CH_3SO_3)_{2(aq)}$ concentration and MSA refers to the free acid in solution. The term *solution* and *electrolyte* are used interchangeably.

Each electrolyte batch was produced in volumetric flasks in amounts varying from 100 cm^3 to 1000 cm^3. Following formation, each batch was allowed to equilibrate to ambient temperature (296 K) for a minimum of 12 hrs. All solutions containing only $Pb(CH_3SO_3)_2$ and MSA appeared transparent when undisturbed. These chemicals, and the main additives reported in the later chapters, are summarised in Table 3.1. The chemicals were all used as received from the manufacturer, Sigma Aldrich.

Chemical	Formula	Purity	ID #
Lead(II) Methanesulfonate	$Pb(CH_3SO_3)_2$	50% wt. in H_2O	462667
Methanesulfonic Acid	CH_3SO_3H	≥99% wt. in H_2O	471356
HDTMA Hydroxide	$CH_3(CH_2)_{15}N(OH)(CH_3)_3$	10% wt. in H_2O	439231
Sodium Lignosulfonate	-	Av. M_w = 8,000	370975
Bismuth(III) Oxide	Bi_2O_3	99.999%	202827
Sodium Fluoride	NaF	ACS reag. ≥99%	201154

Table 3.1: Summary of chemicals used in experiments reported in the following chapters. *HDTMA* hexadecyltrimethylammonium. Purchased from Sigma Aldrich (ID numbers presented).

The type of carbon/polyvinyl ester electrode reported is FCBLK-508305 (Entegris GmBH). The RVC (90 ppi, 3% relative density) reported was sourced from ERG Materials and Aerospace [117]. A further summary is presented in Table 3.2. The tortuosity factor is a dimensionless property of 3D electrodes, which describes the tortuous nature of the flow path within the porous material. In the table, the tortuosity factor shows that the flow path within the RVC is three times longer than the straight path. A detailed expanation of the various ways of characterising RVC tortuosity has previously been published [118].

	Carbon/polyvinyl ester (Entegris)	**Reticulated vitreous carbon (90 ppi) [117]**
Thickness / mm	2	2
Specific Area / cm^2 cm^{-3}	-	57
Conductivity / S cm^{-1}	50*	3.1
Tortuosity factor	-	0.33

Table 3.2: Summary of the electrodes used in the reported experiments.*Full datasheet unavailable; this value was obtained from informal discussions with the manufacturers. The tortuosity factor is based on the electrical model [118].

3.2 Density, Viscosity, Conductivity

The density, ρ, of an electrolyte sample was calculated by measuring 100 cm^3 of the sample in a volumetric flask and then measuring its mass on a digital balance. An Ostwald viscometer,

calibrated to a constant value of 0.009236 mm s^{-2}, was used to measure the kinematic viscosity, ν, of the electrolytes at room temperature, 296 K. Each sample was tested twice and the average recorded. The absolute viscosity, μ, of the electrolyte sample was then calculated by multiplying the kinematic viscosity with the respective density.

The ionic conductivity of the sample was measured using an Analytical Technology ATI Orion 162 (Pt electrode) conductivity meter. This device was calibrated using a high purity 1.0 M KCl solution (Fisher Scientific, no. 10417460) prepared in the lab to give a reading of 108.6 mS cm^{-1} at 298 K and 137.8 mS cm^{-1} at 313 K [119]. Temperatures were maintained using a Grant LTD6G water bath.

3.3 Potential Drop Measurements

A four-compartment glass cell was employed to deduce the potential drop across several separators. The glass cell consisted of two identical halves clamped together with the separator locked in between, exposing a separator area of 1.16 cm^2. A full schematic is provided in Figure 3.1.

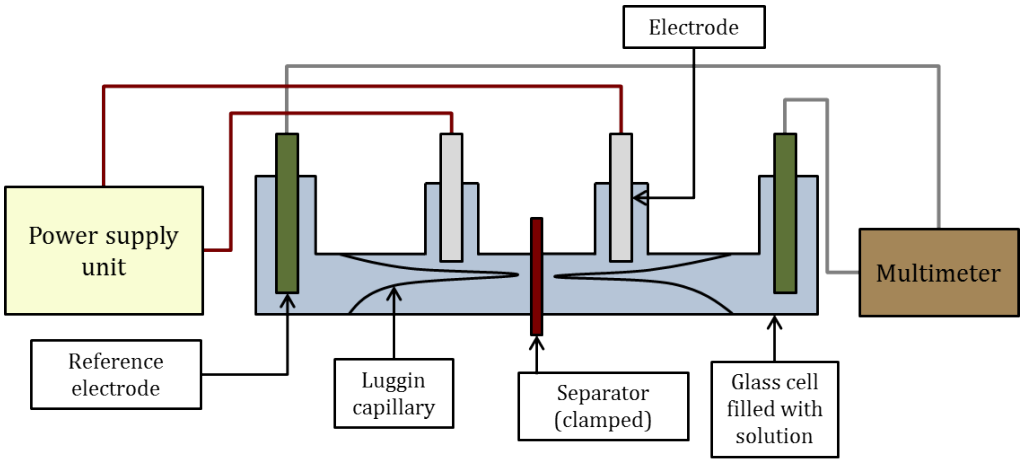

Figure 3.1: Schematic of the glass cell apparatus for measuring the potential drop across a separator.

A TTi TSX1820P programmable DC PSU provided a constant current across the separator via two carbon/polyvinyl ester working electrodes. Luggin capillaries were placed on either side of the separator, approximately 2 mm from the separator surface, and two Radiometer

Analytical XR440 Hg/HgO reference electrodes, connected to a Fluke 73 III multimeter, recorded the potential difference between the two Luggin capillary points, i.e. the potential drop. This type of electrode is typically used in alkaline conditions whereas the soluble lead electrolyte is strongly acidic. However, due to mislabelling of equipment, this type of electrode was used for the majority of tests where a reference electrode was required with the understanding that it was a SCE.

3.4 Voltammetry

Voltammetry was conducted using a three-compartment, three-electrode glass cell containing 100 cm^3 of electrolyte. A glassy carbon electrode, with an active area of 0.13 cm^2, was used as the working electrode and a platinum mesh was inserted as the counter. Potentials were measured relative to a saturated calomel electrode (SCE) via a luggin capillary, with the tip placed approximately 2 mm below the working electrode surface. The temperature was maintained at 298 K using the Grant water bath and the voltammetry was controlled by an Autolab potentiostat, with Nova 1.11 software. Before each test, the working electrode was polished using alumina AP-D suspension (1 micron, then 0.3 micron, Struers) on a surface of moistened polishing cloth. It was then rinsed and cleaned using deionised water.

3.5 The 9 cm^2 Cell

3.5.1 Static Configuration

A static electrolyte, parallel plate cell, designed by Pui-ki Leung, was used for galvanostatic cycling tests. The cell had an active electrode area of 9 cm^2 (4.5 cm length $\times$ 2 cm height). The main frame was made from PVC and two 7 $\times$ 7 $\times$ 0.2 cm carbon/polyvinyl ester electrodes (BMC 18649, Entegris GmBH) were employed, separated by silicone rubber gaskets and two Perspex electrolyte chambers. A steel end plate and silicone rubber spacers provided the necessary compression to prevent leaks. The cell schematic and an aerial view are provided in Figure 3.2. Under full compression, the inter-electrode gap equalled 20 mm (10 mm electrode-separator gap) and the overall internal volume was 18 cm^3.

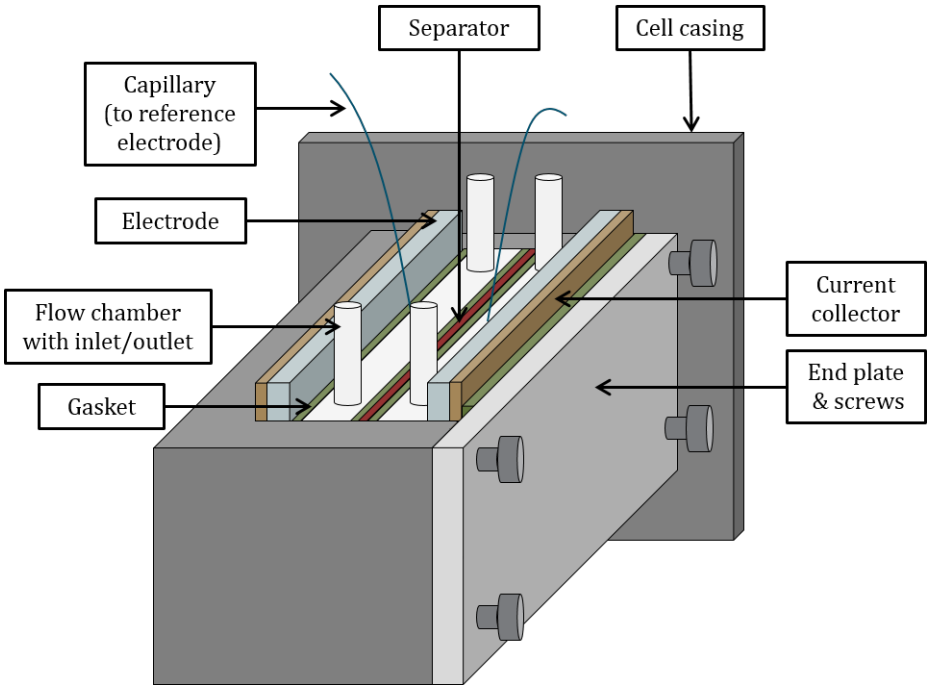

(a)

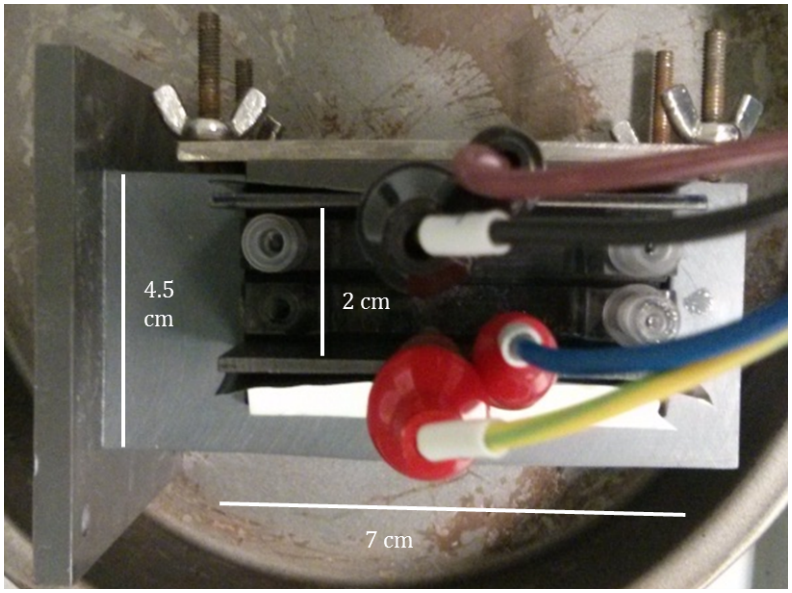

(b)

Figure 3.2: Schematic and aerial view of the 9 cm^2 static cell.

The electrode and current collector protruded slightly above the cell casing so that connections via crocodile clips could be made to the battery analyser. All cycling experiments began with fresh electrolytes and clean electrodes, the latter polished with silicon carbide paper and degreased with acetone. The cell was dismantled, cleaned and rinsed in deionised

water before being dried and reassembled for the next experiment. All static and flow cell cycling experiments, in any cell, took place at room temperature, 296 K, with no temperature control.

3.5.2 Flow Configuration

The static cell was subsequently converted into a 9 cm^2 flow cell, with a flow-by electrode configuration, by connecting the static cell's Perspex chambers to Erlenmeyer flasks where the electrolytes were housed. Saint-Gobain Norprene tubing was used and a Watson-Marlow 323E peristaltic pump circulated the electrolyte around the circuit. As in the static configuration, the cell stood horizontally, providing a slight inclination to the flow path through the cell, as presented in Figure 3.3.

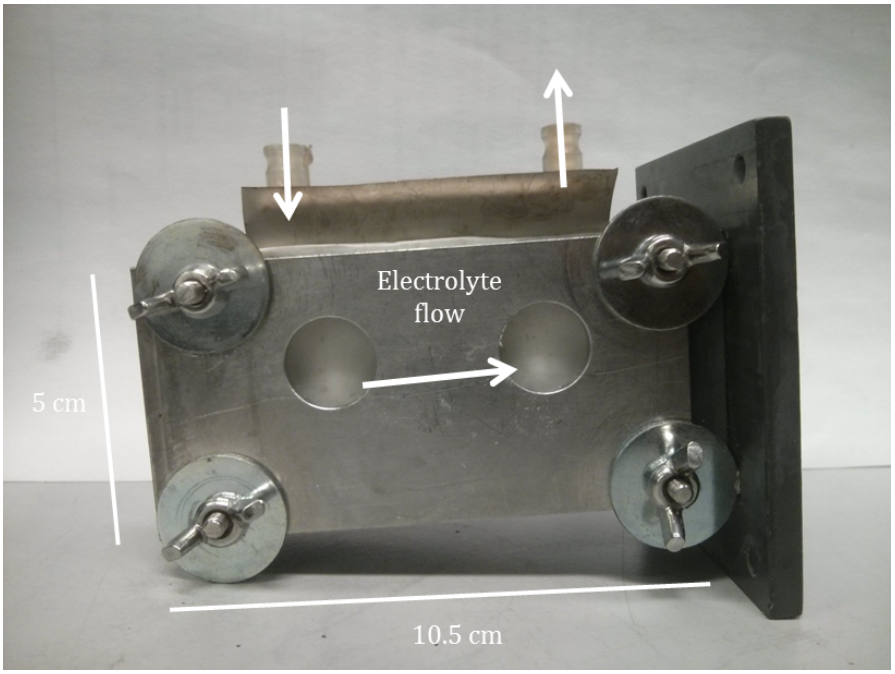

Figure 3.3: Positioning of the 9 cm^2 cell during all static and flow cell experiments. For flowing electrolytes, the electrolyte flow path is slightly inclined, the electrolyte entering from the left and flowing in an upwards-right direction towards the exit.

To measure the potential of an individual electrode, a capillary connected the adjacent Perspex flow chamber to an external test tube, allowing electrolyte to flow in. A saturated Hg/HgO electrode was submerged into the electrolyte in the test tube before the beaker was

hermetically sealed. Separate electrical connections could then be made in order to measure the potential of the electrode vs. the Hg/HgO reference electrode.

3.6 The 100 cm^2 Flow Cell

A filter-press flow cell, designed for the SLFB system by C-Tech Innovation Ltd., was used for further studies. The cell design allowed the use of a separator, differing from soluble-lead flow cells reported in the literature. The active area of the electrodes was 100 cm^2 (10 × 10 cm) and the inter-electrode gap equalled 1.2 mm (6 mm electrode-separator gap), though this could be shortened to as low as 2 mm with RVC included). A flow-by electrode configuration was used for the flow path. Full schematics are presented in Figure 3.4.

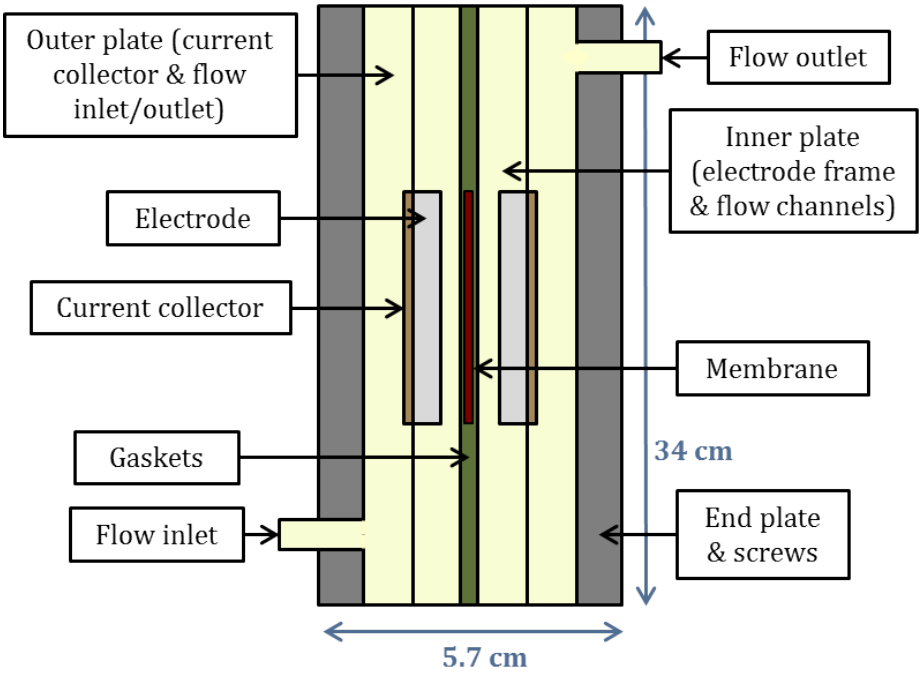

Figure 3.4: Schematic of the 100 cm^2 C-Tech flow cell. The third dimension measures 22 cm (into the page). Note also that there are two sets of inlet and outlet (one for each half-cell).

A separator is compressed between two silicone gaskets, which are then compressed between two inner polypropylene electrode frames. On the inner surface of these frames, grooves for the flow channels have been machined into and out of the electrode section. Two adjacent outer polypropylene plates hold the brass current collectors, and two stainless steel end plates

provide the necessary compression with 12 steel bolts. When assembled, the total width from end plate to end plate was 5.7 cm. The cell height and length equalled 34 cm and 22 cm respectively.

The internal design of the 'inner polypropylene plate' is shown fully in Figure 3.5. The negative half-cell is shown. The electrolyte enters from the bottom-left, dividing into two flow channels which later release the electrolyte into a plenum chamber, which mixes the electrolyte and equalises the pressure, ensuring a more evenly distributed flow across the electrode surface.

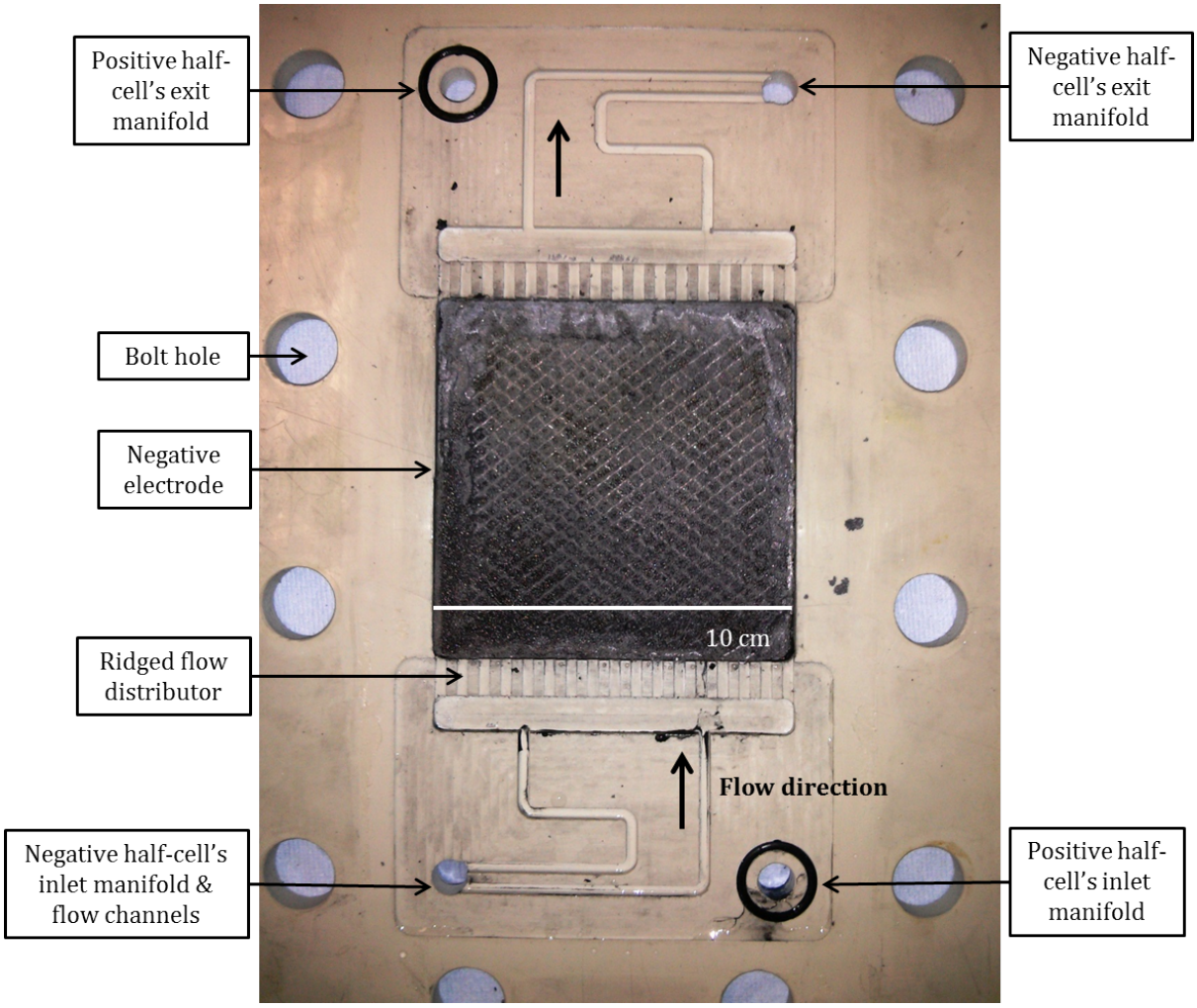

Figure 3.5: View of the internal design of the 100 cm^2 C-Tech flow cell. A plastic cover is clipped over the flow channel sections. Image taken following a cycling experiment, hence the striations on the electrode surface (Chapter 9).

The turnings are all curved in order to minimise the pressure loss due to friction. Beyond the plenum chamber is a ridged flow distributor which further provides mixing. The electrode surface is 3 mm below the front face of the plate (i.e. into the page). The electrolyte exit path is then essentially mirrored, with the electrolyte exiting through a manifold on the upper right. Note that the image was taken following a cycling experiment: the RVC electrode is covered in lead and is marked due to compression against a nylon mesh (Chapter 9). The cell was designed and optimised using CFD simulations across several CAD models.

The flow rig designed for the cell was also provided by C-Tech, and the (a) schematics and (b) actual view can be seen in Figure 3.6. The cell is placed above the the pumps and reservoirs, with the electrolyte being circulated in a clockwise direction. The flow speed is controlled by a throttle built into the flow meter. The cell and rig were used both in the semi and fully-divided cell formats (Chapter 8). In the latter, two sets of reservoirs, pipes and centrifugal pumps were installed into the steel frame.

3.7 Battery Analysers

All charge/discharge cycling experiments took place at constant current (galvanostatic control), which was managed by one of two battery analysers. An MTI 8-Channel BST8-3A battery analyser (max 5 V, 3 A), connected to a laptop installed with BTS Control battery management software, controlled all experiments involving the 9 cm^2 static and flow cell. In order to operate at currents greater than 3 A, all experiments involving the 100 cm^2 flow cell were conducted using a BasyTec battery analyser (max 10 V, 20 A), connected to a computer running BasyTec's battery management software.

The cell potential was recorded every second in the static cell tests and every 5 s in the flow cell tests. The potential-time responses could then be plotted, and the charge efficiency of each cycle calculated. Energy efficiencies were calculated automatically by each software, and from these values the voltage efficiencies were calculated.

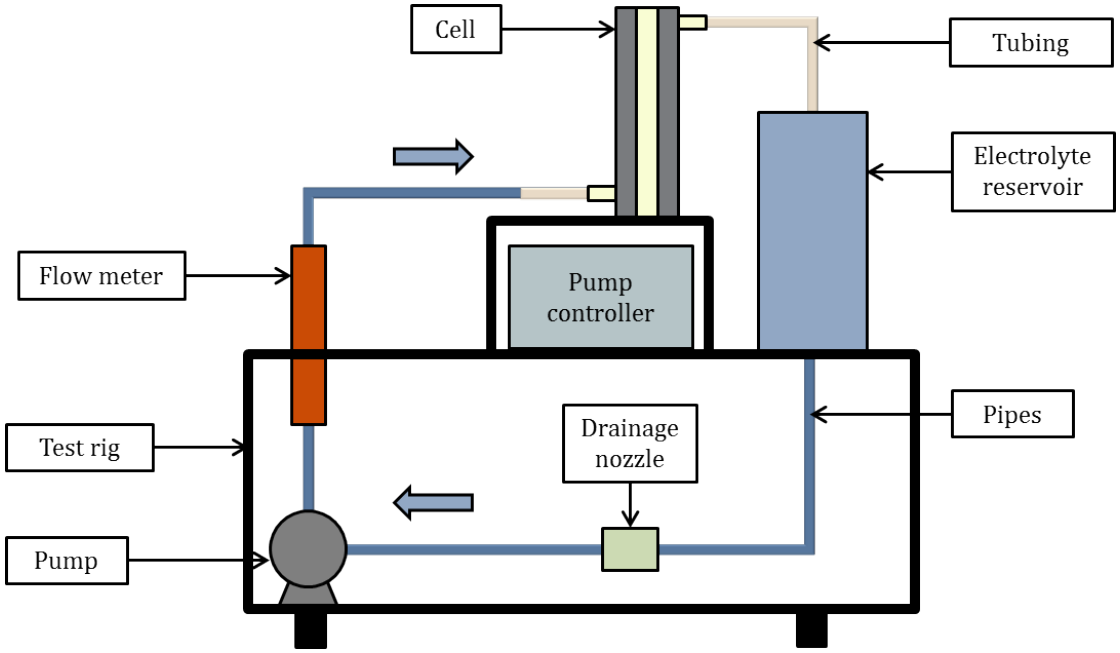

(a)

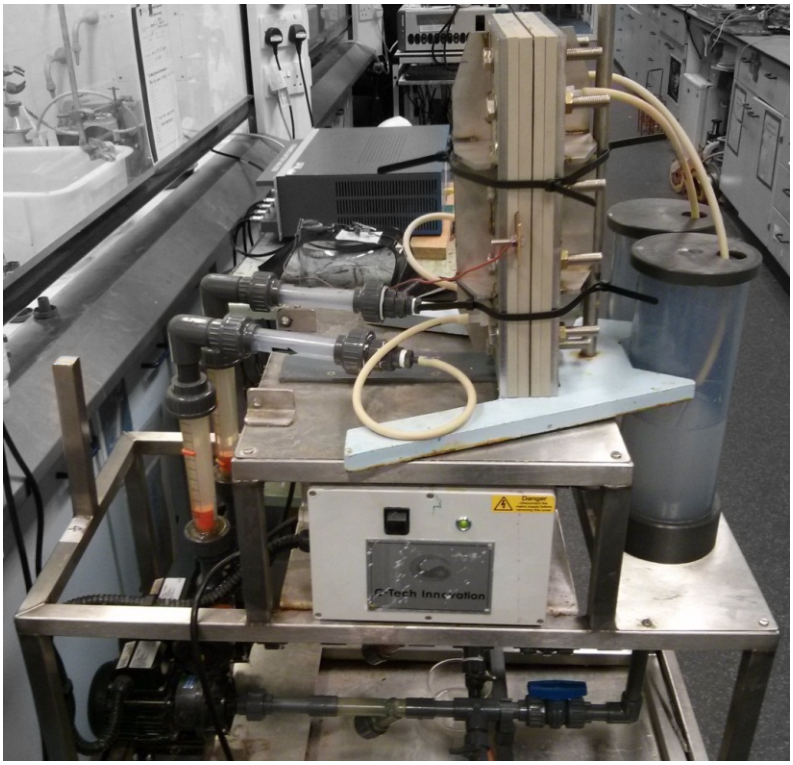

(b)

Figure 3.6: Schematic and actual view of the 100 cm^2 flow cell, designed and built by C-Tech Innovation Ltd.

3.8 Summary

This Chapter has outlined the apparatus used to produce the data discussed in the next chapters. The objective of this project was to make improvements to the soluble lead flow battery. Informed by literature and novel findings regarding the electrolyte, a trial-and-error approach was adopted for the flow cell studies. In the interest of brevity, it was decided that detailed discussion on fewer experiments was more informative than brief discussion on many experiments. The data sets were selected based on their quality and the number of novel conclusions that could be made from their analysis.

Chapter 4

Physical Electrolyte Properties

4.1 Introduction

The physical properties of density, viscosity and ionic conductivity have been explored as a function of Pb^{2+} (lead methanesulfonate) and free MSA concentration over a range relevant for SLFB cycling, i.e. 0 - 1.5 M Pb^{2+} and 0 - 1.5 M MSA. Measuring these properties would enable an understanding of the ionic mobilities of charged species in soluble lead electrolytes and how this affects cell performance. Before testing different electrolytes, the density and viscosities of lead methanesulfonate, MSA and deionised water were each measured separately at 296 K (ambient temperature). The results are presented in Table 4.1.

Parameter	M_r / **g mol**$^{-1}$	ρ / **g ml**$^{-1}$	ν / **mm**^{2} **s**$^{-1}$	μ / **mPa·s**
$Pb(CH_3SO_3)_2$ 50% wt. in H_2O	397.40	1.60	2.12	3.40
CH_3SO_3H 99.5% wt. in H_2O	96.11	1.48	9.78	14.42
Deion. H_2O Ondite Purifier	18.02	0.99	0.96	0.96

Table 4.1: Properties of the individual chemicals that are used for SLFB electrolyte. M_r molecular mass. The following were deduced empirically: ρ density; ν kinematic viscosity; μ dynamic viscosity. Temperature: 296 K.

The density and viscosities are measured values. Previous reports on the viscosity of pure MSA at 298 K are lower: ν = 7.60 mm^2 s^{-1} and μ = 10.5 - 11.7 mPa·s [120]. There are no reports on the viscosity of aqueous lead methanesulfonate.

4.2 Density

The density of the electrolyte as a function of [Pb^{2+}] and [MSA], between 0 M and 1.5 M, was determined at 296 K, calculated from the density values shown in Table 4.1. This was validated using measured values for each data point in the Figure. The measured and calculated values differed by <0.4%. It was assumed that negligible free acid was present in the aqueous lead methanesulfonate 50% wt. solution, so that [H^+] = [MSA]. Figure 4.1 presents the results using the calculated density values.

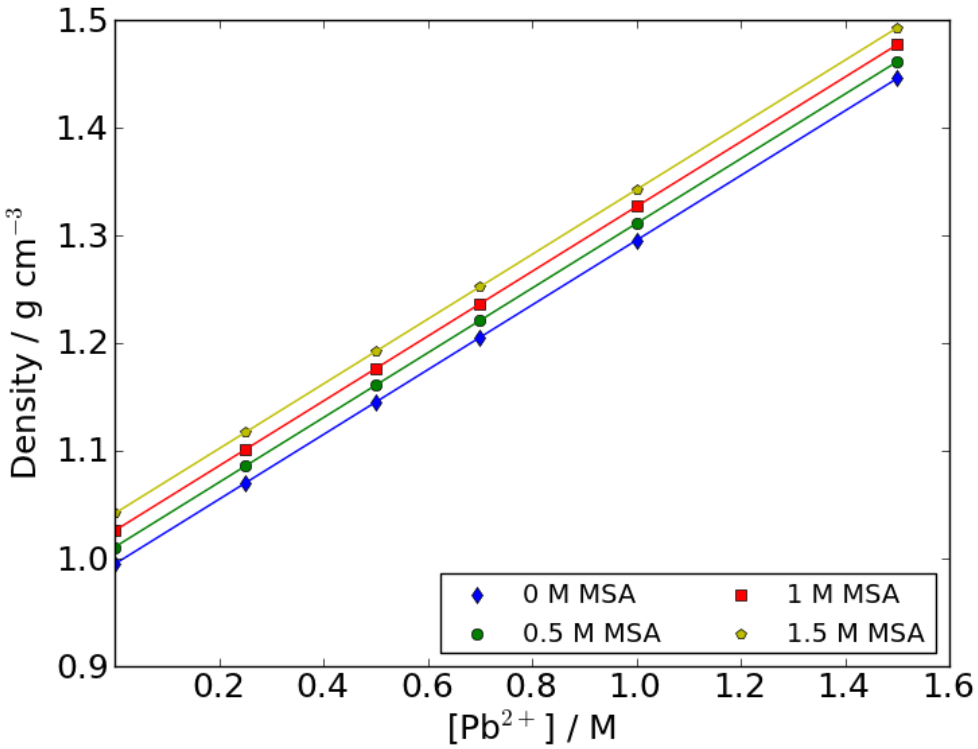

Figure 4.1: Electrolyte density, ρ, as a function of [Pb^{2+}] and [MSA]. Temperature: 296 K.

There is a clear linear relationship between density and [Pb^{2+}]. Without free acid in the solution, the density increases from 1.0 g cm^{-3} at 0 M Pb^{2+} (pure water) to 1.45 g cm^{-3} at

1.5 M Pb^{2+}. When 1.0 M MSA is present in the solution, the density increases from 1.03 g cm^{-3} to 1.48 g cm^{-3} across the same [Pb^{2+}] range. The change in solution density when increasing [MSA] is relatively small, approximately 0.05 g cm^{-3} between 0 and 1.5 M when [Pb^{2+}] is kept constant. The results show that during charge, as Pb^{2+} is removed from the electrolyte, the solution density will decrease overall despite the increase in acidity.

4.3 Viscosity

The kinematic viscosity of several combinations of [Pb^{2+}] and [MSA] were measured and multiplied by their respective densities in order to determine their absolute viscosities. Figure 4.2 illustrates the relationship between dynamic viscosity, in mPa.s, and the concentration of [Pb^{2+}] and [MSA].

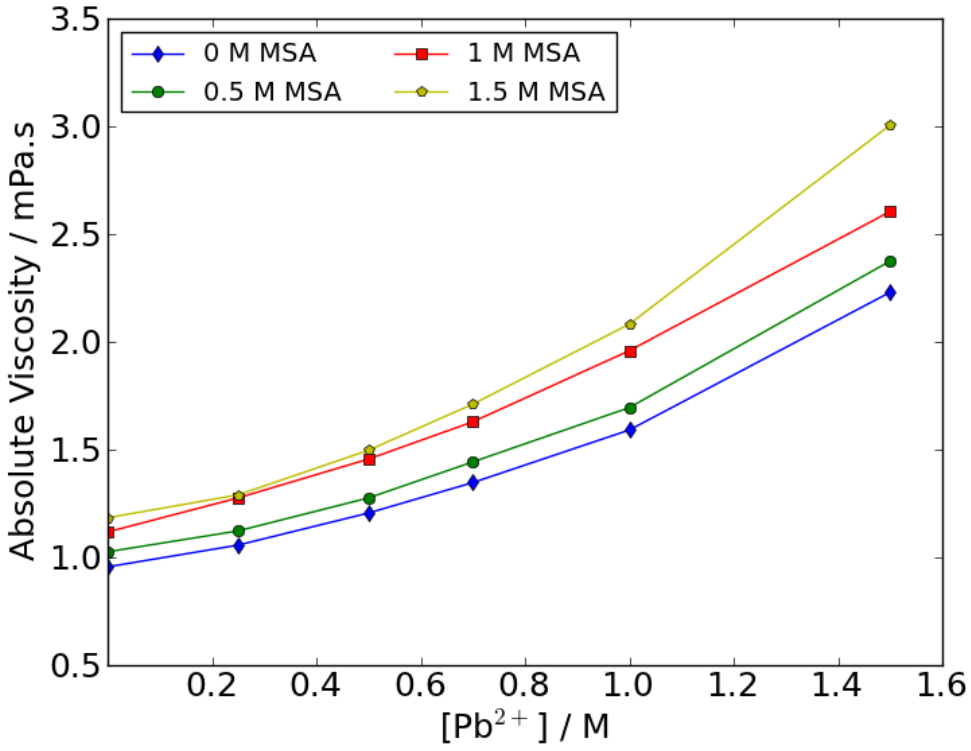

Figure 4.2: Electrolyte viscosity, μ, as a function of [Pb^{2+}] and [MSA]. Kinematic viscosities were first measured using an Ostwald viscometer. Temperature: 296 K.

Because of its influence on density, [Pb^{2+}] has the dominant effect on viscosity, with values increasing by 130% as the Pb^{2+} concentration is increased from 0 M to 1.5 M whilst the

MSA concentration is kept constant. In contrast, the viscosity increases by between 0.2 mPa·s ($[Pb^{2+}] = 0$) and 0.5 mPa·s ($[Pb^{2+}] = 1.0$ M) as the MSA concentration is varied from 0 M to 1.5 M, an increase of just 25% and 32% respectively. During charge of the soluble lead battery, [MSA] increases at twice the rate of the decrease in $[Pb^{2+}]$. Despite this, the overall electrolyte viscosity will decrease. Conversely, viscosity will increase during battery discharge as more Pb^{2+} is released back into the electrolyte. Furthermore, it should be noted that lead methanesulfonate precipitation was seen in the 1.5 M Pb^{2+} and 1.5 M MSA solution, which would have had an impact upon the measurement for this solution.

4.4 Ionic Conductivity

Fresh solutions were prepared, again varying $[Pb^{2+}]$ and [MSA] between 0 M and 1.5 M. The ionic conductivity of these solutions were then determined at 298 K. The results are presented in Figure 4.3.

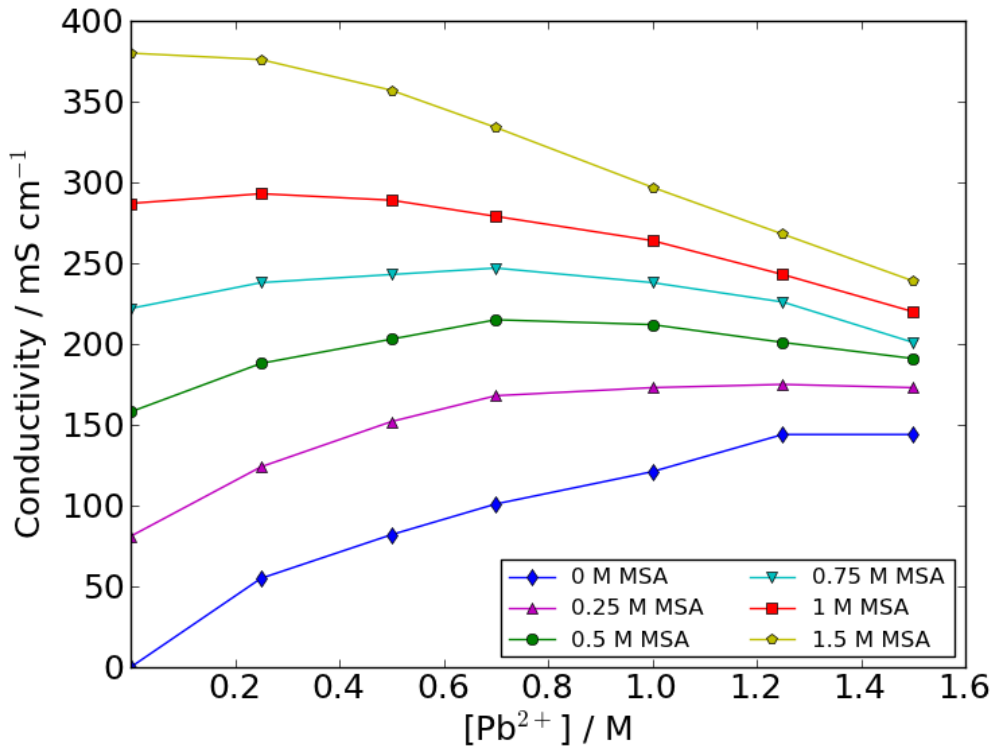

Figure 4.3: Solution conductivity as a function of $[Pb^{2+}]$ and [MSA]. Temperature: 298 K.

Unlike the density and viscosity measurements, there is a more complicated relationship between electrolyte composition and ionic conductivity. The conductivity increases with increasing [MSA] when [Pb^{2+}] is held constant. However, as a function of [Pb^{2+}] the conductivity follows a different relationship: at ≤0.25 M MSA, it increases with [Pb^{2+}]; at ≥1.0 M MSA it decreases with increasing [Pb^{2+}]; between MSA concentrations of 0.25 M and 1.0 M, it peaks at approximately 0.75 M Pb^{2+}. This behaviour is likely due to the complexing behaviour of the methanesulfonate anion to the Pb^{2+} cation and changes in the overall solution viscosity affecting the ionic mobility of the charged species.

A solution of 1.5 M Pb^{2+} and 1.0 M MSA has a conductivity of 220 mS cm^{-1} at 298 K. This is comparable to electrolytes used in the all-vanadium flow battery: an anolyte containing 1.5 M of V^{3+} and 4 M H_2SO_4 has a conductivity of 187.6 mS cm^{-1}, whilst a catholyte of 1.5 M V^{4+} and 4 M H_2SO_4 has a conductivity of 294.8 mS cm^{-1}, both at 298 K [121].

Figure 4.4 illustrates the influence of temperature on the electrolyte conductivity. The plot shows conductivity versus [Pb^{2+}] with 0 M and 1.0 M MSA, and at 298 K and 313 K.

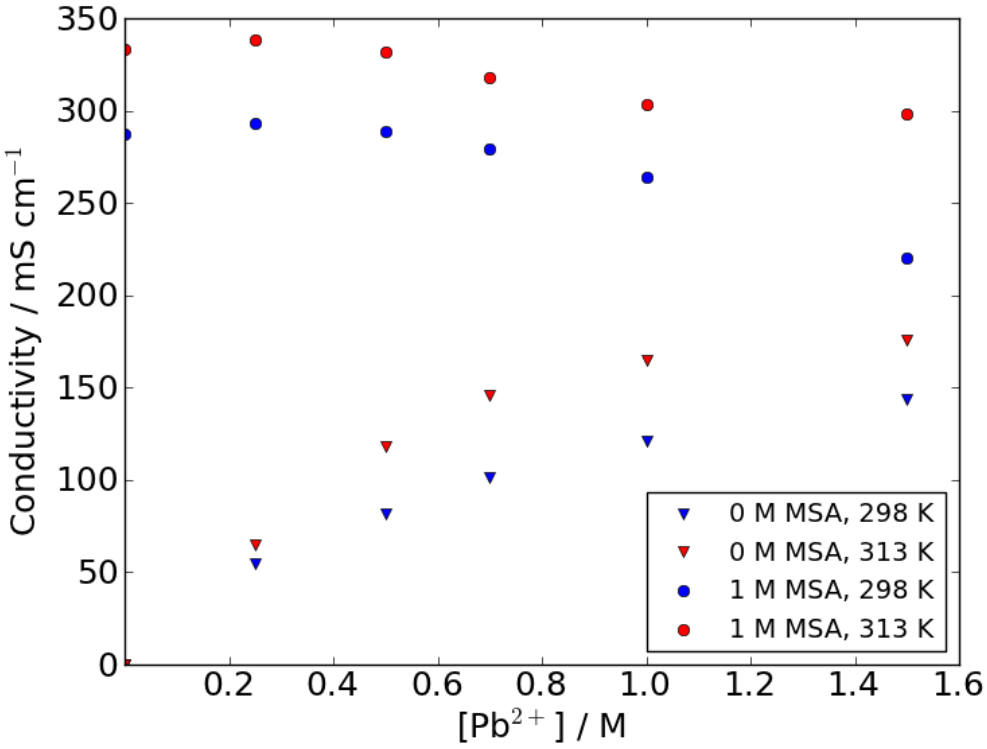

Figure 4.4: Electrolyte conductivity as a function of [Pb^{2+}], [MSA] and temperature.

At either MSA concentration, increasing the temperature increases the conductivity of the solution. The plot further highlights that with an initial MSA concentration of 1.0 M in the electrolyte, the conductivity decreases with increasing [Pb^{2+}], whereas with zero MSA in the electrolyte the conductivity increases with increasing [Pb^{2+}].

4.5 Further Analysis of Viscosity and Ionic Conductivity

Figures 4.2 and 4.3 were redrawn in 3D using MatLab's surface plot function. These are presented in Figures 4.5 and 4.6 respectively. A data-fitting plane can now be used to approximate the viscosity and conductivity of any combination of [Pb^{2+}] and [MSA] between 0 - 1.5 M, even those that were not tested. The average error between the tested measurements and approximated measurements is ±1.125% for viscosity and ±2.079% for conductivity.

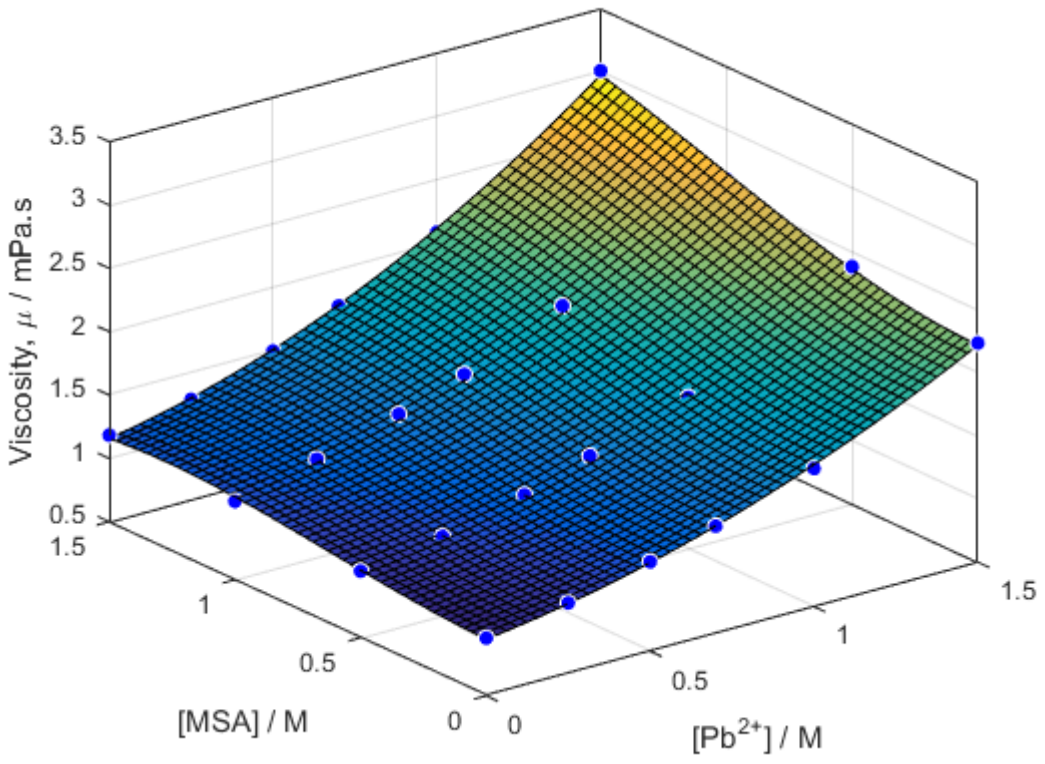

Figure 4.5: Surface plot of the electrolyte viscosity, μ, as a function of [Pb^{2+}] and [MSA]. Kinematic viscosities were first measured using an Ostwald viscometer. Temperature: 296 K.

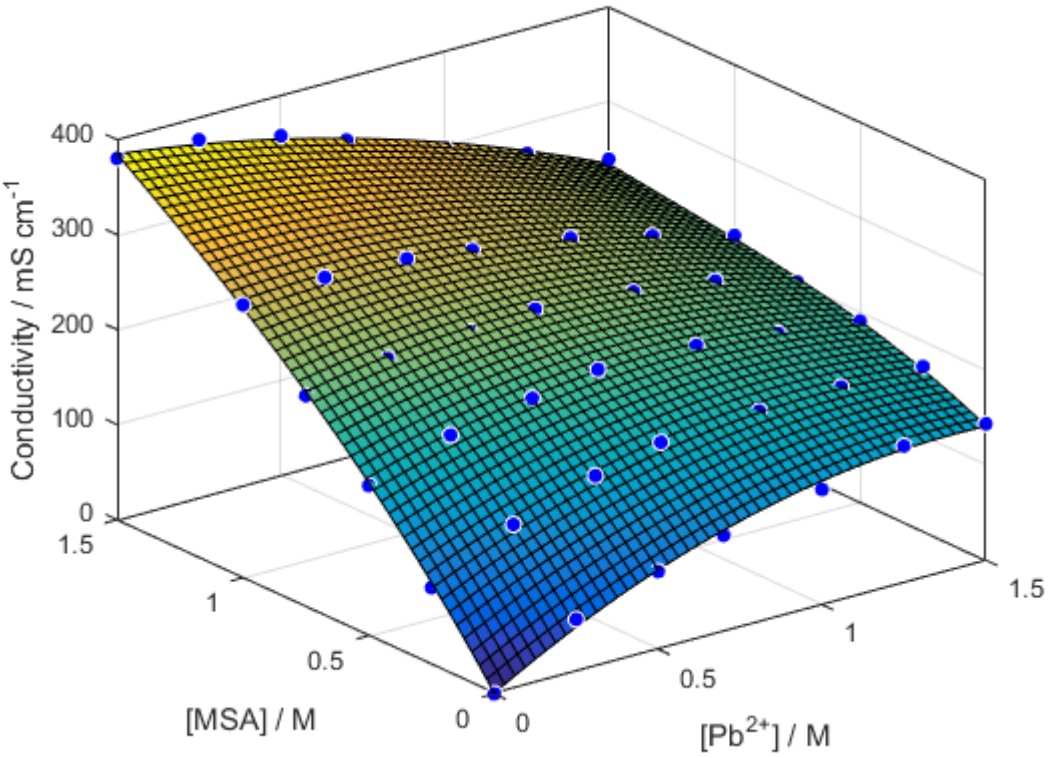

Figure 4.6: Surface plot of the electrolyte conductivity as a function of $[Pb^{2+}]$ and [MSA]. Temperature: 296 K.

Three new electrolytes were made and tested to further validate these models. The results are presented in Tables 4.2 (viscosity) and 4.3 (conductivity). Regarding viscosity, the highest error seen is -3.21% for the 0.23 M Pb^{2+} and 0.94 M MSA solution, and the lowest is +1.44% for the 0.46 M Pb^{2+} and 0.48 M MSA solution. Regarding conductivity, the highest error seen is -2.82% for the 0.46 M Pb^{2+} and 0.48 M MSA solution, and just -0.18% for the 0.23 M Pb^{2+} and 0.94 M MSA solution.

[Pb^{2+} / M]	**[MSA] / M**	**μ meas. / mPa·s**	**μ calc. / mPa·s**	**% Error**
0	1.4	1.152	1.1741	-1.96
0.23	0.94	1.152	1.2399	-3.21
0.46	0.48	1.262	1.2436	+1.44

Table 4.2: Further viscosity measurements to validate the MatLab surface plot approximation.

[Pb^{2+} / M]	[MSA] / M	Cond. meas. / mS cm^{-1}	Cond. calc. / mS cm^{-1}	% Error
0	1.4	365	365.67	-0.18
0.23	0.94	280	277	+1.07
0.46	0.48	190	195.36	-2.82

Table 4.3: Further conductivity measurements to validate the MatLab surface plot approximation.

4.6 Summary

The effect of [Pb^{2+}] and [MSA] on electrolyte density and viscosity, and of [Pb^{2+}], [MSA] and temperature on electrolyte conductivity has been determined. Surface plots have been produced to approximate the conductivity and viscosity of any concentration of Pb^{2+} and MSA up to 1.5 M. In conclusion:

1. The electrolyte density was seen to increase with both [MSA] and [Pb^{2+}], being largely a function of the latter. The density increases linearly from 1.03 g cm^{-3} to 1.48 g cm^{-3} between 0 M and 1.5 M Pb^{2+}, when [MSA] = 1.0 M.

2. Being related to density, the electrolyte dynamic viscosity also followed a similar relationship. For example, the dynamic viscosity increases linearly from 1.12 mPa·s to 2.61 mPa·s between 0 M and 1.5 M Pb^{2+}, when [MSA] = 1.0 M.

3. However, conductivity was observed to follow a non-trivial relationship: at [MSA] $\geq$1.0 M, the conductivity decreases with [Pb^{2+}] while at [MSA] $\leq$0.25 M the conductivity increases with increasing [Pb^{2+}]. Between 0.25 M and 1.0 M MSA, the conductivity peaks at around 0.75 M [Pb^{2+}].

Measuring these fundamental properties is key to understanding how the flow cell pumping requirements and potential loss across the electrolyte varies at different states of charge. For example, a solution consisting of 1.5 M Pb^{2+} and 1.0 M MSA has a viscosity of 2.61 mPa·s at 296 K. By comparison, a solution containing 1.5 M vanadium and 4 M H_2SO_4 has a viscosity of 4.93 mPa·s [109], which is almost twice that of the soluble lead electrolyte. If both electrolytes were pumped through the same flow network, the Hagen-Poiseuille equation

dictates that the vanadium electrolyte would suffer a pressure drop twice that of the soluble lead electrolyte, resulting in a greater pumping energy loss.

Chapter 5

Separators

5.1 Introduction

Dividing the soluble lead flow cell with a separator would allow the use of electrode-specific additives whilst providing a physical barrier to abnormal deposit growth. If a significant improvement in performance can be achieved in this configuration, it would outweigh the added cost and design complexity of a divided cell.

Separators are permeable interfaces that prevent mixing of the electrolytes in the negative and the positive half-cells whilst allowing the passage of charged particles (excluding electrons) through to maintain the current in the overall cell circuit. This can be accomplished by using materials with functional groups that allow the passage of specific ions through whilst rejecting others (known as ion selectivity), or by soaking the separator in the electrolyte. Ionic exchange membranes (either anion or cation) fall under the former category and microporous separators, which are generally cheaper, work by the latter. The separator must be electronically insulating so it does not become a bipolar electrode, and it must possess a low ionic resistance, i.e. a low potential drop, IR_{mem}. It must be chemically stable and mechanically robust to withstand the stresses in cell construction. Furthermore, the separator must minimise the crossover of unwanted species, particularly electrode-specific additives and water molecules. Arora and Zhang [122] have published a review of separators for batteries, which also includes separator categories other than those discussed here.

A variety of suitable separators, chosen for their suitability in electrochemical devices where acidic media is present, were identified and selected for testing. This is presented in Table 5.1. The thickness when dry was calculated using Vernier callipers.

Separator	**Type**	**Dry Thickness/mm**
AmerSil FF60	Microporous separator	0.65
Fumatech FAP-450	Anion exchange membrane	0.05
Fumatech VPX-20	Anion exchange membrane	0.03
Fumatech F930	Cation exchange membrane	0.03
DuPont Nafion 115	Cation exchange membrane	0.10
MPPE	Microporous separator	0.60
C-Tech 'A'	Microporous separator	0.25
Fumatech VX-20	Anion exchange membrane	0.02
Fumatech FAP-325	Anion exchange membrane	0.02

Table 5.1: Separators selected for testing for use in the soluble lead flow cell. Only the first five separators are discussed in detail. *MPPE* microporous polyethylene; *C-Tech 'A'* unknown design, provided by project partner.

In the soluble lead cell, the cation exchange membranes would permit the crossover of Pb^{2+}, H^+ and any cationic additives such as Bi^{3+}. Conversely, the anion exchange membranes would be designed to permit the movement of OH^-, $CH_3SO_3^-$ and anionic additives such as F^-. There would also be the transfer of H_2O across both types of separator. Microporous separators would allow the crossover of all species but will, to some extent, prevent bulk mixing of the electrolytes in each half-cell.

5.2 Experimental Procedure

The separators were tested using four different solutions simulating different states of charge, based on an initial electrolyte composition of 0.7 M Pb^{2+} and 1.0 M MSA:

(a) 0% SoC: 0.7 M Pb^{2+} and 1.0 M MSA

(b) 33% SoC: 0.46 M Pb^{2+} and 1.48 M MSA

(c) 66% SoC: 0.23 M Pb^{2+} and 1.94 M MSA

(d) 100% SoC: 0 M Pb^{2+} and 2.4 M MSA

Each separator was soaked in the test solution for a minimum of 3 hrs before the test to allow thorough wetting, and the glass cell was filled with the same solution for the test. In each test, the supplied current was increased from 0 mA to 100 mA to 200 mA (0, 86 and 172 mA cm^{-2} respectively). Before each test, a baseline measurement of the electrolyte was obtained. This was then subtracted from the measured value when a separator was in place, allowing the potential drop across just the separator to be deduced. The results were plotted on a potential drop, E / mV, vs. current density, j / mA cm^{-2} graph for comparison. All tests were carried out at ambient temperature, 296 K. The reference electrodes used were both Hg/HgO.

5.3 Results

All separators remained stable in each solution; no physical deterioration was observed from visual inspection of samples left submerged in a 2.4 M MSA solution for one year (these samples were not used in any tests). In Figure 5.1, the potential drop across FF60, FAP-40, VPX-20, F930 and Nafion 115 are presented. The resistances of the MPPE, C-Tech 'A' and Fumatech VX-20 and and FAP-325 separators were impractically high to be used in the soluble lead system and so were ruled out and are not discussed further.

The potential drop across each separator was proportional to the current applied, as expected by Ohm's law. The resistance of each separator was expected to decrease with increasing SoC, due to the increase in proton concentration within the pores, and this was the generally observed result, particularly for the cation exchange membranes. Between 0 and 100% SoC, the potential drop across the Nafion membrane decreased approximately linearly over four times from 205 mV to 44 mV at 171 mA cm^{-2}. For perspective, a loss of 205 mV represents a 13% voltage loss if assuming a cell potential of 1.59 V. Over the same SoC range and current density, the potential drop across the FF60 microporous separator reduced from 125 mV to 59 mV.

The anion exchange membranes were not so sensitive to a change in SoC: the potential drop across the FAP-450 membrane decreased from 55 mV to 30 mV between 0 and 100% SoC at 171 mA cm^{-2}. Over the same SoC range and current density, the potential drop across the VPX-20 membrane remained relatively constant, fluctuating between 10 mV (at 33% SoC) and 32 mV (at 0% SoC). In general, the anion exchange membranes, VPX-20 and FAP-450, showed the least resistance across the four solutions, followed by the F930, FF60 and Nafion separators. At full charge, the potential drops across all separators, even at the higher current density, was comparable and below 60 mV.

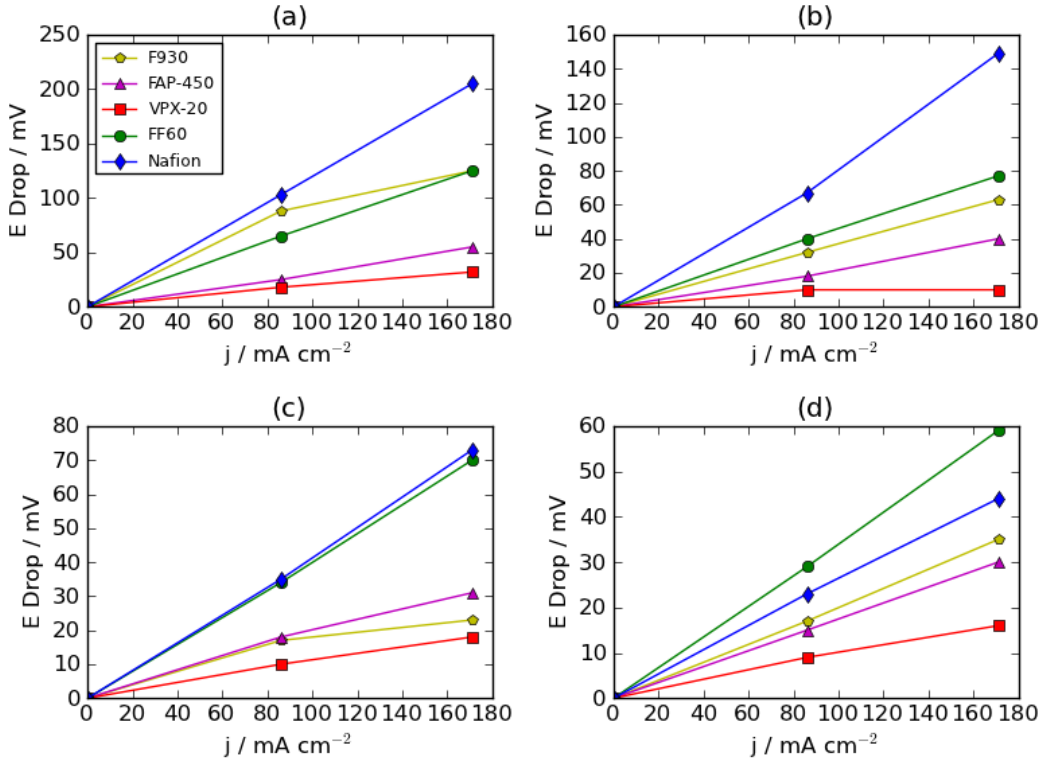

Figure 5.1: The potential drop across several separators in four different solutions simulating various states of charge: (a) 0.7 M Pb^{2+} and 1.0 M MSA; (b) 0.46 M Pb^{2+} and 1.48 M MSA; (c) 0.23 M Pb^{2+} and 1.94 M MSA; (d) 0 M Pb^{2+} and 2.4 M MSA. Temperature: 296 K. Reference electrodes: SCE.

The results are linear and can be used in combination with the separator thickness data to calculate the resistance, in Ω mm^{-1}, of each separator at each state of charge. This is presented in Table 5.2.

	Ω mm^{-1}				
% SoC	**F930**	**FAP-450**	**VPX-20**	**FF60**	**Nafion**
0	25.08	5.25	5.67	0.98	10.28
33	10.58	3.80	2.50	0.60	7.08
66	4.75	3.35	3.17	0.53	3.58
100	5.75	3.00	2.83	0.45	2.25
Average	11.54	3.85	3.54	0.64	5.79

Table 5.2: Separator resistance, in Ω mm^{-1}, as a function of the state of charge: 0%: 0.7 M Pb^{2+} and 1.0 M MSA; 33%: 0.46 M Pb^{2+} and 1.48 M MSA; 66% 0.23 M Pb^{2+} and 1.94 M MSA; 100% 0 M Pb^{2+} and 2.4 M MSA. Temperature: 296 K. Calculated using data from Figure 5.1 and Table 5.1.

Presented in this format, the FF60 clearly stands out as the superior separator, with an average resistance of 0.64 Ω mm^{-1} in all the solutions used. Though there is much improvement between 25.08 Ω mm^{-1} at 0% SoC and 5.75 Ω mm^{-1} at 100% SoC, the F930 is the most resistive separator relative to its thickness, averaging 11.54 Ω mm^{-1}. The VPX-20 and FAP-450 are comparable, with an average resistance of 3.54 and 3.85 Ω mm^{-1} respectively. The average resistance of Nafion is slightly higher, at 5.79 Ω mm^{-1}.

Table 5.3 lists the approximate costs of the VPX-20, FF60 and Nafion separators during informal discussions with the manufacturers.

Separator	**Cost / GBP m^{-2}**
VPX-20	840
FF60	13
Nafion 115	1000

Table 5.3: Separator cost, given in pounds per square meter of separator.

Nafion 115 is the most expensive separator whilst the FF60 is the cheapest option at almost a tenth of the price. These costs were for small samples to use in the lab and may vary considerably for bulk orders.

It was previously discussed in Chapter 2.5.2 that the deposit quality of lead at the negative electrode is exacerbated by a higher proton concentration. By employing an anion exchange membrane, the acidity in the negative half-cell could be maintained at the initial concen-

tration, as protons are only released during charge at the positive electrode when PbO_2 is deposited. The VPX-20 was the best performing anion-exchange membrane and was selected for further testing, presented in Chapter 8. The Nafion and FF60 separators were also chosen for further testing.

5.4 Summary

Several different types of separators were tested in soluble lead electrolytes simulating different states of charge, based on a 0% SoC electrolyte of 0.7 M Pb^{2+} and 1.0 M MSA. The potential drop was recorded at 86 mA cm^{-2} and then at 171 mA cm^{-2}. The following separators were highlighted and will be taken forward for further testing:

1. VPX-20: the lowest potential drop was recorded for this anion exchange membrane ($\leq$32 mV) across all states of charge.

2. FF60: at 13 GBP m^{-2}, this microporous separator is the cheapest option. The initial results showed an acceptable potential drop at higher SoC (<60 mV at 100% SoC) but much more at low SoC (125 mV at 0% SoC). However, in relation to its thickness, this separator had the lowest average resistance (0.64 Ω mm$-$1). Physically, it is rigid but somewhat brittle.

3. Nafion 115: this cation exchange membrane performed better than the FF60 at 100% SoC (<45 mV), but exhibited the worst performance at lower SoC, recording a 205 mV potential drop at 0% SoC. Its cost is also more than that of the VPX-20, at 1000 GBP m^{-2} compared to 840 GBP m^{-2} for the VPX-20. However, Nafion is widely used and will provide a useful benchmark for cell cycling experiments.

Chapter 6

Additives

6.1 Linear Sweep Voltammetry with MSA

Linear sweep voltammetry was used to investigate the potential window of an aqueous MSA solution in order to deduce the hydrogen and oxygen evolution limits. A 100 cm^3 of a 1.0 M MSA solution was used, and the result is plotted in Figure 6.1. Unless otherwise specified, all potentials mentioned in this chapter are relative to a saturated calomel reference electrode (SCE). The temperature was maintained at 298 K in all experiments.

The potential was first increased from 0 V to 2.5 V at 25 mV s^{-1}. The current response is seen to remain at zero until rising sharply from 2.0 V (2.24 V vs. SHE) until 2.5 V as a result of oxygen evolution.

The electrode was cleaned before the experiment was repeated, scanning toward negative potentials from 0 V to -1.5 V at 25 mV s^{-1}. The current response is seen to remain close to zero until a sharp decrease is observed at -1.1 V (-0.86 V vs. SHE) as a result of hydrogen evolution. This provides a wide potential window of 3.1 V, suitable for battery operation. The current response is not corrected for background noise, double-layer charging and other non-faradaic processes, hence the potential varies slightly from zero current before oxygen/hydrogen is evolved.

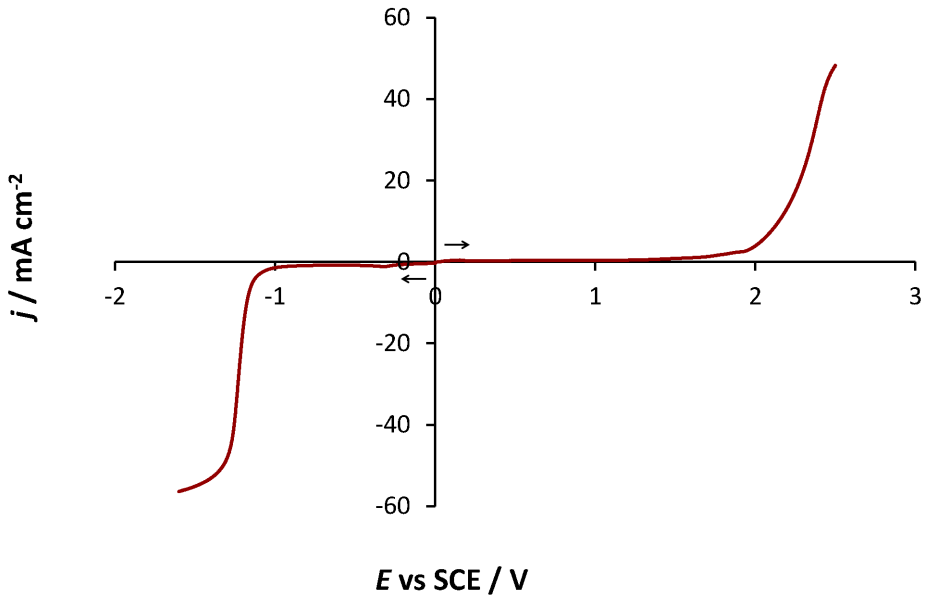

Figure 6.1: Hydrogen and oxygen evolution limits of a 1 M MSA solution. Electrolyte: 100 cm^3, 1.0 M MSA. Electrodes: *RDE* glassy carbon, *counter* platinum mesh, *reference* SCE. Scan rate: 25 mV s^{-1} Rotation rate: 750 rpm. Temperature: 298 K.

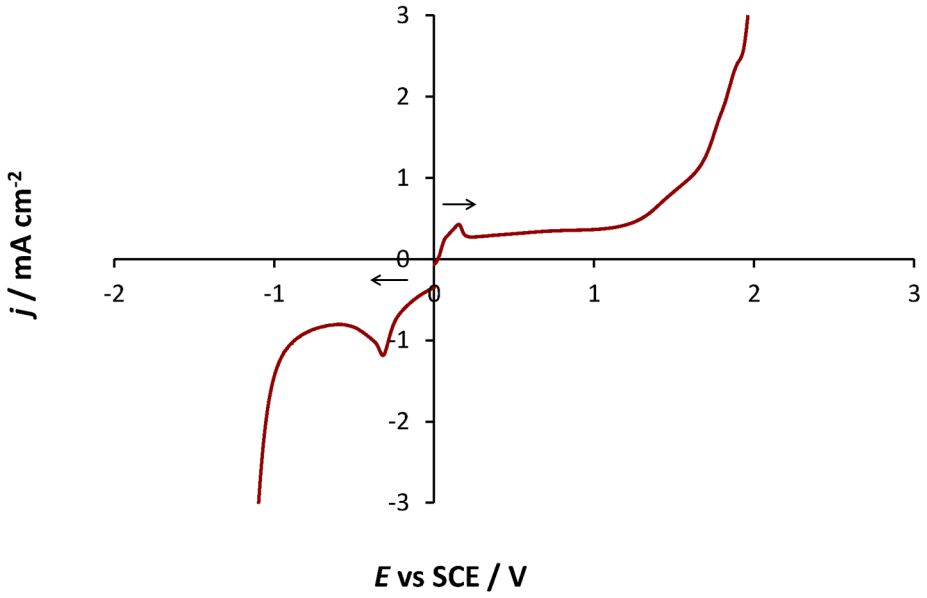

Figure 6.2: Magnified view of Figure 6.1, focusing on the detected interference in the voltammogram. Electrolyte: 100 cm^3, 1.0 M MSA. Electrodes: *RDE* glassy carbon, *counter* platinum mesh, *reference* SCE. Scan rate: 25 mV s^{-1} Rotation rate: 750 rpm. Temperature: 298 K.

Additionally, it should be noted that a slight reduction trough and oxidation peak can be seen at -0.33 V and 0.15 V respectively, likely due to impurities in the solution. This can clearly

be seen in Figure 6.2, where the area of interest in magnified. The solution was not degassed with nitrogen beforehand (in order to replicate conditions during flow cell operation), hence the interference could have arisen from dissolved oxygen.

6.2 Additives

Cyclic voltammetry was used to investigate the influence of several additives on the reaction kinetics of the reactions occurring at either electrode, and this is summarised in Table 6.1. Each additive was tested a maximum of three times, once in three different solutions. The first of the three columns towards the right of the table, *Add. & MSA*, represents studies where the solution contained only the additive and 1.0 M MSA. The second column, *Add. & Negative*, represents tests focusing on the negative electrode reaction where the solution consisted of 15 mM Pb^{2+} and 1.0 M MSA. The third column, *Add. and Positive*, represents tests focusing on the positive electrode reaction, and the solution here consisted of 0.7 M Pb^{2+} and 1.0 M MSA. The rotation rate of the working electrode was held at 750 rpm for both electrode tests and each experiment consisted of 50 consecutive cycles.

Lignosulfonate and HDTMA are needed to improve the morphology of the lead deposit, whilst the other additives were tested to improve the kinetics of the Pb^{2+}/PbO_2 couple. Promising additives were tested at the opposite electrode (to the one they were intended for) to see if they interfered with the reaction there. Lignosulfonate, HDTMA, F^- and Bi^{3+} are discussed first due to their appearance in the literature. With the exception of Zn^{2+}, other additives either had a detrimental effect or did not have any influence on the deposition/stripping mechanism.

Ethylenediaminetetraacetic acid (EDTA) is a carboxylic acid used for the sequestering of metal ions in solution. EDTA has found use in many applications, ranging from cosmetics to food preservation [123]. It was selected in this project to investigate whether its bonding to Pb^{2+} (and its effect therefore on the coordination sphere) could influence the kinetics of lead dioxide deposition and stripping. Polyvinylpyrrolidone (PVP) was selected for testing due to its ability to control the morphology (in terms of particle size) of PbO_2 coatings [124]. Zn^{2+}, Sn^{2+} and Gd^{3+} were selected to investigate if they had a similar pore-creating ability

as Bi^{3+} in the PbO_2 deposit.

Additive	Compound	Concentration	Add. & MSA	Add. & Negative	Add. & Positive
Lignosulfonate	Sodium salt	1 g dm^{-3}	√	√	√
HDTMA	Hydroxide	5 mM	√	√	√
Sn^{2+}*	Methanesulfonate	15 mM	-	-	√
Gd^{3+}*	Gd_2O_3	15 mM	-	-	√
Bi^{3+}	Bi_2O_3	15 mM	√	√	√
Ni^{2+}	$NiCO_3$	50 mM	√	-	√
Zn^{2+}*	ZnO	50 mM	√	-	√
F^-	NaF	60 mM	√	√	√
EDTA*	Disodium salt	15 mM	-	√	√
PVP*	M_w = 10,000	1 g dm^{-3}	√	-	√

Table 6.1: Additives tested with cyclic voltammetry. *Add. & MSA*: additive and 1 M MSA; *Add. & Negative*: additive and 15 mM Pb^{2+} and 1 M MSA; *Add. & Positive*: additive and 0.7 M Pb^{2+} and 1 M MSA. √ indicates that this additive has been tested in this solution. *These are novel additives that have not previously been tested in the soluble lead system. *HDTMA* hexadecyltrimethylammonium hydroxide; *EDTA* ethylenediaminetetraacetic acid; *PVP* polyvinylpyrrolidone. Temperature: 298 K.

6.3 Cyclic Voltammetry at the Negative Electrode

To investigate the deposition and stripping of lead (without additives), the potential was initially swept towards negative potentials from 0 V to -0.7 V, and then back to -0.2 V at a scan rate of 25 mV s^{-1}. With lignosulfonate and HDTMA in solution, the lower potential limit was decreased to -0.75 V and -1.2 V respectively. This cycle occurred 50 times consecutively for each test, and three separate tests are discussed: once with no additives, once with 1 g dm^{-3} lignosulfonate and once with 5 mM HDTMA. The electrode was cleaned and the electrolyte replaced before each test. Lignosulfonate produces an amber coloured collodial suspension whilst HDTMA produces a foamy solution which remains transparent. The 50^{th} scan of the three tests are plotted together in Figure 6.3, and Table 6.2 presents the properties of the scans.

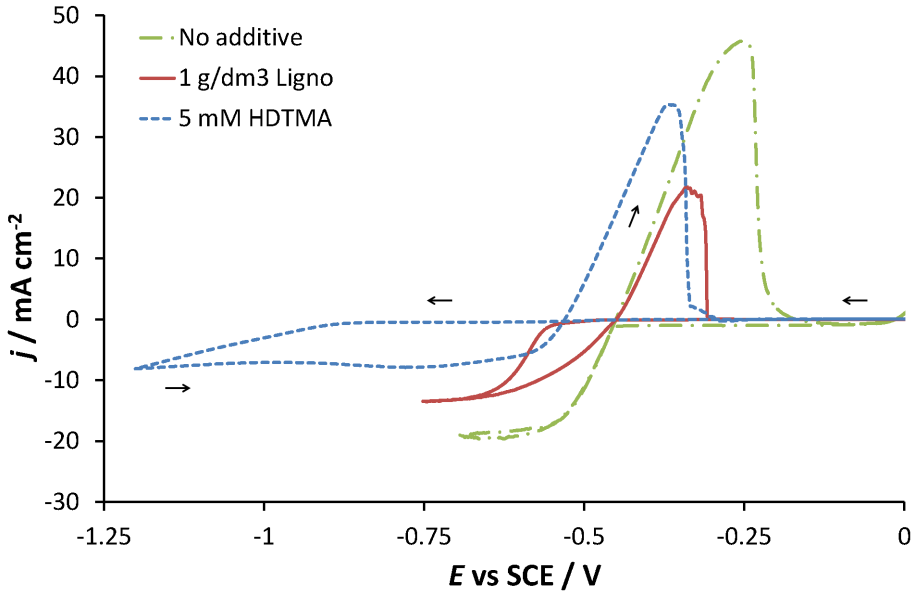

Figure 6.3: Cyclic voltammetry at the negative electrode. The 50th cyclic voltammogram of three different tests are superimposed together: with no additives, with lignosulfonate, with HDTMA. Lower potential limit: -0.7 V no add., -0.75 V lignosulfonate, -1.2 V HDTMA. Electrolyte: 15 mM Pb^{2+} and 1.0 M MSA. Electrodes: *RDE* glassy carbon, *counter* platinum mesh, *reference* SCE. Scan rate: 25 mV s^{-1} Rotation rate: 750 rpm. Temperature: 298 K.

	E_{dep} / V	I_L / mA cm^{-2}	E^e_{-ve} / V	E_{strip} / V
No additive	-0.45	-19.0	-0.45	-0.25
Lignosulfonate	-0.56	-13.5	-0.45	-0.34
HDTMA	-0.87	-8.0	-0.53	-0.37

Table 6.2: Properties of the cyclic voltammograms at the negative electrode, seen in Figure 6.3. E_{dep} potential at which deposition commences, I_L deposition limiting current, E^e_{-ve} equilibrium potential, E_{strip} potential at which the stripping peak is seen. All potentials are vs. SCE.

The lead deposition/stripping process with no additives is extremely facile, with low overpotentials: negligible difference between the reduction potential and the equilibrium potential and 0.2 V difference between the stripping peak and the equilibrium potential. The voltammogram retained the same shape across all cycles, averaging a charge efficiency of approximately 85%, which compares well with the literature [32] (calculated using the voltammetry software, Nova 1.11). There is a sharp reduction slope in the forward scan beginning at -0.45 V, signifying lead deposition. On the reverse scan, the current density becomes positive at -0.45 V, later peaking at 45 mA cm^{-2} at -0.25 V. This is a clear sign of lead dissolution.

The deposition limiting current, I_L is dependent on the mass transport properties of the solution and the overpotentials at which deposition and stripping commence dependent on the reaction kinetics at the electrode surface. In the presence of 1 g dm^{-3} lignosulfonate, the deposition overpotential (difference between the equilibrium potential and the potential at which deposition commences) increases by 0.09 V to -0.56 V. The equilibrium potential remains the same at -0.45 V (-0.21 V vs. SHE), which is slightly higher than the standard deposition potential, -0.13 V vs. SHE. In addition, the stripping peak is shifted negatively to -0.34 V. It is also evident that there is some suppression of the lead deposition process, as seen by the lower limiting current density. Therefore, the mass transport of Pb^{2+} to the electrode surface and the kinetics of charge transfer at the electrode surface are both affected.

In the presence of 5 mM HDTMA, in contrast to the previous two tests, there is a large deposition overpotential (due to the larger concentration of HDTMA compared to Pb^{2+}); deposition only begins at -0.87 V and continues in the reverse scan until -0.53 V. The limiting deposition current density is reduced to 8 mA cm^{-2}, from 13.5 mA cm^{-2} in the presence of lignosulfonate, and 19 mA cm^{-2} without any additives. The deposition inhibition arises due to the adsorption of the additives at the electrode surface, which would reduce the active surface area. This is the compromise for using additives to improve the deposit morphology. In this study, the mass transport is diminished and the electrode kinetics are substantially slower. Note, the concentrations of lignosulfonate and HDTMA here are the same as those that would be used in flow cell cycling, where the $[Pb^{2+}]$ would be almost 50 times higher than used in cyclic voltammetry. Therefore, the additive concentrations should have been adjusted accordingly here.

In a separate experiment containing 15 mM Bi^{3+}, 15 mM Pb^{2+} and 1.0 MSA, a double deposition/stripping voltammogram was observed, which fits well with the literature [32]. This is presented in Figure 6.4, where the 1^{st}, 10^{th}, 30^{th} and 50^{th} cycles are seen.

The potential was swept towards negative potentials from 0.7 V until -0.9 V, and then back to 0.7 V at 25 mV s^{-1}. In all scans, bismuth deposition begins at -0.27 V and lead deposition begins at -0.59 V. in the reverse scan, there is an oxidation peak at -0.4 V as a result of lead dissolution whilst bismuth is still being deposited. Between -0.49 V and -0.39 V (again, in all scans), the current is positive, which suggests that lead is being stripped at a greater

rate than the deposition of bismuth. Between -0.39 V and -0.06 V, bismuth is still being deposited. At more positive potentials than -0.06 V, bismuth is stripped from the electrode. The stripping region of bismuth has a broad arc shape rather than a peak due to a greater amount having been deposited on the forward scan.

No advantage of co-depositing bismuth with lead was observed. Two potential plateaus could be observed during discharge in the potential-time responses of cell cycling experiments, i.e. one for each metal oxidation, which would introduce an unfavourable potential unpredictability to the cell. However, [Pb^{2+}] is likely to be 45 - 100 times higher in flow cell electrolytes than in voltammetry electrolytes, whereas the [Bi^{3+}] would remain roughly the same. This effect therefore may be negligible. Furthermore, bismuth was selected as an additive for the positive electrode; if it is deposited at the negative electrode, it will cease to be effective there. In addition, if thick lead deposits build up over time due to the inefficiencies at reducing the PbO_2 deposit, then bismuth could become trapped as an alloy with lead at the negative electrode.

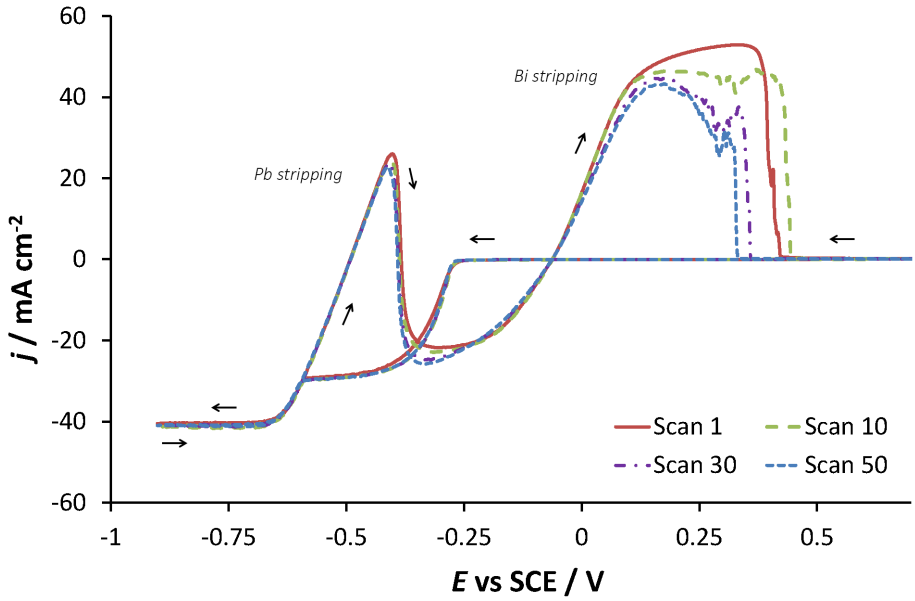

Figure 6.4: Cyclic voltammetry at the negative electrode with 15 mM Bi^{3+}. The 1^{st}, 10^{th}, 30^{th} and 50^{th} cyclic voltammograms are presented. Potential range: 0.7 V to -0.9 V. Electrolyte: 15 mM Pb^{2+} and 1.0 M MSA. Electrodes: *RDE* glassy carbon, *counter* platinum mesh, *reference* SCE. Scan rate: 25 mV s^{-1} Rotation rate: 750 rpm. Temperature: 298 K.

6.4 Cyclic Voltammetry at the Positive Electrode

6.4.1 No additives

To investigate the oxidation and reduction of PbO_2, the potential was swept towards positive potentials from 0.2 V to 1.9 V in the forward scan at a scan rate of 50 mV s^{-1}, and then back to 0.2 V at the same rate in the reverse scan. The results of tests with no additives, with 15 mM Bi^{3+} and 60 mM NaF are presented in Figures 6.5, 6.6 and 6.7 respectively. In each graph, the 1st, 10th, 30th and 50th cycles are presented.

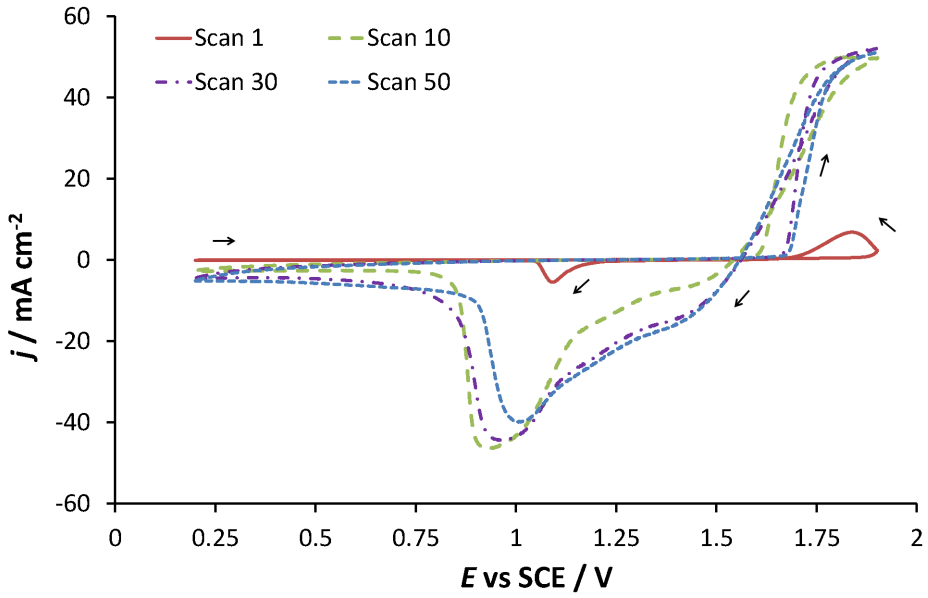

Figure 6.5: Cyclic voltammetry at the positive electrode with no additives. The 1st, 10th, 30th and 50th cyclic voltammograms are presented. Potential range: 0.2 V to 1.9 V. Electrolyte: 0.7 M Pb^{2+} and 1.0 M MSA. Electrodes: *RDE* glassy carbon, *counter* platinum mesh, *reference* SCE. Scan rate: 50 mV s^{-1}. Rotation rate: 750 rpm. Temperature: 298 K.

In Figure 6.5, deposition of PbO_2 begins at 1.88 V on the 1st cycle and continues in the reverse scan until 1.64 V. A reduction peak is then seen at 1.09 V, its sharpness suggesting the reduction of a single compound. In subsequent cycles, this reduction peak becomes broader and less defined, as there is more material on the surface due to accumulation over the previous cycles. However, this could also suggest that several species are being reduced, which fits well with the theory of the formation of different PbO_x compounds (Chapter 2.5.6). In these later cycles, the equilibrium potential shifts to 1.55 V (1.79 V vs. SHE) which is

greater than under standard conditions, 1.46 V vs. SHE.

The charge efficiency in the 1st cycle was found to be 40%, suggesting that some PbO_2 material remains on the electrode surface after each cycle, even though the potential is reduced to as low as 0.2 V. The charge efficiency was seen to improve with each cycle, and a 105% charge efficiency was observed in the 50th cycle. Charge efficiency >100% clearly indicates a build-up of material at the electrode surface. This would suggest that deposition and stripping PbO_2 onto layers of itself is kinetically more favourable than onto glassy carbon. Furthermore, black flakes were seen at the bottom of the cell at the end of the experiment as a result of this build-up of deposit over time, and was also seen in experiments that used Bi^{3+} and F^-.

6.4.2 Fluoride

The experiment was repeated with 60 mM NaF, and the voltammogram is presented in Figure 6.6.

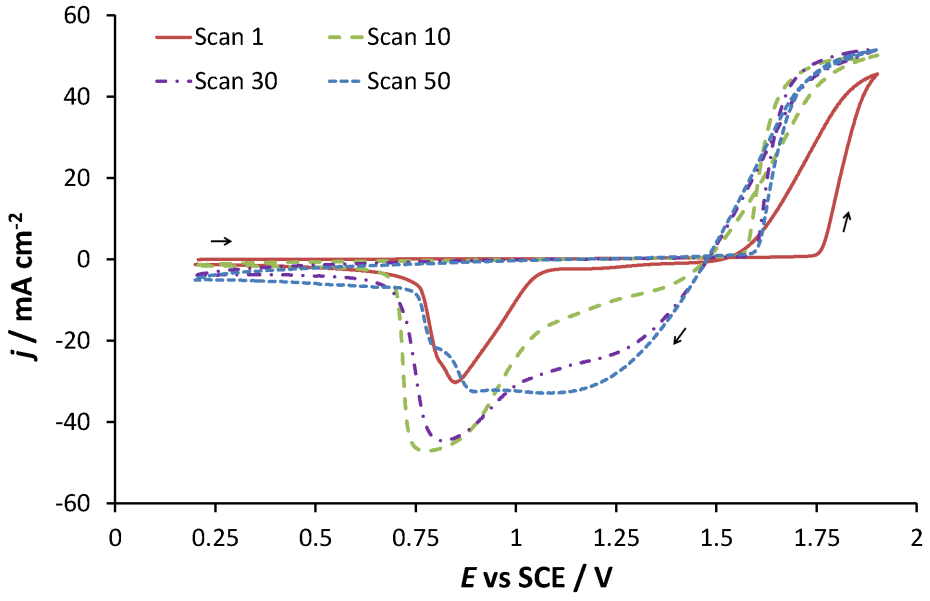

Figure 6.6: Cyclic voltammetry at the positive electrode with 60 mM F^-. The 1st, 10th, 30th and 50th cyclic voltammograms are presented. Potential range: 0.2 V to 1.9 V. Electrolyte: 0.7 M Pb^{2+} and 1.0 M MSA. Electrodes: *RDE* glassy carbon, *counter* platinum mesh, *reference* SCE. Scan rate: 50 mV s^{-1}. Rotation rate: 750 rpm. Temperature: 298 K.

In the presence of F^-, PbO_2 deposition begins at 1.75 V in the 1st cycle, compared to 1.88 V in the no-additive test, leading to a thicker deposit on the electrode. Hence, the current density obtained in the reduction wave is much higher (-30 mA cm^{-2} compared to -5 mA cm^{-2}). The equilibrium potential at cycle 50 between the tests with fluoride and no additives differs by only 0.07 V; there is a larger difference between the reduction peaks at cycle 30. With no additives, the reduction peak was seen at 0.96 V, whereas with F^- in solution, the reduction peak is seen at 0.81 V. Furthermore, by the 50th cycle in the test with F^-, there is no longer a reduction peak, but rather a reduction current plateau at -32 mA cm^{-2}, from 1.12 V to 0.88 V.

It was discussed previously in Chapter 2.6.2 that F^- improves the adhesion of PbO_2 to the electrode. Because of this, it is likely that an increased reduction overpotential would arise, which would explain the lower potential at which PbO_2 stripping peaks. Whether this disadvantage is offset by the advantage of less PbO_2 flaking can only be tested in flow cell experiments.

6.4.3 Bismuth

The procedure was repeated with 15 mM Bi^{3+} in solution and is reported in Figure 6.7. The latter cycles see a more positively shifted equilibrium potential and oxidation region than the 1st cycle. At cycle 50, the equilibrium potential is 1.64 V. The reduction peak is substantially shifted towards positive potentials, at 1.43 V at cycle 50 compared to 1.0 V at cycle 50 in the no-additive test (Figure 6.5). This shape suggests that with Bi^{3+} present, the bulk of the PbO_2 deposit in later cycles can be stripped at low overpotentials. This behaviour compares well to the literature [32]. The decreasing overpotentials suggest an improvement in reaction kinetics and the higher equilibrium potential on discharge would increase the discharge potential in a cell. However, in this voltammogram, this positive shift also means that there is less deposition and stripping than in the no-additive test, i.e. the upper potential limit must be increased for further analysis regarding thicker deposit formation. The discussion is continued further in the next section.

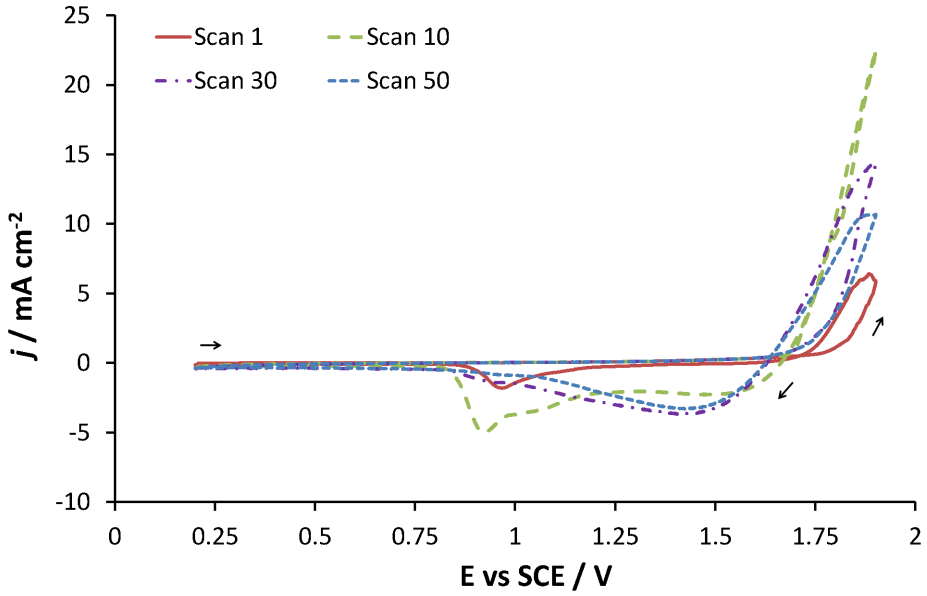

Figure 6.7: Cyclic voltammetry at the positive electrode with 15 mM Bi^{3+}. The 1st, 10th, 30th and 50th cyclic voltammograms are presented. Potential range: 0.2 V to 1.9 V. Electrolyte: 0.7 M Pb^{2+} and 1.0 M MSA. Electrodes: *RDE* glassy carbon, *counter* platinum mesh, *reference* SCE. Scan rate: 50 mV s^{-1}. Rotation rate: 750 rpm. Temperature: 298 K.

6.4.4 Other Additives

Further data from the 50th cycles of the CVs presented in Figures 6.5 - 6.7 and CVs of the other additives presented in Table 6.1 are presented in Table 6.3. The additives are ordered by their effect on the equilibrium potential, E^e_{+ve}. The proportion of the PbO_2 deposit stripped as a function of the cathodic overpotential, η, is presented relative to a 100% stripping at the lower potential limit at 0.2 V. As an example, consider the data for the no-additive test: stripping occurs between 1.55 V and 0.2 V; 23% of the stripping process occurs by 1.25 V, i.e. $\eta = 300$ mV, and 81% of all stripping occurs by 0.8 V, i.e. $\eta = 750$ mV. This is illustrated in Figure 6.8a. The table provides an indication on the effect of each additive on cell potential during a charge/discharge experiment, indicating its effect on the reaction kinetics of the Pb^{2+}/PbO_2 couple.

The addition of F^-, Sn^{2+}, EDTA, Ni^{2+} or PVP decreases the equilibrium potential below 1.55 V whilst the presence of Zn^{2+} and Bi^{3+} result in a rise above 1.6 V, which would increase the cell potential during cycling. It can be seen that with EDTA in solution, there is a narrow region at a high overpotential, between 500 mV and 750 mV, where much of the

stripping occurs (42% at 500 mV and 98% at 750 mV), which would result in the cell discharge potential dropping rapidly to an impractically low value. This additive can therefore be ruled out.

The amount of deposit stripping at $\eta = 500$ mV increases from 53% with no additive to 70% with Bi^{3+} in solution; more of the deposit is stripped at lower overpotentials based around a higher equilibrium potential. This is further illustrated in Figure 6.8b. A similar conclusion can be made with Zn^{2+}-containing electrolytes. These two additives therefore require further testing in cell cycling studies to see if they enable a higher cell discharge potential to be maintained for longer, as predicted by their respective CVs.

			η / **mV**				
Add	**[Add] / M**	E^e_{+ve} / **V**	**100**	**200**	**300**	**500**	**750**
F^-	60 mM	1.48	4	16	27	57	86
Sn^{2+}	15 mM	1.50	1	13	44	66	75
EDTA	15 mM	1.50	<1	2	6	42	98
Ni^{2+}	50 mM	1.52	5	16	32	66	86
PVP	1 g dm^{-3}	1.54	4	14	28	58	90
-	-	1.55	4	12	23	53	81
Gd^{3+}	15 mM	1.56	4	12	23	52	82
Zn^{2+}	50 mM	1.62	8	22	35	64	87
Bi^{3+}	15 mM	1.64	7	24	43	70	84

Table 6.3: % deposit stripped as a function of overpotential (η) at cycle 50, ordered by equilibrium potential, E^e_{+ve}. *EDTA* ethylenediaminetetraacetic acid, *PVP* polyvinylpyrrolidone. Potential range: 0.2 V to 1.9 V. Electrolyte: 0.7 M Pb^{2+} and 1.0 M MSA. Electrodes: *RDE* glassy carbon, *counter* platinum mesh, *reference* SCE. Scan rate: 50 mV s^{-1}. Rotation rate: 750 rpm. Temperature: 298 K.

Aside from the Sn^{2+} test, all tests saw >80% stripping at an overpotential of 750 mV. With Sn^{2+} in solution, 25% of stripping occurs beyond 750 mV, which could result in the cell potential cut-off from being reached before the deposit has been sufficiently stripped, leading to a build-up of the deposit with each cycle. Sn^{2+} therefore would not make a suitable additive for the system. Gd^{3+} clearly does not have any impact on the mechanism, as the data almost exactly matches that of the no-additive test.

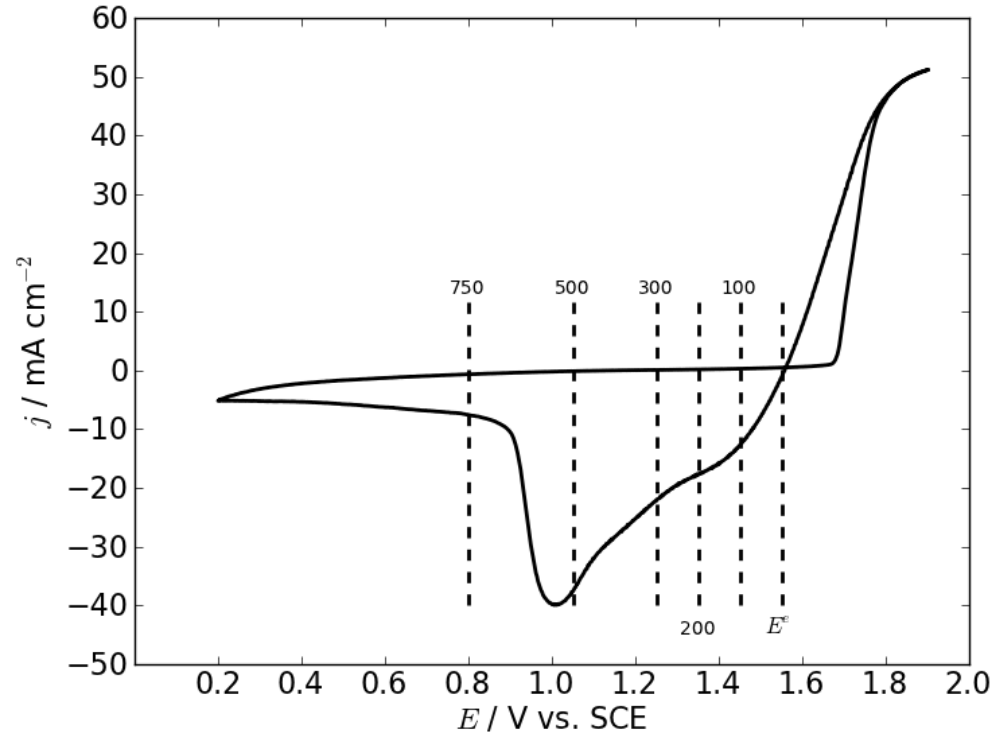

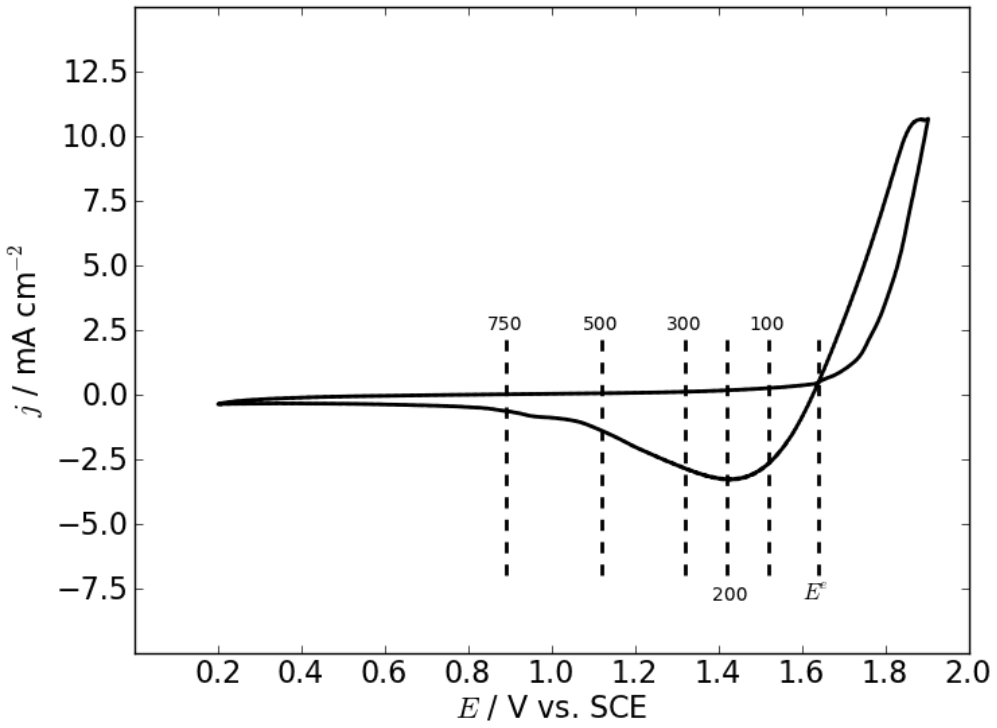

(b)

Figure 6.8: Illustration of proportion of PbO_2 deposit stripped on the 50^{th} cycle as a function of overpotential:(a) no additives, (b) with 15 mM Bi^{3+}.

PVP also has little effect on the stripping of PbO_2, only slightly increasing the % stripping at each overpotential, for example 58% compared to 53% (no additive) at $\eta = 500$ mV. There is some improvement with Ni^{2+} present: based on comparable equilibrium potentials, 66% stripping occurs at 500 mV compared to 53% in the no-additive test. However, there is no increase in the equilibrium potential as seen in tests containing Zn^{2+} or Bi^{3+}.

6.5 Summary

Voltammetric studies were used to study the effect of additives on the deposition/dissolution of Pb and PbO_2 at the negative and positive electrodes respectively, and to provide an indication of how the additive would affect the potential of a soluble lead cell during charge/discharge. In summary:

1. Linear voltammetry was used to establish the potential window of a 1.0 M MSA solution: oxygen evolution commences at 2.0 V vs. SCE, and hydrogen evolution is observed from -1.1 V vs. SCE. This provides a potential window of 3.1 V.

2. Following cyclic voltammetry tests, lignosulfonate and HDTMA were seen to be suitable additives at the negative electrode for use in the flow cell, where the long-term stability of the additive remains to be studied. Pb deposition begins at -0.45 V vs. SCE with no additive in solution, a negligible overpotential from E^e_{-ve}, reaching a I_L of -19 mA cm^{-2}. With lignosulfonate, E_{dep} decreases to -0.56 V vs. SCE and I_L decreases to -13.5 mA cm^{-2}. With HDTMA, E^e_{-ve} shifts to -0.53 V vs. SCE and E_{dep} is shifted considerably to -0.87 V vs. SCE, with I_L further reducing to -8 mA cm^{-2} (Table 6.2). This would suggest a high cell charge potential, but this is unlikely to be seen in a cell cycling experiment, where, unlike here, $[Pb^{2+}] >> [HDTMA]$.

3. A negative shift in the stripping potential peaks was also seen: -0.34 V vs. SCE and -0.37 V vs. SCE with lignosulfonate and HDTMA respectively, compared to -0.25 V vs. SCE with no additive. This would increase the cell discharge potential, thus improving the voltage efficiency.

4. Bi^{3+} is intended for the positive electrode. However, its effect at the negative electrode

was also tested. With Bi^{3+} in solution, Bi deposition occurs at -0.27 V vs. SCE whilst Pb deposition is shifted to -0.59 V vs. SCE, suggesting that a Pb-Bi alloy would be deposited as a result in the soluble lead cell during charge, which could deplete the solution of Bi^{3+}. The result compared well to the literature [32].

5. Cyclic voltammetry ruled out the use of the following additives: Sn^{2+}, Gd^{3+}, Ni^{2+}, EDTA and PVP due to a detrimental or negligible influence on reaction kinetics, summarised in Table 6.3.

6. F^- was seen to reduce the equilibrium potential, from 1.55 V with no additive to 1.48 V with F^-. There is little impact on the % deposit stripping as a function of overpotential: 27% deposit stripping at $\eta = 300$ mV (1.18 V vs. SCE) compared to 23% stripping at the same overpotential with no additives (1.25 V vs. SCE). The CV suggests that F^- would decrease the cell discharge potential. However, this would be offset if an improved adhesion of the PbO_2 to the electrode is observed in cell cycling tests (Chapter 8).

7. With 15 mM Bi^{3+} in solution, the equilibrium potential is shifted higher to 1.64 V vs. SCE. Most of the PbO_2 deposit is stripped at low overpotentials: 70% of stripping takes place at $\eta = 500$ mV (1.14 V vs. SCE) compared to just 53% at the same overpotential with no additives in solution (1.05 V vs. SCE). A comparable response was recorded with 50 mM Zn^{2+} in solution. In a cell, this would result in a higher discharge cell potential being maintained for a longer period of time, which would improve the voltage efficiency and increase the system power density.

Lignosulfonate, HDTMA, F^-, Bi^{3+} and Zn^{2+} are tested further in cell charge/discharge cycling experiments using static electrolytes in the next chapter, where a final combination of additives is highlighted.

Chapter 7

Electrolyte Composition

7.1 Introduction

A static electrolyte, parallel plate cell with 9 cm^2 electrodes was used to assess the electrochemical efficiency of the soluble lead system under varying MSA and Pb^{2+} concentrations, and to study the effect of additives. The cell was filled with 18 cm^3 of electrolyte for galvanostatic charge/discharge cycling. Each cycle began with a charge phase lasting 15 mins at 15 mA cm^{-2}, followed by an open circuit rest period of 3 mins. Discharge then took place at 15 mA cm^{-2} until the cell potential dropped below 0.3 V, or for a maximum of 15 mins. A further 3 mins open circuit rest period followed before commencing the charge phase of the subsequent cycle. A full cycle (i.e. a cycle that is 100% charge efficiency) could last for a maximum of 36 mins. Unlike Li-ion batteries, 100% charge efficiency is rare in the SLFB at its present stage of development. Each cell was cycled until failure, which was defined as the cycle at which the charge efficiency dropped below 70%, from which point the charge efficiency continued to fall in each subsequent cycle until charging could not take place for a whole 15 mins due to Pb^{2+} depletion in the electrolyte. The cycles achieved are a function of charge efficiency and initial [Pb^{2+}]. High charge efficiency implies a low rate of depletion of Pb^{2+} from the solution (i.e. a low rate of deposit build-up at the electrodes), and depletion is delayed if there are greater Pb^{2+} ions initially.

The experiment provides a good initial comparison of different electrolytes in terms of cell

lifetime and charge efficiency, but not voltage efficiency. At 2 cm, the inter-electrode gap of the cell is very wide, which, whilst preventing shorting, would lead to a large potential drop, which would mask the potential drop across the other cell components. Because the electrolyte is static, the mass transport of active species from/to the electrodes is reduced compared to a flowing system. Furthermore, the cell allows for only 18 cm^3 of electrolyte, which leads to a larger % Pb^{2+} utilisation in a shorter period of time compared to a flowing system with a greater electrolyte volume stored in an external reservoir.

The SLFB state of charge is the ratio of moles of Pb in the electrodeposits to the number of moles of Pb^{2+} that were in solution initially. This terminology implies that all the stored charge is available on discharge, which is not often the case as the accumulation of deposits at both electrodes is frequently observed. From this chapter onwards, the term *% Pb^{2+} utilisation* is used instead of SoC to refer to the proportion of Pb^{2+} removed from the electrolyte and deposited at the electrodes.

7.2 Lead and MSA Concentration

Twenty tests were carried out initially, with initial [MSA] ranging from 0.25 M to 1.0 M and [Pb^{2+}] ranging from 0.5 M to 1.5 M. The number of cycles achieved before failure of each test is displayed in Figures 7.1 and 7.2. The cycle life is seen to generally reduce when increasing [Pb^{2+}], and it decreases at a far greater rate when increasing [MSA]. For example, 46 and 36 cycles were achieved at 0.7 M and 1.5 M Pb^{2+} respectively when 0.25 M MSA is used. However, 48 and only 12 cycles are achieved at 0.7 M and 1.5 M Pb^{2+} respectively when using 1.0 M MSA. The data points for the 1.0 M MSA curve (pictured in yellow) are expanded in Figure 7.2, where it can be seen that the cell cycle life peaks when using 0.7 M - 0.75 M Pb^{2+} and 1.0 M MSA, achieving close to 50 cycles. A 0.7 M Pb^{2+} and 1.0 M MSA electrolyte has previously been seen in the literature [59]. The cycle life is seen to reduce as the concentration is reduced to 0.5 M, and even more so when increased past 0.8 M. Table 7.1 presents further performance metrics of the results presented in Figures 7.1 and 7.2. The cycle life and efficiencies averaged across the number of cycles before failure are presented, as well as the percentage of Pb^{2+} utilisation at the failure point.

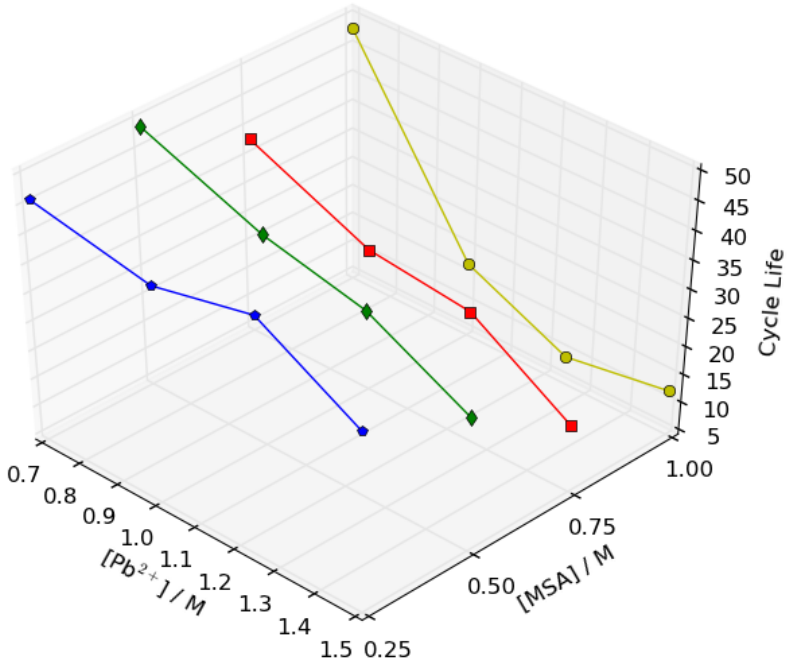

Figure 7.1: The cycle life of the 9 cm^2 static cell during charge/discharge cycling as a function of $[Pb^{2+}]$ and [MSA]. The failure point is defined as the cycle where the charge efficiency drops below 70%.

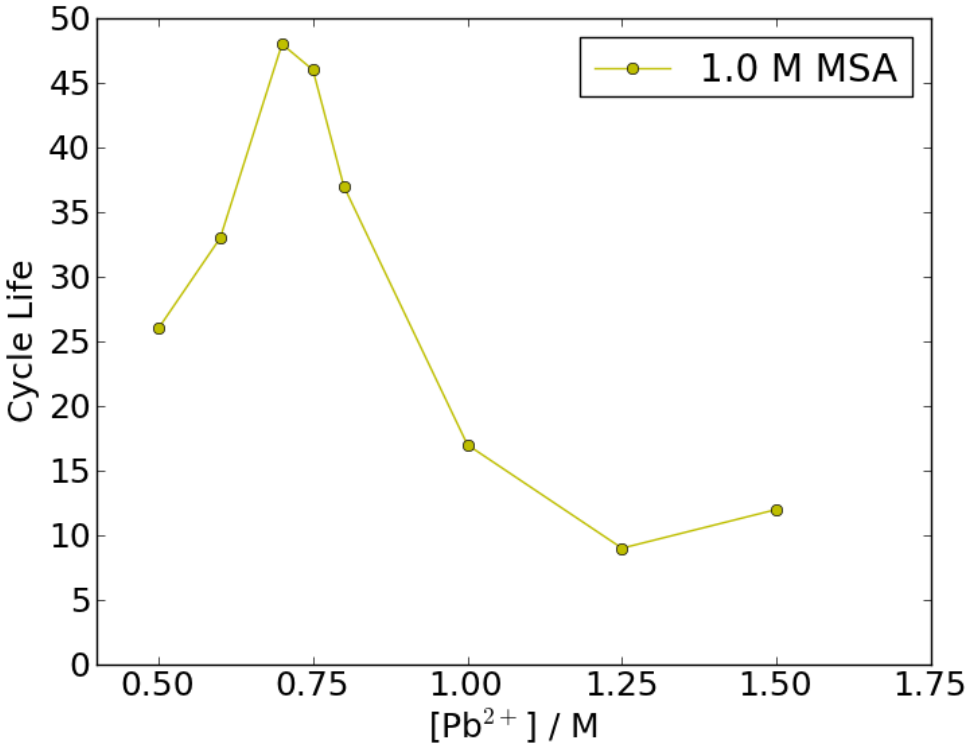

Figure 7.2: The cycle life of the 9 cm^2 static cell during charge/discharge cycling as a function of $[Pb^{2+}]$, where [MSA] = 1.0 M. The failure point is defined as the cycle where the charge efficiency drops below 70%.

The charge efficiency, *Q Eff*, was calculated using Equation 2.19. The energy efficiency, *En Eff*, was calculated by the battery testing software and from these values, the voltage efficiency, *V Eff*, was calculated. % Pb^{2+} utilisation was calculated using Faraday's Law (Equation 2.13), assuming that no parasitic reactions occurred (ϕ=1) and that negligible self discharge takes place at this scale, so that any imbalance between charge and discharge resulted in the build-up of deposits at the electrodes. This metric provides an indication of the depth of charge that the initial electrolyte composition can achieve.

The average charge efficiency remained high throughout each test, peaking at 86% in the 1.0 M Pb^{2+} and 0.5 – 0.75 M MSA tests. Despite the expected high ionic loss across the wide inter-electrode gap, the average voltage efficiency throughout each test was reasonably high, peaking at 72% in the 0.7 M Pb^{2+} and 1.0 M MSA test. At $\leq$1.0 M Pb^{2+}, the voltage efficiency slightly improved with increasing [MSA]. At higher [Pb^{2+}], the voltage efficiency was approximately consistent (66 – 68%), irrespective of [MSA]. This is likely an effect of the electrolyte conductivity; as discussed earlier, at lower [Pb^{2+}], conductivity increases at a greater rate with increasing [MSA] than at higher [Pb^{2+}]. The average energy efficiency increases from 51% to 58% between 0.25 M to 1.0 M MSA at 0.7 M Pb^{2+}. At $\geq$1.0 M Pb^{2+}, there is a reduction in energy efficiency with increasing [MSA].

Furthermore, a greater amount of Pb^{2+} is utilised before failure at lower [Pb^{2+}] and [MSA]. 95% of Pb^{2+} in the electrolyte was deposited before failure in the 0.7 M Pb^{2+} and 0.5 M MSA test, whereas just 13% of the solvated Pb^{2+} was deposited in the 1.25 – 1.5 M Pb^{2+} and 1.0 M MSA tests.

The cell cycling data indicates that an initial electrolyte composition of 0.7 M Pb^{2+} and 1.0 M MSA would provide optimal electrochemical performance in terms of cycle life, energy efficiency and Pb^{2+} utilisation. It is also likely that this composition provides a good compromise between solution conductivity and viscosity. Similar efficiencies and cycle lives were also measured when using 1.0 – 1.25 M Pb^{2+} and 0.25 – 0.5 M MSA, but the Pb^{2+} utilisation was considerably lower, for example just 34% in the 1.25 M Pb^{2+} and 0.25 M MSA test. If more of the remaining 66% of Pb^{2+} could be utilised whilst maintaining the charge efficiency above 70%, then the cycle life would be increased and a higher energy storage capacity become available. This could be attained by the use of a flowing electrolyte or various

additives.

[Pb^{2+}] / M	[MSA] / M	Cycle Life	% Q Eff	% V Eff	% En Eff	% Pb^{2+} Use
0.5	1.0	26	78	69	54	70
0.6	1.0	33	76	66	50	82
0.75	1.0	46	76	74	56	92
0.8	1.0	37	80	73	58	58
0.7	0.25	46	79	65	51	87
	0.50	49	78	68	53	95
	0.75	38	76	70	53	80
	1.0	48	81	72	58	80
1.0	0.25	42	83	67	56	45
	0.50	41	86	68	58	35
	0.75	29	86	66	57	26
	1.0	17	74	69	51	28
1.25	0.25	46	85	67	57	34
	0.50	37	84	68	57	29
	0.75	27	85	68	58	26
	1.0	9	70	67	47	13
1.50	0.25	36	84	66	55	24
	0.50	28	77	66	51	27
	0.75	16	73	66	48	18
	1.0	12	75	67	50	13

Table 7.1: Static cell cycle life, efficiency and % Pb^{2+} utilisation as a function of [Pb^{2+}] and [MSA]. Electrode: 9 cm^2, carbon/polyvinyl ester. Cycling regime: 15 mins charge at 15 mA cm^{-2}, 3 mins rest, discharge to 0.3 V (or max 15 mins) at 15 mA cm^{-2}, 3 mins rest. Temperature: 296 K (no active temperature control).

7.3 The Influence of Additives

7.3.1 Part I

The influence of the Nafion 115, VPX-20 and FF60 separators, and the additives Bi^{3+}, Zn^{2+}, HDTMA and lignosulfonate on cell performance was investigated using an electrolyte composed of 0.7 M Pb^{2+} and 1.0 M MSA (referred to as the 'standard' solution). The separator in all static cell (and, in the next chapter, flow cell) experiments was first soaked in the electrolyte to be tested for a minimum of 12 hrs. The same electrochemical static cell and testing regime as in the previous section was used, and Table 7.2 presents the results. In the initial tests where Bi^{3+} is used alongside a separator, Bi^{3+} was confined to just the positive half-cell. Similarly, in the latter tests where a separator is used, HDTMA or lignosulfonate was added only to the negative half-cell and the Bi^{3+} to the positive half-cell.

In all the tests where additives were not used, the charge efficiencies remained above 70% from the first cycle. In all tests where additives were used, the charge efficiency of the first several cycles was below 70%, as low as 50%, but slowly improved to surpass 70% at the latest by the 10^{th} cycle. The charge efficiency then reached a steady state above 70%, similar to the tests without additives, before deteriorating towards failure. The best performing cell used 10 mM Bi^{3+} and no separator, achieving 65 cycles at an average charge efficiency of 86% (cycles 1 - 8 and 24 - 56 achieved $<$70% and $>$90% charge efficiency respectively). There was only a modest improvement when a separator was inserted to confine the bismuth to the positive half-cell (52 cycles at 83% average charge efficiency when using FF60 or VPX-20). However, comparable performance was seen when the Bi^{3+} concentration was increased to 15 mM. Furthermore, there was comparable performance between all the separators at this scale. As well as separating the positive and negative electrolytes, the separator would act as a barrier to shorting caused by Pb dendrites and PbO_2 creep, which are not seen in this cell due to the wide inter-electrode gap.

Only 40 cycles averaging 77% charge efficiency was recorded with 10 mM Zn^{2+} in solution, and this was the best recorded from several tests ranging in concentration from 5 mM to 50 mM, with or without a separator. Zinc was therefore ruled out as a potential additive at this stage.

Add	**[Add]**	**Separator**	**Cycle Life**	**% Q Eff**	**% V Eff**	**% En Eff**	**% Pb^{2+} Use**
-	-	-	48	81	72	58	80
Bi^{3+}	10 mM	-	65	86	71	60	92
Bi^{3+}	10 mM	VPX-20	52	83	71	59	80
Bi^{3+}	10 mM	FF60	52	83	70	58	77
Bi^{3+}	10 mM	Nafion	49	81	70	57	83
Bi^{3+}	15 mM	FF60	67	86	66	57	93
Zn^{2+}	10 mM	-	40	77	72	56	80
Bi^{3+} & HDTMA	10 mM 5 mM	-	55	82	68	56	88
Bi^{3+} & HDTMA	10 mM 5 mM	FF60	47	79	69	55	88
Bi^{3+} & Ligno.	10 mM 1 g dm^{-3}	-	51	81	68	55	86
Bi^{3+} & Ligno.	10 mM 1 g dm^{-3}	FF60	52	83	69	57	77

Table 7.2: Static cell cycle life, efficiency and % Pb^{2+} utilisation in the presence of various additives. Where a separator is used, Bi^{3+} was confined to just the positive half-cell and lignosulfonate and HDTMA were confined to just the negative half-cell. Electrolyte: 0.7 M Pb^{2+} and 1.0 M MSA. Electrode: 9 cm^2, carbon/polyvinyl ester. Cycling regime: 15 mins charge at 15 mA cm^{-2}, 3 mins rest, discharge to 0.3 V (or max 15 mins) at 15 mA cm^{-2}, 3 mins rest. Temperature: 296 K (no active temperature control).

There does not seem to be any significant effect on performance with the addition of either one of the surfactants. The HDTMA, Bi^{3+}, undivided test achieved 55 cycles at 82% average charge efficiency, a minor improvement to the standard electrolyte. The other separator-surfactant-Bi^{3+} combinations were not as successful and offered only slight improvements. After failure, the cell was disassembled to reveal smoother, more uniform lead deposits whenever lignosulfonate or HDTMA was used. However, the real impact of the surfactants at both the electrodes appears to be unclear at this scale.

7.3.2 Part II

In an attempt to improve the % Pb^{2+} utilisation and the performance of the static cell whilst increasing the energy density of the electrolyte, it was decided to investigate bespoke electrolyte compositions for each half-cell in terms of MSA concentration. It is understood from the literature that the quality of the lead deposit worsens at high levels of acidity (Chapter 2.5.2). Because [H^+] increases on charge only via the positive electrode reaction, it was postulated that the proton concentration in the negative half-cell could be maintained at the initial concentration if an anion exchange membrane were to be used, as this would prevent the crossover of H^+ from the positive to the negative half-cell (the methanesulfonate anion, $CH_3SO_3^-$, would be the charge carrier between half-cells).

The Pb^{2+} concentration was increased from 0.7 M to 1.2 M to improve the electrolyte's energy density. The MSA concentration in the negative and positive half-cell was decreased to 0.5 M and 0 M respectively. 0.5 M was seen as the optimal compromise between being high enough for a good conductivity and low enough to avoid a rough lead deposit. In the positive half-cell, the H^+ concentration would rise by 4.8 M between 0% and 100% Pb^{2+} utilisation, hence it was kept as low as possible initially. NaF was also introduced into the positive half-cell at 25 mM whilst [Bi^{3+}] was increased to 15 mM. In total, three new solutions were tested with the VPX-20 anion exchange membrane and compared to the standard solution:

(I) 0.7 M Pb^{2+} and 1.0 M MSA

(II) VPX20 membrane: 1.2 M Pb^{2+} and 0.5 M MSA (negative) / 1.2 M Pb^{2+} and 0 M MSA (positive)

(III) As (II), with 5 mM HDTMA (negative) / 15 mM Bi^{3+} and 25 mM F^- (positive)

(IV) As (II), with 1 g dm^{-3} sodium lignosulfonate (negative) / 15 mM Bi^{3+} and 25 mM F^- (positive)

The 9 cm^2 static cell and the previously described cycling regime were again employed to test these three new electrolytes, and the results are presented in Table 7.3.

Electrolyte	Cycle Life	% Q Eff	% V Eff	% En Eff	% Pb^{2+} Use
I	48	81	72	58	80
II	66	84	67	56	55
III	132	89	69	61	73
IV	104	83	68	57	90

Table 7.3: Static cell cycle life, efficiency and % Pb^{2+} utilisation of four different electrolytes. Separator: VPX-20. Electrode: 9 cm^2, carbon/polyvinyl ester. Cycling regime: 15 mins charge at 15 mA cm^{-2}, 3 mins rest, discharge to 0.3 V (or max 15 mins) at 15 mA cm^{-2}, 3 mins rest. Temperature: 296 K (no active temperature control).

The performance of composition (II) began like a typical static cell, no-additive test from Section 7.2. Its charge efficiency began and remained above 70% until failure at cycle 66, comparable to the previously best performing composition, which consisted of 0.7 M Pb^{2+} and 1.0 M MSA, with 10 mM Bi^{3+}. In Table 7.1, the 1.25 M Pb^{2+} and 0.5 M test only utilised 29 % of the solvated Pb^{2+} species. In (II), which began with 1.2 M Pb^{2+}, 55% of the solvated Pb^{2+} species was utilised.

A substantial improvement was further achieved when additives were introduced into the cell. The cycle life of (II) was doubled to 132 cycles in (III), which used HDTMA in the negative half-cell, and Bi^{3+} and F^- in the positive. The average charge efficiency across these cycles was also higher, at 89%; however, the first cycle had a charge efficiency of only 10%, increasing to >70% by the 5^{th} cycle. Cycles 14 - 102 then cycled at >90% charge efficiency. A similar pattern was observed in (IV) as well. There is good improvement when using lignosulfonate as well.

By tailoring the initial MSA concentration in each half-cell and by using additives, the % Pb^{2+} utilisation has increased to high levels (>73%) and the efficiency has also improved. This has greatly prolonged the cell lifetime and it now remains to test composition (III) and (IV) in flow cells.

7.4 Summary

The 9 cm^2 cell was used to test numerous static electrolyte compositions using a 15 mins, 15 mA cm^{-2} charge/discharge cycling program. In summary, from the three sections of this chapter:

1. Initial cycling tests with the 9 cm^2 cell, without additives or separators, investigated the optimal combination of [Pb^{2+}] and [MSA] on the cell efficiency and lifetime, as well as the Pb^{2+} utilisation. The combination of 0.7 M Pb^{2+} and 1.0 M MSA was found to be the most efficient, achieving 48 cycles with an average charge efficiency of 81% and a high Pb^{2+} utilisation of 80%. This was closely followed by the 1.25 M Pb^{2+} and 0.25 M MSA test, which achieved 46 cycles with an average charge efficiency of 85%. However, the level of Pb^{2+} utilisation was low, at just 34%.

2. The 0.7 M Pb^{2+} electrolyte was then tested with various additives and separators, where the addition of 10 mM Bi^{3+} improved the cell performance to 65 cycles at an average charge efficiency of 86%, whilst improving the % Pb^{2+} utilisation to 92%. The performance was not as good when a separator was used to confine the Bi^{3+} in just the positive half-cell, suggesting that at this scale, bismuth has some positive influence at the negative electrode. However, when this was repeated at an increased concentration of 15 mM and the FF60 separator, the cell performance was comparable to the 10 mM Bi^{3+}, undivided test. From these studies, 10 - 15 mM is the optimal concentration of Bi^{3+}.

3. The cell was then divided with the VPX-20 membrane and [Pb^{2+}] was increased to 1.2 M in each half-cell. However, the initial MSA concentration was varied, at 0.5 M and 0 M in the negative and positive half-cell respectively. This was seen to improve the performance of the cell, but the most dramatic improvement was observed when additives were introduced. 5 mM HDTMA was added to the negative half-cell, and 15 mM Bi^{3+} and 25 mM F^- were added to the positive; the cell then operated for 132 cycles with an average charge efficiency of 89% and 73% Pb^{2+} utilisation. It is recommended that the VPX-20 membrane, the additives HDTMA, lignosulfonate, Bi^{3+} and F^-, and the following electrolytes are tested in a flow cell configuration:

(I) 0.7 M Pb^{2+} and 1.0 M MSA

(II) 1.2 M Pb^{2+} and 0.5 M MSA (negative) / 1.2 M Pb^{2+} and 0 M MSA (positive)

0.7 M - 1.25 M appears to be the most suitable Pb^{2+} starting concentration range for the soluble lead system. In addition, 0.25 M - 1.0 M appears to be the most suitable MSA concentration. As [Pb^{2+}] is increased towards 1.25 M, [MSA] must be decreased towards 0.25 M.

Chapter 8

Flow Cell Cycling

8.1 Cell Configuration

In the literature, the soluble lead flow cell has only been tested in its standard, undivided format, but separator-divided soluble lead *static* cells were introduced by Wallis and Wills [32]. There has been no clear report of a separator-divided soluble lead flow cell. In the previous chapter, a series of separator-divided soluble lead static cells were investigated, building on the work by Wallis and Wills. The undivided, novel 'semi-divided' and fully-divided cell configuration are explored further in this chapter using a 9 cm^2 flow cell through a series of galvanostatic charge/discharge cycles. These designs are illustrated in Figures 8.1, 8.2 and 8.3 respectively. The effect of additives in flowing electrolytes are also studied.

Presented in Figure 8.1 is the standard, undivided soluble lead flow cell design, which does not use a separator. This is the traditional design whose performance has been shown to be limited by the effects of abnormal deposit growths making contact. However, the lack of a separator means that it remains the cheapest and simplest to assemble.

The semi-divided configuration, illustrated in Figure 8.2, divides the cell using a separator, but like in the undivided set-up, the same electrolyte flows through each half-cell. This provides the benefits of fewer tanks, pumps and pipes compared to a fully-divided system, whilst offering a physical barrier to deposit growth in the cell. As ion crossover is not an issue here, a cheap microporous separator, such as the FF60, could be used. There is also no

concern of differing levels of Pb^{2+} flowing through each half-cell. However, as in the undivided case, electrode-specific additives cannot be used as the same electrolyte passes through each half-cell.

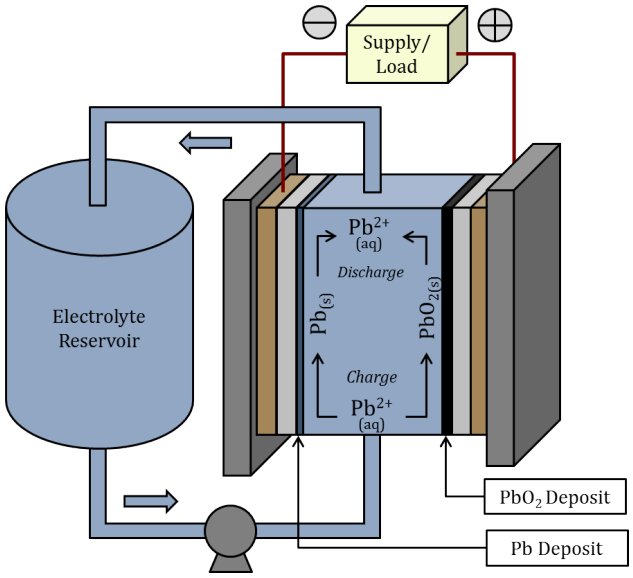

Figure 8.1: Undivided soluble lead flow cell configuration

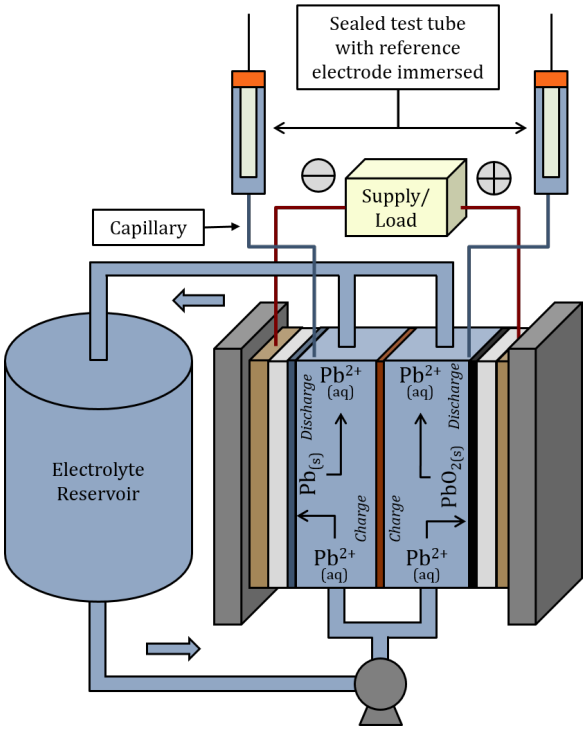

Figure 8.2: Semi-divided soluble lead flow cell configuration. A separator divides the half-cells but the same electrolyte is circulated through each side. Hg/HgO reference electrodes were used to measure individual electrode potentials (Chapter 8.3.3).

Figure 8.3 presents the schematic of the fully-divided system; this is the general redox flow cell format, used in the VRFB and ZBFB. The cell is divided with a separator, allowing the use of electrode-bespoke electrolyte compositions. Electrode-specific additives can also be confined in the target half-cell without interfering with the reactions at the other side. Additionally, the separator also acts as a barrier to shorting. However, in practice crossover of some species is inevitable in the long run, and inefficiencies can cause [Pb^{2+}] imbalance between the half-cells.

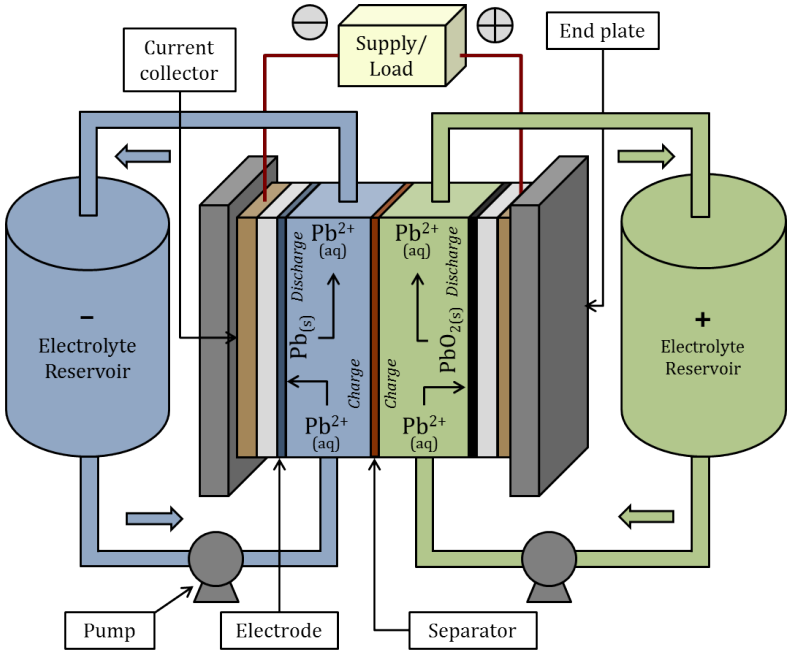

Figure 8.3: Fully-divided soluble lead flow cell configuration. A separator divides the half-cells and two different electrolytes can be circulated through the cell.

8.2 Experimental Procedure

Each experiment, aside from those that were fully-divided, used a fresh 200 cm^3 of electrolyte stored in one Erlenmeyer flask. The fully-divided configuration used two Erlenmeyer flasks, each holding a fresh 100 cm^3 of electrolyte.

The galvanostatic cycling regime was designed to rapidly screen several combinations of electrolyte and separator. Firstly, 20 charge/discharge cycles were implemented. Each cycle began with a charge phase for 63 mins at 20 mA cm^{-2}, followed by a 3 mins rest period

to record the open circuit potential after charge. The cell was then discharged to 0.7 V, or for a maximum of 63 mins, at the same current density. Lastly, another 3 mins rest period was applied to measure the open circuit potential after discharge. Using Faraday's Law, the charge supplied on each charging phase was calculated to amount to a 5% Pb^{2+} utilisation when using 200 cm^3 of a solution initially containing 0.7 M Pb^{2+}, assuming ϕ=1.

Following these 20 cycles, the experiment was continued (with no break in between) with the current density being incremented and the charge/discharge time shortened on each subsequent cycle in order to amount to a 10% Pb^{2+} level of utilisation. For example, cycle 22 charged the cell at 35 mA cm^{-2} for 71 mins, whilst cycle 23 charged at 50 mA cm^{-2} for 50 mins. The charge supplied during each cycle's charging phase would have theoretically been enough to deposit 0.014 moles of Pb^{2+} onto the electrodes (0.007 moles onto each electrode respectively). 0.014 moles is 10% of the total solvated moles of Pb^{2+} at the start of the experiment, as 0.7 mol dm^{-3} × 0.2 dm^3 = 0.14 moles. This second phase of cycling was designed to test the resilience of the system to the failure mechanisms accelerated by the higher currents, such as dendrite growth, lead dioxide creep and the effect of poor deposition quality on charge efficiency. Table 8.1 summarises the testing procedure.

Cycle	**Charge/Discharge** j **/ mA** cm^{-2}	**Charge/Discharge T / mins**
1-20	20	63
21	20	125
22	35	71
23	50	50
24	65	38
25	80	31
26	100	25
27	115	22
28	130	19
29	150	17

Table 8.1: The cycling regime applied to the 9 cm^2 flow cell experiments. The charge phase in cycles 1 - 20 utilised 5% Pb^{2+}, whilst 10% Pb^{2+} is utilised in all the following cycles.

Furthermore, in order to allow comparability of results, these parameters were kept the same even for tests that had an initial Pb^{2+} concentration different to 0.7 M. The flow rate in all experiments was maintained at 2.3 cm s^{-1} across each electrode surface, equivalent to 4.48 cm^3 s^{-1}. Experiments took place under ambient temperature, 296 K, with no active temperature control.

8.3 Results

8.3.1 Undivided vs. Semi-divided vs. Fully-divided

Four experiments are presented in this section. The electrolyte for each experiment initially contained 0.7 M Pb^{2+} and 1.0 M MSA. The VPX-20 membrane was used in all experiments where a separator was required. Where additives were used, 1 g dm^{-3} sodium lignosulfonate and 15 mM Bi^{3+} were in solution. In the fully-divided format, the lignosulfonate was added only to the negative Erlenmeyer flask, with the bismuth only added to the positive.

The 9 cm^2 flow cell was configured in the undivided, semi-divided and fully-divided formats, and the electrolyte in each contained additives. A fourth experiment using the semi-divided configuration was also conducted that did not use additives in order to study the effect of the additives. Each in turn was subjected to the galvanostatic cycling regime with the cell being dismantled, washed and cleaned before being reassembled with fresh electrolyte and polished electrodes at the start of the test. Figure 8.4 presents the charge and voltage efficiencies of the first 20 cycles.

With additives present, the charge efficiency is seen to be initially low, before gradually improving and achieving >90% by the 10^{th} cycle; this behaviour was also reported with the static cells (Chapter 7). The behaviour across the early cycles could be due to an inhibition of deposition caused by the additives. Alternatively, the initial deposit layers may be more resistive to stripping, or the additives could have been involved in side reactions, i.e. ϕ <1.

The undivided configuration performs slightly better than the other formats over the first 6 cycles. However, by the 10^{th} cycle, a sudden drop in performance is observed. In every

cycle after this point, the potential-time profile of the undivided experiment showed signs of electrical shorting during the charge phase as a result of the contact between lead and lead dioxide deposits. The charge efficiency suddenly drops due to a lack of deposition but the voltage efficiency remains fairly constant, averaging 60% across the 20 cycles. When the cell was dismantled, there were clear signs of deposit contact following growth along the lower surface of the internal cell wall. Similar growths were observed in the separator-divided experiments but contact had been prevented by the separator (discussed later in Chapter 8.3.5).

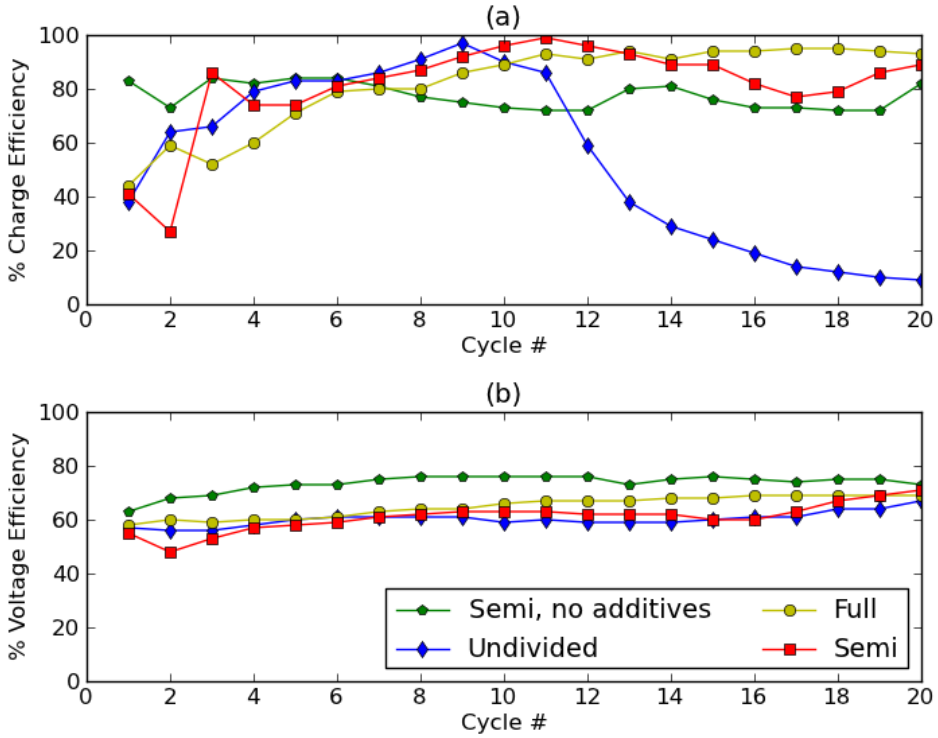

Figure 8.4: Cycles 1 - 20 of the separator configurations comparison study. The efficiency of each cycle is presented: (a) charge, (b) voltage. Electrolyte: 0.7 M Pb^{2+} and 1.0 M MSA. Additives (where applicable): 15 mM Bi^{3+} and 1 g dm^{-3} lignosulfonate. Separator: VPX-20. Electrode: 9 cm^2, carbon/polyvinyl ester. Cycling regime: 63 mins charge at 20 mA cm^{-2}, 3 mins rest, discharge to 0.7 V (or max 63 mins) at 20 mA cm^{-2}, 3 mins rest. Electrolyte volume: 200 cm^3. Flow rate: 2.3 cm s^{-1}. Temperature: 296 K.

In the absence of additives, the charge efficiency at the 1st cycle was 83%, approximately twice that of the other tests. There is not much variation in efficiency over the whole 20 cycles. The separator successfully prevents any shorting from occurring but charge efficiencies above 90% are not seen and the average is only 77%, which is not suitable for long-term

operation, as Pb^{2+} would soon be depleted from the electrolyte. The voltage efficiencies of the three configuration tests are comparable and show little variation with cycle number, averaging 63% (due to the wide inter-electrode gap, there was not much difference in voltage efficiencies). Without additives, this improves to 73%, so that overall the average energy efficiencies across the 20 cycles of all experiments, aside from the undivided, are similar, at 50%, 54% and 57% for the fully-divided, semi-divided, and semi-divided with no additives respectively. The graphs in Figure 8.5 present the second stage of the experiment, where the charging/discharging current is incremented.

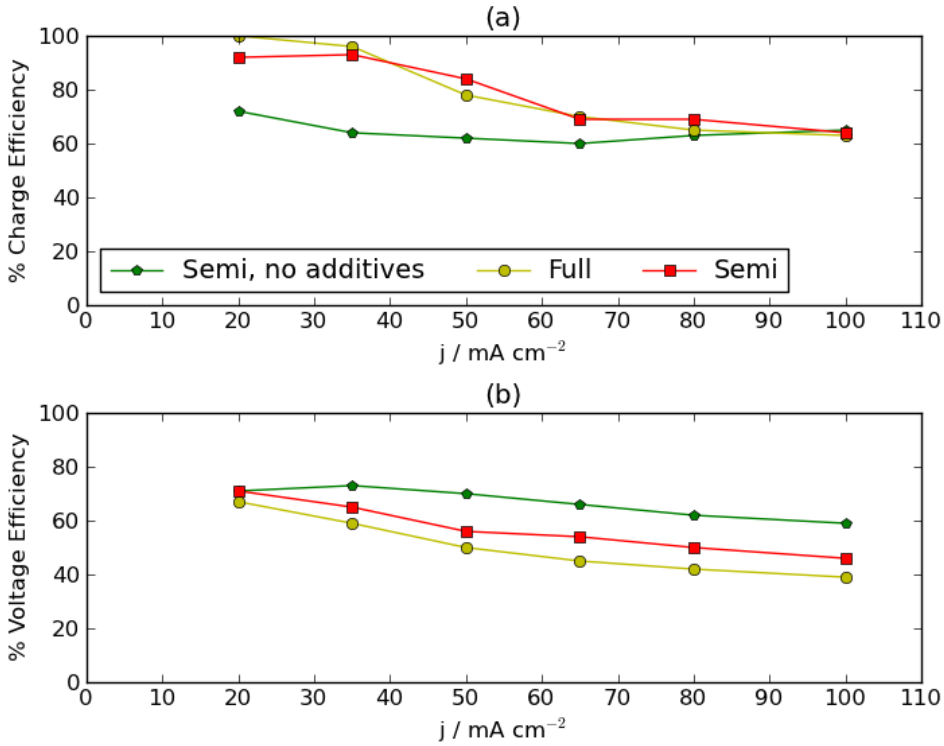

Figure 8.5: Cycles 21 - 29 of the separator configurations comparison study, where the current density is incremented from 20 to 150 mA cm^{-2}. The efficiency of each cycle is presented: (a) charge, (b) voltage. Electrolyte: 0.7 M Pb^{2+} and 1.0 M MSA. Additives (where applicable): 15 mM Bi^{3+} and 1 g dm^{-3} lignosulfonate. Separator: VPX-20. Electrode: 9 cm^2, carbon/polyvinyl ester. Electrolyte volume: 200 cm^3. Flow rate: 2.3 cm s^{-1}. Temperature: 296 K.

As the current is increased from 20 to 150 mA cm^{-2} between cycles 21 and 29, the charge efficiency decreases in the experiments involving additives. Performance is generally good, with >70% achievable when operating below 65 mA cm^{-2}. Even 58% is achieved at 150 mA

cm^{-2}, suggesting that the SLFB could operate for short durations at high currents, which would be ideal for a renewables capacity firming application. From these experiments, there is no clear difference between a semi-divided or fully-divided system in terms of efficiency, despite reports of lignosulfonate adversely affecting the charge efficiency and overpotentials at both electrodes [33].

The charge efficiency does not appear to significantly vary with current density in the absence of additives, averaging 64% across the current increment cycles. At lower current densities, the performance of the semi-divided, no-additive test is significantly lower than the other two tests, only becoming comparable past 80 mA cm^{-2}. This is likely due to the effect of thick deposits forming across all the cycles before the 80 mA cm^{-2} cycle as a result of the low charge efficiencies. There would therefore be more to strip on discharge in the latter cycles than what was deposited during charge in those latter cycles. Furthermore, because H^+ increases as Pb^{2+} decreases in solution, the no-additive electrolyte at the end of 20 cycles is likely to be more conductive than the tests with additives. This would explain the higher voltage efficiencies of the no-additive test that are seen during the current increment cycles.

The voltage efficiency follows a decreasing trend in the semi-divided and fully-divided tests, from approximately 70% at 20 mA cm^{-2}, down to 42% and 33% at 150 mA cm^{-2} for the semi and fully-divided tests respectively. With additives, it is not clear why the semi-divided test offers a better voltage efficiency than the fully-divided test (by roughly 8 percentage points on average), but this leads to slightly greater energy efficiencies in the semi-divided cell at all current densities higher than 20 mA cm^{-2}.

Over the initial 20 cycles and the later current increment tests, in all the tests with additives, there appears to be a voltage efficiency penalty but an improved charge efficiency. This would translate into a longer cycle life, offsetting the disadvantage of a slight reduction in overall energy efficiency. Furthermore, the beneficial effect of the additives on the deposit morphology, which is directly linked to cycle life, can be seen in Figure 8.12.

The amber colour of the solution containing lignosulfonate in all tests retained this colour at the end of the first 20 cycles. In the fully-divided experiment, the lignosulfonate-containing negative electrolyte remained amber and the positive electrolyte remained transparent at the end of the current increment cycles (i.e. at the end of cycle 29), suggesting little crossover

of lignosulfonate throughout the duration of the test (approximately 3.5 days). However, the electrolyte in the lignosulfonate-containing semi-divided experiment was observed to change colour close to transparent after the current increment cycles. This is likely due to certain functional groups being oxidised at the positive electrode, as previously reported [53]. Despite this, it is still not clear whether this leads to a deterioration in lignosulfonate's ability to control the lead deposit.

The semi-divided test was repeated a third time with 5 mM HDTMA replacing the lignosulfonate. The efficiencies were similar to the lignosulfonate semi-divided test. However, the HDTMA created an extremely foamy solution and it was difficult to prevent bubbles from entering the cell. After also considering its high cost, it was ruled out at this stage and future studies used lignosulfonate as the favoured surfactant for the negative electrode.

8.3.2 Separators

The semi-divided, with additives test was repeated using the FF60 and Nafion 115 separators. There was little difference across the initial 20 cycles amongst the three. There was also little difference between the efficiencies during the current increment stage between VPX-20 and Nafion 115, despite VPX-20 recording a considerably lower potential drop in Chapter 4. It is likely that the potential drop across the large inter-electrode gap dwarves the drop across the separator, leading to similar voltage efficiencies. The FF60 separator however was punctured at cycle 23, as seen by the shorting noise in the potential time response and the poor charge efficiencies in later cycles. The puncture line was close to the cell chamber boundary, beyond which the separator is compressed between the flow chambers. FF60 is made of a brittle material and the stress of compression could create a weak zone near the compression boundary, which could be exploited by deposit growth.

8.3.3 Measurement of the Electrode Potentials

The individual electrode potentials were recorded for the reported VPX-20 semi-divided tests, with and without additives. The experimental set-up is shown in Figure 8.2 and the reference electrodes used were Hg/HgO. Figure 8.6 presents the potential-time responses of both

electrodes and the cell over the initial 20 cycles as well as the subsequent current increment stage of the semi-divided test with additives. The recorded cell potential should be exactly the difference between each electrode potential. However, a slight discrepancy can be seen, and this is due to the potential loss across the electrolyte along the length of the capillary. Additionally, bubbles in the system temporarily blocked the capillary from time to time.

This is the first reported potential measurement of a semi-divided soluble lead flow cell cycling test, with lignosulfonate and Bi^{3+} present in solution. The general shape of the potential-time response is similar to those seen in the literature (Chapter 2.5.5). The cell potential on charge decreases with cycle number, typically commencing at around 2 V before rising to 2.2 V. The cell potential on discharge slightly improves with cycle number, commencing at 1.4 V at the 1^{st} cycle and commencing at 1.55 V at the 20^{th} cycle.

The cell potential on charge is defined by the shape of the positive electrode potential, which seems to follow the shape reported in the literature. Over the first 8 cycles, the cell potential on discharge appears to be limited by both electrodes' potential. Firstly, the negative sees a double potential plateau. The first plateau is very close to the charging potential, -0.5 V vs. SCE, and this rises sharply halfway through discharge to the second plateau at around 0 V vs. SCE. This causes a sharp drop in the cell potential, but the cut-off at 0.7 V is only crossed when the positive potential then begins to fall.

The second plateau region gradually diminishes beyond cycle 8, where it eventually takes the shape of a sharp rise in potential. Beyond cycle 8, the reduction of lead dioxide at the positive electrode appears to be a more stable reaction than the oxidation of the lead-bismuth alloy at the negative electrode. The positive discharge potential remains relatively constant initially, with a gradual decrease towards the end of discharge. In later cycles, this becomes more of a gradual, linear decrease in potential.

The negative potential response aligns with the voltammetry evidence (Chapter 6), where bismuth was seen to deposit at more positive potentials than lead. The first potential plateau likely arises from lead oxidation whilst the second from bismuth oxidation, or of a lead-bismuth alloy. The potentials at which they occur also align with the oxidation potentials seen in the voltammograms.

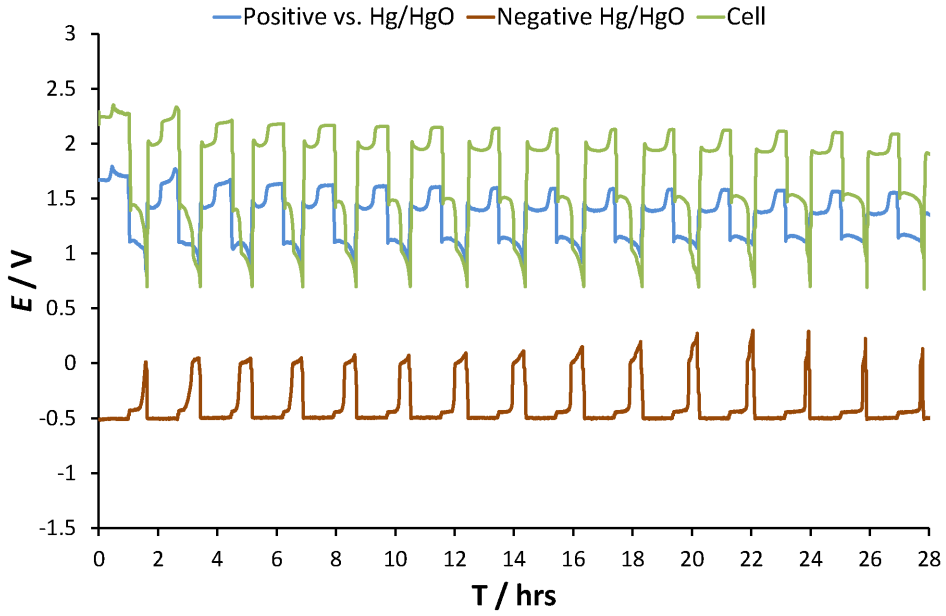

(a)

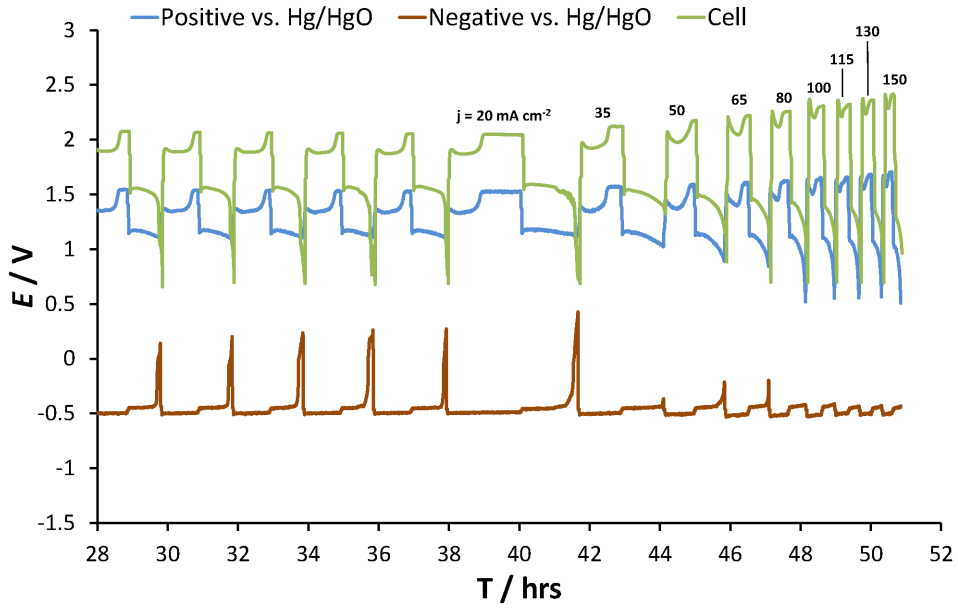

(b)

Figure 8.6: Individual electrode potentials from the semi-divided, with additives test seen in Figures 8.4 and 8.5. (a) Cycles 1 - 15, where j = 20 mA cm^{-2} and charge time = 63 mins. (b) Cycles 16 - 20, where j = 20 mA cm^{-2} and charge time = 63 mins, and cycles 21 - 29, where the current density is incremented from 20 to 150 mA cm^{-2}. Electrolyte: 0.7 M Pb^{2+} and 1.0 M MSA. Additives: 15 mM Bi^{3+} and 1 g dm^{-3} lignosulfonate. Separator: VPX-20. Electrode: 9 cm^2, carbon/polyvinyl ester. Electrolyte volume: 200 cm^3. Flow rate: 2.3 cm s^{-1}. Temperature: 296 K.

Furthermore, as deposits accumulate with time, layers of bismuth could become trapped un-

der layers of lead (or sealed as an alloy with lead), and this depletion is the likely cause of the narrowing of the second negative potential plateau. When the current is incremented, the voltage efficiency drops. This can be seen by the rising cell potential on charge and the decreasing cell potential on discharge. This pattern almost entirely arises from the positive potential, which now becomes the limiting electrode. The negative potential profile in comparison does not appear to vary significantly as the current is increased.

Figure 8.7 presents the individual electrode potential-time response of the first 14 cycles of the semi-divided test with no additives.

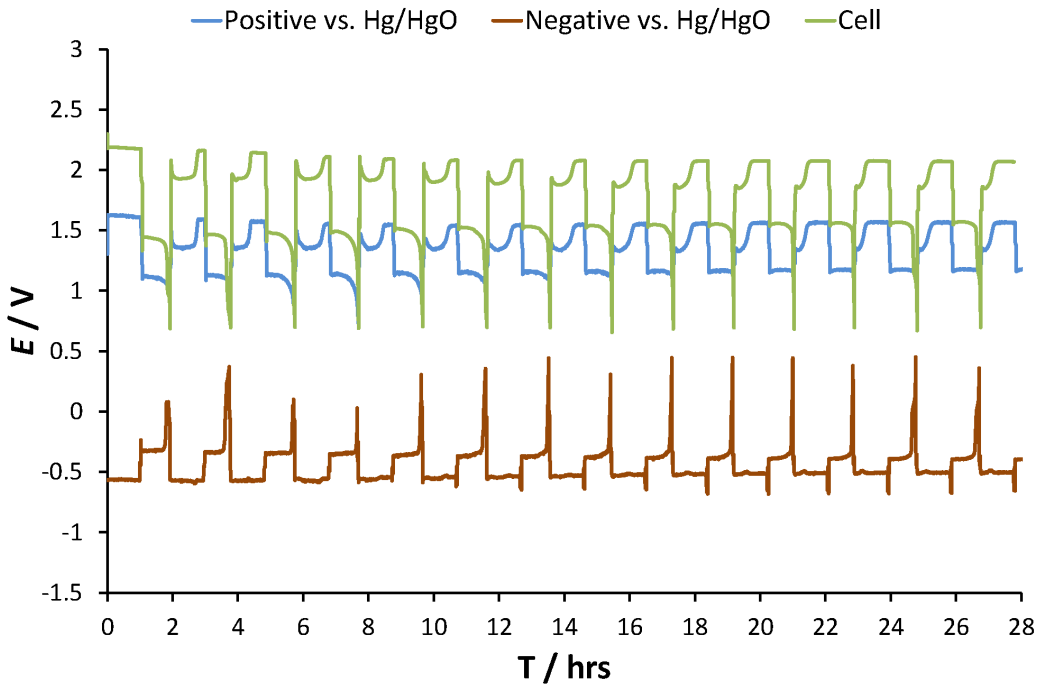

Figure 8.7: Individual electrode potentials from the semi-divided, no-additive test seen in Figures 8.4 and 8.5. Cycles 1 - 14 are shown, where j = 20 mA cm^{-2} and charge time = 63 mins. Electrolyte: 0.7 M Pb^{2+} and 1.0 M MSA. Separator: VPX-20. Electrode: 9 cm^2, carbon/polyvinyl ester. Electrolyte volume: 200 cm^3. Flow rate: 2.3 cm s^{-1}. Temperature: 296 K.

With zero bismuth, there is no double negative potential plateau during discharge. The limiting electrode is still the negative however, as seen by the sharp potential spike signalling the end of discharge. Previous discussions have placed the discharge limitation at the positive electrode, particularly the difficulty in reducing the lead dioxide deposits. However, here it is clearly seen that the positive potential-time response on discharge is smooth and flat whilst it is the negative potential that causes the sudden drop in cell potential.

Figure 8.8 compares the potential profile of cycle 5 from the semi-divided, 1 g dm^{-3} lignosulfonate and 15 mM Bi^{3+} test (from Figure 8.6) and the semi-divided, no-additive test (from Figure 8.7). Figures 8.9a and 8.9b compare the variation in the potential profile of the negative and positive electrodes in cycle 5 respectively.

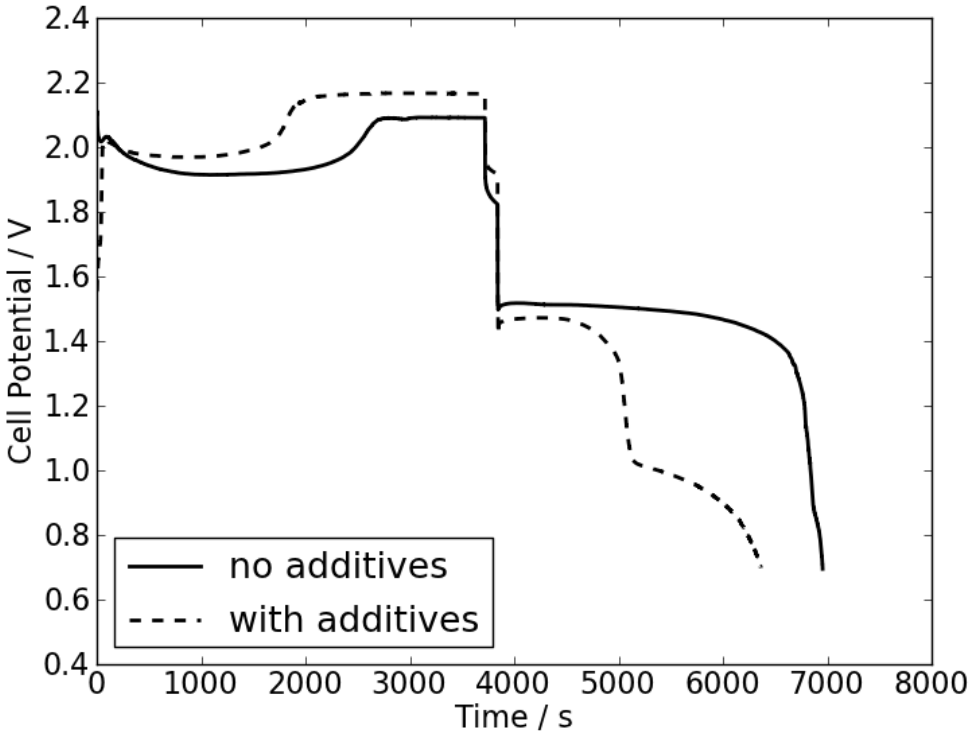

Figure 8.8: Comparison of cycle 5 from Figures 8.6 and 8.7. The cell potential with and without additives are shown. Semi-divided system.

The difference in the potential-time profile can clearly be seen. The main variation is seen in discharge, where at 5000 s, the potential suddenly falls to 1.0 V (with additives) where a second discharge curve begins. The additives cycle has a charge efficiency of 74%, whereas 84% is obtained without additives. By looking at Figure 8.9a, it can be seen that this limitation originates at the negative electrode: discharge at -0.4 V vs. Hg/HgO lasts for only 1000 s, before increasing to 0 V vs. Hg/HgO at 5000 s. The effect of Bi^{3+} improving the charge transfer kinetics at the positive electrode (seen in cyclic voltammetry, Chapter 6) is not recorded. Instead, the opposite is observed: the potential with additives is higher by a maximum of 0.2 V than the potential without additives. On discharge, it is lower at most by 0.7 V.

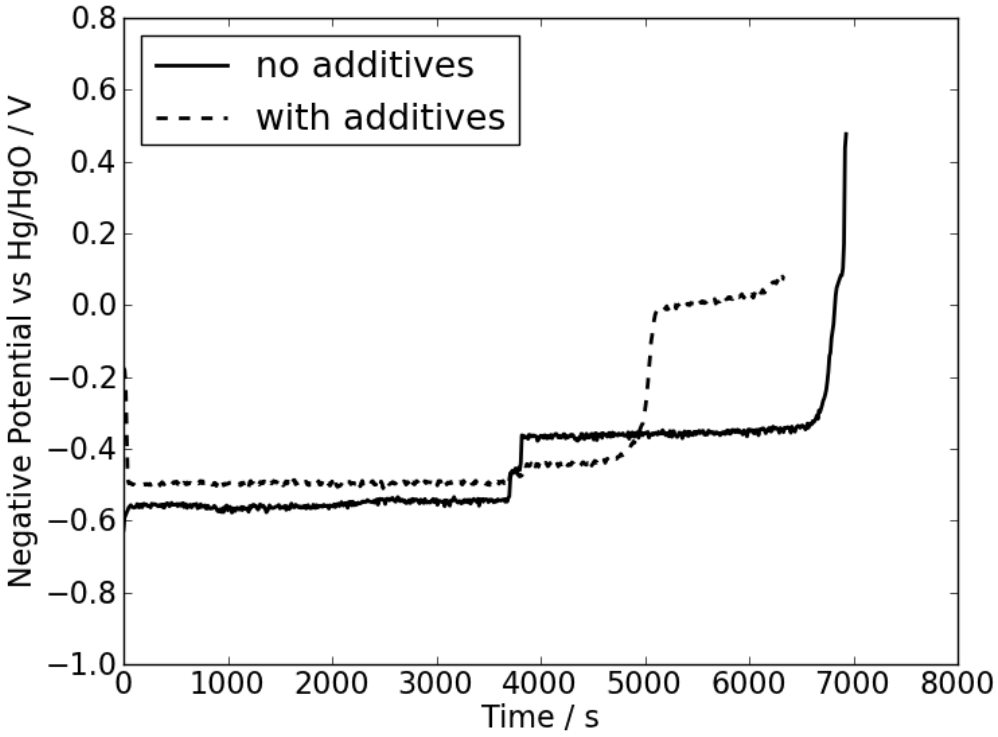

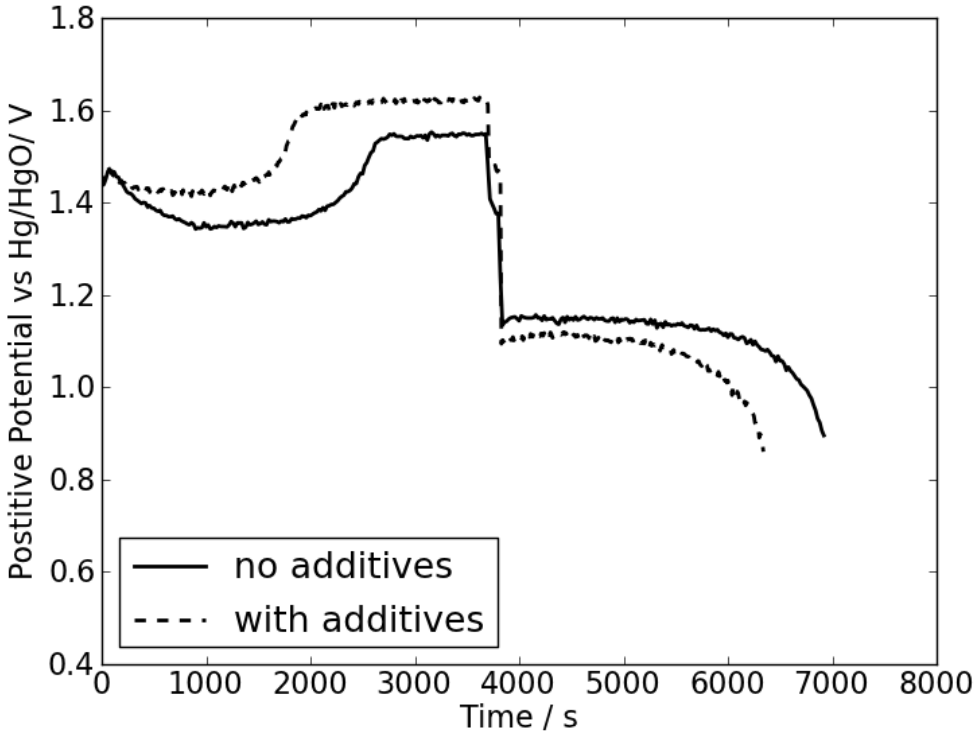

(b)

Figure 8.9: Comparison of cycle 5 from Figures 8.6 and 8.7. The (a) negative and (b) positive potentials with and without additives are shown. Semi-divided system.

The voltage efficiency with additives is just 58%, whereas 73% is achieved without additives. The lower voltage efficiency is a sign of slower kinetics, which is likely caused by the oxidation of lignosulfonate at the positive electrode (reported previously in [33]). It can be concluded that in the semi-divided system, during the early cycles, Bi^{3+} has a more detrimental effect at the negative electrode than a beneficial effect at the positive. Likewise, lignosulfonate has a more detrimental effect at the positive electrode than a beneficial effect at the negative. The semi-divided system either is not practical when either of these additives is present in solution. Either a fully-divided system should be used with these additives, or new additives selected for the semi-divided configuration.

8.3.4 Further Electrolyte Compositions in the Fully-Divided System

Three further electrolyte compositions were trialled in the fully-divided format using the same galvanostatic cycling regime as in the previous section. The VPX-20 membrane was again used in each experiment, and the other parameters remained unchanged. These compositions were:

(I) VPX20 membrane: 1.2 M Pb^{2+} and 0.5 M MSA (negative) / 1.2 M Pb^{2+} and 0 M MSA (positive)

(II) As (I), with 1 g dm^{-3} sodium lignosulfonate (negative) / 5 mM Bi^{3+} and 10 mM F^{-} (positive)

(III) 0.7 M Pb^{2+} and 1.0 M MSA (in both half-cells), with the same additives as in (II)

Composition (I) was trialled in the 9 cm^2 static cell and reported in Chapter 7. Composition (II) was also trialled, but here the additive concentrations are reduced. Figure 8.10 presents the charge and voltage efficiencies of the first 20 cycles.

With no additives in solution (composition I), the performance appears to follow the same trend as the semi-divided and fully-divided experiments, both with additives, in Chapter 8.3.1. The charge efficiency is initially low, fluctuating up and down, before reaching a steady state above 90% by the 6^{th} cycle. This behaviour was previously attributed to the presence of additives inhibiting deposition on charge; however, no additives were present here. Therefore, it is likely that this behaviour is caused by a low MSA concentration, as

the positive half-cell initially contained 0 M MSA. The mechanism of lead dioxide reduction (i.e. discharge) requires the presence of H^+, as previously discussed in the literature review. An insufficient concentration would prevent thorough dissolution, resulting in a low charge efficiency. After several cycles of deposit accumulation, the H^+ concentration would become high enough for more effective stripping of lead dioxide. Future work will need to repeat this experiment whilst measuring the individual electrode potentials to confirm this theory.

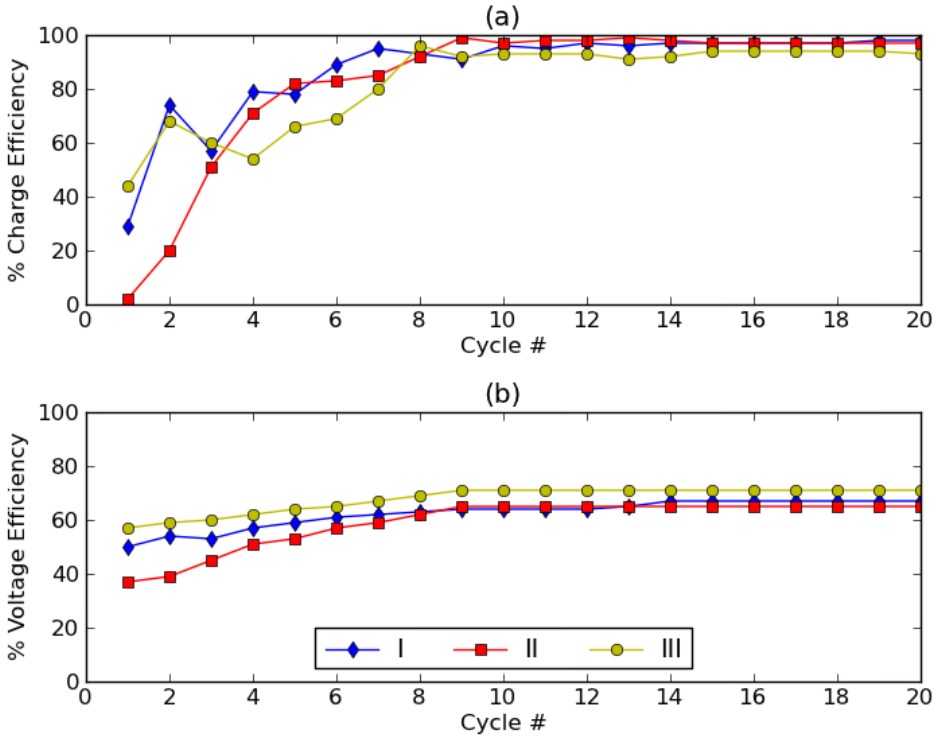

Figure 8.10: Cycles 1 - 20 of the electrolyte comparison study (all fully-divided). The efficiency of each cycle is presented: (a) charge, (b) voltage. Electrolyte: (I) 1.2 M Pb^{2+} and 0.5 M MSA (negative) / 1.2 M Pb^{2+} and 0 M MSA (positive); (II) As (I), and including 1 g dm^{-3} sodium lignosulfonate (negative) / 5 mM Bi^{3+} and 10 mM F^- (positive); (III) 0.7 M Pb^{2+} and 1.0 M MSA (in both half-cells), with the same additives as in (II). Separator: VPX-20. Electrode: 9 cm^2, carbon/polyvinyl ester. Cycling regime: 63 mins charge at 20 mA cm^{-2}, 3 mins rest, discharge to 0.7 V (or max 63 mins) at 20 mA cm^{-2}, 3 mins rest. Electrolyte volume: 200 cm^3. Flow rate: 2.3 cm s^{-1}. Temperature: 296 K.

When additives are used (composition II), their presence and the low initial MSA concentration results in an extremely low charge efficiency on the 1st cycle, at just 2%. This rises to, and remains above, 95% by the 9th cycle. The voltage efficiency for composition (I) is initially higher than that of composition (II) but becomes comparable by the 8th cycle, both averaging approximately 60%. The charge efficiency of composition (III) is initially inferior to

that of (I), but becomes comparable by the 8th cycle. The voltage efficiency of (III) however is superior throughout, averaging 68%. Overall across the 20 cycles, the energy efficiencies are comparable, averaging 55% (I), 51% (II) and 57% (III). Figure 8.11 presents data from the current density increment stage.

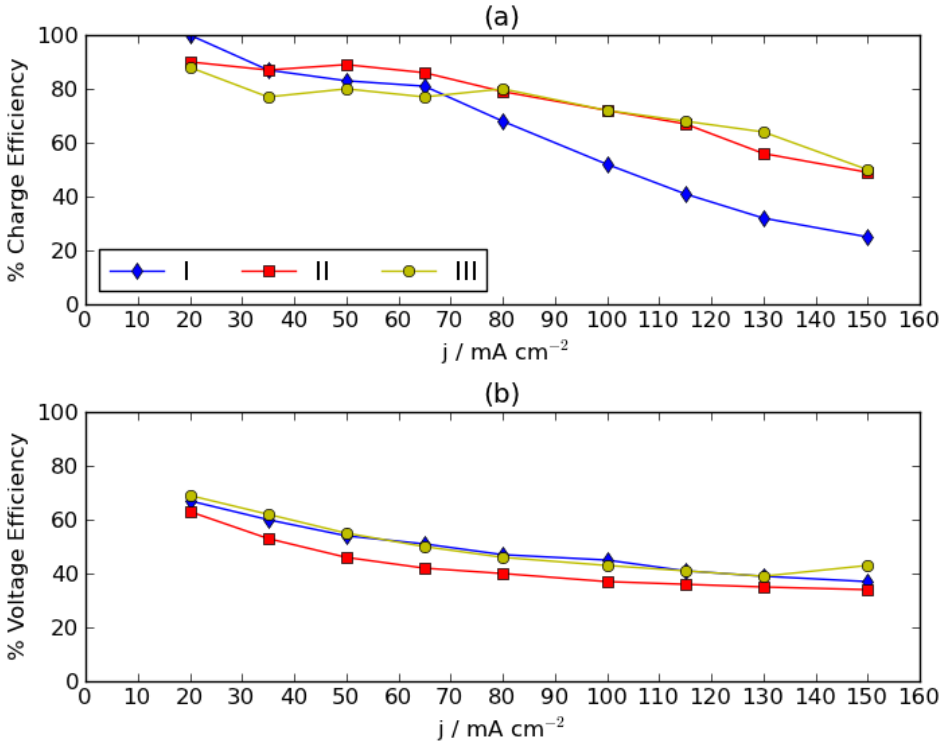

Figure 8.11: Cycles 21 - 29 of the electrolyte comparison study, where the current density is incremented from 20 to 150 mA cm^{-2}. The efficiency of each cycle is presented: (a) charge, (b) voltage. Electrolyte: (I) 1.2 M Pb^{2+} and 0.5 M MSA (negative) / 1.2 M Pb^{2+} and 0 M MSA (positive); (II) As (I), and including 1 g dm^{-3} sodium lignosulfonate (negative) / 5 mM Bi^{3+} and 10 mM F^{-} (positive); (III) 0.7 M Pb^{2+} and 1.0 M MSA (in both half-cells), with the same additives as in (II). Separator: VPX-20. Electrode: 9 cm^2, carbon/polyvinyl ester. Electrolyte volume: 200 cm^3. Flow rate: 2.3 cm s^{-1}. Temperature: 296 K.

The similar trend of falling efficiency with rising current density is seen here. However from 80 mA cm^{-2} onwards, electrical shorting noise is observed in the potential-time response of composition (I), leading to the sharp drop in efficiency. No such noise is seen with composition (II), in which the additives were present; nor in (III), where [Pb^{2+}] was lower and additives were also present. Additionally in (II), at 50 and 100 mA cm^{-2}, the corresponding charge efficiency was 89% and 72%, which were the highest efficiencies seen in all tests at these current densities.

In Figure 8.11b, the voltage efficiency of composition (II) remains lower than that of (I). This was also seen in the previous section, where the semi-divided, no-additive test produced greater voltage efficiencies than the tests that used additives. The additives themselves therefore could be an impediment to ionic mobility, thus increasing the resistance of the solution.

At the end of the composition (II) test, accumulated PbO_2 deposits were removed and ground into a powder. This was then subject to an X-ray diffraction test using a Bruker D2 Phaser, CuKα radiation, diffractometer. The sample was found to consist of 86% β-PbO_2 and 14% α-PbO_2.

In conclusion, composition (II) compares well to (III), and both perform better with additives than without. In addition, (II) offers a higher energy density than (III) due to the higher Pb^{2+} concentration. The benefits of the additives are clearly seen at the higher current densities, and electrolytes based on these compositions appear to be well suited for further characterisation under more extensive cycling and in larger cells.

8.3.5 The Influence of Additives on Deposit Morphology

The deposits from the semi-divided, no additive test seen in Section 8.3.3, and the fully-divided, 1 g dm^{-3} sodium lignosulfonate (negative) / 5 mM Bi^{3+} and 10 mM F^- (positive) test seen in Section 8.3.4 (composition III) were examined after cycling. Both electrolytes used 0.7 M Pb^{2+} and 1.0 M MSA and the VPX-20 membrane. Following the final cycle (cycle 29, the last current increment cycle), each test was charged for a further 20 mins at 20 mA cm^{-2} before the experiment was halted. The cell was dismantled and the electrode surfaces were studied. Images of these electrodes can be seen in Figure 8.12.

Images (a) and (c) are from the no-additive test, which also show the flow chambers and the direction of flow through the cell, and (b) and (d) are from the test with additives. Because of the rocky nature of the thick Pb deposit in (a), it was not possible to remove the negative electrode away from the chamber without damaging the deposit. The deposit is thick, bridging the 1 cm gap between electrode and VPX-20 membrane, growing along the non-conducting flow chamber walls. The deposit surface appears to be flush in certain

places with the external face of the chamber, i.e. the membrane face, which had successfully prevented shorting in this test. However, the upper quarter of the electrode is not covered with deposit. The deposit is structurally weak and the porosity creates an uneven electrical connection between the deposit and the electrode, making it difficult to discharge. This would explain why the negative electrode was seen to be the cell potential-limiting electrode on discharge in Figure 8.7. In contrast, the Pb deposit is uniform and smooth in (b), where the electrolyte contained lignosulfonate. However, there is still some deposit growth along the lower flow chamber wall, near the cell outlet.

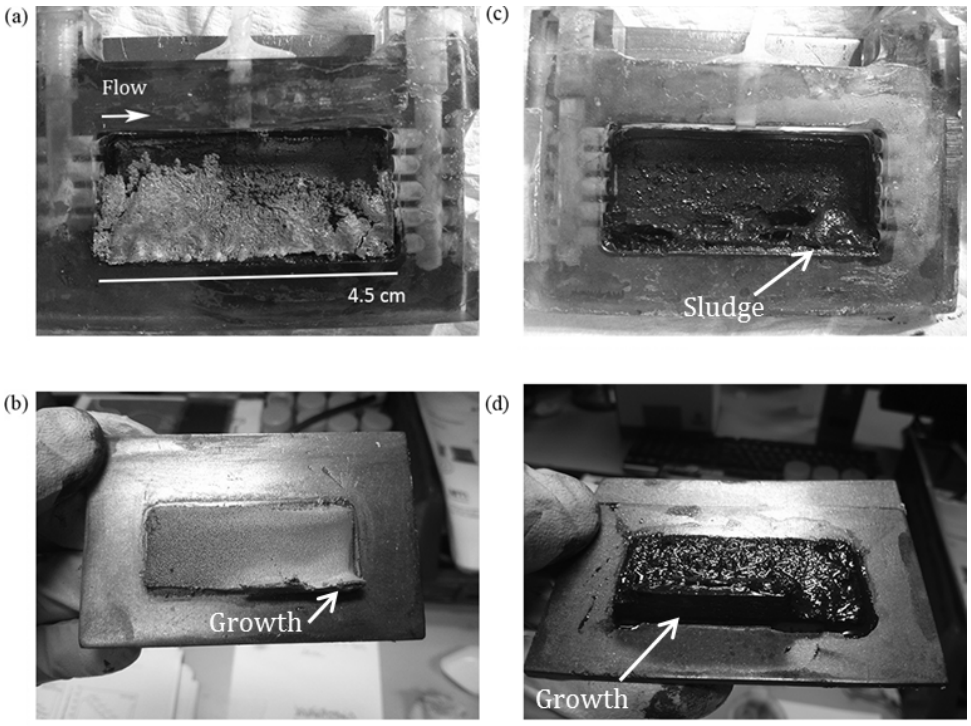

Figure 8.12: Electrode deposits produced after 20 mins of charging at 20 mA cm^{-2}, after following the galvanostatic cycling regime described in Table 8.1.(a) and (c): Pb and PbO_2 deposits respectively when additives were not used (semi-divided). (b) and (d): Pb and PbO_2 deposits when additives were used (fully divided). Electrolyte: 0.7 M Pb^{2+} and 1.0 M MSA. Separator: VPX-20. Electrode: 9 cm^2, carbon/polyvinyl ester. Electrolyte volume: 200 cm^3. Flow rate: 2.3 cm s^{-1}. Temperature: 296 K.

Similarly, the PbO_2 sludge amassed in the bottom right of the chamber in (c) also prevented the removal of the positive electrode. In the absence of additives, the PbO_2 appears to be thinly coating the upper two thirds of the electrode, mostly collecting in the lower third of the cell chamber. In contrast in (d), though there is some deposit growth along the

lower wall near the cell outlet, the electrode appears to be more evenly coated with PbO_2. Furthermore, there were far fewer black PbO_2 particles seen in the electrolyte reservoir when using additives. This is attributed to the presence of fluoride, which was previously reported and discussed to improve the adhesion of PbO_2 to the electrode [82].

8.4 Summary

The first example of a separator-divided soluble lead flow cell has been reported. Tests consisted of 20 cycles of approximately 1 hr charge/discharges at 20 mA cm^{-2}, followed immediately by a series of charge/discharges where the current was incremented from 20 to 150 mA cm^{-2}, with the charge/discharge time reduced accordingly to account for a 10% Pb^{2+} utilisation on each charge. In summary:

1. The VPX-20 membrane was used to create a fully-divided and semi-divided system, both of which produced better results than the standard undivided format by preventing contact between deposits. Only 11 of the initial 20 cycles were achieved before shorting in the undivided set-up.

2. Charge efficiencies across the current increment range for both semi and fully-divided tests decreased from 100% at 20 mA cm^{-2} to close to 60% at 150 mA cm^{-2} respectively. At this scale, the only difference between the semi and fully-divided tests was seen at the higher current densities (>20 mA cm^{-2}), where the voltage efficiency was recorded as slightly higher in the semi-divided case (on average by 8 percentage points).

3. The presence of additives (fully-divided: 1 g dm^{-3} lignosulfonate (-ve)/15 mM Bi^{3+} (+ve) and both mixed for semi-divided) initially limited the charge efficiency but this improved beyond cycle 6, remaining above 75% for the remainder of the 20 cycles. There is a clear voltage efficiency penalty ($\leq$12 percentage points) but an enhanced charge efficiency (especially at higher current densities) when using additives. This would result in a longer cycle life than an equivalent test without additives whilst producing comparable energy efficiencies.

4. Some concerns about stability were raised about the lignosulfonate and Bi^{3+} additives

in the semi-divided format. Electrolytes containing the former tended to become transparent throughout cycling, after having initially turned amber when lignosulfonate was first added. Whether this corresponds to degradation of the additive is unknown. From monitoring the negative electrode potential with and without additives in the semi-divided format, bismuth was seen to deposit at the negative electrode, which could potentially deplete the solution of the additive. However these issues did not affect the semi-divided cell's performance in these studies. Further, longer-term studies are needed to test the suitability of the additives in the semi-divided format.

The second electrolyte composition with an increased Pb^{2+} concentration in the fully-divided format was also trialled, producing promising results that invite further testing. This contained 1.2 M Pb^{2+} and 0.5 M MSA (negative) / 1.2 M Pb^{2+} and 0 M MSA (positive), and this was trialled with and without 1 g dm^{-3} sodium lignosulfonate (negative) / 5 mM Bi^{3+} and 10 mM F^{-} (positive). In summary:

1. The initial cycles again performed poorly even without additives, and this was attributed to the 0 M MSA starting concentration in the positive half-cell. Though between cycles 9 - 20, near 100% charge efficiencies were observed.

2. The composition with additives performed comparably with the previous 0.7 M Pb^{2+} and 1.0 M MSA with additives tests during the current increment cycles, though the added advantage with the new composition is the improved electrolyte energy density due to the 1.2 M Pb^{2+} concentration. Future work could seek to increase the concentration further.

In conclusion, the two electrolyte compositions highlighted from this section are:

(I) Semi-divided: 0.7 M Pb^{2+} and 1.0 M MSA, with 1 g dm^{-3} sodium lignosulfonate and 15 mM Bi^{3+}

(II) Fully-divided: 1.2 M Pb^{2+} and 0.5 M MSA (negative) / 1.2 M Pb^{2+} and 0 M MSA (positive), with 1 g dm^{-3} sodium lignosulfonate (negative) / 5 mM Bi^{3+} and 10 mM F^{-} (positive)

The results of further studies with these electrolytes will be reported in the next chapters. In addition, further gaps in the literature were highlighted:

1. Three important additives were combined together for the first time: 1 g dm^{-3} appears to be the optimal concentration for lignosulfonate (from the literature and this chapter). However, this work has not deduced the optimal concentrations for bismuth or fluoride.

2. Conductivity tests for additive-containing electrolytes are required to see how the additives affect ionic mobility. This would help to understand why the initial cycles show a low efficiency when additives are present.

3. A better understanding of the individual electrode reactions is required to understand which electrode becomes the cell potential-limiting electrode on discharge, and under what conditions.

Chapter 9

Performance of the 100 cm^2 Flow Cell

9.1 Introduction

This chapter presents work regarding the scale up of the soluble lead system from the 9 cm^2 electrode scale to the 100 cm^2 scale. The 100 cm^2, filter-press flow cell and the test rig described in the experimental section were used to obtain all the results reported in this chapter. Close to 300 hrs of continuous operation (including periods of rest) was achieved in a semi-divided experiment, and this is discussed and compared with a fully-divided experiment. Other observations from a failed cycling test are also reported, including SEM images, in Chapter 9.2.4.

The second half of this chapter reports the results of a polarisation experiment of a fully-divided cell at various current densities and different levels of % Pb^{2+} utilisation. Observations on the difficulty of maintaining a constant flow rate are also reported.

9.2 Charge/Discharge Cycling

9.2.1 Experimental Procedure

In this section, a semi-divided test is compared to a fully-divided test. In the semi-divided configuration, the electrolyte was housed in one external tank. 2 dm^3 of electrolyte overall was used in each experiment, and in all tests the electrolyte was composed of 0.7 M Pb^{2+} and 1.0 M MSA, with 15 mM Bi^{3+}. In the fully-divided test, the additive was confined to just the positive half-cell, where two electrolyte tanks were used, each containing 1 dm^3 of electrolyte.

Nafion 115 was used as the separator in all tests. Additionally, reticulated vitreous carbon (RVC) was introduced in order to control the growth of deposits along the cell walls and to prevent dendritic growth over the electrode surface (by reducing the local current density): 2 × squares of 10 × 10 × 0.2 cm, 90 ppi RVC were inserted in each half-cell and compressed against the 2D carbon/polyvinyl ester electrode. The electrode-separator gap was 2 mm. The 4 mm-thick RVC had a volume of 40 cm^3; the specific area of the RVC is 57 cm^2 cm^{-3}, hence the active surface area of the RVC was 57 × 40 = 2280 cm^2. Several layers of nylon mesh were placed in between the separator and the RVC to provide the necessary compression whilst maintaining a flow-by design (Figure 9.1. The nylon mesh also acts as a turbulence promoter; though the flow remains laminar, there is greater mixing between fluid layers near the electrode surface and away from the electrode surface (i.e. near the separator - see Figure 9.6. All tests were started at room temperature, 296 K, with no active control and were not monitored.

The cycling regime was composed of several stages. A single charge/discharge cycle consisted of four phases: 1 hr charge, 10 mins rest, discharge down to 0.8 V or for a maximum of 1 hr, 10 mins rest. The first 22 cycles operated at 20 mA cm^{-2}. This was increased to 25 mA cm^{-2} for the following 11 cycles (cycles 23 - 33), and then to 30 mA cm^{-2} for the 11 cycles after that (cycles 34 - 44). Lastly, the current density was returned to 20 mA cm^{-2} for all subsequent cycles (cycles 45+). The charge associated with 1 hr of a 20 mA cm^{-2} charging phase was sufficient for 5% Pb^{2+} utilisation (0.037 moles deposited onto each electrode). At 30 mA cm^{-2}, this increased to 8% (0.056 moles deposited onto each electrode). The flow rate was

initially set to 150 dm^3 hr^{-1}, or 10.4 cm s^{-1} (linear velocity, based on cell dimensions).

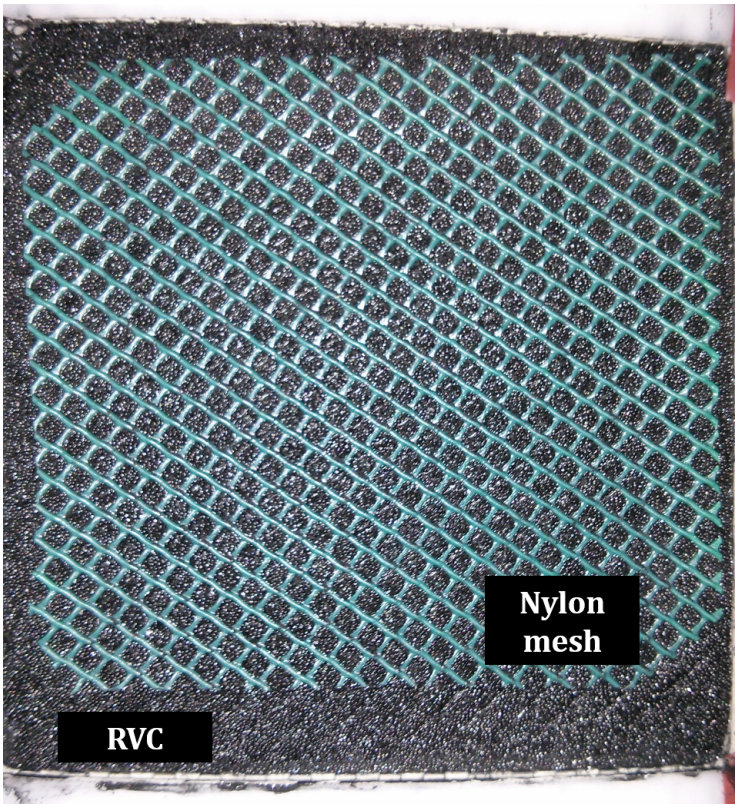

Figure 9.1: A view of the RVC electrode and nylon mesh.

For the fully-divided test, two identical centrifugal pumps were used, one for each half-cell. Both were set at 150 dm^3 hr^{-1}, resulting in a linear velocity of 20.4 cm s^{-1} at each electrode, which was twice of that employed in the semi-divided test. This oversight led to extremely differing results, which will be discussed later. The testing procedure and the results of the two tests are summarised in Table 9.1. The results of an undivided experiment conducted by Collins et al. [34] is also included.

9.2.2 Semi-Divided

150 cycles were achieved using the semi-divided configuration, totalling 300 hrs of operation (including rest periods). There did not seem to be any considerable self-discharge during the regular 10 mins open-circuit periods. The fully-divided test, though highly efficient, managed just 19 cycles due to separator puncture. This is discussed following analysis of the

semi-divided test results.

Cycle	Geometric j / mA cm^{-2}	Actual j / mA cm^{-2}	Av. % Q Eff	Av. % V Eff	Av. % En Eff
Semi-div.					
1-22	20	0.88	84	73	63
23-33	25	1.10	94	83	78
34-44	30	1.32	93	83	77
45-150	20	0.88	87	86	75
1-150	20-30	0.88-1.32	88	84	73
Fully-div.					
1-19	20	0.88	97	81	79
Undiv. Lit. [34]*					
1-40	20	No RVC	88	74	65

Table 9.1: Average charge (Q), voltage (V) and energy (En) efficiencies of the test with the 100 cm^2 flow cell. Geometric current density, j, based on 100 cm^2 (10 × 10 cm) 2D surface area of carbon/polyvinyl ester electrode; actual j, based on 2280 cm^2 RVC sruface area. Individual cyclic efficiencies for the semi-divided test can be seen in Figure 9.2. Charge time: 1 hr. Electrolyte: 0.7 M Pb^{2+} and 1.0 M MSA. Additives: 15 mM Bi^{3+} (added only to +ve tank in the fully-divided test). Separator: Nafion 115. Electrode: 100 cm^2, carbon/polyvinyl ester, with 90 ppi RVC, compressed with nylon mesh. Electrolyte volume: 2 dm^3. Flow rate: 10.4 cm s^{-1} (semi-divided) and 20.8 (fully-divided). Temperature: 296 K. * Undivided literature results, Collins et al. [34], where charge time: 1 hr. Electrolyte: 0.5 M Pb^{2+} and 0.5 M MSA. Additives: 5 mM HDTMA. Electrode: 100 cm^2 Ni (-ve) and carbon/polyvinyl ester (+ve). Electrolyte volume: 1.5 dm^3. Flow rate: 2.3 cm s^{-1}. Temperature: n/a.

Figure 9.2 presents the efficiency of each of the 150 cycles in the semi-divided test. The performance across the early cycles is very similar to the semi-divided test with additives in the 9 cm^2 flow cell (Chapter 8). The charge efficiency rises from 34% at the 1st cycle to 99% at the 5th. There then follows a dip in performance and a period of instability until cycle 22. At cycles 23 and 34, there are further dips in charge efficiency corresponding to an increase in current density, but it can be seen that the charge efficiency improves after the initial dip on both occasions, as the system appears to adjust to the new current density. As soon as the current density is brought down to 20 mA cm^{-2} at cycle 45, the charge efficiency instantly rises to 100% and this peak is maintained until cycle 48. The performance then gradually degrades from cycle 49 to 122, characteristic of the behaviour of the static cell tests. However,

one key difference here is the apparent revival of the system, as the charge efficiency then increases from a low of 69% at cycle 122, to 85% at cycle 150. The likely cause of this is the shedding of large quantities of deposit into the electrolyte (most likely of PbO_2). This would have resulted in a more uniform deposit surface, resulting in a more even current distribution and allowing for more efficient stripping of the deposit in subsequent cycles.

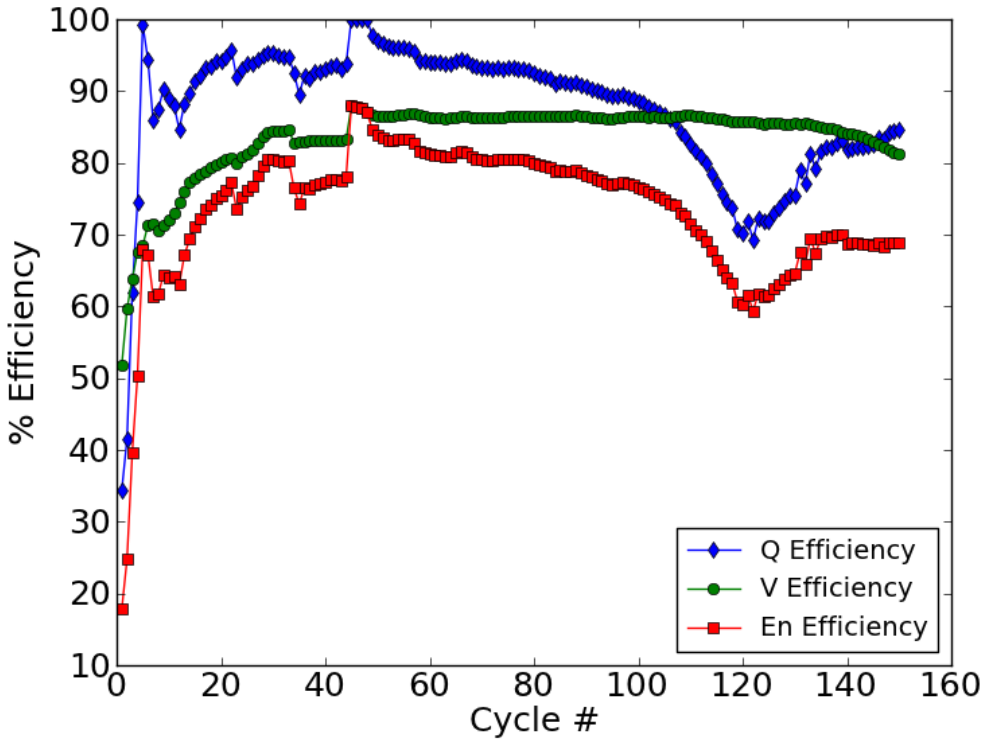

Figure 9.2: Performance of the 100 cm^2 flow cell over the course of 300 hrs, following the procedure summarised in Table 9.1, where the average efficiencies are also summarised. The charge, voltage and energy efficiency of each cycle is presented. Electrolyte: 0.7 M Pb^{2+} and 1.0 M MSA. Additives: 15 mM Bi^{3+} (+ve only). Separator: Nafion 115. Electrode: 100 cm^2, carbon/polyvinyl ester, with 90 ppi RVC, compressed with nylon mesh. Electrolyte volume: 2 dm^3. Flow rate: 10.4 cm s^{-1}. Temperature: 296 K.

The voltage efficiency initially follows a similar trend to the charge efficiency. Beyond cycle 45, it stabilises and remains consistent, averaging 85%. This is despite the added resistance of including RVC at both electrodes. The energy efficiency overall is good (compared to the literature, see Table 2.4), averaging 73% across the entire 150 cycles. Average efficiencies are further summarised in Table 9.1. Table 9.2 compares the charge stored in this test to that stored in three other published experiments. The charge stored on each charge phase of each consecutive cycle is tallied for each experiment. In addition to its improved energy efficiency,

317 Ah of charge has been stored over 150 cycles in this project, doubling the previous record of 164 Ah [34].

Study	**Ref.**	A **/ cm^2**	j **range / mA cm^{-2}**	**Total Charge / Ah**	**% Av. Q eff**
Collins et al.	[34]	100	10	164	94
Collins et al.	[34]	100	30	108	82
Oury et al.	[82]	[i]	1.2 A	120	95[ii]
Krishna	Fig. 9.2	100	20 - 30	317	84

Table 9.2: A comparison of SLFB charge/discharge tests, considering the cumulative amount of charge stored in the cell across all the cycles achieved. [i] From their published information on current density (20 mA cm^{-2} negative, 7 mA cm^{-2} positive) and total current (1.2 A), A (active electrode area) can be calculated to be 60 cm^2 (-ve, 2D electrode) and 171 cm^2 (+ve, 3D 'pseudo-honeycomb' electrode). [ii]'for the majority of the 100 charge/discharge cycles', as reported by the authors.

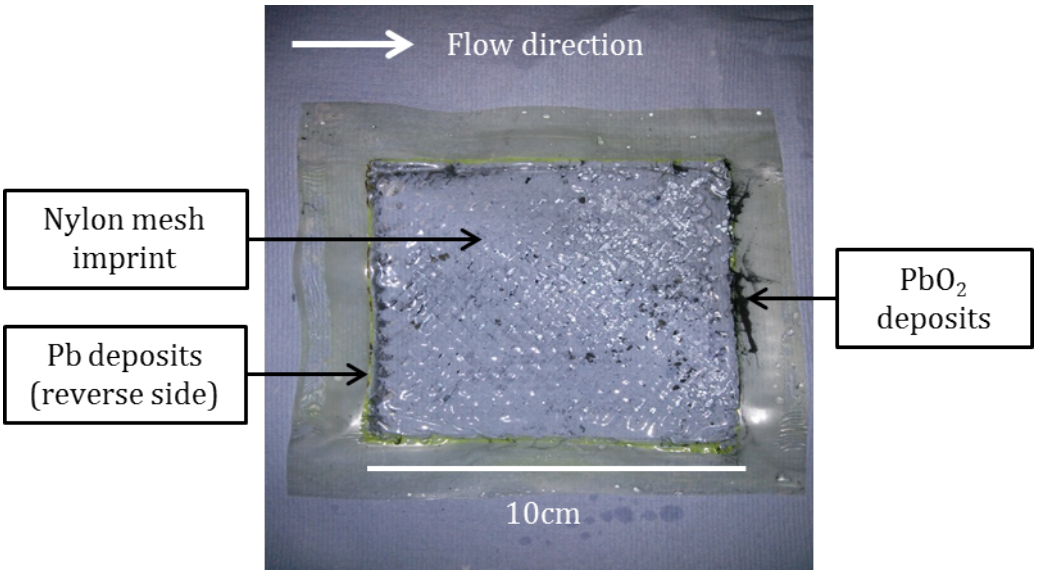

Figure 9.3: Nafion 115 membrane after the semi-divided cycling experiment described in Table 9.1.

The experiment had to be stopped at the 150$^{\text{th}}$ cycle not because of shorting, but due to the formation of several leaks across the rig, mainly between the screw joints between several pipes but also from corroded nozzles just before the cell inlet. Nevertheless, these results are a good improvement to those in the literature, as seen in Table 9.1. The experiment by Collins et al., representing the current level of SLFB research, only achieved 40 cycles, averaging 88% charge and 74% voltage efficiency [34], compared to the 150 cycles achieved

here at 88% charge and 84% voltage efficiency. The lifetime has improved by almost four times whilst the voltage efficiency has substantially improved.

At the end of the experiment, a large amount of black particles were seen in the electrolyte. Upon dismantling, the Nafion membrane was observed to be creased with the imprint of the nylon mesh but on the whole intact, with only traces of deposits scattered across its surfaces. This can be seen in Figure 9.3.

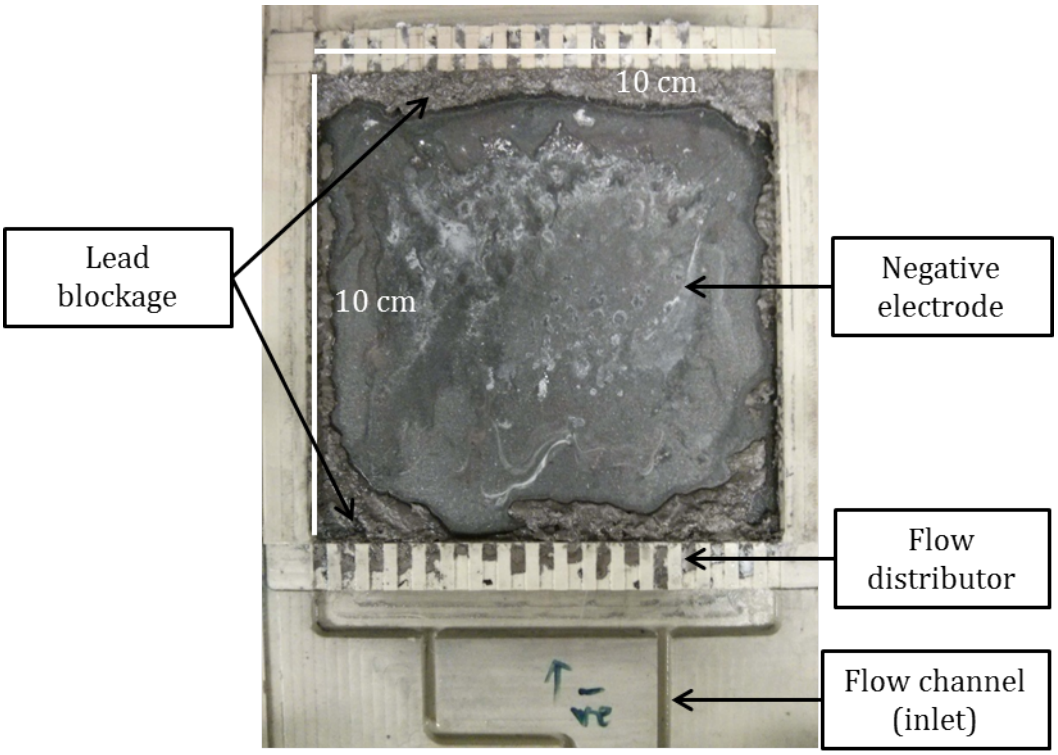

Figure 9.4: Image of a 2D carbon/polyvinyl ester negative electrode from the 100 cm^2 flow cell following five 1 hr charge/discharge cycles at 20 mA cm^{-2}. Lead accumulation can be seen around the edges, particularly at the inlet and outlet, which severely constricted the flow. Electrolyte: 0.7 M Pb^{2+} and 1.0 M MSA. Additives: 15 mM Bi^{3+}. Separator: Nafion 115. Electrode: 100 cm^2, carbon/polyvinyl ester. Electrolyte volume: 2 dm^3. Flow rate: 10.4 cm s^{-1}. Temperature: 296 K.

The RVC at both electrodes was found to be coated evenly throughout, even in deeper levels closer to the electrode surface. Whilst the negative RVC layers remained intact and appeared structurally stronger covered in lead, the positive RVC layers crumbled when an attempt to remove them was made. The 2D carbon electrodes underneath were wet but only showed light traces of deposition in certain patches.

The semi-divided cycling test was also conducted without RVC, i.e. with only 2D, car-

bon/polyvinyl ester electrodes. But after 5 cycles, the flow rate was observed to be substantially diminished. The experiment was halted and the cell disassembled. Severe deposit accumulation was observed around the edges of both electrodes, particularly near the inlet and outlet, and the blockage had reduced the flow through the cell. This can be seen for the negative electrode in Figure 9.4. With RVC included, deposit growth was still found around the electrode edges, but overall the RVC had prevented any blockages near the inlet and outlet, allowing the cell to reach 150 cycles.

The cell was also configured in the semi-divided format using the FF60 microporous separator. However, the separator's brittle nature led to cracks around the compressed areas, weakening the membrane's ability to act as a barrier against shorting. To avoid the problem of compression in filter-press reactors, separators are often welded into a sleeve or a frame so that they are held just in front of the electrode surface; the sleeve surrounding the separator is then compressed against the frame housing the electrode. An example has previously been patented [125], and this would be a suitable option in the future for the FF60 separator.

9.2.3 Fully-Divided

In the fully-divided test, only 19 cycles were achieved, all at 20 mA cm^{-2}. The first and second cycles returned charge efficiencies of 67% and 84% respectively. The remaining 17 cycles all returned 100%. Overall, across the 19 cycles, the average charge, voltage and energy efficiencies were 97%, 86% and 79% respectively. This was initially seen as a remarkable improvement to the previous semi-divided experiment; therefore it was not clear why the experiment failed so early.

The experiment was only halted after cycle 36 of the testing regime set out in Table 9.1, when it was discovered that the positive tank had emptied into the negative; clearly it was a sign of membrane puncture. Later, it was discovered that this must have occurred at cycle 20, where the charge efficiency plummeted to 79%, reducing further to <57% between cycles 22 - 36. Whether the rate of electrolyte crossover from the positive to the negative from this point was rapid or slow is unknown, but when failure was discovered only a small volume of positive electrolyte remained in the positive flow circuit. It is likely that there was a greater pressure in the positive flow circuit, causing the movement of electrolyte into the negative

following the puncture. The cell was disassembled and the membrane removed. Figure 9.5 shows the membrane after cycle 36.

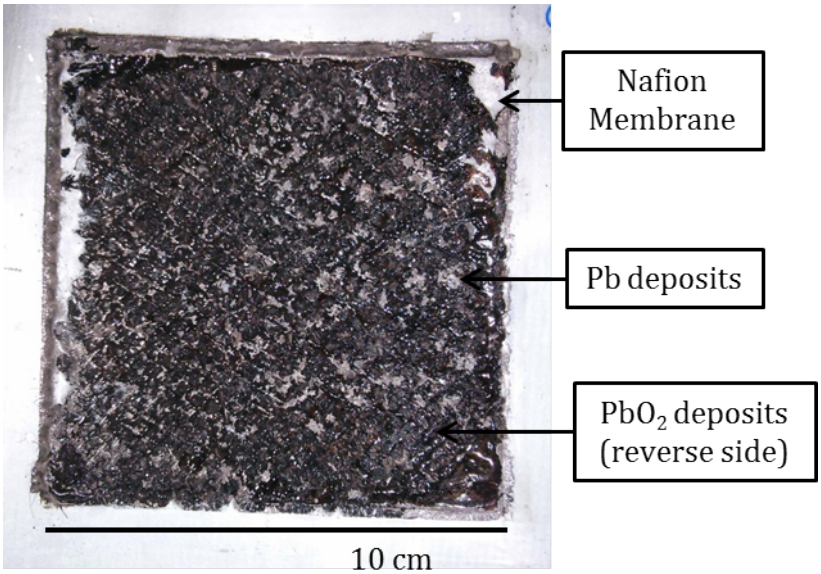

s

Figure 9.5: Nafion 115 membrane after the first 36 cycles (failure at cycle 19) of the fully-divided cycling experiment described in Table 9.1. Electrolyte: 0.7 M Pb^{2+} and 1.0 M MSA. Additives: 15 mM Bi^{3+} (+ve only). Separator: Nafion 115. Electrode: 100 cm^2, carbon/polyvinyl ester, with 90 ppi RVC, compressed with nylon mesh. Electrolyte volume: 2 dm^3. Flow rate: 20.8 cm s^{-1}. Temperature: 296 K.

It was not expected to see almost the entire membrane surface covered with strongly-adhering deposits as this was never seen in the 100 cm^2 semi-divided test, nor in the 9 cm^2 flow cell tests (although the inter-electrode gap was larger in this smaller cell). However, in retrospect it could have been anticipated considering the poor charge efficiencies between cycles 20 - 36. Several small tears around the edges of the membrane were detected, but because the surface was covered with deposits, it was unclear as to whether the puncture was caused by a deposit growth or by the sharpness of the nylon mesh under compression.

The nylon mesh was found to be embedded into the RVC at each electrode, so it is likely that the mesh was used as a scaffold for deposit growth. At 2 mm, the distance between the RVC face and separator was very short. There is far greater PbO_2 covering the surface on the positive face of the membrane than there is Pb on the negative. Because PbO_2 is less conductive than Pb, deposits closer to the electrode surface would likely dissolve first on discharge, electrically isolating deposits further away from the electrode that are attached

to the mesh or cell walls. On the subsequent charge cycle, deposition near the electrode surface would reconnect these outlying deposits, allowing them to creep further away from the electrode surface.

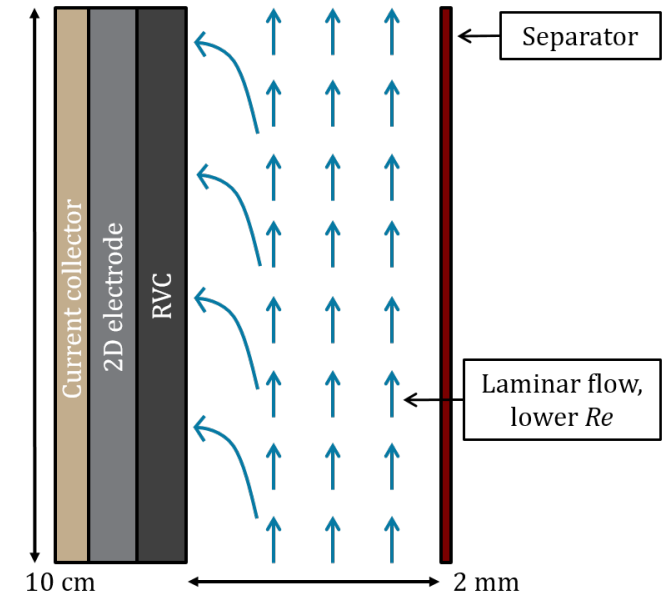

(a)

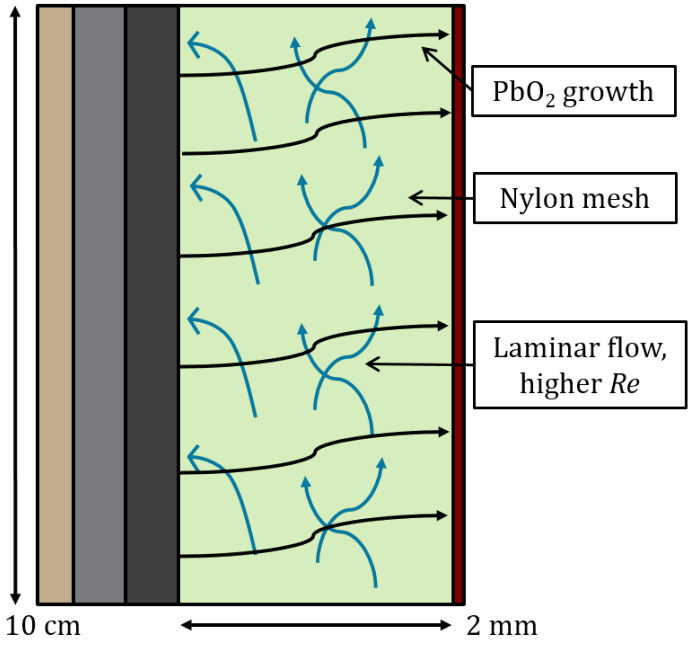

(b)

Figure 9.6: Comparison of the methods used to incorporate RVC into the cell. (a) RVC attached using Leit-C conductive cement. (b) RVC compressed using nylon mesh. There is no direct flow through the RVC, only forced convection into the pores from the bulk electrolyte motion.

Eventually, contact is made with the membrane and growth continues across the surface following the same mechanism. This would have been exacerbated by the reduced and relatively stagnant positive electrolyte. RVC is stable at the negative electrode but should be pressure welded into the electrode or attached using a conductive adhesive in order to remove the scaffold for deposit growth, leaving a gap between electrode and membrane. This method of connection also applies at the positive electrode; however, a different 3D material is required there due to the instability of carbon.

It is likely that the high flow rate enabled high efficiencies seen across cycles 1 - 19 by improving the mass transport properties. However, it may have also contributed to the puncture of the membrane. It is clear that the flow rate must be reduced and the nylon mesh 'scaffolds' removed in future experiments. Furthermore, the pressure in both half-cells must remain equal by using more precise pumps. Figure 9.6 illustrates this in further detail.

Figure 9.6a shows a configuration where the RVC is attached to the electrode using a conductive cement (Leit-C, see Chapter 9.3, creating a gap between the RVC surface and the separator. Forced convection is the dominant form of mass transport, as the electrolyte is driven into the pores due to the flow pressure. However, diffusion of Pb^{2+} (governed by Fick's Laws [64]) would be the dominant form of mass transport throughout the RVC, especially the deeper layers, and to the surface of the RVC within the pores. The effect of deposition and the blocking of the pores will be a key future study.

The surface of the RVC is rough, which will slow the fluid layers near the surface of the RVC. As the flow is laminar, there is less mixing between the fluid layers near the surface of the separator and the surface of the RVC, resulting in slower mass transport properties. In contrast, inserting a meshed field (Figure 9.6b increases the tortuosity of the flow path, which encourages the fluid layers to mix, thus improving the mass transport properties. The compromise is an increased pressure drop across the electrode length (and thus a greater pumping loss), and in the case of the SLFB, the mesh acts as a scaffold for rapid deposit creep of both Pb and PbO_2.

9.2.4 Potential-Time Plots and SEM Images

Figure 9.7 displays the potential-time response of the semi-divided experiment (a) and the fully-divided experiment (b), both with the VPX-20 membrane, as referred to in Table 9.1. Cycles 5 - 20 are presented.

There is a great difference in the potential profiles. In (a), where the cell was semi-divided, there is a small nucleation overpotential at the beginning of charge, which appears to settle just above 1.5 V initially before rising sharply to 1.85 V. Across all the cycles here, the open-circuit potential after discharge is 1.27 V. Across cycles 5 - 7, the open-circuit potential after charge averages 1.37 V, and this increases to 1.7 V for cycles 4 - 20. From cycle 4, a double discharge potential profile can be seen, growing more prominent with every subsequent cycle. By cycle 15, it can clearly be seen that the first discharge curve begins at 1.6 V. Following a period of about 1000 s, the potential suddenly falls to 1.2 V, where the second discharge curve begins. This corresponds well with the semi-divided, with additives test seen with the 9 cm^2 flow cell in the previous chapter, in which case the double discharge profile is due to the deposition and stripping of bismuth alongside lead. However, unlike with the smaller flow cell, where this pattern was seen from the first cycle, the double discharge profile begins only at the 8^{th} cycle.

In (b), where the cell was fully-divided and bismuth added only to the positive electrolyte, there is an exceptionally high nucleation overpotential at the start of charge at each cycle, surpassing 2.5 V. It is not clear which electrode causes this as the individual electrode potentials were not measured. In cycles 5 - 7, the charging potential then appears to settle at 1.9 V before rising to 2.1 - 2.3 V. By cycle 10, the charge potential is relatively constant, averaging 1.9 V. Unlike in (a), the open circuit potentials after charge and after discharge are approximately equal, averaging 1.7 V. There is no double discharge profile, which suggests that the membrane did not puncture early in the test. Instead, the discharge potential is flatter and more constant than in (a) (until cycle 19). Between cycles 5 - 10, the potential also appears to immediately rise at the start of discharge before decreasing, creating an almost parabolic profile.

Figure 9.8 presents four SEM images taken from a sample of the negative electrode (cut from

the centre of the electrode), approximately 5 mm × 3 mm planar area and 2 mm in thickness, after the fully-divided test. Image 9.8a shows the planar surface (the area in contact with the electrolyte) at 25× magnification. The lead is uniformly coated across the majority of the RVC substrate.

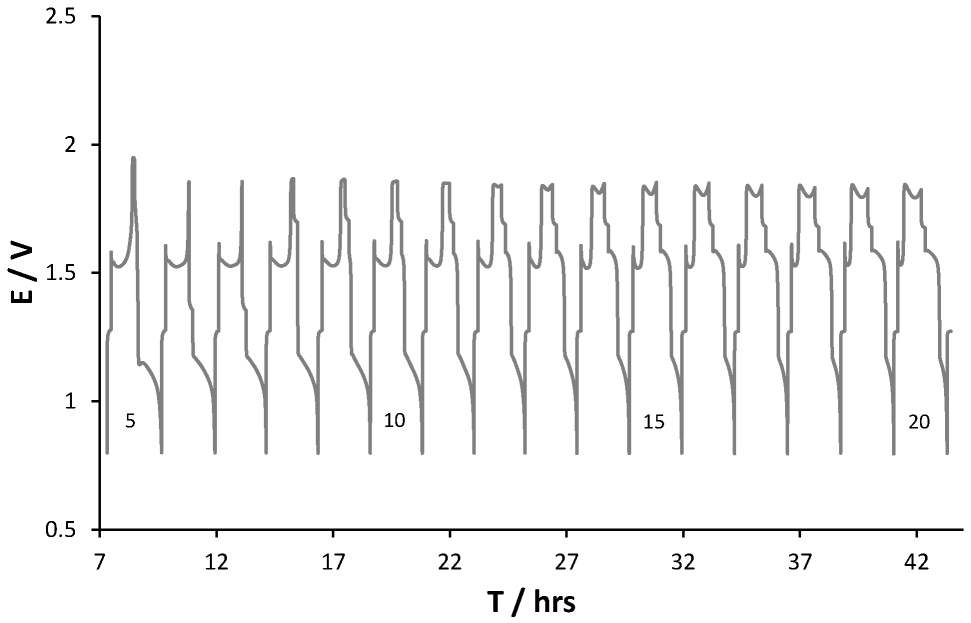

(a)

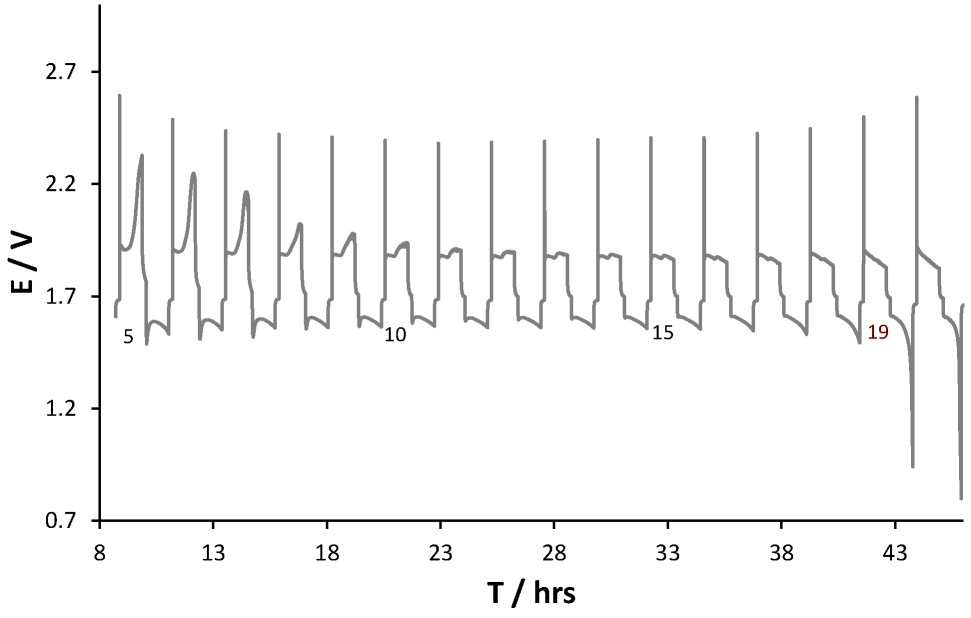

(b)

Figure 9.7: Cell potential-time responses of the (a) semi-divided and (b) fully-divided cycling experiments, as described in Table 9.1. Cycles 5 - 20 are presented, where j = 20 mA cm^{-2} and charge time = 60 mins.

Rocky clusters can be seen in the bottom right, above a long strand almost 1 mm in length of RVC. Image 9.8b presents a 500× magnification of a smooth region, where the deposits are uniformly packed, leaving no voids. Image 9.8c focuses on one of the rocky clusters seen in Image (a), where large, interlocking crystals of lead can be seen. Image 9.8d shows a 25× magnified view of the edge of the sample (this is also the plane where the sample was cut), allowing a view of the inside of the RVC-lead structure. Several pores can be seen throughout the image, but generally the RVC is uniformly coated with lead, even within the deeper layers. Furthermore, energy dispersive X-ray spectroscopy (EDX) analysis confirmed the presence of solid bismuth across the three sites that were scanned. In one location, 6.7% of the sample mass was attributed to bismuth.

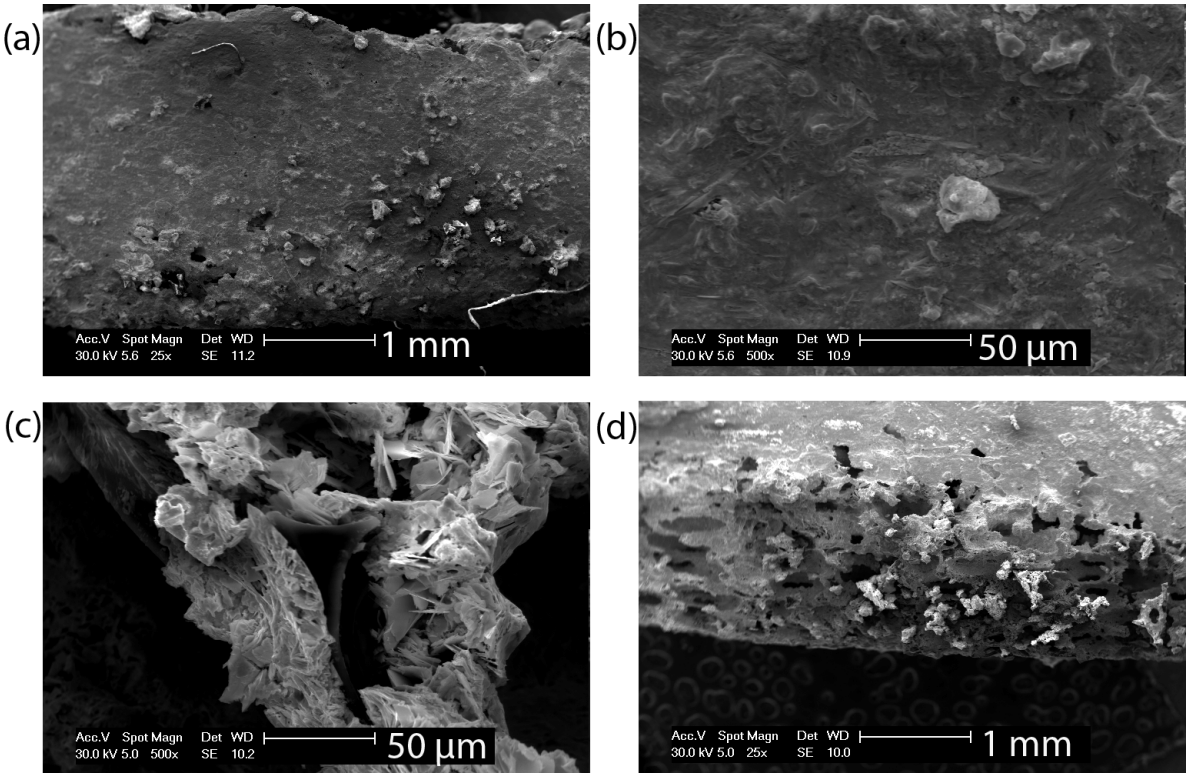

Figure 9.8: SEM images of the negative electrode following failure of the fully-divided cycling experiment described in Table 9.1. (a) overall view, (b) closer view of a smooth region, (c) closer view of a rocky cluster, (d) side view of the electrode sample. Electrolyte: 0.7 M Pb^{2+} and 1.0 M MSA. Additives: 15 mM Bi^{3+} (+ve only, however significant membrane puncturing did occur). Separator: Nafion 115. Electrode: 100 cm^2, carbon/polyvinyl ester, with 90 ppi RVC, compressed with nylon mesh. Electrolyte volume: 2 dm^3. Flow rate: 20.8 cm s^{-1}. Temperature: 296 K.

9.3 Power Density at Varying % Pb^{2+} Utilisation

The performance of the cell at different levels of Pb^{2+} utilisation was investigated through a polarisation experiment. The cell was fully-divided using the VPX-20 membrane. The electrolyte consisted of 1 dm^3 of 1.2 M Pb^{2+} and 0.5 M MSA (negative) / 1 dm^3 of 1.2 M Pb^{2+} and 0 M MSA (positive), with 1 g dm^{-3} sodium lignosulfonate (negative) / 5 mM Bi^{3+} and 10 mM F^- (positive). The initial flow rate setting at each electrode was lowered to 125 dm^3 hr^{-1}, or 8.7 cm s^{-1} across each electrode (the minimum setting for this rig was 100 dm^3 hr^{-1}).

A single square of 10 × 10 cm, 90 ppi, 2 mm thick RVC was attached to each of the carbon/polyvinyl ester electrodes using Leit-C conductive cement and left to dry overnight with a distributed 1 kg weight pressing the RVC into the electrode. There was then no need to compress the RVC against the electrode with mesh, leaving a 4 mm gap between the surface of the RVC and the membrane. Furthermore, the electrodes remained stable throughout the experiment and did not come loose inside the cell. It would have been preferred to heat bond the RVC to the electrode surface, but it was not possible with this type of carbon polymer. The RVC volume totalled 20 cm^3, resulting in an active surface area of 1140 cm^2. All current densities are reported relative to the geometric area of the electrodes (100 cm^2). A conversion between the geometric and actual j is presented in Table 9.3.

mA cm^{-2}	
Geometric j	**Actual** j
20	1.75
30	2.63
35	3.07
50	4.39
65	5.70
80	7.02
100	8.77

Table 9.3: Geometric and actual current density conversion table, based on a RVC volume of 20 cm^3 and active surface area of 1140 cm^2.

The cell was first charged to 10% Pb^{2+} utilisation, by charging at 30 mA cm^{-2} for 2.14 hrs. A series of 6 galvanostatic charge/discharge cycles then followed, each consisting of 60 s of charge and followed straight after by 60 s of discharge. The 1st cycle operated at 20 mA cm^{-2}, and this was incremented at each following cycle to 100 mA cm^{-2} by the 6th cycle. A 2 mins rest phase followed. Then, the cell was charged for a further 3.22 hrs at 30 mA cm^{-2} to 25% Pb^{2+} utilisation and the same procedure repeated. Finally, the cell was charged for a further 5.36 hrs at 30 mA cm^{-2} to 50% Pb^{2+} utilisation where again the same procedure was implemented. An attempt to reach 75% was made, but strong signs of shorting were seen in the potential-time response just before 13 hrs of overall charging at 30 mA cm^{-2}, or 60% Pb^{2+} utilisation, and the experiment had to be stopped.

The potential-time responses of each of the three sets of 6 cycles can be seen in Figure 9.9. Graphs (a), (b) and (c) correspond to 10%, 25% and 50% Pb^{2+} utilisation respectively.

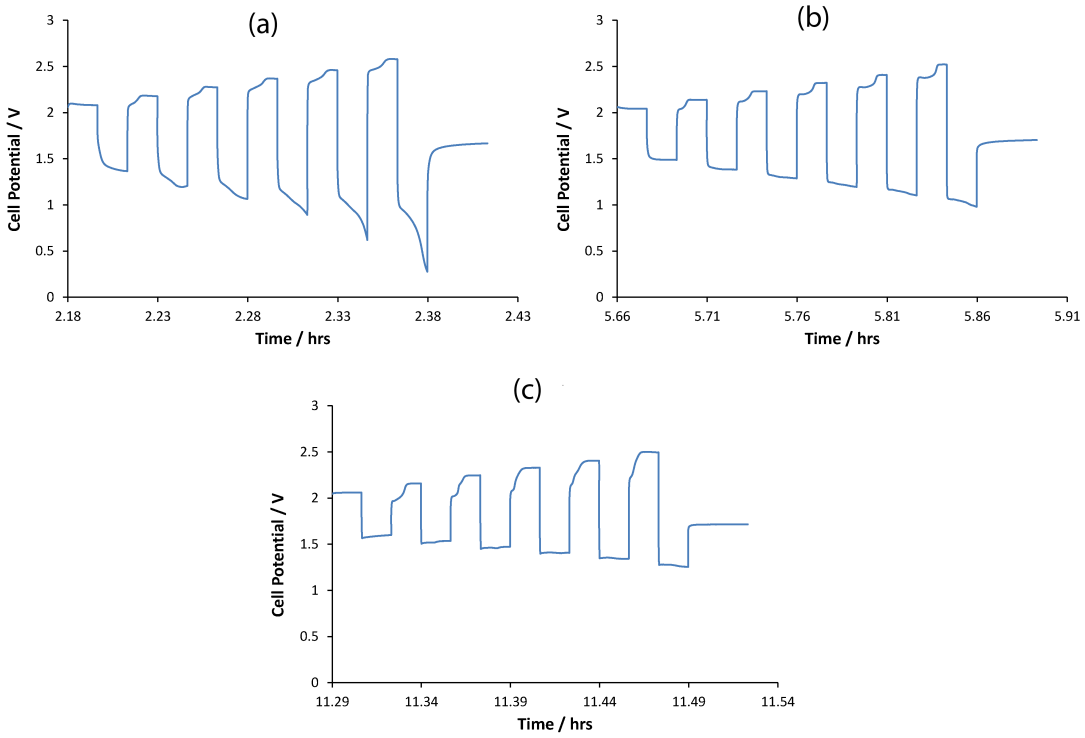

Figure 9.9: Potential-time responses of 60 s charge/discharge cycles at various levels of Pb^{2+} utilisation: (a) 10%, (b) 25%, (c), 50%. Electrolyte: 1.2 M Pb^{2+} and 0.5 M MSA (-ve) / 1 dm^3 of 1.2 M Pb^{2+} and 0 M MSA (+ve). Additives: 1 g dm^{-3} sodium lignosulfonate (-ve) / 5 mM Bi^{3+} and 10 mM F^- (+ve). Separator: VPX-20 (fully-divided). Electrode: 100 cm^2, carbon/polyvinyl ester, with 90 ppi RVC attached using Leit-C conductive cement. Electrolyte volume: 2 dm^3. Flow rate: 8.7 cm s^{-1}. Temperature: 296 K.

The charge efficiency of all the cycles was 100% but the cell clearly performed better at higher levels of Pb^{2+} utilisation where there were thicker deposits available to dissolve. In all three, the charge potential rises and the discharge potential falls as the current density is increased. At 10% Pb^{2+} utilisation, the discharge potential also drops rapidly during each discharge phase, particularly at higher current density, signifying a lack of deposits to strip. The effect of the additives inhibiting deposition and the low $[H^+]$ concentration in the positive half-cell are likely to be the defining factors here as the level of Pb utilisation is still low. In later cycles, the discharge potential becomes higher and more stable, leading to improved voltage efficiencies. At 50% Pb^{2+} utilisation, the discharge potentials are very consistent, which gives the system a degree of reliability that would make power management more favourable.

The potential at the end of each 60 s of charge and discharge was recorded and plotted, and this can be seen in Figure 9.10.

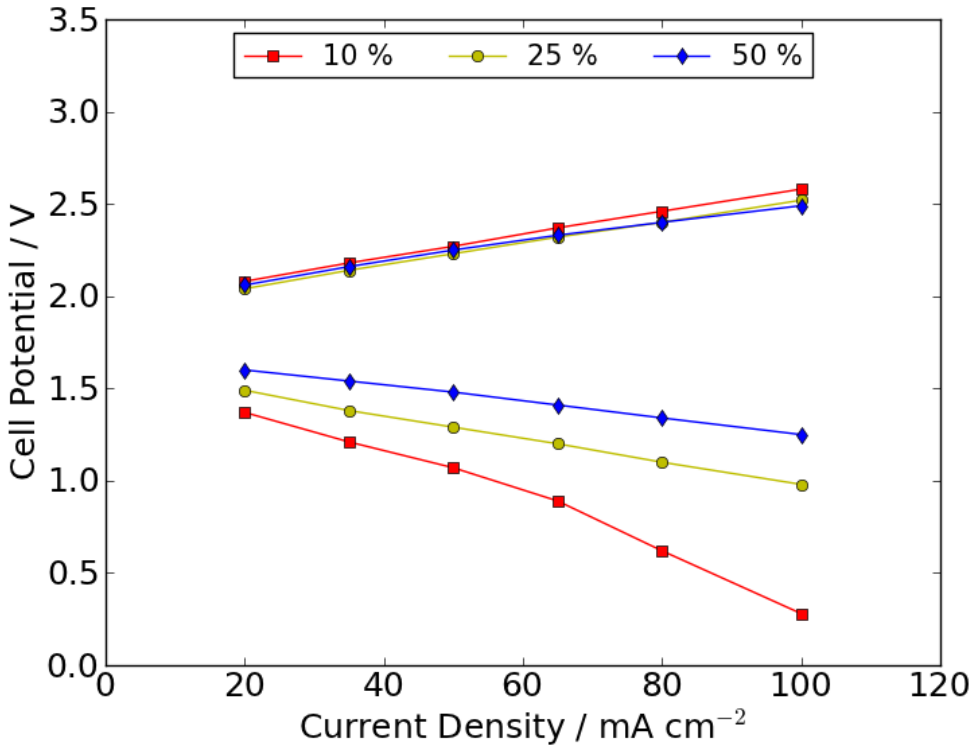

Figure 9.10: Polarisation plot of the 100 cm^2 flow cell at different levels of Pb^{2+} utilisation based on the potential-time responses seen in Figure 9.9.

There is little variation in charge potential with level of Pb^{2+} utilisation. Charging typically

peaks at 2.0 V at 20 mA cm^{-2}, increasing linearly with current density to 2.4 - 2.5 V at 100 mA cm^{-2}. The potential is slightly higher at 10% Pb^{2+} utilisation at the higher current densities. The discharge potentials show a far greater variation, especially above 65 mA cm^{-2}, whilst improving with % Pb^{2+} utilisation: at 20 mA cm^{-2}, the potential varies between 1.37 V to 1.60 V between 10% and 50% respectively; at 100 mA cm^{-2}, this range increases from 0.28 V to 1.25 V at 10% and 50% respectively. The maximum cycling range of this cell appears to be between 10% and <60% Pb^{2+} utilisation (where shorting was observed), but it is clear that performance is superior nearer the higher end of utilisation.

The discharge potentials were then multiplied with their respective current densities to produce a set of power densities. These were then plotted against current density, Figure 9.11a, and the respective cell potential at the end of each sixty seconds of discharge, Figure 9.11b.

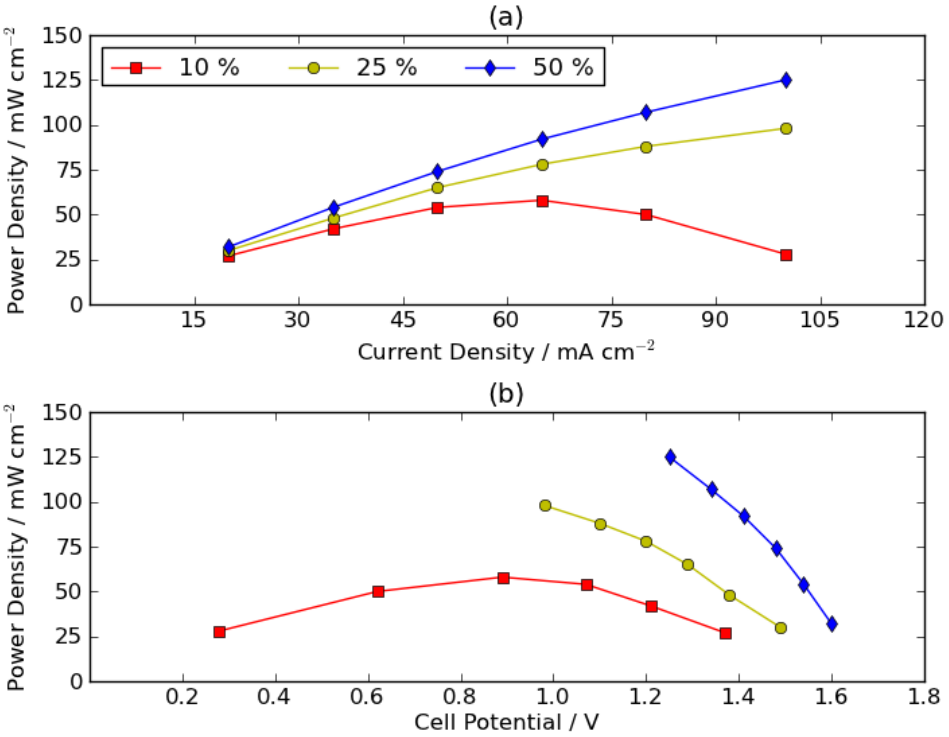

Figure 9.11: Power density of the 100 cm^2 flow cell as a function of (a) current density and (b) cell potential based on the potential-time responses seen in Figure 9.9. Both charge and power density are presented per cm^2 electrode area.

The discharge power density has a parabolic relation to current density, reaching a peak

before decreasing. This is seen clearly in the 10% Pb^{2+} utilisation curve, where 58 mW cm^{-2} is the maximum power density achievable if the current density load is set at 65 mA cm^{-2}. However, it is not a true representation of the power density, as it was seen in Figure 9.9a that the potentials were rapidly reducing on discharge. At low current densities, the power density is similar at all the levels of Pb^{2+} utilisation: at 20 mA cm^{-2}, 27, 30 and 32 mW cm^{-2} are seen at 10%, 25% and 50% Pb^{2+} utilisation respectively. However, at 100 mA cm^{-2}, 28, 98 and 125 mW cm^{-2} are seen respectively. 125 mW cm^{-2} corresponds to 12.5 W in this 100 cm^2 cell, which is the highest reported power of a single soluble lead flow cell. It is likely that greater power is available at higher current densities, especially at the higher levels of utilisation.

Figure 9.11b is representative of the type of studies that would need to be carried out by power electronics engineers in order to integrate the battery into a power network, where voltage management is a key issue. At 10% Pb^{2+} utilisation, the voltage drops rapidly, from 1.37 V at 20 mA cm^{-2} to 0.28 V at 100 mA cm^{-2}, a difference of over 1 V. Whereas across the same current density range at 50% Pb^{2+} utilisation the voltage only drops by 0.35 V, from 1.60 V to 1.25 V. This latter range corresponds to a power swing of 93 mW cm^{-2}, from 32 mW cm^{-2} to 125 mW cm^{-2} respectively. In order to minimise the range of voltage fluctuation corresponding to a power fluctuation, it would be beneficial to operate at higher levels of Pb^{2+} utilisation.

At the end of the experiment,the cell was dismantled and Pb and PbO_2 growth along the cell walls had clearly spread onto the separator, puncturing it in several places. RVC has been an important addition to the cell configuration in this chapter. However, as deposition increases with SoC, the pores are likely to become blocked, and the effect of various grades of RVC and porosity on the deposit quality and therefore cell performance has not been investigated. In this latest experiment, if only 2D electrodes had been used, the respective deposit thicknesses as a function of % Pb^{2+} utilisation are presented in Table 9.4.

In Chapter 2, it was discussed that the optimal thickness of deposits should be 1 mm (assuming 2D electrodes and uniform deposition). Whether this applies when using 3D electrodes remains to be investigated. Due to the high cost of RVC material, it is likely that a future SLFB system will only use 2D electrodes in order to make the battery economical. In this

case, the electrolyte volume, Pb^{2+} concentration and electrode area should be selected accordingly. For example, in the previous study, where 2 dm^3 electrolyte overall was used, in which the Pb^{2+} concentration was 1.2 M, the active electrode area would have to be 300 cm^2. Therefore at 100% Pb^{2+} utilisation, the Pb deposit would be 0.71 mm thick and the PbO_2 deposit 1.02 mm thick.

	Deposit thickness / mm	
% Pb^{2+} Utilisation	**Pb (-ve)**	**PbO_2 (+ve)**
0	0	0
10	0.21	0.31
25	0.53	0.77
50	1.06	1.53
60*	1.28	1.84
100	2.13	3.06

Table 9.4: Theoretical deposit thicknesses assuming 2D electrodes and uniform deposition, based on Equation 2.16, where $[Pb^{2+}]$ = 1.2 M and electrolyte volume = 1 dm^3 (each half-cell). *Point at which shorting was observed.

9.4 Flow Rate

In Chapter 9.3, maintaining a single flow rate through each half-cell proved to be difficult. The flow rate through both flow circuits was observed to fall from 125 dm^3 hr^{-1} at the start of the experiment to <100 dm^3 hr^{-1} at 50% Pb^{2+} utilisation. However, throughout the experiment the flow rate was periodically adjusted by opening the valve in an attempt to maintain the 125 dm^3 hr^{-1} flow rate. Despite being kept at its fully open position, the flow rate still decreased. The drop in flow rate therefore far exceeded 25 dm^3 hr^{-1}.

It is likely that the fall in flow rate is a result of the rise in pressure drop across the cell with increasing % Pb^{2+} utilisation, as deposition restricts the width of the inter-electrode gap. This would be in agreement with the Hagen-Poiseuille law (Chapter 2.2.3). Though the electrolyte viscosity decreases with Pb^{2+} utilisation (Chapter 4), narrowing the inter-electrode gap has a far greater effect on pressure drop. A pump with variable power settings is required for more accurate control of the flow rate, and future experiments will need to further investigate the

effect of increasing pressure drop with increasing deposit thickness.

9.5 Comparison of Flow Properties

The flow cell experiments conducted thus far are summarised in terms of their flow properties in Tables 9.5 and 9.6. Laminar flow was present in each experiment, ranging from a Reynolds number of 233 (at 2.3 cm s^{-1}) in the 9 cm^2 flow cell, to 620 (20.8 cm s^{-1}) in the 100 cm^2 cell.

Test	**[Pb^{2+}] / mol dm^{-3}**	**[MSA] / mol dm^{-3}**	**Cond. / mS cm^{-1}**	**ν / mm^2 s^{-1}**	**Separator (Division)**	**Chapter**
I	0.7	1	279	1.32	VPX-20 (semi)	8.3
II	0.7	1	279	1.32	Nafion (semi)	9.2.2
III*	0.7	1	279	1.32	Nafion (full)	9.2.3
IV (neg)	1.2	0.5	203	1.42	VPX-20 (full)	9.3
IV (pos)	1.2	0	140	1.35	VPX-20 (full)	9.3

Table 9.5: A comparison of flow cell cycling experiments, part I. The conductivity and vicosity (ν) of the electrolytes are compared (not accounting for additives), alongside the cell configuration. *In experiment III, the system was fully-divided but used the same [Pb^{2+}] and [MSA] in each half-cell. The following additives were used: (I) 1 g dm^{-3} sodium lignosulfonate and 15 mM Bi^{3+}; (II) 15 mM Bi^{3+}; (III) Bi^{3+} (+ve half-cell only); (IV neg) 1 g dm^{-3} sodium lignosulfonate; (IV pos) 5 mM Bi^{3+} and 10 mM F$^-$.

Test	**A / cm^2**	**B / cm**	**S / mm**	**d_e / / cm**	**Q_v / dm^3 hr^{-1}**	**v / cm s^{-1}**	***Re***
I	9	2	10	1.33	16.6	2.3	233
II	100	10	4	0.77	150	10.4	608
III*	100	10	2	0.39	150	20.8	620
IV (neg)	100	10	4	0.77	125	8.7	471
IV (pos)	100	10	4	0.77	125	8.7	495

Table 9.6: A comparison of flow cell cycling experiments, part II. The Reynolds number and cell geometry is compared, where A is the active electrode area, B the breadth of the flow channel, S the electrode-separator gap for the fully-divided tests and the inter-electrode gap for the semi-divided tests. d_e is the equivalent hydraulic diameter of the cell. Q_v is the volumetric flow velocity and v the flow velocity. *In III, the dimensions and flow rates are for each individual half-cell.

The electrode-separator gap in the 100 cm^2 cell, used in Tests II - IV, was 6 mm. The electrode configuration of II and III were the same. However, $S = 4$ mm in test II as this was the RVC-RVC gap (with the separator in between, i.e. semi-divided). $S = 2$ mm in test III (fully-divided) due to the presence of 4 mm thick RVC electrodes. $S = 4$ mm in IV due to 2 mm thick RVC electrodes (S = electrode-separator gap in III and IV). It is assumed that there is negligible flow through the RVC compared to the bulk flow through the electrode-separator gap. $Re = 471$ (-ve), 495 (+ve) in IV, which is comparable with 448 seen in the study conducted by Collins et al. [34] (Table 2.3). It is considerably higher than that seen in the study by Wills et al. (144) [31] and Oury et al. (55) [82].

9.6 Summary

All tests in this chapter were conducted with the 100 cm^2 flow cell. The first half of this chapter explored the longevity of the semi-divided 0.7 M Pb^{2+} and 1.0 M MSA system, with 1 g dm^{-3} lignosulfonate and 15 mM Bi^{3+}. In summary, the galvanostatic cycling performance of the semi-divided configuration in the 100 cm^2 flow cell at 20 - 30 mA cm^{-2} was seen to surpass comparable tests previously reported, achieving almost four times as many cycles (150) with an energy efficiency of 73%, compared to 65% in the literature [34]. It should be noted that RVC, with a total surface area of approximately 2280 cm^2, was used here whereas the authors of [34] used 2D carbon composite (positive) and nickel (negative) electrodes each with an area of 100 cm^2.

The second half of this chapter employed the second composition highlighted in Chapter 8, i.e. VPX-20 fully divided 1.2 M Pb^{2+} and 0.5 M MSA (negative) / 1.2 M Pb^{2+} and 0 M MSA (positive), with 1 g dm^{-3} sodium lignosulfonate (negative) / 5 mM Bi^{3+} and 10 mM F^- (positive). The experiment focused on deducing the charge and discharge power density between 10 - 100 mA cm^{-2} at different levels of Pb^{2+} utilisation, simulating different SoC. In summary, a soluble lead flow cell capable of discharging at 125 mW cm^{-2} (12.5 W) for 60 s was demonstrated, with charge and discharge occurring as high as 100 mA cm^{-2}. Furthermore, from this chapter:

1. RVC was seen as a crucial component to controlling deposit morphology and preventing

flow blockage around the electrode sides and near the inlet and outlet. Using just the 2D carbon polymer electrodes, no more than 5 cycles (20 mA cm^{-2}, 1 hr charge/discharge) could be achieved due to blockage caused by deposit accumuation. By placing RVC in front of the electrodes, the deposition morphology at each electrode was successfully managed, and this was further improved when the RVC was glued to the electrode using Leit-C conductive cement rather than physical compression using nylon mesh, which was seen to act as a scaffold much in the same way that the deposits were seen growing along the internal cell walls. SEM images revealed several lead deposit morphologies found on the surface of the RVC electrode as well as showing uniform deposition deep into the electrode. However, a novel, more stable 3D electrode is recommended at the positive electrode, as RVC was seen to degrade over time. Further conductive adhesives could also be tested in future in order to improve the electrical contact between the electrode components. In addition, the porosity of the RVC and its effect on deposition/stripping has not been investigated, as only one grade (90 ppi) of RVC was tested here.

2. It is likely that discharge current densities higher than 100 mA cm^{-2} are achievable and for longer durations (i.e. in chapter 8, the 9 cm^2 flow cell reached 150 mA cm^{-2}). The charge current density however would always be limited to lower current densities (max 50 mA cm^{-2}) to ensure uniform, smooth deposition.

3. The power density characterisation remains incomplete and future work must aim to investigate higher discharge current densities for both the semi and fully-divided configurations at different levels of Pb^{2+} utilisation. This will aid in the design of a cell stack.

4. The flow rate was observed to drop with increasing SoC, suggesting that the narrowing of the inter-electrode gap through deposition causes pressure drop to increase significantly. Little work has been conducted on pressure drop as a function of SoC in the soluble lead flow cell, and this remains an important area of investigation.

Chapter 10

Cell Regeneration

10.1 Introduction

The deposition/stripping mechanisms can be made efficient by optimising the electrolyte, electrode and controlling the flow and operating parameters, and this has been discussed in the previous chapters. Nevertheless, any charge inefficiency, or difference in Faradaic efficiency between the positive and negative electrode reactions or inability to fully discharge the cell would lead to the accumulation of one or both electrode deposits. For extended operation on the scale of several months, it is important to establish techniques to rebalance the cell if required, and which would not require dismantling the cell.

Less than 100% charge efficiency was recorded for most cycles of every cycling experiment in the previous chapters. The cut-off voltages were high, at 0.7 - 0.8 V, and the discharge current density was above 20 mA cm^{-2}. Discharging to 0 V at significantly lower current densities could enable the thorough dissolution of deposits after a charge phase, but this is impractical during a charge/discharge experiment or during operation. In addition, it would be a very slow process.

Incomplete dissolution during discharge is a result of the presence of insoluble, or strongly adhering, deposits on the electrode surfaces from previous cycles, currently understood to be largely lead dioxide at the positive electrode (Chapter 2.5.6), which leads to a build-up of lead at the negative electrode. These deposits could be forcibly stripped over a short time

period by supplying power. By switching the electrode polarities and charging the cell, the new positive electrode (where there is Pb deposited) becomes the anode and the new negative electrode (where there is PbO_2 deposited) becomes the cathode. As long as the voltage is maintained negative to zero, solid lead at the new positive electrode would be oxidised to Pb^{2+} in preference to Pb^{2+} oxidation to PbO_2, and at the new negative electrode PbO_2 would be reduced to Pb^{2+} in preference to Pb^{2+} reduction to Pb (the opposite reactions would occur if the voltage surpassed 0 V). This technique is reported in this chapter. Additionally, this method should be used to prevent ultimate failure in a fully-divided system, defined as when the separator is punctured causing substantial electrolyte mixing.

10.2 Experimental Procedure

The method of forcing the dissolution of deposits was investigated in the 100 cm^2 flow cell using the fully-divided configuration and the VPX-20 membrane. Fresh electrolyte was used: 1 dm^3 of 1.2 M Pb^{2+} and 0.5 M MSA (negative) / 1 dm^3 of 1.2 M Pb^{2+} and 0 M MSA (positive), with 1 g dm^{-3} sodium lignosulfonate (negative) / 5 mM Bi^{3+} and 10 mM F^- (positive). The flow rate was initially set at 8.7 cm s^{-1} and the experiment took place at room temperature, 296 K, with no temperature control.

The cell was charged to 75% Pb^{2+} utilisation by charging at 30 mA cm^{-2} for 16 hrs. However, after 3.74 hrs, shorting was observed in the potential-time response, and it was later noted that the Leit-C conductive cement had not been properly removed from the internal walls of the half-cells after having fixed the RVC into place, likely leading to faster growth of deposits along these areas. The cell subsequently achieved 3500 s of discharge down to 0 V. At this point, the cell regeneration technique was applied: the electrode polarities were switched and the cell charged at low current densities whilst ensuring that the voltage stayed below zero. The procedure consisted of four stages:

(a) 16 hrs of charge at 30 mA cm^{-2} (shorting seen from 3.74 hrs)

(b) 3500 s of discharge achieved at 30 mA cm^{-2}

(c) Electrode polarities switched and regenerative charging started, lasting 34 hrs overall:

(i) >10 mA cm^{-2} for 0.93 hrs

(ii) 10 mA cm^{-2} for 4.4 hrs

(iii) 5 mA cm^{-2} for 5.85 hrs

(iv) 1 mA cm^{-2} for 23.15 hrs

(d) Electrodes returned to original polarities and galvanostatic charge/discharge cycling implemented. One cycle consisted of a 1 hr charge at 30 mA cm^{-2}, 2 mins rest, 30 mA cm^{-2} discharge to 0.7 V or max 1 hr, 2 mins rest.

10.3 Results

The results are presented in Figure 10.1, where images (a) - (d) correspond to the experimental stages described in the previous section.

In Figure 10.1a, the potential-time response of the charge phase can be seen. Shorting noise begins from 3.74 hrs, preceded by a sudden drop in potential from 2.29 V to 2.18 V. At this point, 11.22 Ah of charge had been supplied to the cell. Beyond this point, the proportion of current leading to deposition of lead and lead dioxide is uncertain, but it is likely to be low due to the contact between deposits shorting the cell. Furthermore, no significant crossover of electrolyte from one tank to the other was observed, suggesting that the membrane was not punctured. This then suggests that several lead and lead dioxide deposits were instead only contacting the same position at either side of the membrane, and because the membrane is weakly electrically conductive, shorting could occur. Another speculation is the presence of micro-punctures through the membrane that could produce shorting without significant crossover of electrolyte. It is clear that the cell has failed but regeneration still remains possible as the membrane appeared to be largely intact. This needs to be studied in detail in future, either using SEM imaging of the separator before and after the test to shed light on the separator pore size and general structure, or by using techniques such as X-ray tomography to capture the growth of the deposits that would be causing such punctures.

The cell was then discharged at 30 mA cm^{-2}, as seen in Figure 10.1b, which lasted just 3500 s before the potential dropped to 0 V. The first discharge lasted 1525 s before being cut-off at

1 V, whilst the second discharge lasted 1860 s down to 0 V. The cell was held at rest for 120 s in between the discharges, during which time the cell potential rose to 1.60 V. Stages (a) and (b) produced a charge, voltage and energy efficiency of 25%, 35% and 9% respectively. A total of 2.83 Ah was discharged in (b), leaving 8.39 from the original 11.22 Ah worth of deposits at the electrodes.

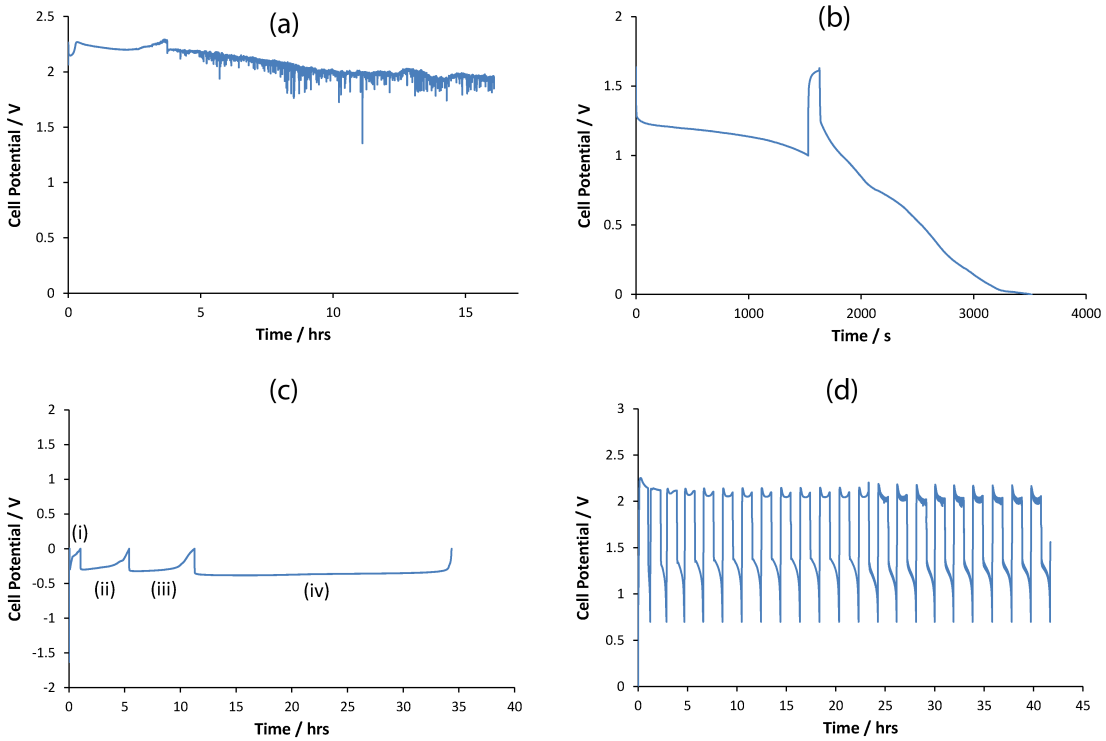

Figure 10.1: Potential-time responses of all stages of the regeneration procedure: (a) failure from shorting during charge; (b) discharge to 1 V, and then to 0 V; (c) the regenerative charging where, in mA cm^{-2}, (i) >10, (ii) 10, (iii) 5, (iv) 1; (d) standard charge/discharge cycling. Electrolyte: 1 dm^3 of 1.2 M Pb^{2+} and 0.5 M MSA (negative) / 1 dm^3 of 1.2 M Pb^{2+} and 0 M MSA (positive). Additives: 1 g dm^{-3} sodium lignosulfonate (negative) / 5 mM Bi^{3+} and 10 mM F^- (positive). Separator: VPX-20, fully-divided. Electrode: 100 cm^2, carbon/polyvinyl ester, with 90 ppi RVC, attached using Leit-C conductive cement. Electrolyte volume: 2 dm^3. Flow rate: 8.7 cm s^{-1}. Temperature: 296 K.

The electrode polarities were then switched and the cell was charged at decreasing current densities from 35 mA cm^{-2} to 1 mA cm^{-2}, which can be seen in Figure 10.1c. The former lasted 113 s, averaging -0.12 V before surpassing 0 V. Stripping at higher current densities would reduce the amount of maintenance time and hence the amount of time the battery remains inoperable. In addition, stripping at higher rates is only possible with thicker deposits; hence the regeneration process should commence at high current densities. As the deposits

deplete, the current density should be decreased accordingly. The amount of stripping was greatest at 10 mA cm^{-2}, where 4.4 Ah worth of deposit was stripped. At 5 mA cm^{-2}, 2.93 Ah was supplied to strip the deposits. At 1 mA cm^{-2}, 2.32 Ah was supplied across the 23.15 hrs. In total, 2.88 Wh of electrical energy and 11.84 Ah of charge was used to strip the deposits. The charge supplied is slightly greater than the net 8.39 Ah calculated after the charge and discharge in stages (a) and (b), but that figure did not include any deposition occurring during the shorting region of the charge phase. These calculations also assume a 100% Faradaic efficiency.

The potential-time response in Figure 10.1c and the charge calculations indicate that the majority of deposits have been stripped, but this was not confirmed as the cell was not dismantled after the regeneration stage. Instead, the cell was put through a series of charge/discharge cycles, seen in Figure 10.1d, to see if the system had returned to its starting conditions. 22 cycles were achieved overall across 42 hrs and the potential-time response is characteristic of cycling experiments seen in other experiments in both the 9 cm^2 and 100 cm^2 flow cells. The charge efficiency is only 20% at the first cycle, rising to 90% by the 8^{th} cycle. The average charge, voltage and energy efficiencies of these 22 cycles were 83%, 59% and 49% respectively, considerably lower than those seen in other cycling tests (Chapter 9). Signs of light shorting can be seen at the 13^{th} cycle causing the performance to decrease and changing the shape of the potential-time profile. Membrane puncture was then observed at the end of the 22 cycles, where the positive electrolyte tank had mostly emptied into the negative. Nevertheless, 22 cycles were achieved from a system that had clearly previously failed.

When the cell was opened at the end of the test, the RVC at both electrodes was thoroughly coated in deposit, but there were no abnormal accumulations or growths detected across the RVC surface; all appeared smooth. Around the electrode edges, deposits were seen growing along the sides of the cell wall and clearly tearing through the membrane.

10.4 Summary

A method of rebalancing a failed cell has been demonstrated. A cell that had clearly failed and rendered inoperable was put through a series of regeneration cycles, which stripped much

of the deposits on the electrodes and allowed 42 hrs of further operation. The membrane punctured at this point from deposit growth, particularly PbO_2, along the cell's internal walls beside the electrode. These are likely to have been isolated from the electrode during the regeneration process (due to deposits closer to the electrode dissolving first). They could then reconnect with the electrode on subsequent cycles due to deposition growth resuming from the electrode surface, allowing the deposit to advance towards the membrane. This would explain the shorting seen at cycle 13 in stage 10.1d.

Future work must focus on improving this regeneration technique and commencing it before the onset of shorting in order to stem the growth of these deposits along the cell walls. Additionally, a novel cell design is also required to slow or prevent the nucleation and growth of deposits in these regions, as this appears to be the main impediment to further development. The nature of shorting must also be studied, as it was seen here that shorting can occur without necessarily entirely puncturing the separator.

Chapter 11

5 kW/10 kWh SLFB Stack Model

11.1 Introduction

This chapter is divided into two sections. In the first, data from the previous chapters is brought together to model the properties of a 5 kW/10 kWh stack. Much of the design is based around the commercial RedFlow ZBM 2 zinc-bromine flow battery, which is used as a benchmark. This is the most similar battery to the SLFB in terms of the chemical reactions, design considerations and maintenance requirements. The subsequent section introduces a possible SLFB cell design to mitigate the accumulation and growth of deposits along the cell walls that border the electrode.

11.2 Stack Model

Two battery models are explored: one containing 1.2 M Pb^{2+} in solution, with a maximum discharge current of 125 A (SLFB I), and one containing a theoretical concentration of 1.7 M Pb^{2+}, with a maximum discharge current of 150 A. Further inputs and properties are summarised in Tables 11.1 and 11.2; the figures provided are rounded to the nearest integer where appropriate. The models also assume galvanostatic operation. Furthermore, the models are

generic and do not specifically refer to a semi or fully-divided system.

	RedFlow ZBM 2	**SLFB I**	**SLFB II**
Reference	[114], [110]	-	-
Inputs			
Energy Capacity / kWh	10	10	10
Discharge Power / kW	5.0	5.0	5.0
Duration at Rated Power / mins	45[i]	-	-
No. of Stacks	3	2	2
Cells in Each Stack	33	32	27
Max., on discharge			
Current Density / mA cm^{-2}	n/a	100	100
Battery Current / A	125	125	150
Stack Current / A	42	63	75
Battery Voltage / V	40	40	33
Cell Potential / V	1.21	1.25	1.23
Electrode Area / cm^2	n/a	625	750
Max., on charge			
Current Density / mA cm^{-2}	n/a	50	50
Battery Current / A	60	63	75
Stack Current / A	20	32	38
Battery Voltage / V	66	77	65
Cell Potential / V	2.0	2.25	2.25
Battery Power / kW	4.0[ii]	4.5	4.6
Charge Capacity / Ah	250	250	300

Table 11.1: A comparison of two SLFB models with the RedFlow ZBM 2 flow battery, with data taken directly from the included references. [i]when discharged at 5 kW from 100% SoC; [ii]calculated based on the published charge current and voltage data.

Battery current is split evenly between the number of stacks whilst each stack voltage equals the overall battery voltage. The ZBM consists of 3 stacks connected in parallel, with 33 cells

connected in series within each stack. This design is likely intended to improve the current of the system, as a single zinc-bromine cell operates at low current densities of around 15 - 30 mA cm^{-2} [16]. Starting at 100% SoC, the ZBM can discharge at 5 kW for a maximum of 45 mins. Only 2 stacks are used in the SLFB models due to the ability of discharging at higher rates. The cell number in each stack is not an input but rather based on the cell potential at the maximum current density and the overall battery current.

In SLFB I, the battery discharge voltage must be 40 V if current is drawn at 125 A in order to supply 5 kW of power. If the current density at this maximum current is 100 mA cm^{-2}, then each cell potential would be 1.25 V, which was seen at 100 mA cm^{-2} at 50% Pb^{2+} utilisation in the battery polarisation tests (Chapter 9). Roughly the same potential is assumed in SLFB II. Therefore in SLFB I, 32 cells are required for a 40 V battery voltage. Similarly in SLFB II, 27 cells are required for a battery voltage of 33 V, based on a maximum current draw of 150 A.

The electrode dimensions for the ZBM are not publicly available. In the SLFB models, the electrode area was taken as a function of the system's maximum discharge current density and the maximum battery discharge current. In SLFB I and II, the current splits evenly into the two stacks connected in parallel; this is then divided by the maximum current density to provide the required electrode area, 625 cm^2 and 750 cm^2 respectively.

The maximum charge current and voltage of the ZBM has previously been characterised, at 60 A and 66 V respectively [110]. In the SLFB models, 50 mA cm^{-2} was selected as the maximum charge current density based on the 9 cm^2 flow cell results, where charge efficiencies close to 90% were achieved (Chapter 8). The charge efficiency was seen to drop to too low a value for practical use at higher current densities beyond 50 mA cm^{-2}. Based on this value, the total battery charge current could be calculated as the electrode area is now defined. This leads to a charge current of 63 A and 75 A for models I and II respectively. From the cell polarisation tests, at 50% Pb^{2+} utilisation, a 50 mA cm^{-2} charge current density caused the cell potential to shift to 2.25 V. As the number of cells in each stack is known, the total charge voltage could be calculated, yielding 77 V and 65 V for models I and II respectively. Hence the battery charge power of all three could be deduced, ranging from 4 kW (ZBM) to 4.6 kW (SLFB II).

Finally, the charge capacity is calculated by dividing the energy capacity, in Wh, by the maximum battery discharge voltage, in V. This yielded 250 Ah for the ZBM and SLFB I, and 300 Ah for the SLFB II. Table 11.2 continues the model, focusing on the electrolyte and electrodes.

	RedFlow ZBM 2	**SLFB I**	**SLFB II**
Reference	[114], [110]	-	-
[Active Species] / M	n/a	1.2	1.7
[Usable Species] / M	1.54[i]	1.0	1.5
Solution Density[ii] / g cm^{-3}	n/a	1.41	1.57
Calculated, based on electrolyte			
Charge Density / Ah dm^{-3}	83[iii]	27	40
Energy Density / Wh dm^{-3}	100	34	50
Specific Energy / Wh kg^{-1}	69	24	32
Electrolyte Volume / dm^3	100	298	201
Electrolyte Mass / kg	146	420	317
***Calculated, each electrode*[iv]**			
Pb Deposit Width, 100% SoC / mm	-	0.66	0.66
PbO_2 Deposit width, 100% SoC / mm	-	0.95	0.95

Table 11.2: A further comparison of two SLFB models with the RedFlow ZBM 2 flow battery, with data taken directly from the included references. The electrolyte volume is overall, including positive and negative. [i]calculated value based on published data, [ii]densities calculated based on the active species concentration and 0.5 M MSA, [iii]calculated based on published data, [iv]based on Equation 2.14.

SLFB I uses 1.2 M Pb^{2+}, the concentration widely used in the previous chapters. Model II is based around a higher concentration of 1.7 M. In both cases, 100% SoC is defined at a 0.2 M Pb^{2+} concentration remaining in the electrolyte as to avoid the problems associated with mass transport limitations. The solution density is then calculated based on the initial active species concentrations and a 0.5 M initial MSA concentration. The density of the electrolyte in SLFB II is greater than that of SLFB I, 1.57 g cm^{-3} and 1.41 g cm^{-3} respectively, due to the higher concentration of Pb^{2+} (Chapter 4).

The charge density could now be calculated from the 'usable species' concentration, i.e the amount that can be deposited at the electrodes, following modification of Equation 2.15. A 0.2 M difference in Pb^{2+} concentration results in a 13 Ah dm^{-3} difference in charge density, from 27 to 40 Ah dm^{-3}. This leads to a higher energy density in model II, after the charge capacity is multiplied with the corresponding maximum discharge cell potentials, 1.25 V and 1.23 V for models I and II respectively. The specific energy was calculated by dividing the energy density by the electrolyte density. The energy density and specific energy values can be improved by increasing the cell potential with a more efficient cell design than the one used to characterise the power density in Chapter 9.

The required electrolyte volume and its mass can now be deduced by dividing the energy capacity, 10 kWh, by the respective energy densities. The presented volumes are overall volumes. In the ZBM, it is assumed that 50 dm^3 is used each in the positive and negative electrolytes respectively; this equal division is definitely the case in the SLFB models. At 298 dm^3, almost three times as much electrolyte is required in SLFB I compared to the ZBM. This is reduced to 201 dm^{-3} in SLFB II, which is still considerably greater than the 100 dm^3 used in the ZBM. However, only two stacks are required for the SLFB models, which would narrow the difference in overall mass of the system (battery + electrolyte).

The energy density, 100 Wh dm^{-3}, and specific energy, 69 Wh kg^{-1}, of the ZBM was calculated from the volume and mass of the electrolyte, which were both publicly available [110]. The energy density was divided by the maximum discharge cell potential, 1.21 V, to produce a charge density of 83 Ah dm^{-3}. From this, the active species concentration was deduced, yielding 1.54 M.

Finally, the theoretical deposit thickness at 100% SoC can be calculated from Equation 2.14. The lead deposit width at each negative electrode in both models is 0.66 mm and the lead dioxide width at each positive electrode in both models is 0.95 mm. Because of the procedure followed to calculate the electrode area and number of cells, the deposit widths are exactly the same. Both are below 1 mm, which would mitigate the problems associated with thick deposits, which were previously discussed in Chapter 2.5.3. The theoretical width of the zinc deposit in the ZBM cannot be calculated as the electrode dimensions are unknown.

11.3 Modifications to the 100 cm^2 Flow Cell

Throughout the project, the growth of both lead and lead dioxide across the internal cell walls around the electrodes over many charge/discharge cycles has been reported. The literature has shown that ultimately this results in shorting of the cell when the growths make contact. In Chapter 9, this resulted in the puncture of the separator before shorting of the cell was seen. A cell design modification is therefore proposed to counter this problem.

As mentioned previously in Chapter 3, the 100 cm^2 cell was designed using engineering analysis conducted by C-Tech Innovation. The cell was redrawn on SolidWorks during this PhD to include 10 mm wide 'bypass' channels, where some of the flow would pass through the cell without coming into contact with the electrode. The inlet/outlet flow channels are unchanged. The filling chamber and ringed distributor are widened to incorporate the bypass channels. The purpose of this inclusion is to stun the deposit creep along the walls. It is theorised that a longer route to the separator could completely prevent deposits contacting the separator, preventing the chances of separator puncture and shorting. The height of the bypass region is set at 3 mm from the electrode surface, with a further 3 mm until the separator. The electrode-separator gap therefore is unchanged, at 6 mm. This is shown in Figure 11.1. Figure 11.2b describes this modification further. Figure 11.2a illustrates the original design by C-Tech.

In Figure 11.2a, the cell frame is perpendicular to the electrode surface and measures 6 mm between the separator and the electrode. It is along this surface at either side of the electrode that both lead and lead dioxide deposits were seen to grow, eventually contacting the separator and tearing through. The conditions affecting this rate of growth need to be understood. This would involve X-ray tomography studies during charge/discharge cycling at different SoC, flow rates, and Pb^{2+}, MSA and additive concentration. If this is understood, a cell frame such as that shown in Figure 11.2b could be designed, where the deposit growth path towards the separator is extended. A bypass region for the flow ensures that deposits would have to grow horizontally across the cell wall, perpendicular to the flow direction. This region is arbitrarily set at 10 mm in this design but if the deposit growth rate is understood, then this length could be increased or decreased to ensure that the deposit does not contact

the second 3 mm vertical rise at 100% SoC.

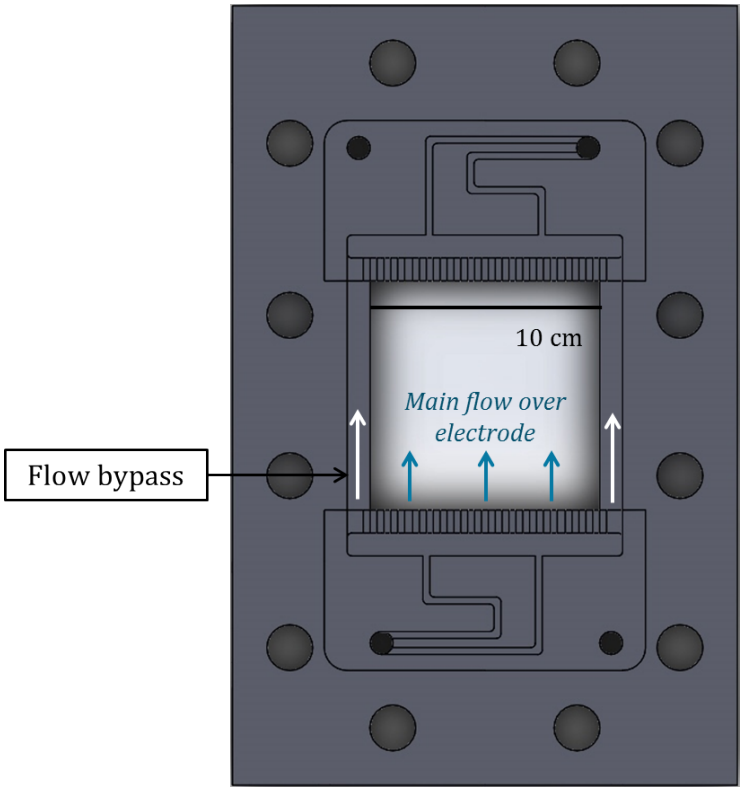

(a)

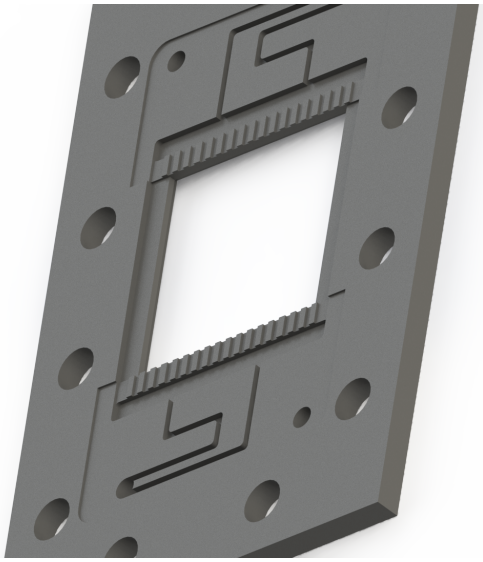

(b)

Figure 11.1: (a) 2D view (front) and (b) 3D view of a 'bypass flow' modification made to the 100 cm^2 flow cell designed by C-Tech (for further dimensions, please refer to Figure 3.5). There are 10 mm wide bypass regions bordering the electrode. They are positioned 3 mm from the front surface (i.e. into the page), with the electrode surface a further 3 mm below. The separator-electrode gap is the same as before, at 6 mm. The electrolyte enters from the bottom left and flows upwards, exiting at the top right.

Additionally in Figure 11.2b, the separator is welded into a polymer sleeve and is kept suspended directly above the electrode area, protecting the separator from any mechanical stress from cell compression. Furthermore, it extends the distance of the deposit growth path between the electrode and separator. The polymer would be of a tougher material than the separator, providing good resistance against tearing.

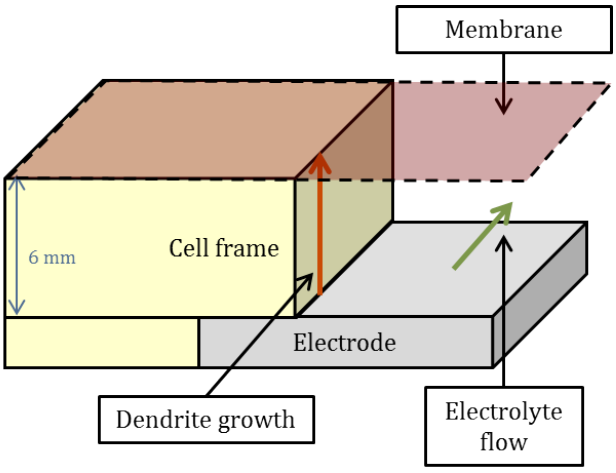

(a) 100 cm^2 cell

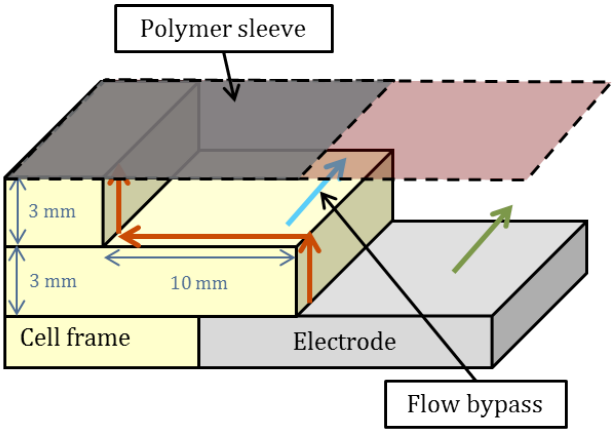

(b) Bypass flow

Figure 11.2: 3D comparison of the 100 cm^2 flow cell's internal design to a theoretical design incorporating a bypass flow stream and a separator welded into a polymer sleeve.

However, a possible disadvantage of the bypass design is that growth along this region could be knocked and dislodged by the flow. This would fall and accumulate at the bottom of the cell which would result in a loss in energy capacity, as well as potentially blocking the inlet channels. If future tests show that this is the most prevalent observation, then further SLFB

development should rather focus on various cell regeneration techniques.

11.4 Summary

Two SLFB models have been proposed using the RedFlow ZBM 2 flow battery as a benchmark. Despite having fewer stacks, the SLFB models are likely to be heavier overall due to the considerably greater amount of electrolyte. Lead is denser than zinc, and because two moles of lead are consumed per unit charge the electrolyte will always have a lower charge density than its zinc-bromine counterpart. However, the electrolyte volume calculations here depended on the discharge potential, which would be greater at lower operational current densities, leading to a lower required volume of electrolyte for the necessary Wh of storage. Hence a compromise exists between maximum current density and electrolyte volume. Increasing the Pb^{2+} concentration in the electrolyte would also decrease the amount of electrolyte required. Also, the effect of additives is not taken into account when calculating the solution density.

The cell potential, 1.25 V, was based on observations made with the 100 cm^2 flow cell in Chapter 9. Optimised cell designs would lead to a lower drop in potential. In addition, the possibility of discharge current densities greater than 100 mA cm^{-2} was discussed in Chapter 9, which would lead to smaller electrodes, or greater power if the electrode areas are kept as they are.

A modification was suggested to the 100 cm^2 C-Tech cell design, in which a bypass region was included to lengthen the deposit growth path of the lead and lead dioxide deposits between the electrode and the separator. Another important inclusion was the use of separators welded into polymer sleeves, which would remove the mechanical stress faced by the separator during cell compression whilst further increasing the growth path. X-ray tomography studies are suggested in future to understand the development of these growths. Furthermore, CFD simulations would inform the positioning of distributor islands and help to define the shape of the inlet and outlet islands.

Chapter 12

Conclusion and Further Research

Several novel developments in soluble lead flow cell research have been described, centred around the electrolyte composition and two different separator-divided cell configurations. A better understanding of the physical electrolyte properties has been established, and cyclic voltammetry and charge/discharge tests have resulted in the formation of more efficient electrolytes. These have been used to successfully scale the system from the 9 cm^2 electrode level to the 100 cm^2 electrode level, surpassing the efficiencies and cell lifetimes seen previously in the literature. In brief:

1. Two novel electrolyte compositions were formulated:

   (I) VPX-20 semi-divided: 0.7 M Pb^{2+} and 1.0 M MSA (1.64 mPa·s, 279 mS cm^{-1}), with 1 g dm^{-3} lignosulfonate and 15 mM Bi^{3+}.

   (II) VPX-20 fully-divided: 1.2 M Pb^{2+} and 0.5 M MSA (negative, 1.97 mPa·s, 203 mS cm^{-1}) / 1.2 M Pb^{2+} and 0 M MSA (positive, 1.85 mPa·s, 140 mS cm^{-1}), with 1 g dm^{-3} lignosulfonate (negative) / 5 mM Bi^{3+} and 10 mM F^- (positive).

   The numbers in parentheses are the dynamic viscosity (296 K) and ionic conductivity (298 K) respectively of the electrolyte without additives. Electrolyte (II) was calculated to hold a specific energy of 24 Wh kg^{-1} (per kg electrolyte) based on a 1 M 'usable' Pb^{2+} concentration and a 1.25 V cell potential (recorded at 100 mA cm^{-2} discharge current density at 50% SoC).

2. A novel 'semi-divided' soluble lead flow cell has been tested on the 100 cm^2 electrode scale using electrolyte (I), achieving 150 cycles at 88% charge and 84% voltage efficiency (20 - 30 mA cm^{-2}, 1 hr charge/discharge). This is a good improvement to the 40 cycles achieved previously at 88% charge and 74% voltage efficiency under similar conditions.

3. The novel 'fully-divided' soluble lead cell was also tested at several SoC (10 - 50%) using electrolyte (II) in the 100 cm^2 cell. A peak discharge power of 12.5 W (125 mW cm^{-2}) was maintained for 60 s, the highest power produced from a single soluble lead flow cell relative to other published work.

Formulating an improved electrolyte composition involved two stages: optimising the Pb^{2+} and MSA concentrations, and then exploring the effect of additives. These studies showed that electrolyte viscosity increases linearly with both [Pb^{2+}] and [MSA], though it is mostly dependent on the former. Electrolyte conductivity was seen to follow a more complex relationship, decreasing and increasing with rising [Pb^{2+}] when [MSA] is $\geq$1.0 M and $\leq$0.25 M respectively. When 0.25 M$\leq$[MSA]$\leq$1.0 M, the conductivity peaks near 0.75 M Pb^{2+}. The conductivity was also observed to increase sharply with increasing MSA. Therefore, in a cycling experiment, the conductivity is expected to increase with SoC (where there is fewer dissolved Pb^{2+} and increased acidity). In contrast, the electrolyte viscosity will decrease with SoC. Static cell cycling showed that 0.7 M - 1.25 M was the most suitable Pb^{2+} starting concentration and 0.25 M - 1.0 M to be the most suitable MSA concentration. Though if [Pb^{2+}] is closer to 1.25 M, [MSA] must be kept low.

Early flow cell cycling tests compared three different cell configurations: undivided, semi-divided and fully-divided. The novel semi-divided configuration divides the cell with a separator, but the same electrolyte flows through each half-cell. The fully-divided format follows the design of traditional flow cells, where a unique electrolyte flows through each half-cell. The VPX-20 membrane was found to exhibit the lowest ohmic resistance, performing better than the more expensive Nafion 115, and was preferred in these experiments and most of the later experiments. By simply inserting a membrane, which acted as a physical barrier against shorting, the lifetime of the cell was seen to increase.

A novel combination of additives was introduced to improve efficiency and % Pb^{2+} utilisation, leading to an improved cycle life. Lignosulfonate at a concentration of 1 g dm^{-3} was preferred

over HDTMA, the more popular additive in the literature [34], to control the deposition of lead at the negative electrode. Bismuth and fluoride were employed to improve the kinetics and adhesion respectively of PbO_2 at the positive electrode. However, the optimal concentrations are yet to be deduced. Generally, 5 mM - 15 mM Bi^{3+} and 10 - 25 mM F^- was preferred. In charge/discharge cycling, where the depth of charge is shallow, i.e. $\leq$10% Pb^{2+} utilisation, the inclusion of additives will limit the charge efficiency of the initial cycles, gradually increasing thereafter to efficiencies superior to those that would be seen if additives were not used. A number of mechanisms were theorised but it is not clear exactly why this behaviour occurs. The higher charge efficiencies invariably lead to an improved lifetime. However, there is a slight voltage efficiency penalty if using additives (though the overall energy efficiencies are comparable).

Further research is required to characterise the semi and fully-divided configurations. Bismuth is not suitable for use in a semi-divided format, where it was seen to interfere with lead deposition/stripping. Additionally, it remains to be seen if lignosulfonate remains stable in the semi-divided format, or if the loss of the amber colour due to the lignosulfonate after several cycles does in fact suggest a breakdown of the additive.

In the fully-divided system, zero crossover of lignosulfonate through the VPX-20 membrane from the negative to the positive half-cell was observed from visual inspection (i.e. the positive electrolyte did not become amber coloured). As the VPX-20 is an anion exchange membrane, it was possible to alter the starting MSA concentration in each half-cell: 0.5 M (negative) and 0 M (positive). 0.5 M therefore could be maintained in the negative half-cell throughout operation, as H^+ is only produced during charge at the positive electrode. If using 1.2 M Pb^{2+}, the acidity in the positive chamber would increase by 4.8 M between 0% and 100%, hence the starting [MSA] was 0 M. However, the crossover of H^+, Bi^{3+} and F^- from the positive to the negative half-cell during extended cycling was not studied.

Two research paths have now been opened by this project: semi-divided and fully-divided. Both systems must be further characterised before the superior of the two can be concluded. At present, the fully-divided configuration is more complicated and will result in a more expensive cell design. The semi-divided system has the advantage that it does not require an expensive separator as preventing crossover is not necessary. The VPX-20 could be replaced

by a cheap microporous separator such as FF60. However, further additives must be tested to replace Bi^{3+} and possibly lignosulfonate as well. It would also be beneficial to repeat the conductivity and viscosity tests with additives present.

Cycling tests on the 100 cm^2 scale produced a significant improvement to the literature. Electrolyte (I) in a semi-divided format and RVC electrodes were used to achieve 150 charge/discharge cycles, averaging 88% charge and 84% voltage efficiency. Under similar conditions, the previously most successful comparable experiment achieved 40 cycles, averaging 88% charge and 74% voltage efficiency [34]. The lifetime has been improved almost fourfold and the energy efficiency has increased 8 percentage points from 65% to 73%. Future work must aim to improve on these results whilst increasing the depth of charge, i.e. ultimately achieving full charges/discharges at high efficiency, repeatable over several hundreds of cycles.

RVC was seen as an important contributor to controlling the deposit morphology. However, the Entegris carbon polyvinyl-ester electrodes used in this project were not suitable foundations for the pressure welding of RVC. RVC was either compressed against the face of the electrodes or glued using Leit-C conductive cement. It would be preferable in future to find a material onto which RVC could be pressure welded, so that the electrical conductivity is greatly enhanced. Additionally, RVC has a low stability as the positive electrode and should be substituted with another material; it is likely that a carbon-based electrode will not be able to remain intact in the oxidising and highly acidic conditions.

Composition (II) was also tested in the 100 cm^2 cell, where its power curve was characterised at multiples levels of Pb^{2+} utilisation, simulating different states of charge. A 100 mA cm^{-2} discharge was achieved, higher than in any previous publication, and sustained for 60 s, discharging at a peak power of 12.5 W. The system was not pushed further; however, 150 mA cm^{-2} was achieved with the 9 cm^2 flow cell. From the studies in this project, it is recommended that the charging current not surpass 50 mA cm^{-2}. The maximum discharge current in contrast could surpass 200 mA cm^{-2} and remains to be seen in future work. Once a full current density/power density characterisation is completed (completing the power curves in Chapter 9), an improved model for a battery stack, including the necessary electrical infrastructure for integration with an energy capture device, can be designed.

The flow rate through each half-cell was seen to reduce as the deposits at each electrode grew thicker, suggesting that pressure drop increases greatly with SoC. This was not explored in this project but would be a useful study in future. Furthermore, the results of this could be combined with the viscosity and conductivity data discussed earlier in order to aid with modelling of the cell operation.

A method of forcing the dissolution of accumulated deposits has also been introduced as part of a regeneration procedure to return the cell to its initial, fully discharged state without having to dismantle the cell. Such strategies will be important in further development of the system. Further sophisticated techniques remain to be trialled, such as those employed in zinc-bromine flow battery maintenance. One such strategy is to short the electrodes across a low-impedance shunt in order to quickly dissolve any accumulated deposits [110]. From this study, it was also seen that shorting occurs near 60% Pb^{2+} utilisation if using composition (II) with 1 dm^3 of electrolyte for each half-cell and 100 cm^2 electrodes. Shorting only occurred along the side walls inside the cell. Future cell design must take into account an electrolyte volume/electrode area optimal ratio and avoid cell designs where a scaffold for deposit growth exists. A simple SLFB stack model was described where electrode area was dependent on the battery's power requirement, with further calculations ensuring that deposit thickness at 100% Pb^{2+} utilisation remained below 1 mm at each electrode.

Regarding cell design, flow channels beside the electrode, where part of the flow could bypass the electrode, were discussed to increase the deposit growth path between separator and electrode. X-ray tomography of cells during charge/discharge cycling would greatly improve the understanding of how these designs enhance or diminish abnormal deposit growth along the edges. CFD simulations would aid in the design of flow distribution, and together these studies could be used to model deposit growth over extended cycling.

Further research must also investigate the tendency of the cell to self-discharge. It is likely that if energy is to be stored for long periods, i.e. for spinning-reserve applications, electrolyte must be removed from the cell and replaced with an inert aqueous substance. Alternately, the ability to dissolve 'dry' deposits could also be researched and compared to deposits stored under wet conditions. Additionally, there has been no consideration of thermal control of the electrolyte. The fully-divided system is now at a stage where cells can be combined to produce

a stack, where thermal management (particularly of inner cells) becomes relevant.

To conclude, the project has improved the understanding of the soluble lead system, improved its overall performance and identified several further research areas, including scientific, engineering and modelling work. In addition, an economic analysis could be made, taking into account large volumes of electrolyte, cell materials and auxiliary systems such as pumping, cooling and the necessary power electronics. Much development still remains for the SLFB, but the promising results in this thesis have indicated that the system is certainly suitable for further scale-up.

References

[1] "World Energy Council: World energy resources 2013 survey." http://www.worldenergy.org/publications/2013/world-energy-resources-2013-survey/. Accessed: April 2015.

[2] "US Energy Information Administration: International Energy Statistics." http://www.eia.gov/cfapps/ipdbproject/IEDIndex3.cfm?tid=44&pid=44&aid=2#/. Accessed: April 2015.

[3] "World Health Organisation: Climate change and health." http://www.who.int/mediacentre/factsheets/fs266/en/, note = Accessed: June 2016,.

[4] "Institute for Health Metrics and Evaluation: Global burden of disease." http://www.healthdata.org/gbd, note = Accessed: June 2016,.

[5] H. Chen, T. Cong, W. Yang, C. Tan, Y. Li, and Y. Ding, "Progress in electrical energy storage system: A critical review," *Progress in Natural Science*, vol. 19, no. 3, pp. 291 – 312, 2009.

[6] "US Office of Electricity Delivery and Energy Reliability: Smart grid." http://energy.gov/oe/services/technology-development/smart-grid. Accessed: April 2015.

[7] "US Department of Energy: Global Energy Storage Database - Glossary." https://www.energystorageexchange.org/application/glossary. Accessed: June 2016.

[8] T. Ross, "The Telegraph: Wind farms paid £1m a week to switch off." http://www.telegraph.co.uk/news/earth/energy/windpower/11323685/Wind-farms-paid-1m-a-week-to-switch-off.html. Accessed: June 2016.

[9] D. Sutanto and W. Lachs, "Battery energy storage systems for sustainable energy development in asia," *Electric Power Systems Research*, vol. 44, no. 1, pp. 61 – 67, 1998.

[10] K. Divya and J. Østergaard, "Battery energy storage technology for power systems—an overview," *Electric Power Systems Research*, vol. 79, no. 4, pp. 511–520, 2009.

[11] J. Baker and A. Collinson, "Electrical energy storage at the turn of the millennium," *Power Engineering Journal*, vol. 13, no. 3, pp. 107–112, 1999.

[12] "US Department of Energy: Global Energy Storage Database." http://www.energystorageexchange.org. Accessed: June 2016.

[13] I. B. T. Lima, F. M. Ramos, L. A. W. Bambace, and R. R. Rosa, "Methane emissions from large dams as renewable energy resources: A developing nation perspective," *Mitigation and Adaptation Strategies for Global Change*, vol. 13, no. 2, pp. 193–206, 2008.

[14] A. A. Agostinho, F. M. Pelicice, and L. C. Gomes, "Dams and the fish fauna of the neotropical region: impacts and management related to diversity and fisheries," *Brazilian Journal of Biology*, vol. 68, no. 4, pp. 1119–1132, 2008.

[15] A. A. Akhil, G. Huff, A. B. Currier, B. C. Kaun, D. M. Rastler, S. B. Chen, A. L. Cotter, D. T. Bradshaw, and W. D. Gauntlett, "DOE/EPRI 2013 electricity storage handbook in collaboration with NRECA," Tech. Rep. SAND2013-5131, Sandia National Laboratories, New Mexico & California, USA, July 2013.

[16] D. Linden and T. Reddy, *Handbook of Batteries 3rd.* McGraw-Hill, New York, 2002, ISBN: 0-07-135978-8.

[17] "Battery University: Global Battery Markets." http://batteryuniversity.com/learn/article/global_battery_markets.

Accessed: June 2017.

[18] "US Department of Energy: Global Energy Storage Database - Kyushu Electric - Buzen substation - Mitsubishi Electric/NGK Insulators." `https://www.energystorageexchange.org/projects/2142`. Accessed: July 2016.

[19] C. P. de León, A. Frías-Ferrer, J. González-García, D. Szánto, and F. Walsh, "Redox flow cells for energy conversion," *Journal of Power Sources*, vol. 160, no. 1, pp. 716 – 732, 2006.

[20] A. Weber, M. Mench, J. Meyers, P. Ross, J. G. Q, and Liu, "Redox flow batteries: a review," *Journal of Applied Electrochemistry*, vol. 41, no. 10, pp. 1137–1164, 2011.

[21] C. Menictas, M. Skyllas-Kazacos, and T. Lim, *Advances in Batteries for Medium and Large-Scale Energy Storage*. Woodhead Publishing, Elsevier, UK, 2014, ISBN: 9781782420132.

[22] N. Hagedorn, "Redox storage system development project," Tech. Rep. DOE/NASA/2726-24, NASA, Lewis Research Center, Ohio, USA, October 1984.

[23] M. Skyllas-Kazacos, M. Chakrabarti, S. Hajimolana, F. Mjalli, and M. Saleem, "Progress in flow battery research and development," *Journal of The Electrochemical Society*, vol. 158, no. 8, pp. R55–R79, 2011.

[24] M. Bartolozzi, "Development of redox flow batteries. a historical bibliography," *Journal of Power Sources*, vol. 27, no. 3, pp. 219–234, 1989.

[25] "US Department of Energy: Global Energy Storage Database - Minami Hayakita Substation Hokkaido Electric Power- Sumitomo." `https://www.energystorageexchange.org/projects/2043`. Accessed: July 2016.

[26] P. Leung, X. Li, C. P. De León, L. Berlouis, C. J. Low, and F. C. Walsh, "Progress in redox flow batteries, remaining challenges and their applications in energy storage," *RSC Advances*, vol. 2, no. 27, pp. 10125–10156, 2012.

[27] D. Pavlov, *Lead-acid batteries: science and technology*. Elsevier, UK, 2011, ISBN: 9780444528827.

[28] B. R. Chalamala, T. Soundappan, G. R. Fisher, M. R. Anstey, V. V. Viswanathan, and M. L. Perry, "Redox flow batteries: An engineering perspective," *Proceedings of the IEEE*, vol. 102, no. 6, pp. 976–999, 2014.

[29] J. Larminie, A. Dicks, and M. S. McDonald, *Fuel cell systems explained*, vol. 2. J. Wiley Chichester, UK, 2003, ISBN: 0-470-84857-X.

[30] A. Hazza, D. Pletcher, and R. Wills, "A novel flow battery: A lead acid battery based on an electrolyte with soluble lead(II) part I: Preliminary studies," *Phys. Chem. Chem. Phys.*, vol. 6, pp. 1773–1778, 2004.

[31] R. Wills, J. Collins, D. Stratton-Campbell, C. Low, D. Pletcher, and F. Walsh, "Developments in the soluble lead-acid flow battery," *Journal of Applied Electrochemistry*, vol. 40, no. 5, pp. 955–965, 2010.

[32] L. Wallis and R. Wills, "Membrane divided soluble lead battery utilising a bismuth electrolyte additive," *Journal of Power Sources*, vol. 247, no. 0, pp. 799 – 806, 2014.

[33] A. Hazza, D. Pletcher, and R. Wills, "A novel flow battery—a lead acid battery based on an electrolyte with soluble lead(II) part IV: The influence of additives," *Journal of Power Sources*, vol. 149, no. 0, pp. 103 – 111, 2005.

[34] J. Collins, G. Kear, X. Li, C. Low, D. Pletcher, R. Tangirala, D. Stratton-Campbell, F. Walsh, and C. Zhang, "A novel flow battery: A lead acid battery based on an electrolyte with soluble lead(II) part VIII: The cycling of a 10 x 10 cm^2 flow cell," *Journal of Power Sources*, vol. 195, no. 6, pp. 1731 – 1738, 2010.

[35] D. Pletcher and R. Wills, "A novel flow battery: A lead acid battery based on an electrolyte with soluble lead(II) part II: Flow cell studies," *Phys. Chem. Chem. Phys.*, vol. 6, pp. 1779–1785, 2004.

[36] D. Pletcher and R. Wills, "A novel flow battery—a lead acid battery based on an electrolyte with soluble lead(II) part III: The influence of conditions on battery performance," *Journal of Power Sources*, vol. 149, no. 0, pp. 96 – 102, 2005.

[37] M. Schlesinger and M. Paunovic, *Modern electroplating*, vol. 55. John Wiley & Sons Ltd., New York, 2011, ISBN-13: 9780471168249.

[38] G. Fitzgerald, J. Mandel, J. Morris, and H. Touati, "The Economics of Energy Storage: How multi-use, customer-sited batteries deliver the most services and value to customers and the grid," tech. rep., Rocky Mountain Institute, Colorado, USA, October 2015, http://www.rmi.org/electricity_battery_value.

[39] "US Department of Energy: Global Energy Storage Database - Fort Sill Microgrid - EnSync (Formerly ZBB)." https://www.energystorageexchange.org/projects/94. Accessed: July 2017.

[40] "US Department of Energy: Global Energy Storage Database - Gyeongsan Substation ESS - 48 MW ESS - KEPCO / Woojin / LG Chem." https://www.energystorageexchange.org/projects/2104. Accessed: July 2017.

[41] "US Department of Energy: Global Energy Storage Database - Germany Residential Energy Storage Systems - 34,000 PV Battery Storage Systems @ 2 kW." https://www.energystorageexchange.org/projects/2153. Accessed: July 2017.

[42] Y. Ma, T. Houghton, A. Cruden, and D. Infield, "Modeling the benefits of vehicle-to-grid technology to a power system," *IEEE Transactions on power systems*, vol. 27, no. 2, pp. 1012–1020, 2012.

[43] Yuasa, "Technical Manual, Powersports Batteries." http://www.yuasabatteries.com/pdfs/TechManual_2014.pdf. Accessed: July 2017.

[44] C. Vincent and B. Scrosati, *Modern Batteries 2nd Edition*. Elsevier, 1997, ISBN: 9780340662786.

[45] "Battery University: How does the lead acid battery work?." http://www.batteryuniversity.com/learn/article/lead_based_batteries. Accessed: October 2016.

[46] L. Lam and R. Louey, "Development of ultra-battery for hybrid-electric vehicle applications," *Journal of Power Sources*, vol. 158, no. 2, pp. 1140–1148, 2006.

[47] C. Zhang, S. Sharkh, X. Li, F. Walsh, C. Zhang, and J. Jiang, "The performance of a soluble lead-acid flow battery and its comparison to a static lead-acid battery,"

Energy Conversion and Management, vol. 52, no. 12, pp. 3391 – 3398, 2011.

[48] J. Baldwin, E. Peebles, W. Power, and J. White, "Lead perchloric acid primary cell," Dec. 27 1949. US Patent 2,492,206.

[49] G. McDonald, E. Weissman, and T. Roemer, "Lead-fluoroboric acid battery," *Journal of the Electrochemical Society*, vol. 119, no. 6, pp. 660–663, 1972.

[50] F. Beck, "Titanium and graphite base plates," Jan. 4 1977. US Patent 4,001,037.

[51] R. Wurmb, F. Beck, and K. Boehlke, "Secondary battery," May 30 1978. US Patent 4,092,463.

[52] P. Henk, Z. Piontkowski, and C. Carlsen, "Anode of graphitized textile, resin closure, lead siliconfluoride and methanesulfonate electrolyte mixture," May 25 1982. US Patent 4,331,744.

[53] D. Pletcher, H. Zhou, G. Kear, C. Low, F. Walsh, and R. Wills, "A novel flow battery—a lead-acid battery based on an electrolyte with soluble lead(II) part V: Studies of the lead negative electrode," *Journal of Power Sources*, vol. 180, no. 1, pp. 621 – 629, 2008.

[54] D. Pletcher, H. Zhou, G. Kear, C. Low, F. Walsh, and R. Wills, "A novel flow battery—a lead-acid battery based on an electrolyte with soluble lead(II) part VI: Studies of the lead dioxide positive electrode," *Journal of Power Sources*, vol. 180, no. 1, pp. 630 – 634, 2008.

[55] X. Li, D. Pletcher, and F. Walsh, "A novel flow battery: A lead acid battery based on an electrolyte with soluble lead(II) part VII: Further studies of the lead dioxide positive electrode," *Electrochimica Acta*, vol. 54, no. 20, pp. 4688 – 4695, 2009.

[56] J. Collins, X. Li, D. Pletcher, R. Tangirala, D. Stratton-Campbell, F. Walsh, and C. Zhang, "A novel flow battery: A lead acid battery based on an electrolyte with soluble lead(II) part IX: Electrode and electrolyte conditioning with hydrogen peroxide," *Journal of Power Sources*, vol. 195, no. 9, pp. 2975 – 2978, 2010.

[57] A. A. Shah, X. Li, R. G. Wills, and F. C. Walsh, "A mathematical model for the soluble lead-acid flow battery," *Journal of the Electrochemical Society*, vol. 157, no. 5, pp. A589–A599, 2010.

[58] R. Clarke, B. Dougherty, S. Harrison, J. Millington, and S. Mohanta, "Battery with bifunctional electrolyte," Jan. 17 2006. US Patent 6,986,966.

[59] M. Verde, K. Carroll, Z. Wang, A. Sathrum, and Y. Meng, "Achieving high efficiency and cyclability in inexpensive soluble lead flow batteries," *Energy Environ. Sci.*, vol. 6, pp. 1573–1581, 2013.

[60] A. Velichenko, R. Amadelli, E. Gruzdeva, T. Luk'yanenko, and F. Danilov, "Electrodeposition of lead dioxide from methanesulfonate solutions," *Journal of Power Sources*, vol. 191, no. 1, pp. 103 – 110, 2009. Special Issue on the 7th International Conference on Lead-Acid Batteries, Varna, Bulgaria, 9-12 June 2008.

[61] P. Atkins, *Physical Chemistry*, vol. 6. Oxford University Press, 1997.

[62] A. Tang, J. Bao, and M. Skyllas-Kazacos, "Studies on pressure losses and flow rate optimization in vanadium redox flow battery," *Journal of Power Sources*, vol. 248, pp. 154–162, 2014.

[63] W. Safranek and C. Layer, "Fast rate electrodeposition," *Trans Inst Met Finish*, vol. 53, no. 3, pp. 121–125, 1975.

[64] D. Pletcher, *A first course in electrode processes.* Royal Society of Chemistry, UK, 2009, ISBN: 978-1-84755-893-0.

[65] F. C. Walsh, *A first course in electrochemical engineering.* The Electrochemical Consultancy, UK, 1993, ISBN: 0-9517307-1-1.

[66] J. McCabe, W. Smith, *Unit Operations of Chemical Engineering.* McGraw Hill Kogakusha Ltd, Tokyo, 1976.

[67] R. Perry, D. Green, J. Maloney, M. Abbott, C. Ambler, and R. Amero, *Perry's Chemical Engineers' Handbook*, vol. 7. McGraw-Hill, New York, 1997.

[68] J. Yan, *Handbook of Clean Energy Systems*, vol. 5. John Wiley & Sons Ltd., New York, 2015, 978-1-118-38858-7.

[69] K. M. Cecil, C. J. Brubaker, C. M. Adler, K. N. Dietrich, M. Altaye, J. C. Egelhoff, S. Wessel, I. Elangovan, R. Hornung, K. Jarvis, *et al.*, "Decreased brain volume in adults with childhood lead exposure," *PLoS Med*, vol. 5, no. 5, p. e112, 2008.

[70] S. C. Gilfillan, "Lead poisoning and the fall of Rome.," *Journal of Occupational and Environmental Medicine*, vol. 7, no. 2, pp. 53–60, 1965.

[71] M. A. Riva, A. Lafranconi, M. I. D'orso, and G. Cesana, "Lead poisoning: historical aspects of a paradigmatic "occupational and environmental disease"," *Safety and Health at Work*, vol. 3, no. 1, pp. 11–16, 2012.

[72] M. Pourbaix, *Atlas of Electrochemical Equilibria in Aqueous Solutions*. National Association of Corrosion Engineers, 1974, ISBN: 9780915567980.

[73] S. Barnes and R. Mathieson, *Batteries 2*. Pergamon Press, 2 ed., 1965.

[74] X. Li, D. Pletcher, and F. Walsh, "Electrodeposited lead dioxide coatings," *Chemical Society Reviews*, vol. 40, no. 7, pp. 3879–3894, 2011.

[75] W. Mindt, "Electrical properties of electrodeposited pbo_2 films," *Journal of The Electrochemical Society*, vol. 116, no. 8, pp. 1076–1080, 1969.

[76] A. Kuhn, *The Electrochemistry of Lead*. Academic Press, 1979, ISBN: 978-0124283503.

[77] C. Rosenstein, "Methane sulfonic acid as an electrolyte for tin, lead and tin–lead plating for electronics," *Met. Finish.*, vol. 88, no. 1, pp. 17–21, 1990.

[78] M. Gernon, M. Wu, T. Buszta, and P. Janney, "Environmental benefits of methanesulfonic acid. comparative properties and advantages," *Green Chemistry*, vol. 1, no. 3, pp. 127–140, 1999.

[79] "Sigma Aldrich." `https://www.sigmaaldrich.com/united-kingdom.html`. Accessed: May 2015.

[80] F. C. Walsh and C. P. de León, "Versatile electrochemical coatings and surface layers from aqueous methanesulfonic acid," *Surface and Coatings Technology*, vol. 259, pp. 676–697, 2014.

[81] D. P. Kelly and J. C. Murrell, "Microbial metabolism of methanesulfonic acid," *Archives of Microbiology*, vol. 172, no. 6, pp. 341–348, 1999.

[82] A. Oury, A. Kirchev, and Y. Bultel, "Cycling of soluble lead flow cells comprising a honeycomb-shaped positive electrode," *Journal of Power Sources*, vol. 264, pp. 22–29, 2014.

[83] R. Wills, *A lead-acid flow battery for utility scale energy storage and load levelling.* PhD thesis, University of Southampton, UK, 2004.

[84] M. Fleischmann, J. Mansfield, H. Thirsk, H. Wilson, and L. Wynne-Jones, "The investigation of the kinetics of electrode reactions by the application of repetitive square pulses of potential," *Electrochimica Acta*, vol. 12, no. 8, pp. 967–982, 1967.

[85] I. Sirés, C. Low, C. Ponce-de León, and F. Walsh, "The characterisation of PbO2-coated electrodes prepared from aqueous methanesulfonic acid under controlled deposition conditions," *Electrochimica Acta*, vol. 55, no. 6, pp. 2163–2172, 2010.

[86] C. H. Yeh, C. C. Wan, and J. S. Chen, "Physical and electrochemical characterization of pbo 2 electrode prepared at different H2SO4/H2O/PbO ratios," *Journal of Power Sources*, vol. 101, no. 2, pp. 219–225, 2001.

[87] P. Rüetschi, "Influence of crystal structure and interparticle contact on the capacity of PbO2 electrodes," *Journal of The Electrochemical Society*, vol. 139, no. 5, pp. 1347–1351, 1992.

[88] I. Petersson, E. Ahlberg, and B. Berghult, "Parameters influencing the ratio between electrochemically formed α-and β-pbo 2," *Journal of Power Sources*, vol. 76, no. 1, pp. 98–105, 1998.

[89] H. Chen, L. Wu, C. Ren, Q. Luo, Z. Xie, X. Jiang, S. Zhu, Y. Xia, and Y. Luo, "The effect and mechanism of bismuth doped lead oxide on the performance of lead-acid

batteries," *Journal of Power Sources*, vol. 95, no. 1–2, pp. 108 – 118, 2001. Seventh European Lead Battery Conference.

[90] M. Heinemann, H. Terpstra, C. Haas, and R. De Groot, "Electronic structure of β-PbO2 and its relation with bapbo$_3$," *Physical Review B*, vol. 52, no. 16, p. 11740, 1995.

[91] H. Bode, *Lead-Acid Batteries*. John Wiley & Sons Ltd., New York, 1977, ISBN: 978-0471084556.

[92] R. Kiessling, "Lead acid battery formation techniques." `http://mathscinotes.com/wp-content/uploads/2012/12/lead_acid.pdf`. Accessed: June 2016.

[93] A. Oury, A. Kirchev, Y. Bultel, and E. Chainet, "PbO2/pb^{2+} cycling in methanesulfonic acid and mechanisms associated for soluble lead-acid flow battery applications," *Electrochimica Acta*, vol. 71, no. 0, pp. 140 – 149, 2012.

[94] J. Feng and D. C. Johnson, "Electrocatalysis of anodic oxygen-transfer reactions: Titanium substrates for pure and doped lead dioxide films," *Journal of The Electrochemical Society*, vol. 138, no. 11, pp. 3328–3337, 1991.

[95] J. Cao, H. Zhao, F. Cao, J. Zhang, and C. Cao, "Electrocatalytic degradation of 4-chlorophenol on f-doped pbo 2 anodes," *Electrochimica Acta*, vol. 54, no. 9, pp. 2595–2602, 2009.

[96] R. Amadelli, L. Armelao, A. Velichenko, N. Nikolenko, D. Girenko, S. Kovalyov, and F. Danilov, "Oxygen and ozone evolution at fluoride modified lead dioxide electrodes," *Electrochimica Acta*, vol. 45, no. 4, pp. 713–720, 1999.

[97] M. Chakrabarti, N. Brandon, S. Hajimolana, F. Tariq, V. Yufit, M. Hashim, M. Hussain, C. Low, and P. Aravind, "Application of carbon materials in redox flow batteries," *Journal of Power Sources*, vol. 253, pp. 150–166, 2014.

[98] F. Walsh, L. Arenas, C. P. de León, G. Reade, I. Whyte, and B. Mellor, "The continued development of reticulated vitreous carbon as a versatile electrode material:

Structure, properties and applications," *Electrochimica Acta*, vol. 215, pp. 566–591, 2016.

[99] J. Friedrich, C. Ponce-de León, G. Reade, and F. Walsh, "Reticulated vitreous carbon as an electrode material," *Journal of Electroanalytical Chemistry*, vol. 561, pp. 203–217, 2004.

[100] J. Wang and H. Dewald, "Deposition of metals at a flow-through reticulated vitreous carbon electrode coupled with on-line monitoring of the effluent," *Journal of The Electrochemical Society*, vol. 130, no. 9, pp. 1814–1818, 1983.

[101] C. D. Iacovangelo and F. G. Will, "Parametric study of zinc deposition on porous carbon in a flowing electrolyte cell," *Journal of The Electrochemical Society*, vol. 132, no. 4, pp. 851–857, 1985.

[102] A. Czerwiński and M. Żelazowska, "Electrochemical behavior of lead deposited on reticulated vitreous carbon," *Journal of Electroanalytical Chemistry*, vol. 410, no. 1, pp. 55–60, 1996.

[103] A. Czerwiński and M. Żelazowska, "Electrochemical behavior of lead dioxide deposited on reticulated vitreous carbon (rvc)," *Journal of Power Sources*, vol. 64, no. 1, pp. 29–34, 1997.

[104] A. Oury, A. Kirchev, and Y. Bultel, "A numerical model for a soluble lead-acid flow battery comprising a three-dimensional honeycomb-shaped positive electrode," *Journal of Power Sources*, vol. 246, pp. 703–718, 2014.

[105] F. Rivera, C. Ponce de León, J. Nava, and F. Walsh, "The filter-press fm01-lc laboratory flow reactor and its applications," *Electrochimica Acta*, vol. 163, pp. 338–354, 2015.

[106] L. Arenas, C. P. de León, and F. Walsh, "Engineering aspects of the design, construction and performance of modular redox flow batteries for energy storage," *Journal of Energy Storage*, vol. 11, pp. 119–153, 2017.

[107] F. Walsh, "Electrochemical technology for environmental treatment and clean energy conversion," *Pure and Applied Chemistry*, vol. 73, no. 12, pp. 1819–1837, 2001.

[108] V. Viswanathan, A. Crawford, D. Stephenson, S. Kim, W. Wang, B. Li, G. Coffey, E. Thomsen, G. Graff, P. Balducci, *et al.*, "Cost and performance model for redox flow batteries," *Journal of Power Sources*, vol. 247, pp. 1040–1051, 2014.

[109] C. Yin, S. Guo, H. Fang, J. Liu, Y. Li, and H. Tang, "Numerical and experimental studies of stack shunt current for vanadium redox flow battery," *Applied Energy*, vol. 151, pp. 237–248, 2015.

[110] D. M. Rose and S. R. Ferreira, "Initial test results from the redflow 5 kw, 10 kwh zinc-bromide module, phase 1," Tech. Rep. SAND2012-1352, Sandia National Laboratories, California, USA, February 2012.

[111] "Absolyte GP." `http://www.exide.com/gb/en/product-solutions/network-power/product/absolyte-gp.aspxl`. Accessed: August 2016.

[112] "Tesla Powerwall." `https://www.tesla.com/en_GB/powerwall`. Accessed: August 2016.

[113] "RedT module datasheet." `http://www.redtenergy.com/products`. Accessed: August 2016.

[114] "RedFlow ZBM." `http://redflow.com/wp-content/uploads/2015/11/Redflow-ZBM-Datasheet.pdf`. Accessed: August 2016.

[115] "Apple: Maximizing battery life and lifespan." `http://www.apple.com/batteries/maximizing-performance/`. Accessed: August 2016.

[116] Q. Wang, P. Ping, X. Zhao, G. Chu, J. Sun, and C. Chen, "Thermal runaway caused fire and explosion of lithium ion battery," *Journal of Power Sources*, vol. 208, pp. 210–224, 2012.

[117] "ERG Materials & Aerospace." `http://www.ergaerospace.com/Descriptors.htm`. Accessed: June 2017.

[118] H. Saomoto and J. Katagiri, "Direct comparison of hydraulic tortuosity and electric tortuosity based on finite element analysis," *Theoretical and Applied Mechanics Letters*, vol. 5, no. 5, pp. 177–180, 2015.

[119] D. Feng and L. Holland, "A dc method for the absolute determination of conductivities of the primary standard kcl solutions from 0 c to 50 c," *Journal of Research of the National Institute of Standards and Technology*, vol. 99, no. 3, 1994.

[120] D. B. Roitman, J. McAlister, and F. L. Oaks, "Composition characterization of methanesulfonic acid," *Journal of Chemical and Engineering Data*, vol. 39, no. 1, pp. 56–60, 1994.

[121] F. Wandschneider, S. Röhm, P. Fischer, K. Pinkwart, J. Tübke, and H. Nirschl, "A multi-stack simulation of shunt currents in vanadium redox flow batteries," *Journal of Power Sources*, vol. 261, pp. 64–74, 2014.

[122] P. Arora and Z. Zhang, "Battery separators," *Chemical Reviews*, vol. 104, no. 10, pp. 4419–4462, 2004.

[123] C. T. J. Wreesmann, "Reasons for raising the maximum acceptable daily intake of edta and the benefits for iron fortification of foods for children 6–24 months of age," *Maternal & Child Nutrition*, vol. 10, no. 4, pp. 481–495, 2014.

[124] G. Darabizad, M. S. Rahmanifar, M. F. Mousavi, and A. Pendashteh, "Electrodeposition of morphology-and size-tuned pbo_2 nanostructures in the presence of pvp and their electrochemical studies," *Materials Chemistry and Physics*, vol. 156, pp. 121–128, 2015.

[125] T. Seipp, S. Berthold, J. Burfeind, and L. Kopietz, "Cell and cell stack of a redox flow battery," July 4 2014. US Patent App. 14/905,025.